



ISSN 1605-2730

# **MATERIALS PHYSICS AND MECHANICS**

**Vol. 42, No. 2, 2019**

# MATERIALS PHYSICS AND MECHANICS

## Principal Editors:

**Dmitrii Indeitsev**  
*Institute of Problems of Mechanical Engineering  
of the Russian Academy of Science (RAS), Russia*

**Andrei Rudskoi**  
*Peter the Great St.Petersburg Polytechnic University, Russia*

## Founder and Honorary Editor: Ilya Ovid'ko (1961-2017)

*Institute of Problems of Mechanical Engineering  
of the Russian Academy of Sciences (RAS), Russia*

## Associate Editors:

**Anna Kolesnikova**  
*Institute of Problems of Mechanical Engineering  
of the Russian Academy of Sciences (RAS), Russia*

**Alexander Nemov**  
*Peter the Great St.Petersburg Polytechnic University, Russia*

## Editorial Board:

**E.C. Aifantis**  
*Aristotle University of Thessaloniki, Greece*

**K.E. Aifantis**  
*University of Florida, USA*

**U. Balachandran**  
*Argonne National Laboratory, USA*

**A. Bellosi**  
*Research Institute for Ceramics Technology, Italy*

**A.K. Belyaev**  
*Institute of Problems of Mechanical Engineering (RAS), Russia*

**S.V. Bobylev**  
*Institute of Problems of Mechanical Engineering (RAS), Russia*

**A.I. Borovkov**  
*Peter the Great St.Petersburg Polytechnic University, Russia*

**G.-M. Chow**  
*National University of Singapore, Singapore*

**Yu. Estrin**  
*Monash University, Australia*

**A.B. Freidin**  
*Institute of Problems of Mechanical Engineering (RAS), Russia*

**Y. Gogotsi**  
*Drexel University, USA*

**I.G. Goryacheva**  
*Institute of Problems of Mechanics (RAS), Russia*

**D. Hui**  
*University of New Orleans, USA*

**G. Kiriakidis**  
*IESL/FORTH, Greece*

**D.M. Klimov**  
*Institute of Problems of Mechanics (RAS), Russia*

**G.E. Kodzhaspirov**  
*Peter the Great St.Petersburg Polytechnic University, Russia*

**S.A. Kukushkin**  
*Institute of Problems of Mechanical Engineering (RAS), Russia*

**T.G. Langdon**  
*University of Southampton, U.K.*

**V.P. Matveenko**  
*Institute of Continuous Media Mechanics (RAS), Russia*

**A.I. Melker**  
*Peter the Great St.Petersburg Polytechnic University, Russia*

**Yu.I. Meshcheryakov**  
*Institute of Problems of Mechanical Engineering (RAS), Russia*

**N.F. Morozov**  
*St.Petersburg State University, Russia*

**R.R. Mulyukov**  
*Institute for Metals Superplasticity Problems (RAS), Russia*

**Yu.V. Petrov**  
*St.Petersburg State University, Russia*

**N.M. Pugno**  
*Politecnico di Torino, Italy*

**B.B. Rath**  
*Naval Research Laboratory, USA*

**A.E. Romanov**  
*Ioffe Physico-Technical Institute (RAS), Russia*

**A.M. Sastry**  
*University of Michigan, Ann Arbor, USA*

**B.A. Schrefler**  
*University of Padua, Italy*

**N.V. Skiba**  
*Institute of Problems of Mechanics (RAS), Russia*

**A.G. Sheinerman**  
*Institute of Problems of Mechanics (RAS), Russia*

**R.Z. Valiev**  
*Ufa State Aviation Technical University, Russia*

**K. Zhou**  
*Nanyang Technological University, Singapore*

## "Materials Physics and Mechanics" Editorial Office:

**Phone:** +7(812)591 65 28 **E-mail:** mpmjournal@spbstu.ru **Web-site:** <http://www.mpm.spbstu.ru>

International scientific journal "Materials Physics and Mechanics" is published by Peter the Great St.Petersburg Polytechnic University in collaboration with Institute of Problems of Mechanical Engineering of the Russian Academy of Sciences in both hard copy and electronic versions.

The journal provides an international medium for the publication of reviews and original research papers written in English and focused on the following topics:

- Mechanics of composite and nanostructured materials.
- Physics of strength and plasticity of composite and nanostructured materials.
- Mechanics of deformation and fracture processes in conventional materials (solids).
- Physics of strength and plasticity of conventional materials (solids).
- Physics and mechanics of defects in composite, nanostructured, and conventional materials.
- Mechanics and physics of materials in coupled fields.

Owner organizations: Peter the Great St. Petersburg Polytechnic University; Institute of Problems of Mechanical Engineering RAS.

*Materials Physics and Mechanics is indexed in Chemical Abstracts, Cambridge Scientific Abstracts, Web of Science Emerging Sources Citation Index (ESCI) and Elsevier Bibliographic Databases (in particular, SCOPUS).*



# **МЕХАНИКА И ФИЗИКА МАТЕРИАЛОВ**

## **Materials Physics and Mechanics**

**Том 42, номер 2, 2019 год**

Учредители:

ФГАОУ ВО «Санкт-Петербургский политехнический университет Петра Великого»  
ФГБУН «Институт проблем машиноведения Российской Академии Наук»

## Редакционная коллегия журнала

### Главные редакторы:

д.ф.-м.н., чл.-корр. РАН **Д.А. Индейцев**  
Институт проблем машиноведения Российской Академии Наук  
(РАН)

д.т.н., академик РАН **А.И. Рудской**  
Санкт-Петербургский политехнический университет  
Петра Великого

**Основатель и почетный редактор:** д.ф.-м.н. **И.А. Овидько (1961-2017)**

Институт проблем машиноведения Российской Академии Наук (РАН)

### Ответственные редакторы

д.ф.-м.н. **А.Л. Колесникова**  
Институт проблем машиноведения Российской Академии Наук  
(РАН)

к.т.н. **А.С. Немов**  
Санкт-Петербургский политехнический университет Петра  
Великого

### Международная редакционная коллегия:

д.ф.-м.н., проф. **А.К. Беляев**  
Институт проблем машиноведения РАН, Россия  
д.ф.-м.н. **С.В. Бобылев**  
Институт проблем машиноведения РАН, Россия  
к.т.н., проф. **А.И. Боровков**  
Санкт-Петербургский политехнический у-т Петра Великого, Россия  
д.ф.-м.н., проф. **Р.З. Валнев**  
Уфимский государственный технический университет, Россия  
д.ф.-м.н., академик РАН **И.Г. Горячева**  
Институт проблем механики РАН, Россия  
д.ф.-м.н., академик РАН **Д.М. Климов**  
Институт проблем механики РАН, Россия  
д.т.н., проф. **Г.Е. Коджаспиров**  
Санкт-Петербургский политехнический у-т Петра Великого, Россия  
д.ф.-м.н., проф. **С.А. Кукушкин**  
Институт проблем машиноведения РАН, Россия  
д.ф.-м.н., академик РАН **В.П. Матвеев**  
Институт механики сплошных сред РАН, Россия  
д.ф.-м.н., проф. **А.И. Мелькер**  
Санкт-Петербургский политехнический у-т Петра Великого, Россия  
д.ф.-м.н., проф. **Ю.И. Мещеряков**  
Институт проблем машиноведения РАН, Россия  
д.ф.-м.н., академик РАН **Н.Ф. Морозов**  
Санкт-Петербургский государственный университет, Россия  
д.ф.-м.н., чл.-корр. РАН **Р.Р. Мулюков**  
Институт проблем сверхпластичности металлов РАН, Россия  
д.ф.-м.н., чл.-корр. РАН **Ю.В. Петров**  
Санкт-Петербургский государственный университет, Россия  
д.ф.-м.н., проф. **А.Е. Романов**  
Физико-технический институт им. А.Ф. Иоффе РАН, Россия  
д.ф.-м.н. **Н.В. Скиба**  
Институт проблем машиноведения РАН, Россия  
д.ф.-м.н., проф. **А.Б. Фрейдли**  
Институт проблем машиноведения РАН, Россия  
д.ф.-м.н. **А.Г. Шейнман**  
Институт проблем машиноведения РАН, Россия

Prof., Dr. **E.C. Aifantis**  
Aristotle University of Thessaloniki, Greece  
Dr. **K.E. Aifantis**  
University of Florida, USA  
Dr. **U. Balachandran**  
Argonne National Laboratory, USA  
Dr. **A. Bellosi**  
Research Institute for Ceramics Technology, Italy  
Prof., Dr. **G.-M. Chow**  
National University of Singapore, Singapore  
Prof., Dr. **Yu. Estrin**  
Monash University, Australia  
Prof., Dr. **Y. Gogotsi**  
Drexel University, USA  
Prof., Dr. **D. Hui**  
University of New Orleans, USA  
Prof., Dr. **G. Kiriakidis**  
IESL/FORTH, Greece  
Prof., Dr. **T.G. Langdon**  
University of Southampton, UK  
Prof., Dr. **N.M. Pugno**  
Politecnico di Torino, Italy  
Dr. **B.B. Rath**  
Naval Research Laboratory, USA  
Prof., Dr. **A.M. Sastry**  
University of Michigan, Ann Arbor, USA  
Prof., Dr. **B.A. Schrefler**  
University of Padua, Italy  
Prof. Dr. **K. Zhou**  
Nanyang Technological University, Singapore

Тел.: +7(812)591 65 28 E-mail: mpmjournal@spbstu.ru Web-site: <http://www.mpm.spbstu.ru>

### Тематика журнала

Международный научный журнал "Materials Physics and Mechanics" издается Санкт-Петербургским политехническим университетом Петра Великого в сотрудничестве с Институтом проблем машиноведения Российской Академии Наук в печатном виде и электронной форме. Журнал публикует обзорные и оригинальные научные статьи на английском языке по следующим тематикам:

- Механика композиционных и наноструктурированных материалов.
- Физика прочности и пластичности композиционных и наноструктурированных материалов.
- Механика процессов деформации и разрушения в традиционных материалах (твердых телах).
- Физика прочности и пластичности традиционных материалов (твердых тел).
- Физика и механика дефектов в композиционных, наноструктурированных и традиционных материалах.
- Механика и физика материалов в связанных полях.

Редколлегия принимает статьи, которые нигде ранее не опубликованы и не направлены для опубликования в другие научные издания. Все представляемые в редакцию журнала "Механика и физика материалов" статьи рецензируются. Статьи могут отправляться авторам на доработку. Не принятые к опубликованию статьи авторам не возвращаются.

*Журнал "Механика и физика материалов" ("Materials Physics and Mechanics") включен в систему цитирования Web of Science Emerging Sources Citation Index (ESCI), SCOPUS и PИИЦ.*

© 2019, Санкт-Петербургский политехнический университет Петра Великого

© 2019, Институт проблем машиноведения Российской Академии Наук

## Contents

<b>Nucleation of islands with vertical or truncated corner facets in vapor-liquid-solid nanowires.....</b>	<b>159-164</b>
V.G. Dubrovskii, Zh.V. Sokolova, M.V. Rylkova, A.A. Zhiglinsky	
<b>Densification rate influence on nanopowder compactibility .....</b>	<b>165-177</b>
G.Sh. Boltachev, E.A. Chingina, A.V. Spirin, N.B. Volkov	
<b>Mechanism of molecule migration of carbon and silicon monoxides in silicon carbide crystal .....</b>	<b>178-182</b>
S.A. Kukushkin, A.V. Osipov, E.V. Osipova	
<b>Artifacts of stress relaxation technique to fit recovery activation parameters for low carbon steels.....</b>	<b>183-190</b>
Alexander A. Vasilyev, Semen F. Sokolov, Nikita A. Golubkov, Alexander A. Zisman, Dmitry F. Sokolov, Andrey I. Rudskoy	
<b>Bulk Green's functions in one-dimensional unsteady problems of elastic diffusion .....</b>	<b>191-197</b>
L.A. Igumnov, D.V. Tarlakovskii, A.V. Zemskov	
<b>The influence of gamma rays radiation on optically induced luminescence of copper-containing potassium-lithium-borate glass .....</b>	<b>198-203</b>
P.S. Shirshnev, V.A. Spiridonov, D.I. Panov, E.V. Shirshneva-Vaschenko, A.R.Gafarova, R.M. Eremina, A.E. Romanov, V.E. Bougrov	
<b>Boron and nitrogen dopant atoms precise tuning (increment and reduction) of charge-transfer rates in hydrogenated graphene .....</b>	<b>204-210</b>
G.K. Sunnardianto, F. Triawan, A.M. Aamer, S. Hastuty, A.B.D. Nandiyanto, A.G. Abdullah	
<b>The structural transformation and mechanical strength OF Ni, Ti nanowires and Nitinol alloys at various vacancy rates: molecular dynamic study using Cleri-Rosato potential.....</b>	<b>211-223</b>
M.M. Aish	
<b>A molecular dynamics study of the buckling behaviour of graphene-reinforced aluminum nanocomposite plate .....</b>	<b>224-233</b>
Mithilesh K. Dikshit, Gokul S. Nair, Vimal Kumar Pathak, Ashish K. Srivastava	
<b>First principle electronic, magnetic and thermodynamic characterization of heavy fermion ternary rare earth metal alloys.....</b>	<b>234-241</b>
Ashish K. Srivastava, Mithilesh K. Dikshit, Vimal K. Pathak, Lakshya Khurana	
<b>Applied theory for electro-elastic plates with non-homogeneous polarization .....</b>	<b>242-255</b>
A.N. Soloviev, V.A. Chebanenko, P.A. Oganesyanyan, Shih-Fong Chao, Y.-M. Liu	
<b>Boundary element time-harmonic analysis of 3D linear piezoelectric solids.....</b>	<b>256-264</b>
L.A. Igumnov, I.P. Markov, A.V. Boev	



## NUCLEATION OF ISLANDS WITH VERTICAL OR TRUNCATED CORNER FACETS IN VAPOR-LIQUID-SOLID NANOWIRES

V.G. Dubrovskii\*, Zh.V. Sokolova, M.V. Rylkova, A.A. Zhiglinsky

ITMO University, Kronverkskiy pr. 49, 197101 St. Petersburg, Russia

\*e-mail: dubrovskii@mail.ioffe.ru

**Abstract.** We develop a model for nucleation of islands in vapor-liquid-solid nanowires with either vertical or truncated corner facets. Under the assumption of two-dimensional geometry of the growing island, it is shown that the earlier energetic condition for the truncated edge at the growth interface is modified by chemical potential. Therefore, the islands may nucleate at the trijunction during growth even if the truncation is preferred at the no growth conditions on surface energetic grounds. This conclusion may be used as the first step for understanding the peculiar oscillatory behavior of the growth interface and the related crystal phases of III-V nanowires.

**Keywords:** nanowires, vapor-liquid-solid growth, nucleation, truncation, surface energy, chemical potential, contact angle

### 1. Introduction

Vapor-liquid-solid (VLS) III-V nanowires (NWs) are promising as fundamental building blocks for nanoscience and nanotechnology [1,2]. In particular, these NWs enable dislocation-free growth of highly mismatched semiconductor materials in III-V heterostructures or on silicon substrates [3,4], which is unattainable in thin films or even quantum dots [5]. VLS III-V NWs exhibit interesting properties, such as the zincblende-wurtzite (ZB-WZ) polytypism which can be controlled by the growth parameter tuning [6]. Earlier theoretical models for Au-catalyzed [7-9] or self-catalyzed [10,11] VLS growth of III-V NWs considered planar liquid-solid interface at the NW top, and nucleation of two-dimensional (2D) islands with vertical sidewalls. For such planar geometry, the models of polytypism of Glas *et al.* [12,13] assumed nucleation at the trijunction, where the vapor, liquid and solid phases meet, as the necessary condition for the WZ phase formation. This view gained much support and was widely used for controlling the crystal phases of different III-V NWs (see, for example, Ref. [14] for a review)

Further progress in understanding the VLS growth of NWs was achieved through *in situ* monitoring inside a transmission electron microscope (TEM) [15-17]. In particular, it was found that VLS NWs often present a truncated corner facet at the trijunction, whose size oscillates with the period of the monolayer (ML) formation [15]. There is only one theory developed so far that explains the oscillatory behavior of the truncated edge in NWs [15,16] according to which, whenever a truncated facet is present, it never shrinks to zero size. If this is true, 2D islands cannot nucleate at the trijunction [15] and hence the crystal phase should be pure ZB [16]. According to the model of Tersoff [15,16], the occurrence of truncated edge requires a certain condition for the surface energies of different interfaces (the inclined wetted facet should be energetically preferred to the vertical non-wetted one). This condition depends on the contact angle of the droplet catalyzing the VLS growth of a given NW. Truncated geometry is preferred for larger contact angles and this is often believed to explain the

[http://dx.doi.org/10.18720/MPM.4222019\\_1](http://dx.doi.org/10.18720/MPM.4222019_1)

© 2019, Peter the Great St. Petersburg Polytechnic University

© 2019, Institute of Problems of Mechanical Engineering RAS

presence or absence of polytypism at smaller or larger contact angles, respectively [16,18]. This view is very different from the original model of Glas *et al.* [12] which assumes nucleation at the trijunction for both WZ and ZB types of 2D islands.

However, it is not impossible the truncation starts from zero size at the beginning of each ML growth cycle and shrinks to zero at the end, reaching substantial values in the middle. The crystal phase of the whole NW must be determined at the moment of nucleation [12]. This explains the importance of answering the question of whether or not the initial nucleation of an island develops the truncated edge. In this work, we try to answer this by considering a simplified model for nucleation of 2D islands with either vertical or truncated corner facets having the ML height. We show that, under this simplifying assumption for geometry, the Tersoff energetic condition for the truncation [15,16] is modified by chemical potential and hence islands with vertical facets may nucleate at the trijunction even if the truncation is preferred when no growth occurs.

## 2. Model

Let us consider nucleation and growth of 2D islands of the ML height  $h$ , assuming only two types of possible lateral facets: vertical solid-vapor (having the surface energy  $\gamma_{ov}$ ), and truncated solid-liquid (having the surface energy  $\gamma_{\theta L}$ ), making the angle  $\theta$  to the vertical. The other surface energies of interest are those of the liquid-vapor interface, with the surface energy  $\gamma_{LV}$ , and the planar solid-liquid interface, with the surface energy  $\gamma_{SL}$ . The contact angle of the droplet is denoted  $\beta$ . The geometry and relevant parameters are illustrated in Fig. 1. The single island can emerge with either (1) vertical non-wetted facet at the trijunction or (2) only truncated facets surrounded by liquid. Generally, the island changes its shape as it grows [17]. Our aim is to compare the free energies of forming the islands in the two configurations and to find out the conditions for the preferred nucleation of the truncated island.

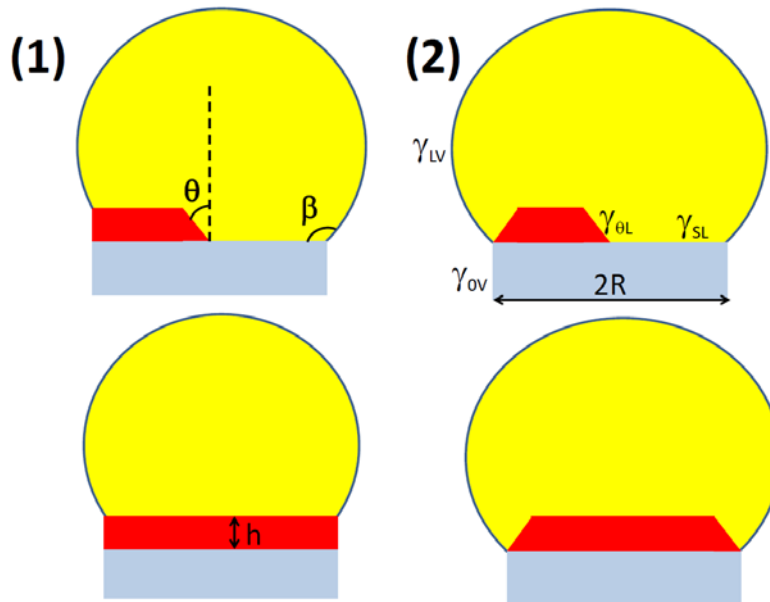


**Fig. 1.** Geometries and parameters of 2D ML islands with vertical (1) and truncated wetted (2) corner facets (top), extending to the full NW MLs (bottom)

Let us introduce the linear size of island  $r$ , its perimeter  $k_1 r$  and surface area  $k_2 r^2$ , with  $k_1$  and  $k_2$  as the corresponding shape constants. These constants may change in the

course of growth, i.e., they generally depend on  $r$ . Let  $\chi k_1 r$  and  $(1-\chi)k_1 r$  be the parts of the island perimeter at the trijunction and away from it, respectively. The fraction of the perimeter at the trijunction also changes as the island grows; in particular,  $\chi \rightarrow 1$  when  $r \rightarrow R$ , where  $R$  is the NW radius.

Quite generally, the free energy of forming the island in configuration (1) is

$$\Delta G_1 = -\Delta\mu \left[ k_2 r^2 h - (1-\chi)k_1 r h^2 \frac{\tan \theta}{2} \right] + (1-\chi)k_1 r h \left( \frac{\gamma_{\theta L}}{\cos \theta} - \gamma_{SL} \tan \theta \right) + \chi k_1 r h (\gamma_{0V} - \gamma_{LV} \sin \beta), \quad (1)$$

where  $\Delta\mu$  is the liquid-solid chemical potential difference per unit volume of the solid. Similarly, for configuration (2) we have

$$\Delta G_2 = -\Delta\mu \left[ k_2 r^2 h - k_1 r h^2 \frac{\tan \theta}{2} \right] + k_1 r h \left( \frac{\gamma_{\theta L}}{\cos \theta} - \gamma_{SL} \tan \theta \right). \quad (2)$$

These expressions show that the volume of the fully truncated island in configuration (2) is smaller than that of the island with vertical corner facet at the trijunction in configuration (1). Therefore, there is a difference in the chemical potential terms in the two cases.

Let us first compare the two formation energies for fully formed MLs, i.e., when  $\chi = 1$  and  $r = R$ . In this case, we obtain

$$\Delta G_2 - \Delta G_1 = k_1 R h \left( \frac{\gamma_{\theta L}}{\cos \theta} + \gamma_{LV} \sin \beta - \gamma_{0V} - \gamma_{SL} \tan \theta + \Delta\mu h \frac{\tan \theta}{2} \right). \quad (3)$$

For the critical nucleus which typically consists of only a few III-V pairs, it is reasonable to assume a fixed shape, i.e.  $r$ -independent shape constants and  $\chi$ . Re-writing equations (1) and (2) as

$$\Delta G_1 = -\Delta\mu k_2 r^2 h + k_1 r h \left\{ (1-\chi) \left( \frac{\gamma_{\theta L}}{\cos \theta} - \gamma_{SL} \tan \theta + \Delta\mu h \frac{\tan \theta}{2} \right) + \chi (\gamma_{0V} - \gamma_{LV} \sin \beta) \right\}, \quad (4)$$

$$\Delta G_2 = -\Delta\mu k_2 r^2 h + k_1 r h \left( \frac{\gamma_{\theta L}}{\cos \theta} - \gamma_{SL} \tan \theta + \Delta\mu h \frac{\tan \theta}{2} \right), \quad (5)$$

we notice that they have the same structure  $\Delta G_k = -Ar^2 + B_k r$ , where only the effective surface energies  $B_k$  are different. Maximizing this in  $r$ , we find the sizes of the critical nuclei  $r_* = B_k / (2A)$  and the corresponding nucleation barriers  $\Delta G_k^* = B_k^2 / (4A)$ . Therefore, the nucleation of the truncated island is preferred when  $B_2 - B_1 < 0$ , or

$$\frac{\gamma_{\theta L}}{\cos \theta} + \gamma_{LV} \sin \beta - \gamma_{0V} - \gamma_{SL} \tan \theta + \Delta\mu h \frac{\tan \theta}{2} < 0. \quad (6)$$

The surface energy term here is exactly identical to the earlier results of Tersoff *et al.* [16,19] and Dubrovskii [18]. However, it is modified by the chemical potential term. The condition for the preferred nucleation of the truncated islands is also identical to the one for the full MLs, as seen from comparing Eqs. (6) and (3).

### 3. Discussion

The last term in Eq. (6) is not at all negligibly small under the typical growth conditions. Assuming, for example, a modest  $\Delta\mu = 100$  meV per GaAs pair for the parameters of GaAs ( $h = 0.326$  nm, the elementary volume per GaAs pair  $\Omega_s = 0.0452$  nm<sup>3</sup>) and  $\theta = 50^\circ$ , we obtain a substantial correction for the surface energy,  $\Delta\mu h (\tan \theta) / 2 \cong 0.07$  J/m<sup>2</sup>.

Therefore, the condition for forming the truncated corner facet is given by

$$c + \Delta\mu h \frac{\tan \theta}{2} < 0, \quad (7)$$

where  $c = \gamma_{oL} / \cos \theta + \gamma_{LV} \sin \beta - \gamma_{oV} - \gamma_{SL} \tan \theta$  as introduced earlier [15,16,18,19], not just  $c < 0$ . The latter is valid only at zero chemical potential corresponding to the "no growth" conditions. Our inequality given by Eq. (7) contains the chemical potential term which may overcome the capillary forces. Hence, there is a range of contact angles  $\beta$  where  $\Delta\gamma$  is negative but the corner facet remains vertical and the growth interface is planar.

Let  $\beta_*$  be the contact angle of the droplet corresponding to  $c = 0$ , i.e. where the truncation starts to develop at the no-growth conditions ( $\Delta\mu = 0$ ). Then it is easy to find the difference  $\Delta\beta = \beta_1 - \beta_*$ , where  $\beta_1$  is the contact angle at which the truncated corner starts in a growing NW at the moment of nucleation for a given  $\Delta\mu$  (in other words, where the truncation never shrinks to zero size as in the Tersoff model [15,16]). Indeed,  $\Delta c$  can be related to  $\Delta\beta$  as  $\Delta c = -\gamma_{LV} |\cos \beta_*| \Delta\beta$  (assuming that  $\beta_* > \pi/2$ ) and the condition  $\Delta c + \Delta\mu h \tan \theta / 2 = 0$  is reduced to the linear relationship between  $\Delta\beta$  and  $\Delta\mu$

$$\Delta\beta = h \frac{\tan \theta}{2} \frac{\Delta\mu}{\gamma_{LV} |\cos \beta_*|}. \quad (8)$$

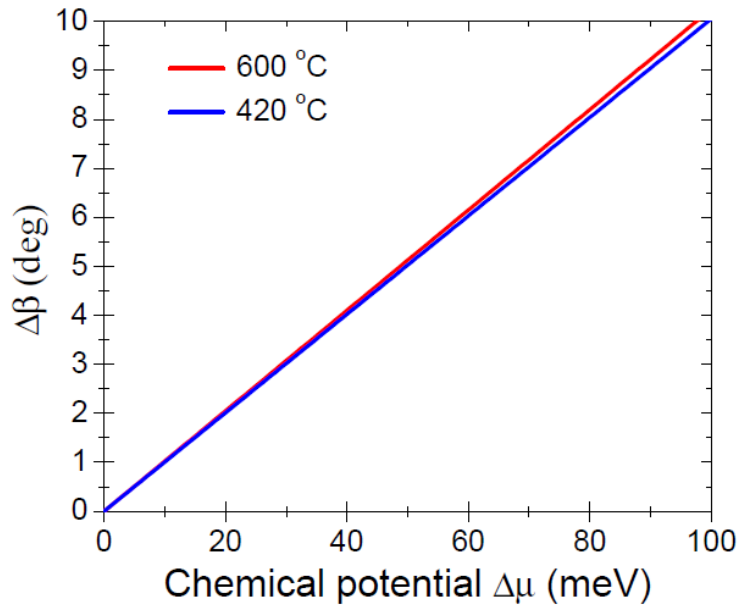


**Fig. 2.** Linear dependences of the range of contact angles with zero initial truncation  $\Delta\beta$  on the chemical potential during growth  $\Delta\mu$  for the parameters of GaAs NWs listed in the Table 1 for the growth temperatures of 600 °C and 420 °C

Figure 2 shows the linear correlation of  $\Delta\beta$  with  $\Delta\mu$  for the parameters of GaAs NWs listed in the Table 1. We took a value of 50 °C for the truncation angle  $\theta$  in this example, which can be further refined by the *in situ* TEM measurements. As for the surface energy of the droplet,  $\gamma_{LV}$ , it should not be significantly different for Au-catalyzed or Ga-catalyzed GaAs NWs due to the surface enrichment by the lower energy liquid gallium [18]. The linear correlation is only slightly influenced by the growth temperature due to the weak temperature dependence of the surface energy of liquid gallium [20]. Finally, this linear dependence can be used for obtaining or refining some unknowns, such as  $\theta$  or  $\gamma_{LV}$  (in the Au-catalyzed

case) from the measured  $\Delta\beta$  at the known chemical potentials (which can be deduced from the NW growth rates [21,22]). It is seen that, with our parameters, the  $\Delta\beta$  reaches a large value of about  $10^\circ$  for  $\Delta\mu = 100$  meV.

Table 1. Parameters of GaAs NWs used in Fig. 2

Elementary volume $\Omega_s$ (nm <sup>3</sup> )	Monolayer height $h$ (nm)	Critical contact angle at no-growth $\beta_*$ (deg)	Truncation angle $\theta$ (deg)	Droplet surface energy $\gamma_{LV}$ at 600°C (J/m <sup>2</sup> )	Droplet surface energy $\gamma_{LV}$ at 420°C (J/m <sup>2</sup> )
0.0452	0.326	125	50	0.671	0.684

In conclusion, our simple model predicts the existence of a range of contact angles for which 2D islands nucleate with vertical corner facet at the trijunction even if the truncation is preferred on surface energetic grounds. This supports the earlier models for the ZB-WZ polytypism in III-V NWs, with nucleation at the trijunction [12,13]. A more comprehensive treatment should include a more macroscopic truncation, the possibility to transfer the building material to the island in a kinetic treatment, and possible stopping effect at low arsenic concentrations. These interesting problems will be considered elsewhere.

**Acknowledgement.** The authors thank the Ministry of Science and Higher Education of the Russian Federation for financial support under grant 14.587.21.0040 (project ID RFMEFI58717X0040).

## References

- [1] Zhang A, Zheng G, Lieber CM. *Nanowires: Building blocks for nanoscience and nanotechnology*. Springer; 2016.
- [2] Dubrovskii VG. Theory of VLS growth of compound semiconductors. In: Fontcuberta i Morral A, Dayeh SA, Jagadish C. (eds.) *Semiconductors and Semimetals*. Burlington: Academic Press. 2015;93: 1-78.
- [3] Ng KW, Ko WS, Tran T-TD, Chen R, Nazarenko MV, Lu F, Dubrovskii VG, Kamp M, Forchel A, Chang-Hasnain CJ. Unconventional Growth Mechanism for Monolithic Integration of III-V on Silicon. *ACS Nano*. 2013;7(1): 100-107.
- [4] Glas F. Critical dimensions for the plastic relaxation of strained axial heterostructures in free-standing nanowires. *Physical Review B*. 2006;74(12): 121302 (R).
- [5] Cirlin GE, Dubrovskii VG, Petrov VN, Polyakov NK, Korneeva NP, Demidov VN, Golubok AO, Masalov SA, Kurochkin DV, Gorbenko OM, Komyak NI, Ustinov VM, Egorov AY, Kovsh AR, Maximov MV, Tsatusul'nikov AF, Volovik BV, Zhukov AE, Kop'ev PS, Alferov ZI, Ledentsov NN, Grundmann M, Bimberg D. Formation of InAs quantum dots on a silicon (100) surface. *Semiconductor Science & Technology*. 1998;13(11): 1262-1265.
- [6] Dick KA, Caroff P, Bolinsson J, Messing ME, Johansson J, Deppert K, Wallenberg LR, Samuelson L. Control of III-V nanowire crystal structure by growth parameter tuning. *Semiconductor Science and Technology*. 2010;25(2): 024009.
- [7] Dubrovskii VG, Soshnikov IP, Cirlin GE, Tonkikh AA, Samsonenko YB, Sibirev NV, Ustinov VM. On the non-monotonic lateral size dependence of the height of GaAs nanowhiskers grown by molecular beam epitaxy at high temperature. *Physica Status Solidi B*. 2004;241(7): R30-R33.

- [8] Dubrovskii VG, Sibirev NV, Cirlin GE. Kinetic model of the growth of nanodimensional whiskers by the vapor-liquid-crystal mechanism. *Technical Physics Letters*. 2004;30(8): 682-686.
- [9] Dubrovskii VG, Soshnikov IP, Sibirev NV, Cirlin GE, Ustinov VM. Growth of GaAs nanoscale whiskers by magnetron sputtering deposition. *Journal of Crystal Growth*. 2006;289(1): 31-36.
- [10] Colombo C, Spirkoska D, Frimmer M, Abstreiter G, Morral AF. Ga-assisted catalyst-free growth mechanism of GaAs nanowires by molecular beam epitaxy. *Physical Review B*. 2008;77(15): 155326.
- [11] Matteini F, Dubrovskii VG, Ruffer D, Tütüncüoğlu G, Fontana Y, Morral AF. Tailoring the diameter and density of self-catalyzed GaAs nanowires on silicon. *Nanotechnology*. 2015;26(10): 105603.
- [12] Glas F, Harmand JC, Patriarche G. Why does wurtzite form in nanowires of III-V zinc blende semiconductors? *Physical Review Letters*. 2007;99(14): 146101.
- [13] Dubrovskii VG, Sibirev NV, Harmand JC, Glas F. Growth kinetics and crystal structure of semiconductor nanowires. *Physical Review B*. 2008;78(23): 235301.
- [14] Dubrovskii VG. *Nucleation theory and growth of nanostructures*. Berlin: Springer; 2014.
- [15] Wen CY, Tersoff J, Hillerich K, Reuter MC, Park JH, Kodambaka S, Stach EA, Ross FM. Periodically Changing Morphology of the Growth Interface in Si, Ge, and GaP Nanowires. *Physical Review Letters*. 2011;107(2): 025503.
- [16] Jacobsson D, Panciera F, Tersoff J, Reuter MC, Lehmann S, Hofmann S, Dick KA, Ross FM. Interface dynamics and crystal phase switching in GaAs nanowires. *Nature*. 2016;531: 317-322.
- [17] Harmand JC, Patriarche G, Glas F, Panciera F, Florea I, Maurice JL, Travers L, Ollivier Y. Atomic step flow on a nanofacet. *Physical Review Letters*. 2018;121: 166101.
- [18] Dubrovskii VG. Refinement of nucleation theory for vapor-liquid-solid nanowires. *Crystal Growth & Design*. 2017;17(5): 2589-2593.
- [19] Ross FM, Tersoff J, Reuter MC. Sawtooth faceting in silicon nanowires. *Physical Review Letters*. 2005;95: 146104.
- [20] Dubrovskii VG, Sibirev NV, Cirlin GE, Soshnikov IP, Chen WH, Larde R, Cadel E, Pareige P, Xu T, Grandidier B, Nys JP, Stievenard D, Moewe M, Chuang LC, Chang-Hasnain C. Gibbs-Thomson and diffusion-induced contributions to the growth rate of Si, InP and GaAs nanowires. *Physical Review B*. 2009;79(20): 205316.
- [21] Dubrovskii VG, Grecenkov J. Zeldovich nucleation rate, self-consistency renormalization, and crystal phase of Au-catalyzed GaAs nanowires. *Crystal Growth & Design*. 2015;15(1): 340-347.
- [22] Glas F, Ramdani MR, Patriarche G, Harmand JC. Predictive modeling of self-catalyzed III-V nanowire growth. *Physical Review B*. 2013;88(19): 195304.

## DENSIFICATION RATE INFLUENCE ON NANOPOWDER COMPACTIBILITY

G.Sh. Boltachev<sup>\*</sup>, E.A. Chingina, A.V. Spirin, N.B. Volkov

Institute of Electrophysics, Ural Branch of RAS, Amundsen str. 106, Ekaterinburg, Russia

\*e-mail: grey@iep.uran.ru

**Abstract.** The paper concerns processes of high-speed compaction of nanosized powders. The processes of uniform and uniaxial compaction have been simulated by the granular dynamics method. Nanoparticles interaction, in addition to known contact laws, includes dispersive attraction, formation of a strong interparticle bonding as well as the forces caused by viscous stresses in the contact region. For different densification rates, the densification curves (pressure vs. density) have been calculated. Relaxation of the stresses after the compression stage has been analyzed. The densification curves analysis allows us to suggest the dependence of compaction pressure as a function of strain rate in the form of  $p \propto v^{1/8}$ . The rate dependence obtained has been applied for interpretation of experimental data concerning high-speed processes of magnetic pulsed compaction of nanopowders.

**Keywords:** nanosized powders, granular dynamics method, high-speed compaction

### 1. Introduction

The nanopowder cold compaction is a very important stage of novel nanostructured materials production by the powder metallurgy [1,2]. As known, nanopowders in contrast to coarse-grained materials are very hard to densify due to the strong interparticle "friction", which is caused by the intense dispersion attraction, and agglomeration of particles [2,3,4]. To achieve a proper compact density for sintering the high quality, defect-free ceramic article, applying the high pressure of about several gigapascals is required. Such high pressures can even exceed the durability of pressing tools [2,3,5]. Thus, the theoretical description of powder body and reliable forecasting the compaction processes take on high topicality.

The present paper is devoted to development of theoretical description of oxide nanosized powders cold compaction processes [1,2] by taking into account the densification rate influence on the nanopowder compactibility. The microscopic study of nanopowders high-speed compaction processes is performed in the frameworks of the granular dynamics method [6,7]. This method is of interest due to the oxide nanoparticles, for example, produced by the method of wires electric explosion [8] or target laser evaporation [9], usually have high strength properties and a spherical form. Therefore, such powders are the most convenient object for simulations. Nowadays the granular dynamics method is extensively used for description of compaction processes of different micro- and nanopowders [6,7,10,11]. However quasistatic compaction processes are investigated as a rule. After every step of model cell deformation the new equilibrium locations of particles are determined during a large number of equilibration steps [6,7]. At the same time, in view of necessity to achieve extremely large compaction pressures the magnetic pulsed methods [2,5] attract a great attention. These methods allow increasing the pressure into compacts owing to the inertial effects. The relative rate of compact densification is here about  $0.1 \mu\text{s}^{-1}$ . It is known that

dynamical yield strength is not equal to static one. For example, the yield strength of metal at high-speed loading can exceed the static limit by several times [12-14]. Corresponding studies of the rate influence on the nanopowders compaction processes have not been conducted yet.

## 2. Details of the granular dynamics method

We simulate the dynamical processes of uniform and uniaxial pressing, which are characterized with the relative densification rate  $\nu = (1/\rho)(d\rho/dt)$ , where  $\rho$  is the density and  $t$  is the time, from value  $10^1 \mu\text{s}^{-1}$  up to  $10^4 \mu\text{s}^{-1}$ . Such high rates are caused by numerical troubles, i.e., the large times for simulations of small-rate processes. As can be seen below, the simulation results obtained are easy extrapolated to the region of smaller rates.

The model cell has a form of cube with volume  $V_{\text{cell}} = L_{\text{cell}}^3$  in the case of uniform compaction processes and a form of rectangular parallelepiped with a base  $L_{\text{cell}}^2$  and a height  $H_z$  along the direction of pressing in the case on uniaxial compaction. The density is implied as a relative volume of the model cell occupied by the particles, i.e.,  $\rho = N_p(\pi/6)d_g^3/V_{\text{cell}}$ , where  $N_p = 2000$  is the number of particles in the cell,  $d_g$  is the particle diameter. Periodic boundary conditions are used on all the sides of the cell. For initial packing generation, the algorithm defined in [6] is used, which allows us to create isotropic and uniform structures in a form of the connected 3D-periodic cluster. The initial density is  $\rho_0 = 0.24$ . The system deformation is performed by simultaneous changes of cell sizes (all sizes at uniform pressing or the value of  $H_z$  only at uniaxial pressing) and proportional rescaling of corresponding particles coordinates. The relative displacements and rotations of particles are determined by the usual equations

$$m \frac{d^2 r}{dt^2} = f, \quad J \frac{d^2 \theta}{dt^2} = M, \quad (1)$$

where  $m = (\pi/6)\rho_m d_g^3$  is the particle mass,  $\rho_m$  is the density of the particle material,  $f$  and  $M$  are the total force and torque caused by other particles,  $J = md_g^2/10$  is the inertia moment,  $\theta$  is the rotation angle. The Verlet algorithm [15] is applied for the numerical solve of Eq. (1).

The stress tensor  $\sigma_{ij}$  averaged over the model cell is calculated by the known expression [6,10,11]

$$\sigma_{ij} = \frac{-1}{V_{\text{cell}}} \sum_{k < l} f_i^{(k,l)} r_j^{(k,l)}, \quad (2)$$

where the summation is performed over all pairs of interacting particles ( $k, l$ );  $f^{(k,l)}$  is the total force affecting the particle "k" from the particle "l";  $r^{(k,l)}$  is the vector connecting the centers of the particles. The particle interactions described in detail elsewhere [6,7] include the elastic repulsion (modified Hertz law), the "friction" forces (Cattaneo – Mindlin and Jäger laws), the dispersive attraction force (Hamaker's formula), and the contact elasticity of flexure because of strong interparticle bonding. Alumina is implied as the particle material for which, in particular, the Young modulus  $E$  is 382 GPa and the Poisson ratio  $\nu$  is 0.25. Other parameters of interaction laws are close to the parameters of system II in Refs. [6,7], which imitates alumina nanopowders [16] with particle diameter  $d_g = 10$  nm.

The high value of speed of modeled processes requires taking into account the viscous stresses in the vicinity of the contact area of particles. Using the similarity of Hooke's elastic law and the Navier – Stokes equations the authors of Ref. [17] obtained the rigorous solution of the problem on contact interaction of viscoelastic spheres. In general case the influence of the viscous stresses has a form [17,18]

$$f_{visc} = A \frac{df_e}{d\xi} \frac{d\xi}{dt}, \quad (3)$$

where  $f_{visc}$  is the total force of the viscous stresses,  $f_e$  is the elastic force,  $\xi$  is the variable, which describes the body deformation, and the coefficient  $A$  neglecting the bulk viscosity is described as:

$$A = \frac{\eta(1-\nu^2)(1-2\nu)}{3E\nu^2}. \quad (4)$$

The shear viscosity coefficient  $\eta$  is estimated [19] by the known data on ultrasound damping into alumina. The coefficient of damping [20] into the isotropic medium  $\gamma_t = \eta\omega^2 / (2\rho_m c_t^3)$ , where  $\omega$  and  $c_t$  are the frequency and speed of sound. Using the value  $\gamma_t \cong 230$  dB/m at the frequency of  $\omega/2\pi = 1.0$  GHz [21] the shear viscosity coefficient  $\eta$  for alumina of 0.001 Pa s was obtained.

Starting from Eq. (3) it is not difficult to write all expressions which describe the interactions of viscoelastic spherical particles. For example, for linearized tangential force of "friction" we have

$$\frac{f_t}{E} = c_m a \delta + A c_m a \frac{d\delta}{dt}, \quad c_m = \frac{4}{(2-\nu)(1+\nu)}, \quad (5)$$

where  $\delta$  is the relative tangential displacement of contacting particles,  $a = \sqrt{hd_g} / 2$  is the contact spot radius,  $h = d_g - r$  is the depth of particle overlapping.

The characteristic time,  $T = [(\pi\rho_m d_g^2) / (6E)]^{1/2}$ , which transforms Eqs. (1) to dimensionless form, is equal to  $0.74 \times 10^{-12}$  s for our systems. The reduced time step of the numerical solving the equations (1) is  $h_t = 0.04 T$ .

### 3. Simulation results

With the purpose of statistical averaging we have performed 10 independent calculations for each compression rate. Figure 1 presents the time-dependent hydrostatic pressure  $p = -\text{Sp}(\sigma_{ij})$  averaged and typical calculation curves for uniform compaction process with the compression rate  $\nu = 100 \mu\text{s}^{-1}$ . It is helpful to note that the initial structures are being generated by the algorithm of Ref. [6], which places the neighboring particles at equilibrium distances when attraction compensates repulsion. However the algorithm requires a preliminary relaxation step. It is needed since the dispersion forces between further particles are not taken into account in the algorithm that results in slight fluctuations of particles in the initial structure. In order to extinguish the fluctuations, initially generated structure relaxes for 5 ns (see the inset in Fig. 1).

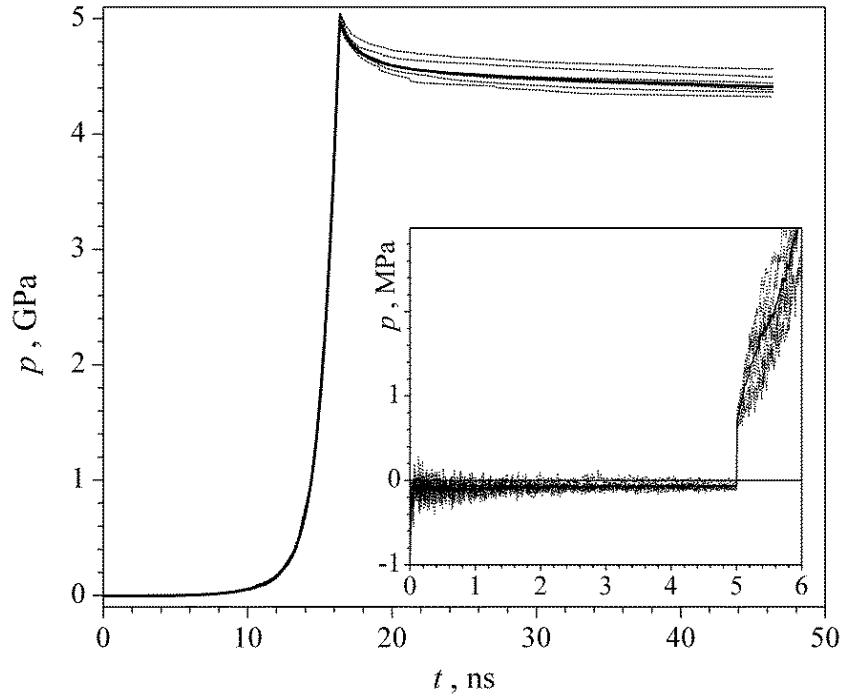


**Fig. 1.** Time dependence of pressure for the densification rate  $\nu = 100 \mu\text{s}^{-1}$ . Dotted lines are examples of calculation curves; solid line is the average over 10 independent calculations. Inset shows the period of the preliminary relaxation (5 ns) and the beginning of the compression

Compression of the model cell was performed up to the pressure  $p = 5$  GPa for uniform pressing and up to the  $p_z = -\sigma_{zz} = 5$  GPa for uniaxial pressing. After that the system was relaxed during 30 ns. A considerable reduction of stresses is observed at the relaxation stage after pressing. This reduction for the hydrostatic pressure (after uniform compaction) and for the pressure  $p_z$  (after uniaxial compaction) is well approximated by an expression

$$p(t) = p_0 + p_1 \exp\left(\frac{-t}{\tau_1}\right) + p_2 \exp\left(\frac{-t}{\tau_2}\right). \quad (6)$$

The numerical analysis has showed that post-compression relaxation proceeds in two stages: "rapid" with a characteristic time  $\tau_1$  of about tenths of nanoseconds, and "slow" with characteristic time of about  $\tau_2 = 18$  ns.

Figure 2 shows the total pressure drops after compaction processes,  $\Delta p$ , estimated by the approximations (6). The dependences of  $\Delta p$  on the compression rate are approximated as  $\Delta p = (k_1 \nu)^{k_2}$ , (7) with parameters:  $k_1 = 0.020 \mu\text{s}$ ,  $k_2 = 0.17$  for the uniaxial process, and  $k_1 = 7.4 \times 10^{-4} \mu\text{s}$ ,  $k_2 = 0.19$  for the uniform process. The extrapolation to the rate value of  $0.1 \mu\text{s}^{-1}$  (see Fig. 2) gives  $\Delta p \cong 350$  MPa for the uniaxial compaction, and 160 MPa for the uniform compaction. These values can be considered as preliminary estimates for the rate influence on the compaction curves at the processes of magnetic pulsed compaction [2,5].

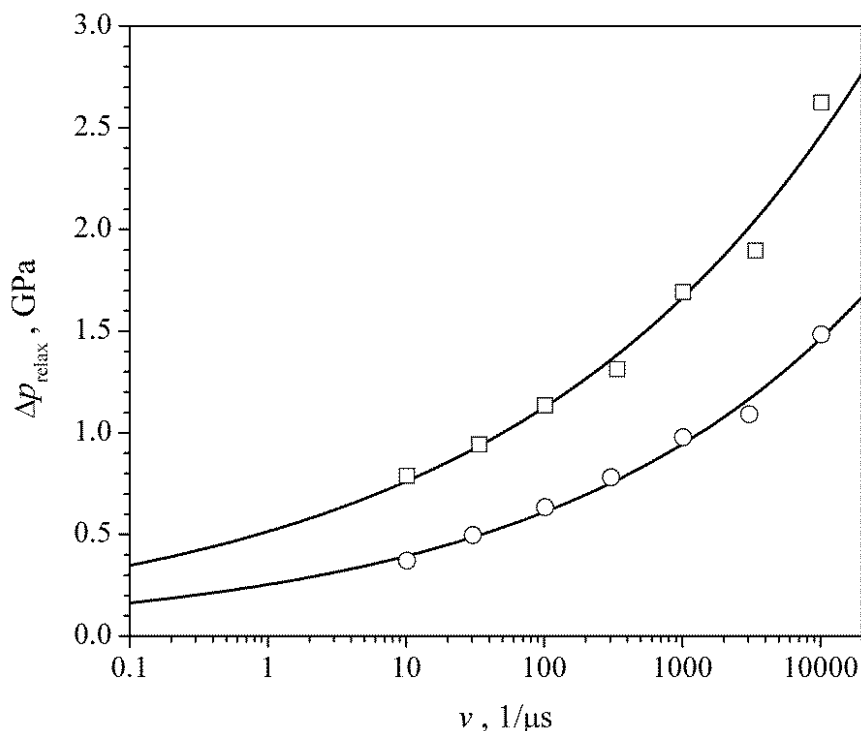


**Fig. 2.** Dependence of pressure drop at the stage of 30 ns relaxation after pressing on the compression rate for the uniform compaction (circles) and the uniaxial compaction (squares). Lines are the approximation of Eq. (7)

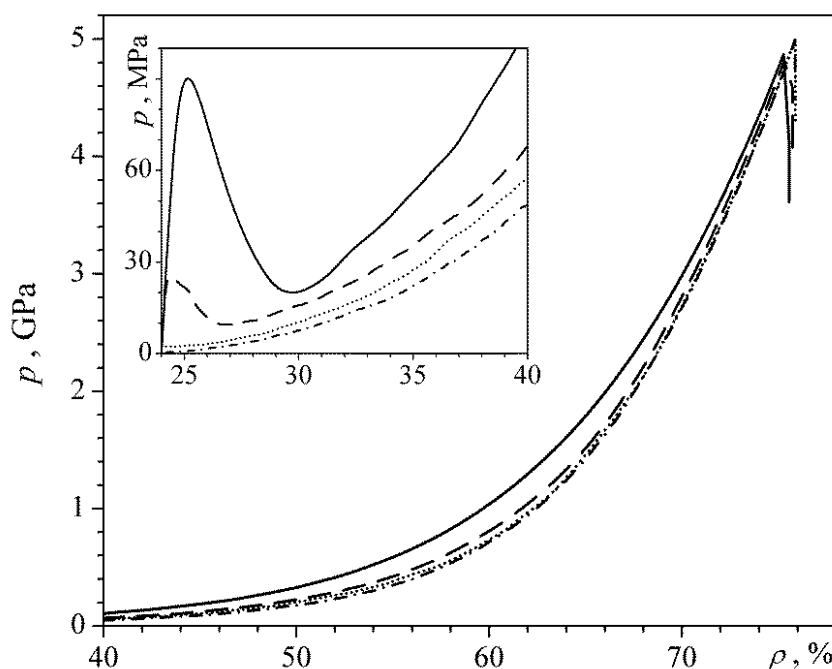


**Fig. 3.** Densification curves in "density – pressure" coordinates for strain rates  $\nu$  (in  $\mu\text{s}^{-1}$ ):  $10^4$  (solid line),  $3 \times 10^3$  (dashed line), 300 (dotted line), and 10 (dashed-dotted line). Inset shows the low pressure region

Figure 3 presents the compaction curves  $p(\rho)$  for uniform compaction processes corresponding to the different densification rates. For uniaxial compaction processes the compaction curves  $p_z(\rho)$  have a similar form. It is interesting that the  $p(\rho)$  curves for large

rates has a local maximum at the beginning (see an inset in Fig. 3), which is very similar to the yield drop at stress-strain curves of metals [22]. At the densification rate  $\nu = 10^4 \mu\text{s}^{-1}$  the pressure at the maximum is achieved the values of 90 MPa for uniform pressing and 165 MPa for uniaxial pressing. This maximum has a dynamical nature and is caused by the retardation of relaxation processes from the powder compression. According to the simulation results, an increase in pressure up to the local maximum takes about 5 ps. This time is significantly less than the time of the “rapid” relaxation, which is about 50 ps in accordance with the analysis of relaxation stages after pressing (see Fig. 1). At slower densification rates, when  $\nu < 300 \mu\text{s}^{-1}$ , this maximum disappears.

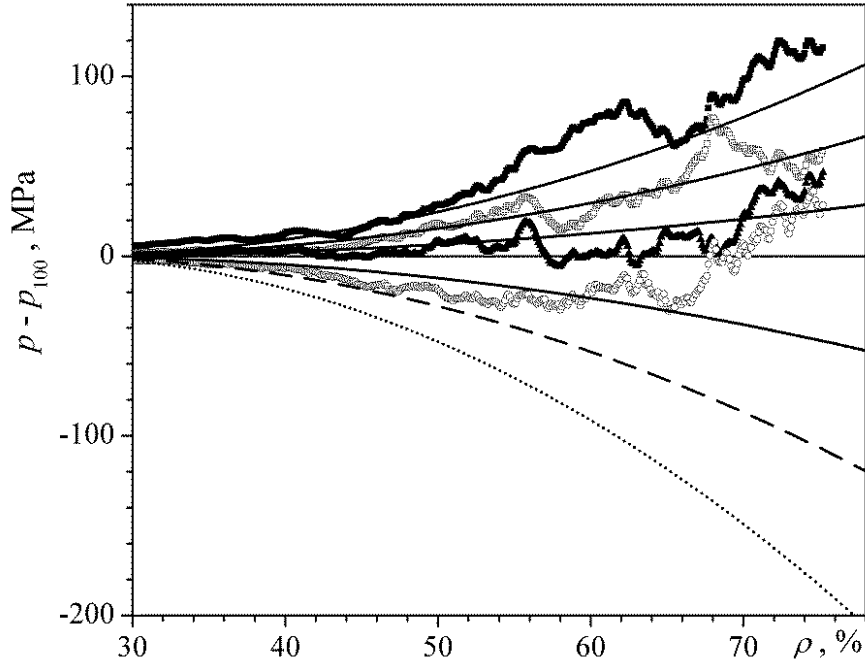


**Fig. 4.** The differences of compaction pressure from the pressure  $p_{100}$  corresponding to the rate  $\nu = 100 \mu\text{s}^{-1}$  as a function of density for the uniform pressing. Symbols are the simulation results for rates  $\nu$  (in  $\mu\text{s}^{-1}$ ): 3000, 1000, 300, and 10 (from the top); smooth solid lines are the dependences of Eqs. (8), and (9) for the same rates; dashed line corresponds to the rate  $\nu = 0.1 \mu\text{s}^{-1}$ ; dotted line is the static limit ( $\nu = 0$ )

To analyze the relative location of dependencies  $p(\rho)$  (in the case of uniform pressing) and  $p_z(\rho)$  (in the case of uniaxial pressing) the densification curves corresponding to the rate  $\nu = 100 \mu\text{s}^{-1}$  have been used as a reference one and the differences of compaction pressure corresponding other rates from the reference curve  $p_{100}(\rho)$  have been analyzed. Figure 4 shows these differences for uniform compaction process. Taking into account a quite large statistical error of simulation results at the maximal density  $\rho \cong 0.75$ , where the pressure error comes up to 100 MPa, these differences are well approximated by the expression:

$$p(\rho, \nu) - p_{100}(\rho) = p_\nu(\nu)(\rho - \rho_0)^\gamma. \quad (8)$$

The analysis performed reveals that the index  $\gamma \cong 2$ . The strain-rate-dependent coefficient  $p_\nu$  is presented in Fig. 5. It can be seen that in the range of densification rates  $\nu < 1000 \mu\text{s}^{-1}$  the values  $p_\nu$  for uniform and uniaxial processes is well described by the common expression

$$p_\nu = p_{\nu 0} + (k_\nu \nu)^{1/8}, \quad (9)$$

with parameters:  $p_{v0} = -0.705$  GPa,  $k_v = 5.7 \times 10^{-4}$   $\mu$ s. As a result, passing on to the quasistatic conditions ( $v \rightarrow 0$ , the dotted line in Fig. 4) as a reference line ( $p_{stat} = p_{100} + p_{v0}(\rho - \rho_0)^2$ ), we have obtained

$$p(\rho, v) = p_{stat}(\rho) + (k_v v)^{1/8} (\rho - \rho_0)^2. \quad (10)$$

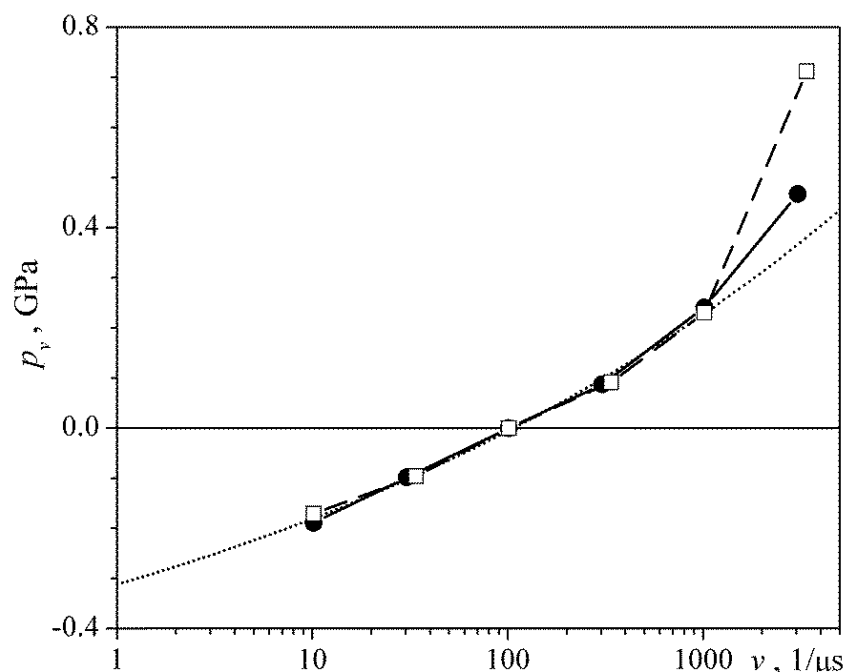


**Fig. 5.** The coefficient  $p_v$  of Eq. (8) as a function of strain rate. Squares are the simulation results for uniaxial compaction processes, circles are the simulation results for uniform compaction processes; dotted line is the common approximation of (9)

Figure 4 demonstrates the pressure differences corresponding to Eqs. (8)–(10). As a result, it can be seen that the pressure required for nanopowder compaction up to the density of  $\rho \cong 0.75$ , when using a dynamical process with rate about  $\nu = 10^5$   $\text{s}^{-1}$  (for example, magnetic pulsed methods), exceeds the pressure at a quasi-static compaction process by the value of about 80 MPa.

#### 4. Experiments

In order to approve the relation (10) obtained within the granular dynamic method, two series of experiments on magnetic pulsed compaction (MPC) of alumina nanopowder were performed. Laboratory made  $\text{Al}_2\text{O}_3$  nanopowder composed of  $\delta$  and  $\gamma$  phases with average particle diameter  $d_{BET} \cong 50$  nm was produced by electric explosion of aluminum wire. Theoretical density of material is  $\rho_m \cong 3.66$   $\text{g/cm}^3$ . The powder compaction was performed magnetically using cylindrical inductor as magnetic field source and copper shell (tube) as pressing mold (so-called  $\theta$ -pinch mode, e.g. [2,23,24]). Two series of pulsed experiments (3 samples each) differed in the rate of external loading via the changing the magnetic field pulse duration. It was realized by using two inductors (tool coils): single-turn coil (inductor 1) and multi-turn coil (inductor 2), which were being connected to the capacitor battery ( $C = 425$   $\mu\text{F}$ ). In both cases magnetic field amplitude was kept at the same value, about 25 T, by adjusting the charging voltage of the capacitor battery.

To densify the powder it was placed inside a mold consisted of an outer copper tube and a coaxially mounted rod of hard steel. Outer diameter, thickness, and length of the copper tubes were 28, 0.75, and 23 mm, respectively. Steel rods had the radius  $R_m = 9.24$  mm and were single-used in each experiment. The nanopowder was filled in a gap formed by a copper tube and a rod with the usage of a vibrating table. Apparent density of nanopowder,  $\rho_0$ , was  $0.35 \text{ g/cm}^3$  (about 10% of theoretical density  $\rho_m$ ). Moreover, to exclude the edge effect on compact density, the mold had a special design. As shown in Fig. 6, the end plugs were installed in the ends of the copper tube and capsulated with plastic washers. Before the MPC the mold was evacuated to residual pressure of 5 Pa and then placed inside an inductor to be compacted. Figure 6 also demonstrates a mold view after the MPC.



**Fig. 6.** View of fitted mold (sample No. 804) before (left) and after (right) the MPC

During the experiments the magnetic field applied to the outer surface of the copper tube was carefully measured using a loop inductive probe arranged in a circle in the gap between the inductor and the copper tube. The probe was set in the middle plane of the mold. Typical magnetic field pulses generated by the inductors used are shown in Fig. 7. One can observe that the magnetic system with multi-turn coil is very sensitive to copper shell movement (its radial compression) since it substantially changes the inductance of "inductor – shell" system. In this case the end of the compaction process can be easily determined by the oscillogram. Thus, the shell stop corresponds to a time moment  $t = 32 \mu\text{s}$  from the pulse beginning, where a break in the  $B_m(t)$  dependence is observed. In experiments with the single-turn coil, a similar effect is not observed, because, firstly, as will be shown below, the shell stops much later than the pulse half-period duration ( $t = 14 \mu\text{s}$ ), and secondly, the inductor and the external circuit have comparable inductances.

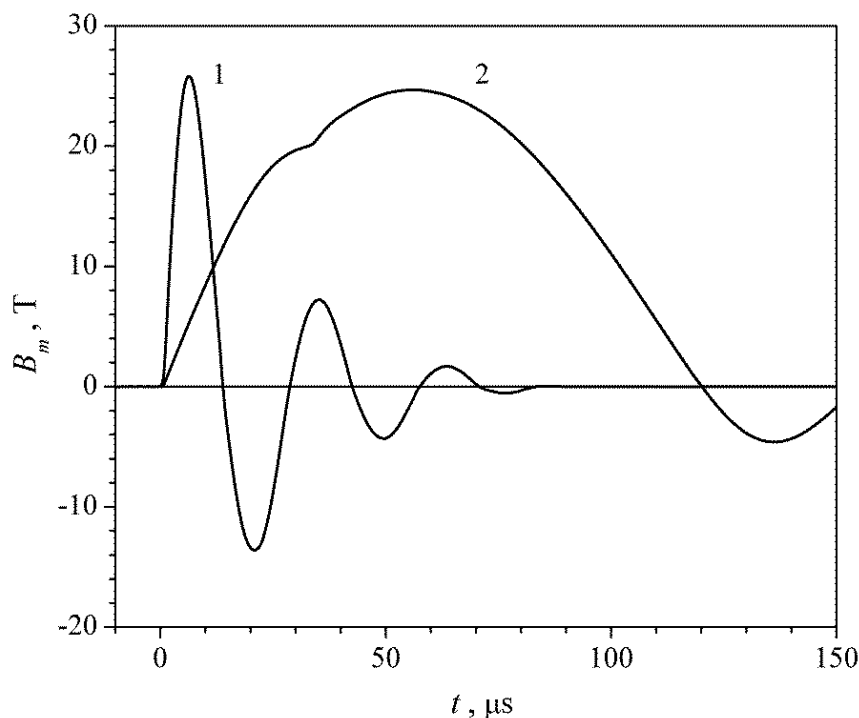


**Fig. 7.** Time dependence of magnetic field generated by single-turn (curve 1) and multi-turn (curve 2) coils

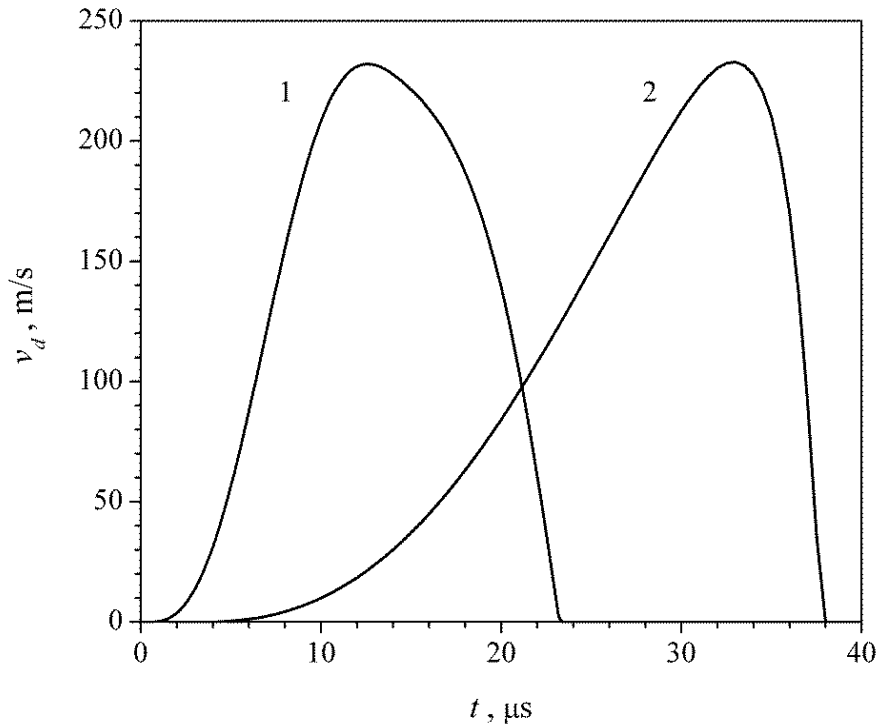
Characteristics of compact samples obtained are listed in Table 1. It can be seen that the usage of a longer field pulse (inductor 2 case) makes it possible to use magnetic energy more efficiently and to obtain a higher density of the compact.

Table 1. Sample characteristics:  $D_{\text{end}}$  is the outer diameter of a copper tube after the compression,  $\rho_0$  and  $\rho_{\text{end}}$  are the starting and the final density of a compact;  $B_m$  is the magnetic field amplitude

Inductor	No.	$D_{\text{end}}$ , mm	$\rho_0$ , g/cm <sup>3</sup>	$\rho_{\text{end}}$ , g/cm <sup>3</sup>	$B_m$ , T
1	807	22.0±0.3	0.35	2.00	25.9
	808	22.1±0.3	0.35	1.90	25.8
	809	21.9±0.2	0.36	2.20	25.8
2	804	21.6±0.1	0.33	2.70	24.3
	805	21.7±0.1	0.34	2.53	24.7
	806	21.6±0.1	0.34	2.77	23.6

A theoretical analysis of the performed experiments and the data obtained was carried out within the framework of the  $\theta$ -pinch pressing model described in detail in [2,23,24]. Dynamics of compaction of experimental samples, "powder + shell", is characterized in Fig. 8 by the time dependencies of the velocity of an inner surface of conductive shell,  $v_d = dR_d / dt$  ( $R_d$  – the inner radius of the shell), when pressed using the inductors 1 and 2. It is interesting to note here that an order of magnitude faster loading, which is realized when the single-turn coil (inductor 1) is used, does not lead to a corresponding increase in the shell velocity. For both inductors used, the velocity  $v_d$  is approximately the same by the amplitude and is about 240 m/s. Thus, in conditions of relatively fast loading, the dynamics of the deformable

system, "powder + shell", is primarily determined by the inertial properties of the sample itself, rather than time characteristics of an external pressure pulse [2].



**Fig. 8.** The velocity of the inner shell surface when compressed by the inductor 1 (curve 1) and the inductor 2 (curve 2)

For the shorter pulse (inductor 1 case), the main accelerating effect is exerted by the first half-wave of magnetic field pulse (at an amplitude of about 25 T) which was about 14  $\mu\text{s}$ . The amplitude of the second half-wave (see Fig. 7) is already half as low, and the "magnetic pressure",  $p_m = B^2 / (2\mu_0)$ , developed at the same time is correspondingly reduced by a factor of four. In the theoretical calculation, the elimination of the second and subsequent half-waves practically does not affect the dynamics of the deformed system and the final density of the compact. At the same time, as shown in Fig. 8, the pressing process in the inductor 1 has not yet been completed to the end of the first half-period of the accelerating pulse. The compression of the shell and the compaction of the powder continue after the end of the external pulse, up to the instant time  $t = 23 \mu\text{s}$ . At this stage, the deformation of the mechanical system "powder + shell" occurs not under the action of external pressure, but "by inertia", i.e. due to stored kinetic energy. In this case, the pressure realized in the compacted powder can significantly exceed the initial "magnetic" pressure  $p_m$  which is about 250 MPa for magnetic field of 25 T in amplitude. According to the calculations the pressure realized by the inertial effect in the powder being compacted reaches 450 MPa. Usage of a longer pulse (inductor 2 case), as noted above, makes it possible to use the energy of the magnetic field even more efficiently. Calculations show that in this case the pressure in the powder reaches about 1.3 GPa, i.e. it exceeds more than 5 times the amplitude of the external pulse.

Despite the approximate equality of the amplitudes of the shell velocities,  $v_d$ , as is seen from Fig. 8, the powder compaction rate,

$$v_\rho = \frac{-1}{\rho} \frac{d\rho}{dt} = \frac{2R_d v_d}{R_d^2 - R_m^2}, \quad (11)$$

differs significantly when pressed using the inductors 1 and 2. If one use a shorter pulse (inductor 1), the shell velocity,  $v_d$ , reaches its maximum at a thickness of the powder layer  $R_d - R_m \cong 1.4$  mm that gives  $v_\rho \cong 0.13 \mu\text{s}^{-1}$ . For a longer pulse (inductor 2), the same conditions realize at  $R_d - R_m \cong 0.9$  and  $v_\rho \cong 0.23 \mu\text{s}^{-1}$ , respectively. Thus, contrary to the relatively slow loading of the deformable mechanical system "powder + shell" when using the inductor 2, a faster powder compaction process is realized here, and as a consequence, the influence of the "viscous" term in Eq. (10) should be more significant.

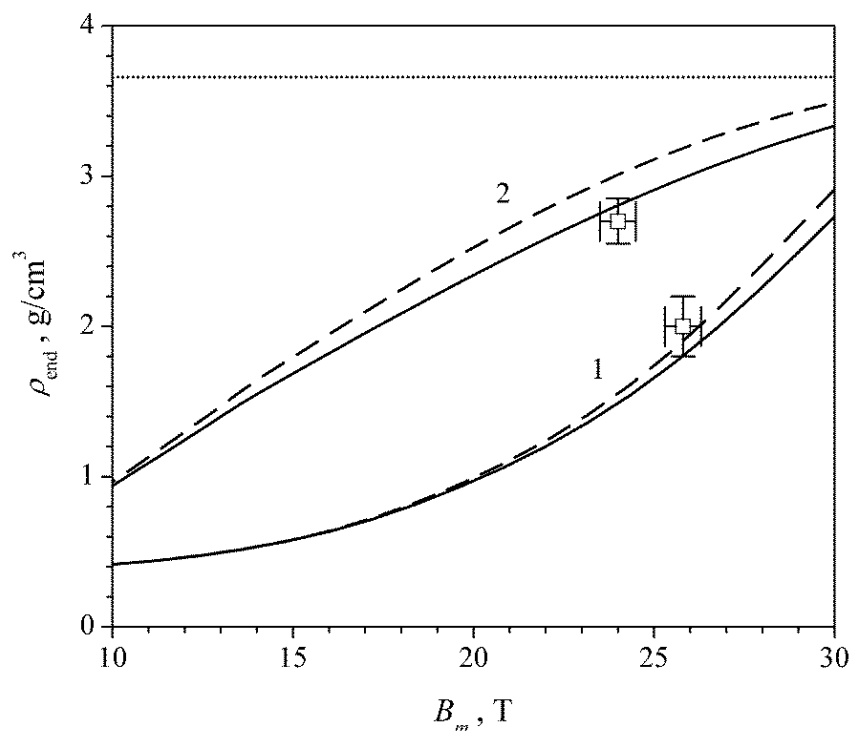


**Fig. 9.** The final compact density as a function of magnetic field amplitude when pressed using the inductors 1 and 2. The points correspond to the experimental data (see Table 1). The solid lines are the theoretical calculation taking into account the "viscous" term in the powder densification curve (10); dashed lines are the case, when the "viscous" term is off, i.e.  $p(\rho) = p_{stat}(\rho)$ . The dotted line is the theoretical density level

The influence of the "viscous" term in Eq. (10) on the values of the achieved compact density,  $\rho_{end}$ , is demonstrated in Fig. 9. The calculations are performed in the range of the magnetic field amplitudes from 10 to 30 T. The experimental points in the Fig. 9 correspond to the averaged data from Table 1. The dashed lines demonstrate a theoretical calculation in the quasistatic approximation,  $p(\rho) = p_{stat}(\rho)$ , when the coefficient  $k_v$  in Eq. (10) is assumed to be zero. The figure shows that taking into account the "viscous" term with the value of the coefficient  $k_v$  obtained in the framework of modeling by the method of granular dynamics makes it possible to improve the agreement of the theoretical model [2,23,24] and the experimental data obtained on the MPC of nanopowder in the  $\theta$ -pinch mode. First of all this refers to a faster process, i.e. when using an inductor 2. At the amplitude of the magnetic field of 24 T, taking into account the influence of the compaction rate leads to a decrease in the value of the reached final density of the compact,  $\rho_{end}$ , from  $2.99 \text{ g/cm}^3$ , which is much higher than the experimental data, to  $2.79 \text{ g/cm}^3$ . For a relatively slow compaction process

(inductor 1 case), the effect of the compaction rate decreases and leads to a shift in the values of  $\rho_{end}$  from 1.93 g/cm<sup>3</sup> to 1.83 g/cm<sup>3</sup>.

## 5. Conclusion

For the first time, the influence of the compression rate on the compactibility of oxide nanopowders has been studied by a three-dimensional granular dynamics method. Processes of stress relaxation after the stage of high-speed compression with the strain rates of  $10^7 - 10^{10} \text{ s}^{-1}$  up to the relative density  $\rho \cong 0.75$  have been analyzed. In particular, it has been found that the characteristic time of the stress relaxation is about 18 ns. The explicit dependence of the compaction pressure, which is connected with the yield strength within phenomenology of powder body [1,2], on the strain rate has been established. It turns out that the rate dependence of pressure is not depending on the compaction conditions (the uniform or the uniaxial pressing). It has been found that nanosized powders demonstrate the power-law dependence of pressure on strain rate:  $p \propto v^{1/8}$ . In view of small value of the index (0.125) the rate dependence obtained is in general agreement with plastic flow of solid bodies (metals), where the yield strength is proportional to the logarithm of the strain rate [13]. The strain rate dependence of the compaction pressure obtained in the framework of the granular dynamics was used to interpret the experimental data on high-speed compaction of alumina nanopowder (strain rate is about  $0.1 \mu\text{s}^{-1}$ ). It is shown that taking into account the strain rate factor makes it possible to improve the agreement between theory and experimental data on the magnetic pulsed compaction of nanopowder.

**Acknowledgements.** *The authors are indebted to Dr. I.V. Beketov and Dr. A.I. Medvedev for supplying us with alumina nanopowders and performing the powders certification. The work has been supported in part by RFBR (project No. 16-08-00277).*

## References

- [1] Shtern MB, Serdyuk GG, Maksimenko LA, Truhan YV, Shulyakov YM. *Phenomenological Theories of Powder Pressing*. Kiev: Naukova Dumka; 1982. (In Russian)
- [2] Boltachev GS, Nagayev KA, Paranin SN, Spirin AV, Volkov NB. *Magnetic Pulsed Compaction of Nanosized Powders*. New York: Nova Science Publishers, Inc.; 2010.
- [3] Filonenko VP, Khvostantsev LG, Bagramov RK, Trusov LI, Novikov VI. Compacting tungsten powders with varying particle size using hydrostatic pressure up to 5 GPa. *Powder Metall. Met. Ceram.* 1992;31(4): 296-299.
- [4] Ushakov AV, Karpov IV, Lepeshev AA, Fedorov LY. Copper Oxide of Plasma-Chemical Synthesis for Doping Superconducting Materials. *Int. J. Nanosci.* 2017;16(4): 1750001.
- [5] Olevsky EA, Bokov AA, Boltachev GS, Volkov NB, Zayats SV, Ilyina AM, Nozdrin AA, Paranin SN. Modeling and optimization of uniaxial magnetic pulse compaction of nanopowders. *Acta Mech.* 2013;224(12): 3177-3195.
- [6] Boltachev GS, Lukyashin KE, Shitov VA, Volkov NB. Three-dimensional simulations of nanopowder compaction processes by granular dynamics method. *Phys. Rev. E.* 2013;88(1): 012209.
- [7] Boltachev GS, Volkov NB, Kochurin EA, Maximenko AL, Shtern MB, Kirkova EG. Simulation of the macromechanical behavior of oxide nanopowders during compaction processes. *Granul. Matter.* 2015;17(3): 345-358.
- [8] Kotov YA. Electric Explosion of Wires as a Method for Preparation of Nanopowders. *J. Nanopart. Res.* 2003;5(5-6): 539-550.
- [9] Kaygorodov AS, Ivanov VV, Khrustov VR, Kotov YA, Medvedev AI, Osipov VV, Ivanov MG, Orlov AN, Murzakaev AM. Fabrication of Nd:Y<sub>2</sub>O<sub>3</sub> transparent ceramics by

pulsed compaction and sintering of weakly agglomerated nanopowders. *J. Eur. Ceram. Soc.* 2007;27(2-3): 1165-1169.

[10] Agnolin I, Roux JN. Internal states of model isotropic granular packings. I. Assembling process, geometry, and contact networks. *Phys. Rev. E.* 2007;76: 061302.

[11] Gilabert FA, Roux JN, Castellanos A. Computer simulation of model cohesive powders: Plastic consolidation, structural changes, and elasticity under isotropic loads. *Phys. Rev. E.* 2008;78: 031305.

[12] Regel' VR, Slutsker AI, Tomashevskii EE. The kinetic nature of the strength of solids. *Sov. Phys. Usp.* 1972;15: 45-65.

[13] Vasin RA, Lensky VS, Lensky EV. *Problems of the dynamics of elastic-plastic continuum. Chapter 7.* Moscow: Mir; 1975.

[14] Belan VG, Durmanov ST, Ivanov IA, Levashov VF, Podkovyrov VL. Energy loss by plastic deformation in radial compression of a cylindrical shell. *J. Appl. Mech. Tech. Phys.* 1983;24(2): 236-242.

[15] Allen MP, Tildesley DJ. *Computer Simulation of Liquids.* Oxford: University Press; 2003.

[16] Boltachev GS, Volkov NB, Kaygorodov AS, Loznukho VP. The Peculiarities of Uniaxial Quasistatic Compaction of Oxide Nanopowders. *Nanotechnologies in Russia.* 2011;6(9-10): 639-646.

[17] Brilliantov NV, Spahn F, Hertzsch JM, Pöschel T. Model for collisions in granular gases. *Phys. Rev. E.* 1996;53(5): 5382-5392.

[18] Brilliantov NV, Pöschel T. *Kinetic Theory of Granular Gases.* Oxford: University Press; 2004.

[19] Boltachev GS, Spirin AV, Chingina EA. Simulation of high-speed compaction processes of nanopowders by 2D granular dynamics method. *Proc. XVII All-Russian school-seminar on condensed matter problems (SPFKS-17).* Ekaterinburg: IMP UB RAS; 2016. p. 185. (In Russian)

[20] Landau LD, Lifshitz EM. *Theory of Elasticity.* Oxford: Pergamon Press; 1993.

[21] Grigoriev IS, Meilikhov EZ. (eds.) *Physical Quantities: Handbook.* Moscow: Energoatomizdat; 1991. (In Russian)

[22] Petrov YV, Borodin EN. Relaxation mechanism of plastic deformation and its justification using the example of the sharp yield point phenomenon in whiskers. *Phys. Solid State.* 2015;57(2): 353-359.

[23] Boltachev GS, Volkov NB, Pararin SN, Spirin AV. Dynamics of Cylindrical Conducting Shells in a Pulsed Longitudinal Magnetic Field. *Technical Physics.* 2010;55(6): 753-761.

[24] Boltachev GS, Volkov NB, Chingina EA. Nanopowders in Dynamic Magnetic Pulse Compaction Processes. *Nanotechnologies in Russia.* 2014;9(11-12): 650-659.

# MECHANISM OF MOLECULE MIGRATION OF CARBON AND SILICON MONOXIDES IN SILICON CARBIDE CRYSTAL

S.A. Kukushkin<sup>1,2\*</sup>, A.V. Osipov<sup>3</sup>, E.V. Osipova<sup>1</sup>

<sup>1</sup>Institute of Problems of Mechanical Engineering, Russian Academy of Sciences, St. Petersburg, Russia

<sup>2</sup>Peter the Great Saint Petersburg State Polytechnic University, St. Petersburg, Russia

<sup>3</sup>ITMO University, St. Petersburg, Russia

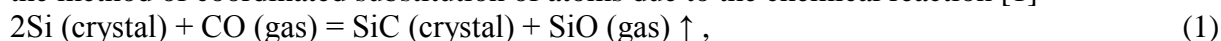
\*e-mail: sergey.a.kukushkin@gmail.com

**Abstract.** The main processes occurring during the migration of molecules of carbon monoxide CO and silicon monoxide SiO gases through a layer of monocrystalline silicon carbide SiC of a cubic polytype have been described by the *ab initio* methods. This problem arises when a single-crystal SiC layer is grown by the method of coordinated substitution of atoms due to the chemical reaction of a crystalline silicon substrate with the CO gas. The reaction products are epitaxial SiC layer and SiO gas. It has been shown that CO and SiO molecules decompose into separate atoms in the SiC crystal. The Oxygen atoms migrate through interstices only in the [110] direction (activation energy is 2.6 eV). The Si and C atoms transit by the vacancy mechanism in the corresponding SiC sublattices with activation energies of 3.6 eV and 3.9 eV respectively (and also only in the [110] direction).

**Keywords:** silicon carbide, epitaxy, diffusion, *ab initio* modelling

## 1. Introduction

During the growth of the epitaxial film of silicon carbide (SiC) from a silicon (Si) crystal by the method of coordinated substitution of atoms due to the chemical reaction [1]



the transport of carbon monoxide (CO) reagent gas and silicon monoxide (SiO) reaction product gas through the SiC layer plays a key role in determining the growth rate of SiC. At present, neither the mechanisms of diffusion of CO and SiO through SiC nor the corresponding values of the diffusion coefficients or the diffusion activation energies are known. It is not even known what stage limits the growth rate of SiC. In order to investigate these questions, all the main processes of transport of CO and SiO gases through the SiC layer have been modeled in this work by the methods of quantum chemistry.

## 2. Modeling methods

For the modeling, the Medea-Vasp package was used, which applies pseudopotentials for the projected augmented wave (PAW) method [2,3]. In all calculations, the density functional method with a plane-wave basis was used, and the exchange-correlation energy was calculated in the framework of the SCAN meta-functional approximation [4-6], which essentially refines the generalized gradient approximation (GGA). The cutoff energy of the plane waves was 400 eV in all calculations.

A supercell of  $8.72 \times 6.17 \times 9.25 \text{ \AA}^3$  of 48 independent atoms of silicon carbide of the cubic SiC-3C polytype was used for the modeling. The supercell was oriented so that the *x*-axis was directed along [001], the *y*-axis was along  $[\bar{1}10]$ , and the *z*-axis was along [110].

[http://dx.doi.org/10.18720/MPM.4222019\\_3](http://dx.doi.org/10.18720/MPM.4222019_3)

© 2019, Peter the Great St. Petersburg Polytechnic University

© 2019, Institute of Problems of Mechanical Engineering RAS

The size of the supercell in the [110] direction was specially chosen to be the largest and equal to 3 periods in this direction since the atoms move mainly along [110]. The integration in the first Brillouin zone was carried out over k-points in  $3 \times 4 \times 3$  Monkhorst-Pack grid. The studies have shown that CO and SiO molecules, once inside the SiC crystal, immediately decompose into separate atoms, since the size of the voids in SiC is too small for them. The oxygen atom, in principle, can move in different directions, however, the activation energy of migration in the direction [110] turned out to be much less than in other directions. In quantum chemistry, the migration process is best described by the method of nudged elastic band (NEB) [7,8]. The idea of this method is that knowing the initial and final positions of the atoms, one can freeze the system and introduce additional forces that will direct the atoms from the initial state to the final state. If certain conditions are met, the system will follow the minimal energy pathway (MEP) [8]. This is such a path of a system transformation that any local change in the path leads to an increase in the energy of the system in the vicinity of a given point of the path. In other words, this is the path of the fastest descent from the initial configuration of atoms to the final configuration, i.e. the most probable path of atomic migration in this case. Accordingly, the cross-section of the potential energy surface along the transformation path is the energy profile of this process.

### 3. Modeling results

The NEB calculation gives the energy profile of the oxygen atom moving in cubic SiC for one period of 3.08 Å in the [110] direction, as shown in Fig. 1.

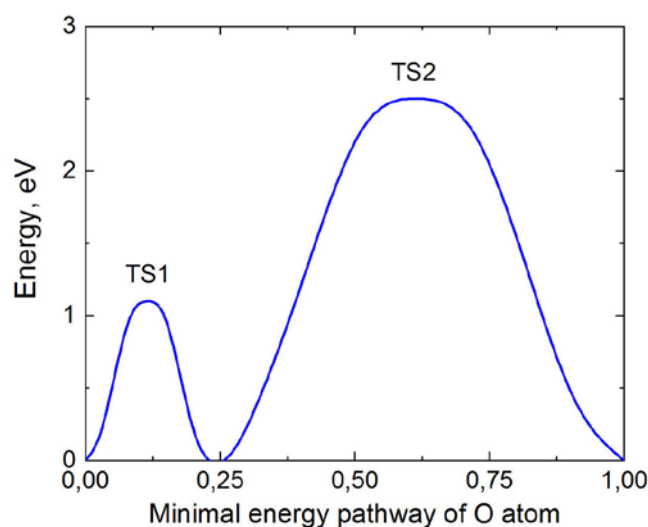


**Fig. 1.** The energy profile of the process of migration of an oxygen atom in SiC-3C in the [110] direction for one lattice period. The energy barriers corresponding to the two transition states TS1 and TS2 are equal to 1.1 eV and 2.5 eV, respectively

The height of the activation barrier for the migration of the O atom in cubic SiC in the [110] direction is 2.5 eV. In order for the forces acting on the atoms to be less than  $0.05 \text{ eV}/\text{\AA}$ , it took 50 iterations with 15 images in the NEB method. Atomic configurations corresponding to the initial, final, intermediate, and two transition states TS1 and TS2 are shown in Fig. 2.



**Fig. 2.** The geometrical configuration of atoms corresponding to 5 ground states (3 energy minimums and 2 saddle points TS1 and TS2) during the migration of an oxygen atom in SiC-3C in the [110] direction for one lattice period of 3.08 Å. Atoms Si, C, O are signed by letters

The highest barrier for the migration of the O atom corresponds to the TS2 state, in which the O atom forms a single bond with the Si atom (Fig. 2). The length of this bond is 1.58 Å, i.e. it is stretched by about 5%, which provides the migration barrier. Analysis of the spectrum of the natural frequencies of the TS2 configuration shows that the spectrum contains a single negative (imaginary) frequency equal to  $-600 \text{ cm}^{-1}$ . This proves that the TS2 configuration is indeed a transition state in the process of migration of the O atom in the [110] direction. In other directions, the migration activation energy is noticeably higher; therefore, the migration most likely occurs only in the [110] direction constituting six equivalent directions in the SiC-3C crystal.

Similar calculations by the NEB method show that Si and C atoms practically cannot migrate through SiC interstices since the migration energy exceeds 8 eV. Therefore, the main mechanism of migration of these atoms is the vacancy one. There are a sufficiently large number of vacancies in the Si and C sublattices due to the SiC synthesis mechanism for the following reasons. First, the chemical adsorption of a CO molecule on a SiC notch leads to the formation of a silicon vacancy  $V_{\text{Si}}$  that immediately begins to migrate to the SiC/Si interface where the drain is located. Second, the substitution of a Si atom by a C atom in silicon at the SiC/Si interface leads to the formation of a carbon vacancy in SiC, since the C atom has left SiC, and the entered Si atom will fall sooner or later into the silicon vacancy. The carbon vacancy migrates from the SiC/Si interface to the SiC surface, where a C atom from the CO molecule will fall into it sooner or later. Third, after a part of Si atoms in silicon is substituted by C, the silicon lattice will “collapse,” since the volume of the SiC-3C cell is half the size of the Si cell. In such event, very strong compressive stresses arise and actuate the effect of upward diffusion leading to the formation of additional silicon vacancies [9]. In addition, it was shown in the paper [10] that it is favorable for a silicon vacancy to transform into a carbon vacancy plus the  $C_{\text{Si}}$  antisite, i.e. the carbon atom located on the site of the silicon atom. However, for this to happen, it is necessary to overcome the barrier of 3.1 eV. The antisite is an immobile structure, while the carbon vacancy after transformation continues to move toward the SiC surface. Thus, there are two gases of vacancies, silicon  $V_{\text{Si}}$  and carbon  $V_{\text{C}}$ , which interact with each other.

The energy profiles of the migration of silicon and carbon vacancies in SiC-3C in different directions have been calculated by the NEB method. As in the case of O atoms, the smallest migration barrier happened to be in the [110] direction. Figure 3 shows the dependences of the system energy on the minimal energy pathway for the  $V_{\text{Si}}$  and  $V_{\text{C}}$  vacancies in the [110] direction. The largest energy barrier of migration, equal to 3.9 eV, corresponds to the migration of the carbon vacancy (Fig. 3).

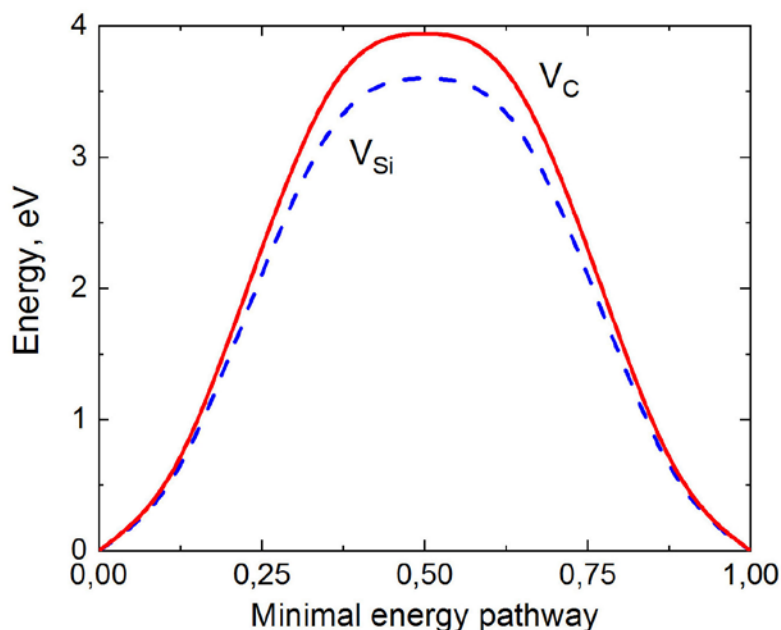


**Fig. 3.** The energy profile of the migration process of silicon  $V_{Si}$  and carbon  $V_C$  vacancies in SiC-3C in the [110] direction for one lattice period. The energy barriers for  $V_{Si}$  and  $V_C$  are 3.6 eV and 3.9 eV, respectively

Therefore, in pure SiC at low temperatures, it is carbon vacancies that limit the growth of the SiC film (the energy barrier of the chemical reaction itself is 2.6 eV [11]). However, for doped materials, as well as with increasing temperature, the situation may change. For example, if the original silicon is doped with boron, then the activation barrier for the migration of silicon vacancies may increase and they will begin to limit the growth of SiC. In addition, if the temperature rises to 1100 – 1200 °C, a significant part of silicon vacancies will turn into carbon vacancies plus immobile carbon structures (antisites) constituting almost a flat cluster of 4 C atoms (the activation energy of this process is 3.1 eV [10]). In this case, silicon vacancies limit the growth of SiC, since the product of the concentration of silicon vacancies and their mobility is less than that for carbon vacancies. Apparently, this case is most often observed in practice, since these carbon structures are detected both by infrared spectroscopy (they give a new line of  $960\text{ cm}^{-1}$ ) [10] and ellipsometry that allows to measure their volume concentration [10]. Usually, the concentration is in the range of 1 – 3%, depending on the type and degree of doping of the original silicon [10]. If silicon vacancies limit the SiC growth, then the reaction product SiO will accumulate inside the SiC layer, failing to escape. Sometimes this leads to microexplosions of the SiC layer, resembling a volcanic eruption. Such “eruptions” are regularly detected experimentally at low CO pressures [1].

#### 4. Conclusion

In summary, in the present work, we have shown by quantum chemistry methods that  $V_{Si}$  and  $V_C$  vacancies play a key role in the kinetics of the reaction (1). The transport of the CO reagent gas to the reaction zone and the transport of the SiO reaction product gas from the reaction zone are carried out only in the [110] direction and directions equivalent to it, i.e. in the direction of the SiC channels. The migration of CO and SiO molecules is equivalent to the migration of the O atom and the  $V_{Si}$  and  $V_C$  vacancies, since it is not necessary for the Si and C atoms to migrate, because the O atom easily forms a chemical bond with any atoms of the SiC crystal. The energy barrier of the migration of vacancies is more than 2 times lower than the barrier of the migration of atoms, and it is equal to 3.6 eV for  $V_{Si}$  and 3.9 eV for  $V_C$  in the

ideal crystal. Therefore, at low temperatures, the SiC synthesis is limited by the migration of  $V_C$ . In a SiC-3C crystal containing twin boundaries, the migration barriers can be 10 – 20% lower. Starting with a temperature of 1100 – 1200 °C, a significant part of silicon vacancies turns to carbon vacancies plus immobile carbon structures (the activation energy of this process is 3.1 eV). Therefore, a lack of silicon vacancies can limit the SiC synthesis. In this case, in SiC synthesized by the method of coordinated substitution of atoms, there are both carbon clusters and traces of microexplosions caused by the accumulation of a large amount of SiO inside the SiC layer. Both features are determined experimentally at low CO pressures.

**Acknowledgments.** S.A. Kukushkin thank Russian Scientific Foundation for the financial support (RNF grant N 14-12-01102). The growth of SiC layers and the study of their properties were carried out using a unique scientific setup "Physics, Chemistry, and Mechanics of Crystals and Thin Films" (IPMash RAS, St. Petersburg).

## References

- [1] Kukushkin SA, Osipov AV. Quantum mechanical theory of epitaxial transformation of silicon to silicon carbide. *J. Phys. D: Appl. Phys.* 2017;50(46): 464006.
- [2] Kresse G, Furthmüller J. Efficient iterative schemes for ab initio total-energy calculations using a plane-wave basis set. *Phys. Rev. B.* 1996;54(16): 11169 –11186.
- [3] Hafner J. Ab-initio simulations of materials using VASP: Density-functional theory and beyond. *J. Comp. Chem.* 2008;29(13): 2044-2078.
- [4] Sun J, Ruzsinszky A, Perdew JP. Strongly Constrained and Appropriately Normed Semilocal Density Functionals. *Phys. Rev. Lett.* 2015;115(3): 036402.
- [5] Buda IG, Lane C, Barbiellini B, Ruzsinszky A, Sun J, Bansil A. Characterization of Thin Film Materials using SCAN meta-GGA, an Accurate Nonempirical Density Functional. *Sci. Reports.* 2017;7: 44766.
- [6] Jana S, Sharma K, Samal P. Assessing the performance of the recent meta-GGA density functionals for describing the lattice constants, bulk moduli, and cohesive energies of alkali, alkaline-earth, and transition metals. *J. Chem. Phys.* 2018;149(16): 164703.
- [7] Henkelman G, Uberuaga BP, and Jonsson HJ. A climbing image nudged elastic band method for finding saddle points and minimum energy paths. *Chem. Phys.* 2000;113(22): 9901-9904.
- [8] Caspersen KJ, Carter EA. Finding transition states for crystalline solid–solid phase transformations. *PNAS.* 2005;102(19): 6738-6743.
- [9] Kukushkin SA, Osipov AV. The Gorsky Effect in the Synthesis of Silicon-Carbide Films from Silicon by Topochemical Substitution of Atoms. *Techn. Phys. Lett.* 2017;43(7): 631-634.
- [10] Kukushkin SA, Osipov AV. Mechanism of Formation of Carbon–Vacancy Structures in Silicon Carbide during Its Growth by Atomic Substitution. *Phys. Sol. State.* 2018;60(9): 1891-1896.
- [11] Kukushkin SA, Osipov AV. Theory and practice of SiC growth on Si and its applications to wide-gap semiconductor films. *J. Phys. D.: Appl. Phys.* 2014;47(31): 313001.

# ARTIFACTS OF STRESS RELAXATION TECHNIQUE TO FIT RECOVERY ACTIVATION PARAMETERS FOR LOW CARBON STEELS

Alexander A. Vasilyev\*, Semen F. Sokolov, Nikita A. Golubkov, Alexander A. Zisman,  
Dmitry F. Sokolov, Andrey I. Rudskoy

Peter the Great St. Petersburg Polytechnic University, Polytekhnicheskaya 29

195251, St. Petersburg, Russian Federation

\*e-mail: vasilyev\_aa@mail.ru

**Abstract.** The paper compares model predictions of recovery kinetics of low carbon steels with activation parameters determined by various experimental techniques. It is concluded that the stress relaxation method overestimates the recovery rate because the creep of stressed specimens is ignored. To avoid such errors, it is recommended to use an alternative method of double loading. The more realistic (lesser) rate of recovery with the related activation parameters complies with independent data of mechanical tests.

**Keywords:** steels, recovery, modeling, stress relaxation

## 1. Introduction

Recrystallization of cold rolled automotive steels in annealing has a significant effect on their final structure and mechanical properties. This stimulates experimental studies of this phenomenon and evokes attempts to model it [1-3]. However, its numerical modeling is seriously complicated due to the concurrent recovery process that consumes the same thermodynamic driving force i.e. specific energy of lattice dislocations accumulated in the previous deformation. Moreover, this is the case both before and during recrystallization since the latter propagates gradually while admitting the recovery to go on within the remaining material part [4,5]. Therefore, to predict the recrystallization effects, accurate allowance for the recovery is necessary; in particular, related activation parameters (energy  $Q_a$  and volume  $V_a$ ) should be determined with appropriate experimental techniques. The present paper reconsiders them in order to exclude artifacts in determination of these parameters and, hence, to improve the modeling of recovery kinetics.

The pioneering study of recovery in  $\alpha$ -iron of high purity at temperatures 300 to 500°C after a low strain of 5% undertaken by Michalak [6] revealed a notable growth of the recovery degree in terms of flow stress reduction when increasing the annealing temperature; in particular, at 500°C this degree approaches about 80%. An IF-steel (0.002%C, 0.1%Mn, 0.023%Ti, 0.007%Nb (wt.%)) cold rolled to the thickness reduction of 80% and then treated at temperatures 500 to 625°C has been investigated by means of XRD technique [7]. According to the obtained results, the recovery of this material at 500°C develops much slower than in pure  $\alpha$ -iron and does not exceed 40%.

Experimental study and numerical modeling of the kinetics of recovery in low carbon steels were performed in [8-11]. The stress relaxation technique, implemented on Gleeble thermo-mechanical simulators, has been employed in [8,11] in order to register the recovery

kinetics. To this end, after the given compression deformation at some selected temperature, the specimen length is fixed whereas the gradually diminishing external stress displays the apparent softening presumably related to relaxation phenomena in the material. According to [8] the recovery degree of investigated steel (0.19% C, 0.445% Si, 1.46% Mn, 0.03% Al) after the strain of 15% exceeds 70% at 500°C and reaches about 90% at 550 to 600°C. However, the so strong softening of steel, different from pure iron, does not seem realistic and necessities consideration of possible experimental artifacts. In particular, the permanently applied compressive stress could result in some non-stationary creep so that an apparent softening is partly due to the weakening of specimen constraint rather than an internal recovery process. The same remark is also relevant to findings of work [11] where the stress relaxation in steel (0.05% C, 1.5% Al, 1.0% Mn, 0.4% Si) at 700 and 750°C approached 80% regardless of previous true strains (0.12 and 0.60).

To simulate quantitatively the recovery kinetics in annealing of the considered steels, the authors of [8,10,11] made use of the model [12] by Verdier, Brechet and Guyot (VBG), which employs two experimentally fitted parameters related to the underlying rearrangement of dislocations that results in reduction of their density. One of them is the recovery activation energy  $Q_a$  and another is the activation volume  $V_a$  suggested to be proportional to the average length of movable dislocation segments and the cross section area of dislocation core [5,13]. It is worth noting that the VBG model with  $Q_a$  and  $V_a$  fitted to different experimental data [8,10,11] predicts rather various recovery kinetics hardly consistent with each other and, hence, complicates selection of the most adequate and practicable model. In other words, the employed experimental methods do not ensure appropriately accurate determination of  $Q_a$  and  $V_a$ .

The present paper is aimed to determine the recovery activation parameters in a way free of experimental artifacts in order to provide reliable numerical modeling of the recovery in annealed automotive steels.

## 2. Investigated steels

In this work the recovery kinetics is investigated with the stress relaxation technique and with the so called double loading technique. In the latter, after the first deformation the specimen is unloaded, undergoes recovery for a stated time lapse and then is deformed again so that comparison of the two loading diagrams enables evaluation of softening degree. Experiments by both methods are implemented on  $\text{Ø}10 \times 15$  mm specimens subject to the compressive stress in the unit HydraWedge of thermo-mechanical simulator Gleeble 3800. Under consideration are IF-steel (0.004% C, 0.14% Mn, 0.06% Ti) and 08ps steel (0.06% C, 0.17% Mn). Pieces of these steels taken at an intermediate stage of rolling in order to fabricate specimens for experiments on Gleeble 3800 had rather coarse grained ferrite structures different from those of final products. To improve this, 30 mm thickness of initial plates has been reduced to about 12 mm by hot rolling on a laboratory mill; then the plates have been cooled in air. Resulting average sizes of ferrite grains in IF and 08ps steels are 70 and 30  $\mu\text{m}$ , respectively (Fig. 1).

## 3. Experimental procedures and results

Before the stress relaxation during an isothermal treatment of specimens with a fixed total deformation, they been heated with the rate 10°C/s to the stated temperature (250 to 600°C) and then compressed with the rate of 1 s<sup>-1</sup> to the true strain of about 0.6. The obtained results (Fig. 2) evidence that in both steels stress relaxation degree increases with the annealing temperature from 20 to 40% (250°C) to about 80% (600°C). The so high values are close to those determined by the same method in [8,11]. In order to verify whether or not the

employed technique provides a proper evaluation of the material recovery, an alternative "direct" method is then applied to the same steels in the cold rolled state.

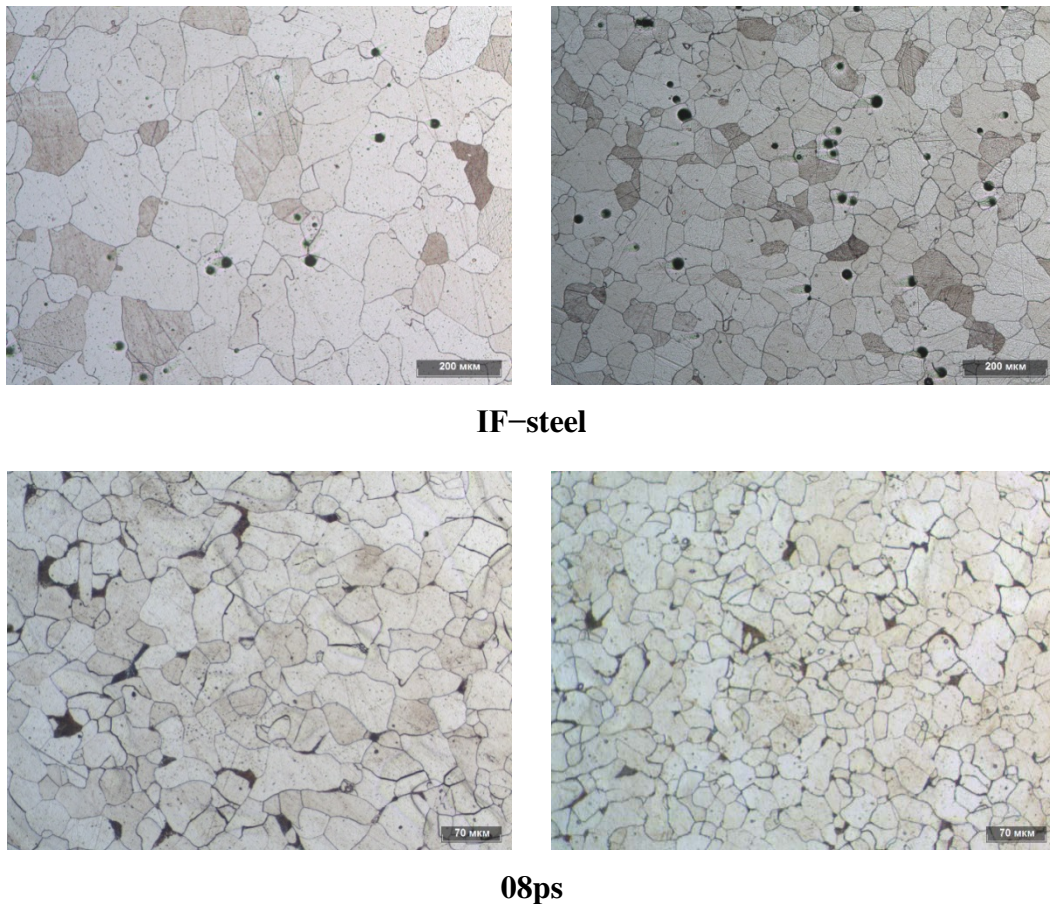


**Fig. 1.** Microstructures of the investigated steels after industrial rough rolling (left) and after additional hot rolling in laboratory conditions (right)

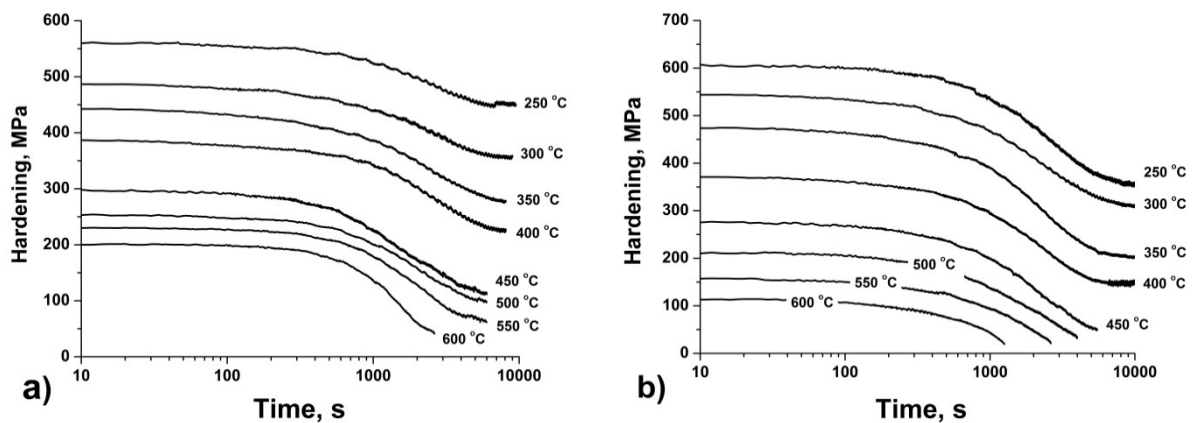


**Fig. 2.** Diagrams of stress relaxation of IF (a) and 08ps (b) steels at various temperatures

Standard tensile specimens for mechanical testing at room temperature have been cut from steels IF and 08ps cold rolled to the thickness reduction of 57 and 58%, respectively. Corresponding increments of yield stress for these steels relative to their previous hot rolled states are 330 and 465 MPa. These reference values can be used to normalize absolute magnitudes of softening in annealing at various temperatures in the range 300 to 550°C for

six hours and at 550°C for five hours. The annealing treatment has been made in the Nabertherm furnace, and tensile test machine Zwick/Roell Z100 has been used to determine mechanical properties of both the cold rolled and annealed steels. Respective values of relative softening are represented in Fig. 3.

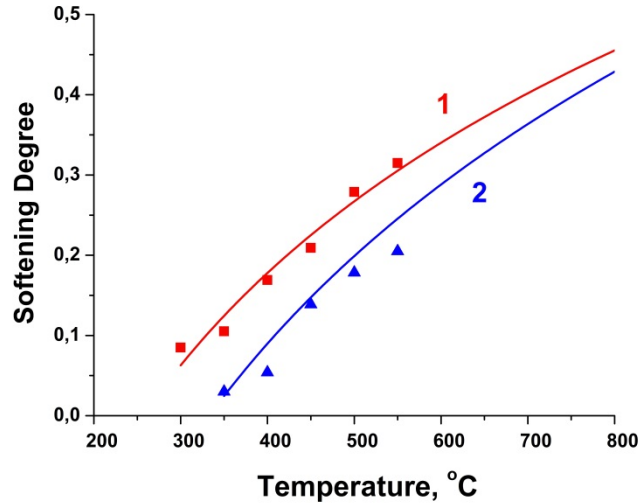


**Fig. 3.** Maximum softening degrees depending on the annealing temperature for cold rolled IF (1) and 08ps (2) steels

Note that the applied annealing times notably exceed durations of stress relaxation in Fig. 2 and, accordingly, are sufficient to complete this phenomenon. The plots of Fig. 3 indicate that the softening degree at the maximum temperature 550°C approach only about 30 and 20% for IF and 08ps steels, respectively. Even when roughly extrapolating the plots to 800°C, these degrees will not exceed 50%. In all, comparison of the considered results to the data of Fig. 2 indicates that the material softening degree evaluated by the stress relaxation method [8,11] is always overestimated. As previously mentioned, this can be due to the specimen creep developing under compressive loads in parallel with the softening as such.

In order to avoid artifacts of the stress relaxation approach to the recovery evaluation while making use of the convenient Gleeble 3800 machine, an alternative double loading method has been applied to the same materials as follows. Specimens are heated with the rate of 10°C/s to the temperature of deformation (400 to 550°C for IF-steel, 400 and 500°C for 8ps steel) compressed with the rate of 1 s<sup>-1</sup> to the true strain of 0.6, unloaded and kept at the same temperature for a stated time interval and then compressed again with the same rate to the true strain of 0.2. To analyze absolute softening due to the recovery for time  $t$  between two deformations, the current hardening magnitude relative to the first yield stress  $\sigma_{0.2}^{(1)}$  is calculated as:

$$\Delta\sigma(t) = \sigma_{0.2}^{(2)}(t) - \sigma_{0.2}^{(1)}. \quad (1)$$

This is plotted in Fig. 4 so that  $\Delta\sigma(0) = \sigma_{\max} - \sigma_{0.2}^{(1)}$ , where  $\sigma_{\max}$  is the flow stress at the end of the first deformation;  $\sigma_{0.2}^{(1)}$  and  $\sigma_{\max}$  have been averaged over all tests. According to these data, the maximum relative softening  $\Delta\sigma(t) / \Delta\sigma(0)$  at 500°C remains within 15 and 20% for IF and 8ps steels, respectively, that is significantly lesser than previous estimates with the stress relaxation technique.

It is worth noting in Fig. 4 that the softening of IF-steel is monotonous and mostly expires for 1000 to 2000 s, whereas a stage of softening for about 2000 s in steel 08ps is followed by some hardening during about 10<sup>4</sup> s; then this material slowly softens again. This

behavior of steel 08ps is due to dissolution of cementite situated in perlite colonies and between ferrite grains that is quite possible at temperatures above 400°C. Specifically, free carbon atoms form dislocation atmospheres responsible for the considered hardening, and the following softening is due to the eventual diffusion rearrangement of such atmospheres. Formation of the latter in the annealed steel has been confirmed by presence of yield drops on diagrams of its loading at room temperature.

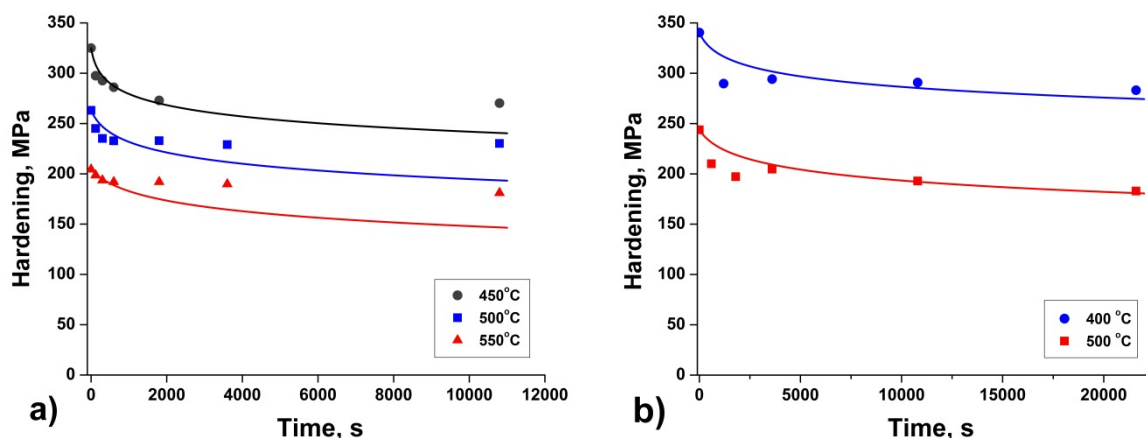


**Fig. 4.** Reduction of hardening relative to the reference (hot rolled) state when annealing IF (a) and 08ps (b) steels at various temperatures. Continuous dependences are provided by VBG model fitted to respective sets of experimental points

Let us compare in more detail the data on recovery of investigated steels at 500°C (Fig. 4). In steel 08ps, the initial stage of quick recovery is longer and the related recovery degree is higher. Besides, unlike IF-steel where the softening is practically completed at the stress of about 230 MPa, steel 08ps approaches the lower stress of 175 MPa. It is worth noting that such a difference is the case despite the pinning of dislocations by carbon segregations in 08ps. The observed stagnation of recovery in IF-steel at notably higher stresses evidence for presence of rather strong barriers impeding dislocation rearrangements. Presumably, the effect is due to Ti-C complexes (steel contain 0.06% of Ti) which result in high tetragonal distortions of crystal lattice interacting with both the edge and screw dislocations. Unlike the atmosphere pinning that weakens in annealing because of carbon redistribution, the considered effect is insensitive to an isothermal treatment insofar as the considered complexes are thermodynamically stable. Thus, the chemical composition can notably affect the kinetics of steel recovery.

### 3. Modeling results

In order to evaluate relevance of our findings to the recovery phenomenon, it is expedient to reconsider them in terms of the popular VBG model [12]. The latter employs the following expression for the rate of softening:

$$\frac{d\Delta\sigma}{dt} = -\frac{64\Delta\sigma^2\nu_D}{9M^3\alpha^2E(T)} \exp\left(-\frac{Q_a}{RT}\right) \sinh\left(\frac{V_a\Delta\sigma}{kT}\right), \quad (2)$$

including Debye's frequency  $\nu_D$  ( $\sim 2 \cdot 10^{12} \text{ s}^{-1}$ ), energy  $Q_a$  and volume  $V_a$  of recovery activation, Taylor's factor  $M$  suggested to be 2.7 for ferrite, dimensionless  $\alpha \approx 0.33$ , absolute gas constant  $R$ , Boltzmann's constant  $k$ , absolute temperature  $T$ , and the Young modulus  $E$ . Temperature dependence of the latter:

$$E(T) = 2.11 \times 10^{11} \left[ 1 - \frac{T - 300}{1989} \right] \text{ (MPa)}, \quad (3)$$

is compiled from [14]. The main parameters  $Q_a$  and  $V_a$  of Eq. (2) should be fitted to appropriate experimental data. However their simultaneous fitting, particularly to limited data of real accuracy, often leads to a great variation of related modeling results. To avoid this issue we fix  $Q_a$  by taking for it the activation energy  $E_{SD}$  of self-diffusion in  $\alpha$ -iron. According to [15] this energy is equal to:

$$E_{SD}(T) = 236.5 + \Delta E_{SD}(T) \text{ (kJ/mol)}, \quad (4)$$

where  $\Delta E_{SD}(T)$  is the temperature dependent contribution of magnetic effects. Experimental data on this contribution, as shown in Fig. 5, can be accurately approximated by Boltzmann's function:  $\Delta E_{SD}(T) = a + b(1 + \exp((T/T_C - c)/d))$ , where parameters fitted to experimental data [15] are equal to:  $a = -11.895$  kJ/mol,  $b = 65.984$  kJ/mol,  $c = 0.934$  and  $d = 0.128$ , respectively;  $T_C$  is Curie's temperature.

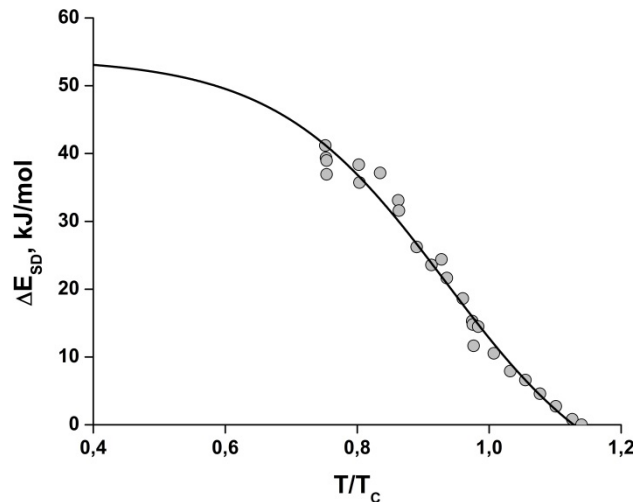


**Fig. 5.** Dependence of the magnitude contribution of  $\Delta E_{SD}(T)$  on ratio  $T/T_C$  ( $T_C$  is Curie's temperature). The presented experimental data [15] are approximated using Boltzmann's function

Thus  $V_a$  remains the only parameter of Eq. (2) to be fitted to experimental data represented in Fig. 4. We have implemented the fitting to the total data of both steels thus neglecting the rather weak effect of their difference in chemical composition. The resulting value of  $V_a$  is  $5.23 \times 10^{-28} \text{ m}^3$ , i.e.  $31.7b^3$  where  $b$  is the Burgers vector magnitude; this result satisfactorily complies with [5,10,12].

The time dependences of softening, determined when substituting the above-considered parameters in Eq. (2) and shown in Fig. 4 by continuous curves, prove to be satisfactorily close to experimental points. The average relative error of the modeling does not exceed 4% for both steels, whereas the most error at the longest annealing time of IF-steel reaches about 20%. Note that the corresponding absolute deviation within 40 MPa is comparable to the experimental stress error of about 15 MPa. Thus, with all simplifications of the employed model kept in mind, even the maximum deviation of calculated stress from its experimental counterpart seems to be acceptable.

Let us compare predictions of softening kinetics at 500°C by VBG model with the above-considered activation parameters and those fitted by other authors to the data of stress relaxation experiments; under consideration are IF-steel (0.004% C, 0.14% Mn, 0.06% Ti) as

well as steels (0.19% C, 0.445% Si, 1.46% Mn, 0.03% Al) [8] and (0.05% C, 1.5% Al, 1.0% Mn, 0.4% Si) [11]. Owing to the difference of these materials in chemical composition and the previous strain degree, related softening processes start at different stresses. Therefore, to reveal clearly the effect of activation parameters in application of Eq. (2), it is expedient to employ in modeling a virtually unique stress at  $t = 0$ . We take for this the initial stress in our stress relaxation experiment on IF-steel as shown in Fig. 6, where the meaning of vertical axis is similar to that of Fig. 4. This figure, also represents the results of modeling with  $Q_a$  and  $V_a$  as determined in the present work by the double loading and in [8,11] by the stress relaxation technique. Evidently, in the latter case the softening rate is notably overestimated as compared to those based on the former technique, more relevant as free of such artifacts as creep of stressed specimens.

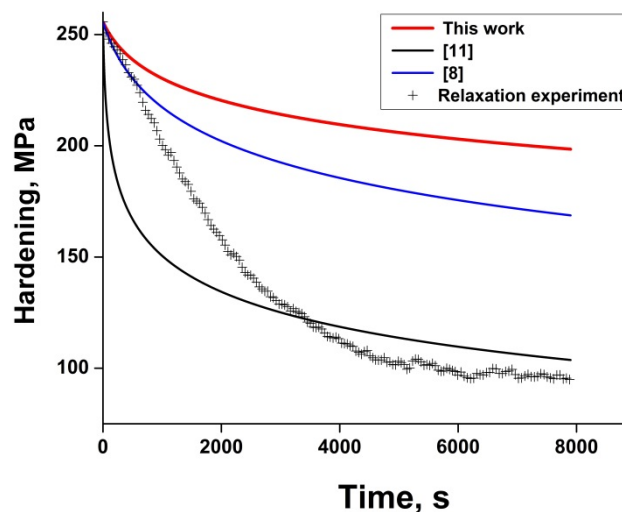


**Fig. 6.** Results of the modeling of recovery at 500°C with activation parameters determined in this work and in [8] and [11]. For reference, an experimental diagram of stress relaxation of IF-steel at the same temperature is shown

#### 4. Conclusions

To sum up, the obtained results evidence that  $Q_a$  and  $V_a$  determined in stress relaxation experiments generally lead to excessive rates of recovery in modeling this phenomenon. In order to avoid such errors while making use of the up-to-date Gleeble simulators, it is recommended to apply an alternative double loading method. As confirmed by independent mechanical tests, parameters based on this method provide the more accurate modeling of recovery kinetics. Moreover, this approach saves satisfactory accuracy even if the unique activation energy of self-diffusion is used for  $Q_a$  so that only  $V_a$  is fitted to experimental data.

**Acknowledgments.** This work was supported by grant from Russian Science Foundation (project No. 17-19-01178).

#### References

[1] Ferry M, Muljono D, Dunne DP. Recrystallization kinetics of low and ultra low carbon steels during high-rate annealing. *Iron and Steel Institute of Japan International*. 2001;41(20): 1053-1060.

- [2] Senuma T. Present status and future prospects of simulation models for predicting the microstructure of cold-rolled steel sheets. *Iron and Steel Institute of Japan International*. 2012;52(4): 679-687.
- [3] Zhu B, Militzer M. 3D phase field modeling of recrystallization in a low-carbon steel. *Materials Science and Engineering: A*. 2012;20(8): 1-17.
- [4] Verhoeven JD. *Fundamentals of Physical Metallurgy*. New-York: John Wiley & Sons; 1975.
- [5] Humphreys FJ, Hatherly M. *Recrystallization and Related Annealing Phenomena*. 2nd ed. Oxford: Elsevier; 2004.
- [6] Michalak JT, Paxton H. Some recovery characteristics of zone-melted iron. *Transactions Metallurgical Society AIME*. 1961;221(4): 850-857.
- [7] Mukunthan K, Hawbolt EB. Modeling recovery and recrystallization kinetics in cold-rolled Ti-Nb stabilized interstitial-free steel. *Metallurgical and Materials Transactions: A*. 1996;27(11): 3410-3423.
- [8] Smith A, Luo H, Hanlon DN, Sietsma J, Zwaag S. Recovery Processes in the Ferrite Phase in C-Mn Steel. *Iron and Steel Institute of Japan International*. 2004;44(7): 1188-1194.
- [9] Martinez-de-Guerenu A, Arizti F, Diaz-Fuentes M, Gutiérrez I. Recovery during annealing in a cold rolled low carbon steel. Part I: kinetics and microstructural characterization. *Acta Materialia*. 2004;52(12): 3657-3664.
- [10] Martinez-de-Guerenu A, Arizti F, Gutiérrez I. Recovery during annealing in a cold rolled low carbon steel. Part II: modeling the kinetics. *Acta Materialia*. 2004;52(12): 3665-3670.
- [11] Maeda K, Zhou T, Zurob HS. Hot deformation behavior of an Fe-Al alloy steel in the two phase region. In: *TMS 2014: 143rd Annual Meeting & Exhibition Annual Meeting Supplemental Proceedings*. Springer; 2014. p.927-933.
- [12] Verdier M, Brechet Y, Guyot P. Recovery of AlMg alloys: flow stress and strain-hardening properties. *Acta Materialia*. 1999;47(1): 127-134.
- [13] Nes E. Recovery revisited. *Acta Materialia*. 1995;43(6): 2189-2207.
- [14] Frost J, Ashby MF. *Deformation-Mechanism Maps*. Oxford: Pergamon Press; 1982.
- [15] Kucera J, Stransky K. Diffusion in iron, iron solid solutions and steels. *Materials Science and Engineering*. 1982;52: 1-38.

# BULK GREEN'S FUNCTIONS IN ONE-DIMENSIONAL UNSTEADY PROBLEMS OF ELASTIC DIFFUSION

L.A. Igumnov<sup>1</sup>, D.V. Tarlakovskii<sup>1,2,3</sup>, A.V. Zemskov<sup>2,3</sup>

<sup>1</sup>Research Institute for Mechanics, National Research Lobachevsky State University of Nizhny Novgorod, 603950, Prospekt Gagarina (Gagarin Avenue), 23, bldg. 6, Nizhny Novgorod, Russia

<sup>2</sup>Institute of Mechanics (Lomonosov Moscow State University), 119192, Moscow, Michurinsky prospekt 1, Russia

<sup>3</sup>Moscow Aviation Institute, 125993, Moscow, Volokolamskoye shosse 4, A-80, GSP-3, Russia

\*e-mail: azemskov1975@mail.ru

**Abstract.** We consider a one-dimensional unsteady problem of elasticity with diffusion and preset unsteady volumetric disturbances. The mathematical model is based on a local equilibrium model of elastic diffusion. The solution is sought in integral form. The bulk Green's functions are found via Laplace transform and Fourier transform for unbounded medium, sine and cosine transform for semi-bounded medium, Fourier's series for bounded medium.

**Keywords:** elastic diffusion, unsteady problems, Green's functions, integral transformations

## 1. Introduction

In a number of cases, to calculate the stress-strain state of the medium, it is necessary to take into account the action of mass forces (weight, temperature field, etc.) or some initial spatial distribution of physical fields. The solution of such problems is expressed in terms of the bulk Green's functions.

The problems of elastic diffusion were considered in [1-9]. As a rule, these problems are solved in a stationary formulation [6]. The solution of unsteady problems is sought using the Laplace transform. The inversion of the Laplace transform is performed numerically using the Durbin algorithm and its modifications [7-9]. Publications devoted to the construction of Green's functions of unsteady problems for elastic diffusion are not known at present.

The algorithm of finding the bulk Green's functions for a one-dimensional unsteady problem of elastic diffusion is considered.

## 2. Statement of the problem

Let us consider a homogeneous  $N$ -component solid continuum affected by volumetric unsteady elastic diffusion disturbances.

Physical and mechanical processes in a rectangular Cartesian coordinate system are described by coupled equations of motion and mass transfer (the point is time derivative by  $\tau$ , the prime is coordinate derivatives by  $x$ ) [5-13]:

$$\begin{aligned} \ddot{u}(x, \tau) &= u''(x, \tau) - \sum_{j=1}^N \alpha_j \eta_j'(x, \tau) + F_1(x, \tau), \\ \dot{\eta}_q(x, \tau) &= D_q \eta_q''(x, \tau) - \Lambda_q u'''(x, \tau) + F_{q+1}(x, \tau) \quad (q = \overline{1, N}). \end{aligned} \quad (1)$$

All values here are dimensionless. Their connection with dimensional analogues will be expressed as follows:

$$x = \frac{x_1}{L}, u = \frac{u_1}{L}, \tau = \frac{Ct}{L}, \eta_q = \frac{\eta^{(q)}}{n_0}, C^2 = \frac{\lambda + 2\mu}{\rho}, F_1 = \frac{\rho LF}{\lambda + 2\mu}, F_{q+1} = \frac{LF^{(q)}}{C},$$

$$n_0 = \sum_{q=1}^N n_0^{(q)}, \alpha_q = \frac{\alpha^{(q)}}{\lambda + 2\mu}, D_q = \frac{D^{(q)}}{CL}, \Lambda_q = \frac{\Lambda^{(q)}}{CL}, \Lambda^{(q)} = \frac{n_0^{(q)} m^{(q)} D^{(q)} \alpha^{(q)}}{\rho RT_0},$$

where  $x_i$  is Cartesian coordinate ( $Ox_1$  axis is normal to the boundary of the domain);  $t$  is time;  $u_i$  is displacement;  $T_0$  is initial temperature;  $\eta^{(q)} = n^{(q)} - n_0^{(q)}$  is concentration increment;  $n^{(q)}$  and  $n_0^{(q)}$  is actual and initial concentration of component  $q$ ;  $\alpha^{(q)}$  is coefficient of volume expansion due to mass transfer;  $R$  is the universal gas constant;  $D^{(q)}$  is coefficient of self-diffusion;  $\lambda, \mu$  are the elastic Lamé constants;  $\rho$  is density of the medium,  $m^{(q)}$  is molar mass;  $F$  and  $F^{(q)}$  are the bulk perturbations;  $L$  is the layer thickness or is the characteristic length of half-space.

Then we consider initial boundary value problems for the following domains:

- unbounded domain (Cauchy problem)  $-\infty < x < \infty$ ;

- semi-bounded problem (one-dimensional half-space)  $x > 0$ , with boundary conditions as follows:

$$u|_{x=0} = 0, J_q|_{x=0} = 0, u, \eta_q, \sigma, J_q = O(1) \quad (x \rightarrow \infty), \quad q = \overline{1, N}, \quad (2)$$

or

$$\sigma|_{x=0} = 0, \eta_q|_{x=0} = 0, u, \eta_q, \sigma, J_q = O(1) \quad (x \rightarrow \infty), \quad q = \overline{1, N}. \quad (3)$$

- bounded domain (one-dimensional layer)  $0 < x < 1$  with the boundary conditions:

$$u|_{x=0} = 0, J_q|_{x=0} = 0, u|_{x=1} = 0, J_q|_{x=1} = 0, \quad q = \overline{1, N}, \quad (4)$$

or

$$\sigma|_{x=0} = 0, \eta_q|_{x=0} = 0, \sigma|_{x=1} = 0, \eta_q|_{x=1} = 0, \quad (5)$$

or

$$u|_{x=0} = 0, J_q|_{x=0} = 0, \sigma|_{x=1} = 0, \eta_q|_{x=1} = 0, \quad (6)$$

with initial conditions for each problems assumed to be zero

$$u_i|_{\tau=0} = \dot{u}_i|_{\tau=0} = \eta_q|_{\tau=0} = 0. \quad (7)$$

Here  $J_q$  is density of diffusion flow for component  $q$ ,  $\sigma = \sigma_{11}$  is stress tensor component, which is found by the formula [5-13]:

$$J_q = \Lambda_q u'' - D_q \eta'_q, \quad \sigma = u' - \sum_{j=1}^N \alpha_j \eta_j.$$

### 3. Solution method

Let us introduce functions  $G_{km}(x, \xi, \tau)$ , which will be understood as follows:  $G_{km}^h(x, \xi, \tau)$  - bulk Green's functions for half-space,  $G_{km}^l(x, \xi, \tau)$  - bulk Green's functions for a layer.

In accordance with (1) they satisfy the system of equations ( $q = \overline{1, N}, m = \overline{1, N+1}$ ):

$$\ddot{G}_{1m} = G_{1m}'' - \sum_{j=1}^N \alpha_j G'_{j+1,m} + \delta_{1m} \Delta_1, \dot{G}_{q+1,m} = D_q G''_{q+1,m} - \Lambda_q G'''_{1m} + \delta_{q+1,m} \Delta_{q+1}, \quad (8)$$

$$\Delta_m = \delta(x - \xi) \delta(\tau),$$

and homogeneous boundary conditions (2) or (3) for functions  $G_{km}^h$ , (4) or (5) or (6) for functions  $G_{km}^l$ .

Here  $\delta_{1m}$  is the Kronecker symbol,  $\delta(\tau)$  is the Dirac delta function, the prime is coordinate derivatives by  $x$ . The initial condition of all functions are represented as (7).

A general solution of the problem (1) with corresponding homogeneous boundary conditions will take the form:

$$u(x, \tau) = \sum_{k=1}^{N+1} \int_0^\tau \int_0^Z G_{1k}(x, \xi, \tau - t) F_k(\xi, t) d\xi dt, \quad \eta_q(x, \tau) = \sum_{k=1}^{N+1} \int_0^\tau \int_0^Z G_{q+1,k}(x, \xi, \tau - t) F_k(\xi, t) d\xi dt. \quad (9)$$

where  $Z = +\infty$  in problems for half-space,  $Z = 1$  in problems for a layer.

Let us find functions  $G_{km}^l$ . For this, purpose we will apply the Laplace transform and Fourier series to the system (8). This will result into (here small upper indices « $s$ » and « $c$ » stand for sine and cosine harmonics of Fourier series, upper index « $L$ » is Laplace's transform, « $s$ » is parameter of Laplace transform,  $\lambda_n = \pi n$ ):

- for boundary conditions (4)

$$G_{q+1,m}^{LLc}(0, \xi, s) = s^{-1} \delta_{q+1,m}; \quad (10)$$

$$(\lambda_n^2 + s^2) G_{1m}^{LLs}(\lambda_n, \xi, s) - \sum_{j=1}^N \alpha_j \lambda_n G_{j+1,m}^{LLc}(\lambda_n, \xi, s) = 2\delta_{1m} \cos \lambda_n \xi, \quad (11)$$

$$-\Lambda_q \lambda_n^3 G_{1m}^{LLs}(\lambda_n, \xi, s) + (s + D_q \lambda_n^2) G_{q+1,m}^{LLc}(\lambda_n, \xi, s) = 2\delta_{q+1,m} \sin \lambda_n \xi;$$

$$G_{1m}^{LL}(x, \xi, s) = \sum_{n=1}^{\infty} G_{1m}^{LLs}(\lambda_n, \xi, s) \sin \lambda_n x, \quad G_{q+1,m}^{LL}(x, \xi, s) = \sum_{n=0}^{\infty} G_{q+1,m}^{LLc}(\lambda_n, \xi, s) \cos \lambda_n x, \quad (12)$$

$$G_{1m}^{LLs}(\lambda_n, \xi, s) = 2 \int_0^1 G_{1m}^{LL}(x, \xi, s) \sin \lambda_n x dx, \quad G_{q+1,m}^{LLc}(\lambda_n, \xi, s) = 2 \int_0^1 G_{q+1,m}^{LL}(x, \xi, s) \cos \lambda_n x dx.$$

- for boundary conditions (5)

$$G_{1m}^{LLc}(0, \xi, s) = s^{-2} \delta_{1m}; \quad (13)$$

$$(\lambda_n^2 + s^2) G_{1m}^{LLc}(\lambda_n, \xi, s) + \sum_{j=1}^N \alpha_j \lambda_n G_{j+1,m}^{LLs}(\lambda_n, \xi, s) = 2\delta_{1m} \sin \lambda_n \xi, \quad (14)$$

$$\Lambda_q \lambda_n^3 G_{1m}^{LLc}(\lambda_n, \xi, s) + (s + D_q \lambda_n^2) G_{q+1,m}^{LLs}(\lambda_n, \xi, s) = 2\delta_{q+1,m} \cos \lambda_n \xi;$$

$$G_{1m}^{LL}(x, \xi, s) = \sum_{n=0}^{\infty} G_{1m}^{LLc}(\lambda_n, \xi, s) \cos \lambda_n x, \quad G_{q+1,m}^{LL}(x, \xi, s) = \sum_{n=1}^{\infty} G_{q+1,m}^{LLs}(\lambda_n, \xi, s) \sin \lambda_n x, \quad (15)$$

$$G_{1m}^{LLc}(\lambda_n, \xi, s) = 2 \int_0^1 G_{1m}^{LL}(x, \xi, s) \cos \lambda_n x dx, \quad G_{q+1,m}^{LLs}(\lambda_n, \xi, s) = 2 \int_0^1 G_{q+1,m}^{LL}(x, \xi, s) \sin \lambda_n x dx.$$

The solutions of the system (11) are written as follows:

$$\left\{ \begin{array}{l} G_{11}^{lls}(\lambda_n, \xi, s) \\ G_{1,q+1}^{lls}(\lambda_n, \xi, s) \end{array} \right\} = 2 \left\{ \begin{array}{l} P_{11}(\lambda_n, s) \sin \lambda_n \xi \\ P_{1,q+1}(\lambda_n, s) \cos \xi \lambda_n \end{array} \right\} \frac{1}{P(\lambda_n, s)} \quad (p, q = \overline{1, N}),$$

$$G_{q+1,1}^{llc}(\lambda_n, \xi, s) = 2 \frac{P_{q+1,1}(\lambda_n, s)}{P(\lambda_n, s)} \sin \lambda_n \xi, \quad (16)$$

$$G_{q+1,p+1}^{llc}(\lambda_n, \xi, s) = 2 \left[ \frac{\delta_{pq}}{s + D_q \lambda_n^2} + \frac{P_{q+1,p+1}(\lambda_n, s)}{Q_q(\lambda_n, s)} \right] \cos \lambda_n \xi,$$

$$P_{1,q+1}(\lambda_n, s) = \alpha_q \lambda_n \prod_{r \neq q}^N (s + D_r \lambda_n^2), \quad P_{q+1,p+1}(\lambda_n, s) = \alpha_p \Lambda_q \lambda_n^4 \prod_{r \neq p}^N (s + D_r \lambda_n^2),$$

$$P_{11}(\lambda_n, s) = \prod_{j=1}^N (s + D_j \lambda_n^2), \quad P_{q+1,1}(\lambda_n, s) = \lambda_n^3 \Lambda_q \prod_{j=1, j \neq q}^N (s + D_j \lambda_n^2) \quad (p, q = \overline{1, N}).$$

Similarly, the solutions of the system (14) are written as follows:

$$G_{q+1,1}^{lls}(\lambda_n, \xi, s) = 2 \frac{P_{q+1,1}(\lambda_n, s)}{P(\lambda_n, s)} \cos \xi \lambda_n,$$

$$\left\{ \begin{array}{l} G_{11}^{llc}(\lambda_n, \xi, s) \\ G_{1,q+1}^{llc}(\lambda_n, \xi, s) \end{array} \right\} = 2 \left\{ \begin{array}{l} P_{11}(\lambda_n, s) \cos \xi \lambda_n \\ P_{1,q+1}(\lambda_n, s) \sin \xi \lambda_n \end{array} \right\} \frac{1}{P(\lambda_n, s)}, \quad (17)$$

$$G_{q+1,p+1}^{lls}(\lambda_n, \xi, s) = 2 \left[ \frac{\delta_{pq}}{s + D_q \lambda_n^2} + \frac{P_{q+1,p+1}(\lambda_n, s)}{Q_q(\lambda_n, s)} \right] \sin \xi \lambda_n,$$

$$P_{1,q+1}(\lambda_n, s) = -\alpha_q \lambda_n \prod_{r \neq q}^N (s + D_r \lambda_n^2), \quad P_{q+1,p+1}(\lambda_n, s) = \alpha_p \Lambda_q \lambda_n^4 \prod_{r \neq p}^N (s + D_r \lambda_n^2),$$

$$P_{11}(\lambda_n, s) = \prod_{j=1}^N (s + D_j \lambda_n^2), \quad P_{q+1,1}(\lambda_n, s) = -\lambda_n^3 \Lambda_q \prod_{j=1, j \neq q}^N (s + D_j \lambda_n^2) \quad (p, q = \overline{1, N}).$$

The polynomials  $P$  and  $Q_q$  in the equations (16) and (17) are determined by the formulas:

$$P(\lambda_n, s) = (s^2 + \lambda_n^2) \prod_{j=1}^N (s + D_j \lambda_n^2) - \sum_{j=1}^N \alpha_j \Lambda_j \lambda_n^4 \prod_{r=1, r \neq j}^N (s + D_r \lambda_n^2),$$

$$Q_q(\lambda_n, s) = P(\lambda_n, s) (s + D_q \lambda_n^2).$$

*Note.* The Green's functions for the layer and for the half-space are related as follows ( $\lambda$  is a parameter of sine and cosine transform, upper index «C» is cosine transform, upper index «S» is a sine transform)

$$\left\{ \begin{array}{l} G_{km}^{hLC}(\lambda, \xi, s) \\ G_{km}^{hLS}(\lambda, \xi, s) \end{array} \right\} = \left\{ \begin{array}{l} G_{km}^{llc}(\lambda, \xi, s) \\ G_{km}^{lls}(\lambda, \xi, s) \end{array} \right\}, \quad G_{km}^{hL}(x, \xi, s) = \frac{1}{\pi} \int_0^\infty \left\{ \begin{array}{l} G_{km}^{hLS}(\lambda, \xi, s) \sin \lambda x \\ G_{km}^{hLC}(\lambda, \xi, s) \cos \lambda x \end{array} \right\} d\lambda.$$

The Laplace transition to domain of originals in the equations (10), (12), (13), (15) - (16) is reduced to inversion of the following expressions ( $v$  is any of parameters  $\lambda$  or  $\lambda_n$ ):

$$\frac{1}{s}, \quad \frac{1}{s^2}, \quad \frac{1}{s + D_q v^2}, \quad \frac{P_m(v, s)}{P(v, s)}, \quad \frac{P_{q+1,m}(v, s)}{Q_q(v, s)}.$$

Their originals are found through deductions and on operational calculus tables and [12,13]:

$$L^{-1}\left[\frac{1}{s}\right] = H(\tau), \quad L^{-1}\left[\frac{1}{s^2}\right] = \tau, \quad L^{-1}\left[\frac{1}{s + D_q v^2}\right] = \exp(-D_q v^2 \tau),$$

$$L^{-1}\left[\frac{P_{1m}(v, s)}{P(v, s)}\right] = \sum_{j=1}^{N+2} A_{1m}^{(j)}(v) \exp(s_j(v) \tau), \quad L^{-1}\left[\frac{P_{q+1,m}(v, s)}{Q_q(v, s)}\right] = \sum_{j=1}^{N+3} A_{q+1,m}^{(j)}(v) \exp(s_j(v) \tau), \quad (18)$$

$$A_{km}^{(j)}(v) = \frac{P_{km}(v, s_j)}{P'(v, s_j)}, \quad A_{q+1,m}^{(j)}(v) = \frac{P_{q+1,m}(v, s_j)}{Q'_q(v, s_j)},$$

where  $s_k = s_k(v) (k = \overline{1, N+2})$  - zeros of polynomial  $P(v, s)$ ,  $s_{N+3}(v) = -D_q v^2$ ,  $H(\tau)$  - Heaviside function,  $L^{-1}$  - inverse operator of Laplace transform.

Inverse Fourier transform, sine and cosine transformation are done numerically through an algorithm presented in [12, 13].

Applying the Laplace transform and the Fourier series expansion (12) to system (8) for the mixed boundary-value problem (1) with homogeneous boundary conditions (6) leads to the system of linear algebraic equations (11). Its solution is (16), where  $\lambda_n = \pi(2n-1)/2$ . Accordingly, the transition to the originals space can be done using formulas (18).

#### 4. Example

As a calculation example let us consider a problem for a two-component layer ( $N=2$ ) with homogeneous boundary conditions (4). For body forces it is assumed:

$$F_1(x, \tau) = f_1(x)H(\tau), \quad F_2(x, \tau) = F_3(x, \tau) = 0, \quad f_1(x) = 1 - x.$$

The layer material is aluminum with the following properties [14]:

$$\lambda = 6.93 \cdot 10^{10} \frac{N}{m^2}, \quad \mu = 2.56 \cdot 10^{10} \frac{N}{m^2}, \quad T_0 = 800 \text{ K}, \quad \rho = 2700 \frac{kg}{m^3}, \quad L = 10^{-3} \text{ m},$$

$$\alpha_1 = 1.55 \cdot 10^7 \frac{J}{m^3}, \quad \alpha_2 = 6.14 \cdot 10^7 \frac{J}{m^3}, \quad D_1 = 7.73 \cdot 10^{-14} \frac{m^2}{s}, \quad D_2 = 3.11 \cdot 10^{-18} \frac{m^2}{s},$$

$$n_0^{(1)} = 0.95, \quad n_0^{(2)} = 0.05, \quad m^{(1)} = 0.027 \frac{kg}{mol}, \quad m^{(2)} = 0.064 \frac{kg}{mol}.$$

The calculation of convolutions (9) with considering (12) and (18) will result into ( $q=1, 2$ ):

$$u = 2 \sum_{n=1}^{\infty} \sum_{l=1}^4 A_{1l}^{(l)}(\lambda_n) \left[ \exp(s_l(\lambda_n) \tau) - 1 \right] \frac{\sin \lambda_n x}{\lambda_n s_l(\lambda_n)},$$

$$\eta_q = 2 \sum_{n=1}^{\infty} \sum_{l=1}^5 A_{q+1,l}^{(l)}(\lambda_n) \left[ \exp(s_l(\lambda_n) \tau) - 1 \right] \frac{\cos \lambda_n x}{\lambda_n s_l(\lambda_n)}.$$

The results of calculations are represented at the graphics below. Solid line is  $x=0.1$ , dotted is  $x=0.3$ , dashed is  $x=0.5$ .

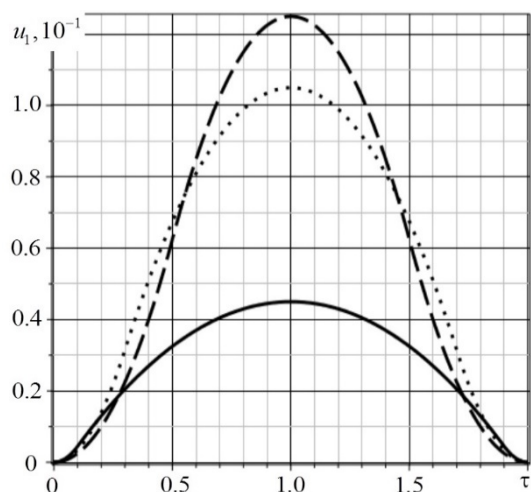


**Fig. 1.** The dependence of  $u(x, \tau)$  on  $\tau$

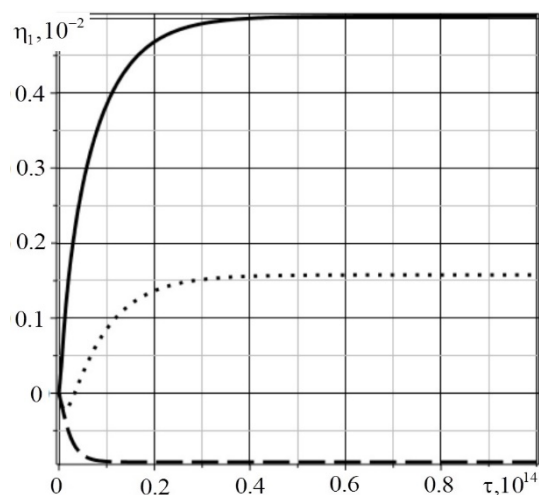


**Fig. 2.** The dependence of  $\eta_1(x, \tau)$  on  $\tau$

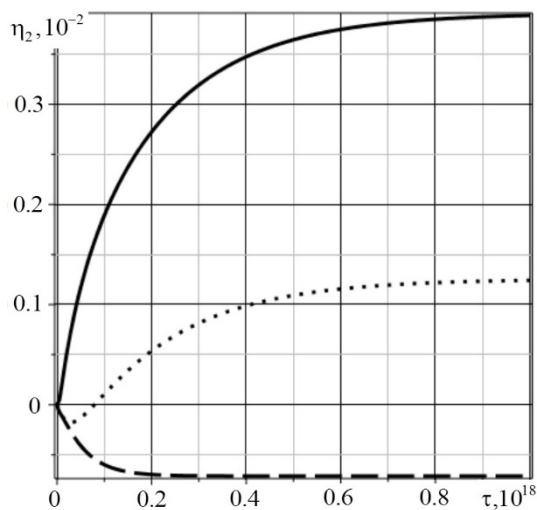


**Fig. 3.** The dependence of  $\eta_2(x, \tau)$  on  $\tau$

This result is in addition to the results obtained earlier in [11-13,15] when were considered problems of constructing surface Green's functions.

## 5. Conclusions

The proposed algorithm for finding Green's function allows one to determine the fields of displacements and the concentrations increments of the medium components for given bulk perturbations. The numerical-analytical method used in the article made it possible to obtain exact solutions in the explicit form. To demonstrate the algorithm operation, an example is considered for a two-component medium (duralumin) which illustrating the interaction effects of mechanical and diffusion fields.

*Acknowledgements.* The work is financially supported by the Federal Targeted Program for Research and Development in Priority Areas of Development of the Russian Scientific and Technological Complex for 2014-2020 under the contract No. 14.578.21.0246 (unique identifier RFMEFI57817X0246).

**References**

- [1] Aifantis EC. On the problem of diffusion in solid. *Acta Mechanica*. 1980;37(3-4): 265-296.
- [2] Eremeev VS. *Diffuziia I napriazheniia [Diffusion and stresses]*. Moscow: Energoatomizdat; 1984. (in Russian)
- [3] Podstrigach YS. Diffusion theory of anelasticity of metals. *Journal of Applied Mechanics and Technical Physics*. 1965;(2): 67-72. (in Russian)
- [4] Nowacki W. Dynamical Problems of Thermodiffusion in Solids. *Proc. Vib. Prob.* 1974;15: 105-128.
- [5] Knyazeva AG. Model of medium with diffusion and internal surfaces and some applied problems. *Mater. Phys. Mech.* 2004;7(1): 29-36.
- [6] Kumar R, Kansal T. Propagation of Lamb waves in transversely isotropic thermoelastic diffusive plate. *Int. J. Solid Struct.* 2008;45: 5890-5913.
- [7] Aouadi M. Variable electrical and thermal conductivity in the theory of generalized thermoelastic diffusion. *Zeitschrift fur Angewandte Mathematik und Physik*. 2005;57(2): 350-366.
- [8] Elhagary MA. A two-dimensional generalized thermoelastic diffusion problem for a half-space subjected to harmonically varying heating. *Acta Mech.* 2013;224: 3057-3069.
- [9] Sherief HH, El-Maghraby NM. A Thick Plate Problem in the Theory of Generalized Thermoelastic Diffusion. *Int. J. Thermophys.* 2009;30: 2044-2057.
- [10] Tarlakovskii DV, Vestyak VA, Zemskov AV. Dynamic Processes in Thermoelastoelectromagnetic and Thermoelastodiffusive Media. In: *Encyclopedia of thermal stress*. NY: Springer; 2014;2. p. 1064-1071.
- [11] Zemskov AV, Tarlakovskiy DV. Approximate solution of three-dimensional problem for elastic diffusion in orthotropic layer. *Journal of Mathematical Sciences*. 2014;203(2): 221-238.
- [12] Davydov SA, Zemskov AV, Tarlakovskii DV. An Elastic Half-Space under the Action of One-Dimensional Time-Dependent Diffusion Perturbations. *Lobachevskii Journal of Mathematics*. 2015;36(4): 503-509.
- [13] Zemskov AV, Tarlakovskiy DV. Two-dimensional nonstationary problem elastic for diffusion an isotropic one-component layer. *Journal of Applied Mechanics and Technical Physics*, 2015;56(6): 1023-1030.
- [14] Babichev AP, Babushkina NA, Bratkovsky AM. In: Grigoriev IS, Malikova EH. (eds) *Fizicheskiye velichiny: Sprovochnik [Physical quantities: reference manual]*. Moscow: Energoatomizdat; 1991. (In Russian)
- [15] Vestyak AV, Zemskov AV, Tarlakovskiy DV. Two-dimensional nonstationary problem of elastic diffusion for an orthotropic one-component half-plane. *Problems of strength and plasticity*, 2016;78(1): 5-13. (in Russian)

# THE INFLUENCE OF GAMMA RAYS RADIATION ON OPTICALLY INDUCED LUMINESCENCE OF COPPER-CONTAINING POTASSIUM-LITHIUM-BORATE GLASS

P.S. Shirshnev<sup>1\*</sup>, V.A. Spiridonov<sup>1</sup>, D.I. Panov<sup>1</sup>, E.V. Shirshneva-Vaschenko<sup>1</sup>,  
A.R.Gafarova<sup>2</sup>, R.M. Eremina<sup>2</sup>, A.E. Romanov<sup>1</sup>, V.E. Bougrov<sup>1</sup>

<sup>1</sup>ITMO University, Kronverkskiy prospect 49, Saint-Petersburg, 197101, Russia

<sup>2</sup>Zavoisky Physical-Technical Institute, FRC Kazan Scientific Center of RAS, Sibirskiy tract 10/7, Kazan, 420029, Russia

\*e-mail: pavel.shirshnev@gmail.com

**Abstract.** The paper presents the results of potassium-lithium-borate glass containing copper ions investigations. The glass was irradiated by 1.25 MeV gamma rays. The dose of radiation was 360 Gy. The exciting of the irradiated glass at 360 nm led to the long-wavelength photoluminescence band shift from 635 nm to 671 nm in comparison with non-irradiated glass. A new luminescence band at 685 nm also appeared for excitation wavelength 405 nm in the irradiated glass. It has been assumed that the luminescence band in glass at 671 nm – 685 nm corresponds to the luminescence of copper ions in the modified environment of the first coordination sphere. Copper-containing luminescent structures in borate glass with the luminescence maximum at 671-685 nm have been obtained for the first time. For the detailed study of these luminescent centers properties, thorough study of the structural variations in the gamma rays irradiated glass is required.

**Keywords:** gamma ray radiation, cluster, copper, borate glass, photoluminescence

## 1. Introduction

The borate glasses with ions and clusters of luminescent ions occupy some intermediate place between phosphate and silicate glasses. On the one hand, these glasses are thermally stable at the temperatures more than 200 degrees Celsius compared to phosphate glasses. On the other, the solubility limit of borate glasses is higher than of silicate ones. Therefore, copper-containing borate glass attracts attention in relation to its technical application. Moreover, due to the peculiarities of boron ions in composition of the borate glass, the strong modifying of the coordination environment, including luminescent ions, that are introduced to the glass composition, is possible [1,2].

These days, the luminescent structures with monovalent copper, in particular, copper-containing glasses, are relevant as down-converters and ultraviolet detectors [3]. In addition, copper-containing glass is also a promising phosphor material [4]. Copper attracts researchers as a cheap luminescent activator.

In recent times works it was shown that in borate glass with copper a quantum yield of at least 50% is achievable for the excitation wavelength 320 nm. It was also suggested the scheme of the spark sensor based on this glass [3]. Electron paramagnetic resonance (EPR) method demonstrated the existence of additional copper-containing structures in glass – may be dimers in addition to the copper ions [5]. It was previously found [6], that lithium-borate

copper-containing glass has luminescence in the 400–600 nm region for excitation wavelength 320 nm. The luminescence maximum shifts depending on the lithium concentration — with increasing lithium concentration, the shift occurs to the short-wavelengths.

It was also revealed that after heat treatment and nanocrystals segregation in glass, the luminescence maximum shifts to the long wavelength region [7]. Copper itself is extremely sensitive to the environment, and that makes it an interesting scientific object in borate glasses. It is also known that copper can segregate into clusters in glass and, depending on the cluster size, the wavelength of the luminescence can vary [8,9].

In recent studies of ionizing effects on the luminescent properties of borate glasses and crystals studies have been carried out. These studies are mainly focused on thermoluminescence investigations [10, 11]. In [12] the gamma rays irradiation of borate glass with bismuth ions changes its luminescence due to the breaking of covalent bonds in trigonal and tetrahedral boron groups. In 2017, the effect of X-rays on the luminescence of phosphate glass activated by silver and copper was studied [13]. It was demonstrated that an additional luminescence band appears in glasses, including in the copper-containing glass.

The purpose of this work is to study the gamma ray radiation effect on the luminescent properties of copper-containing borate glass. Since it is known that the structure modifying in borate glass under the action of gamma rays is possible, as well as copper can segregate into clusters and luminesce.

## 2. Objects and methods

Glasses with  $15\text{K}_2\text{O}-10\text{Li}_2\text{O}-25\text{Al}_2\text{O}_3-50\text{B}_2\text{O}_3$  (molar percent) composition with additions of 0.5  $\text{Cu}_2\text{O}$  and 4% graphite powder (weight percent) were synthesized for this study. The synthesis was carried out at the temperature of  $1450^\circ\text{C}$  for 2 hours, then the glass was poured out on a metal plate heated up to  $400^\circ\text{C}$  and then was cooled in a muffle from  $400^\circ\text{C}$  to room temperature for 10 hours. From the synthesized glass the sample was prepared. The size of the sample was  $10\times 8\times 8$  mm.

The sample was irradiated by gamma rays. The average energy of quanta was 1.25 MeV. The irradiation was carried out with the isotope element  $^{60}\text{Co}$ . The radiation dose was 360 Gy.

The luminescence spectra for excitation wavelength 405 nm were measured with an Avantes Avaspec 2048 spectrometer. The excitation with wavelength of 360 nm was carried out by UV light emitting diode (LED) with an intensity of 30 mW, the excitation with wavelength of 405 nm was carried out by a 100 mW laser diode.

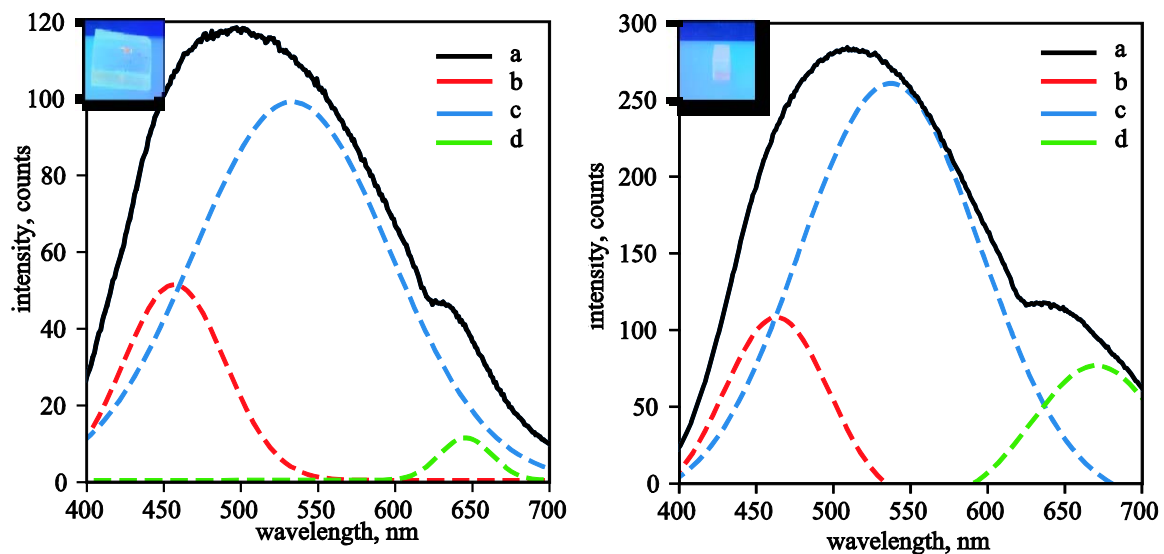
## 3. Results

The main photoluminescence parameters of the samples are given in the Table 1.

Figure 1 (left) presents that the glass sample before gamma ray irradiation for excitation wavelength 360 nm has three luminescence bands (a): the first band is at 450 nm with a half-width of 88 nm (b), the second band is at 530 nm with a half-width of 130 nm (c), and the third band is at 635 nm with a half-width of 80 nm. After gamma ray irradiation (Fig. 1 (right) (a)), the intensity peak of the short-wave band shifts to 460 nm (b). The band at 530 nm is 7 nm shifted with an increase in half-width by 8 nm (c). The band at 630 nm shifts to 685 nm with a change in half-width to 92 nm (d). Visually, the intensity and color of the luminescence, when the glass is irradiated with a mercury lamp with excitation wavelength of 360 nm, does not change.

Table 1. The main parameters of the luminescence of the samples,  $\lambda_{\text{exc}}$  – excitation wavelength, FWHM – full width at half maximum

Parameter	$L_{\text{max}}$ , $\lambda_{\text{ex}} =$ 360	FWHM $\lambda_{\text{ex}} =$ 360	$L_{\text{max}2}$ $\lambda_{\text{ex}} =$ 360	FWHM2 $\lambda_{\text{ex}} =$ 360	$L_{\text{max}3}$ $\lambda_{\text{ex}} =$ 360	FWHM3 $\lambda_{\text{ex}} =$ 360	$L_{\text{max}}$ $\lambda_{\text{ex}} =$ 405	FWHM $\lambda_{\text{ex}} =$ 405
Wavelength before irradiation, nm	530	130	450	88	635	80	584	116
Wavelength after irradiation, nm	537	138	460	80	671	92	685	79



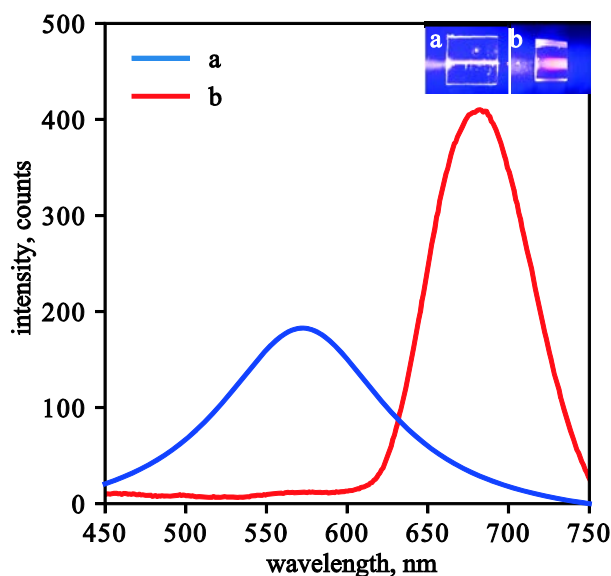
**Fig. 1.** Luminescence spectra upon excitation wavelength of 360 nm. left – before gamma rays irradiation, right – after gamma rays irradiation. Solid curves (a) – measured spectra, dashed curves (b, c, d) – decomposition by Gaussians

Figure 2 presents the luminescence spectra of the reference and irradiated by gamma rays samples for excitation wavelength 405 nm. The reference sample before gamma rays irradiation has a luminescence spectrum with a maximum at 584 nm. The half-width of the band is 116 nm. After gamma rays irradiation, the luminescence band shifts to 100 nm, and its half-width changes almost one and a half times to 79 nm. The luminescence color changes visually from yellow-orange to red, which is also shown in the insert (Fig. 2). It should be noted that the luminescence band at 685 nm is an order of magnitude higher than the luminescence band at 584 nm. In Fig. 2 these bands are given in proportion for understanding their structure.

#### 4. Discussion

The luminescence band at 450–460 nm upon exciting copper-containing borate glass at 360 nm corresponds to the monovalent copper ion luminescence [14, 15]. As it can be seen from the literature, the excitation band edge of monovalent copper is 360 nm. The luminescence band may vary depending on the degree of tetrahedral distortion of the copper environment [16]. The gamma ray irradiation causes a slight shift in the copper luminescence band, which can be explained by a slight change in the structure of the glass around the ion.

According to [17–21], the luminescence band at 530 nm upon excitation wavelength of 360 nm can correspond to  $\text{Cu}^+ - \text{Cu}^+$  dimers [8]. After gamma ray irradiation, the  $\text{Cu}^+ - \text{Cu}^+$  dimers band, as well as luminescence band of copper ions, shifts by 10 nm to the long wavelengths, which also indicates a change in the structure of copper dimers environment.



**Fig. 2.** Photoluminescence spectra and photos of samples upon excitation wavelength of 405 nm: a – before gamma rays irradiation, b – after gamma rays irradiation

The 635 nm band most definitely corresponds to  $(\text{Cu}_2\text{O})_n$  clusters. In [9], the luminescence band with a maximum at 600 nm was indicated for copper oxide clusters. However, it can vary depending on the cluster size.

We assume that the band with a maximum at 635 nm for the excitation wavelength 360 nm is related to the band of copper oxide [17, 8] and  $\text{Cu}_4$  [9].

It should be pointed out that, in [8], molecular clusters in borate copper-containing glass were obtained after a long time (20 hours) heat treatment at high temperatures ( $480^\circ\text{C}$ ). In our glass, the clusters are obtained "immediately", as it is evidenced by the luminescence peak at 635 nm. This result can be explained by the fact that the lithium-borate matrix has unique segregation properties [22]. Therefore, the formation of clusters during the synthesis of glass is already possible at the stage of its cooling after melt.

The existence of the luminescence band at 671 nm that appears after gamma rays irradiation can be explained similar to [13]. There it was demonstrated the appearance of the third luminescence band in copper-containing phosphate glass, which is similar by its structure to our band for the excitation wavelength 360 nm. In both cases the same "broadening" of the right wing of the luminescence band occurs. However, in the phosphate glass, such band appears after X-ray irradiation and heat treatment. In [13], luminescence is excited by shorter-wavelength light sources (320 nm) and luminescence band itself is also at a shorter-wavelength 570–580 nm.

The question of the 671 nm band belonging to luminescent structures will be discussed below.

Let us analyze the luminescence bands for the excitation wavelength 405 nm. As it can be seen from the luminescence spectra, there is a luminescence band at 584 nm in the reference sample (before gamma ray irradiation) for the excitation wavelength 405 nm. According to [17, 8], the edge of the excitation band of  $(\text{Cu}_2\text{O})_n$  clusters passes through 405 nm, with luminescence at 600 nm.

Consequently, considering the results of the sample irradiation, it can be said that the "abnormal" band is at 685 nm, which is not described in the literature concerning copper-containing borate glasses.

We will try to explain its origin. It was revealed in [23] that copper ions surrounded by organic complexes had luminescence spectra with a maximum at a wavelength 680 nm for the excitation wavelength 405 nm.

In the case of the above-mentioned phosphate glass [13], irradiation was carried out with less energy X-ray radiation. The X-ray wavelength in [13] was 0.15 nm, in our experiment it was 0.000992 nm, that is 150 times smaller, respectively. Thus, the irradiation energy in our study is 150 times more than in [13].

It can be assumed that at such radiation energies, the covalent bonds of a part of boron ions are destroyed in such a way that the configuration of the environment, where copper ions are located, changes. Consequently, the system of levels is modified, which ultimately gives the above-mentioned effect of the appearance of the luminescence at 685 nm for the excitation wavelength 405 nm, as well as a band of 671 nm for the excitation wavelength 360 nm.

## 5. Conclusion

It has been shown that, upon gamma rays irradiation with dose of 360 Henry, a new intense luminescence band appears in lithium borate glass. The luminescence band at 685 nm corresponds to the exciting wavelength 405 nm, the luminescence band at 671 nm corresponds to the exciting wavelength 360 nm. The effect has not been previously mentioned in the literature and can be useful from a practical point of view for creating fluorescent dosimeters of gamma radiation. In order to understand exactly which structures luminesce in glass, a detailed study of the samples structure by other methods is necessary.

**Acknowledgments.** We glad to Igor Arkadievich Gladskih for photoluminescence spectra corrections. Research was conducted under the support of the Russian Science Foundation, Grant no. 17-72-10216.

## References

- [1] Rimbach AC, Steudel F, Ahrens B, Schweizer S. Tb<sup>3+</sup>, Eu<sup>3+</sup>, and Dy<sup>3+</sup> doped lithium borate and lithium aluminoborate glass: Glass properties and photoluminescence quantum efficiency. *Journal of Non-Crystalline Solids*. 2018;499: 380-386.
- [2] Loos S, Mungra M, Ahrens B, Leonard RL, Evans A, Johnson JA, Steudel F, Schweizer F. Concentration-dependent luminescence and energy transfer in Tb<sup>3+</sup>/Eu<sup>3+</sup> doped borate and fluorozirconate glasses. *Journal of Luminescence*. 2017;187: 298-303.
- [3] Shirshnev PS, Romanov AE, Bougrov VE, Shirshneva-Vaschenko EV, Snezhnaia ZG. Potassium-alumina-boron glass doped with copper ions for solar cell down-convertors. In: Wehrspohn RB. (ed.) *Proceedings Volume 10688, Photonics for Solar Energy Systems VIII*. 2018. p.106881D.
- [4] Guo H, Wei R, Liu X. Tunable white luminescence and energy transfer in (Cu<sup>+</sup>)<sub>2</sub>, Eu<sup>3+</sup> codoped sodium silicate glasses. *Opt. Lett.* 2012;37(10): 1670-1672.
- [5] Shirshnev PS, Eremina RM, Yatsyk IV, Snezhnaia ZG, Panov DI, Shirshneva-Vaschenko EV, Romanov AE, Bougrov VE. The Electron Spin Resonance (ESR) Spectra of Potassium-Alumina-Borate Glass Doped with Copper Ions. *Reviews on Advanced Materials Science*. 2018;57(2): 212-214.
- [6] Shirshnev PS, Snezhnaia ZG, Shirshneva-Vaschenko EV, Romanov AE, Bougrov VE. Relation of the optical properties of boron copper-containing glasses on the concentration of lithium. *Materials Physics and Mechanics*. 2018;40(1): 78-83.

- [7] Shirshnev PS, Ugolkov VL, Snezhnaia ZG, Panov DI, Shirshneva-Vaschenko EV, Lipnitskaya SN, Romanov AE, Bougrov VE. The effect of heat treatment on the optical properties of copper-containing lithium-potassium-borate glasses. *Reviews on Advanced Materials Science*. 2018;57(1): 116-120.
- [8] Nikonorov NV, Sidorov AI, Tsekhomskii VA, Shakhverdov TA. Broadband copper luminescence in potassium-aluminum borate glasses. *Optics and Spectroscopy*. 2013;114(3): 379-383.
- [9] Ozin GA, Mitchell SA, McIntosh DF, Mattar S. Copper atoms and copper clusters in solid xenon. Special atom and dimer sites and covalently bound clusters with three to five atoms. *The Journal of Physical Chemistry*. 1983;87(23): 4651-4665.
- [10] Anjaiah J, Laxmikanth C, Kistaiah P, Veeraiah N. Dosimetric and kinetic parameters of lithium cadmium borate glasses doped with rare earth ions. *Journal of Radiation Research and Applied Sciences*. 2014;7(4): 519-525.
- [11] Saidu A, Wagiran H, Saeed MA, Alajerami YSM. Thermoluminescence characteristics of zinc lithium borate glass activated with  $\text{Cu}^+$  ( $\text{ZnO-Li}_2\text{O-B}_2\text{O}_3:\text{Cu}^+$ ) for radiation dosimetry. *Journal of Radioanalytical and Nuclear Chemistry*. 2015;304(2): 627-632.
- [12] Hegde V, Prabhu N, Wagh A, Sayyed MI, Agar O, Kamath SD. Influence of 1.25 MeV gamma rays on optical and luminescent features of  $\text{Er}^{3+}$  doped zinc bismuth borate glasses. *Results in Physics*. 2019;12: 1762-1769.
- [13] Murashov AA, Sidorov AI, Stolyarchuk MV, Boiko ME. Effect of X-ray irradiation and thermal treatment on luminescent properties of barium-phosphate glasses doped with silver and copper. *Journal of Non-Crystalline Solids*. 2017;477: 1-6.
- [14] Jacob A, Parent C, Marcel C, Le Flem G, Moine B, Pedrini C. Copper Luminescence in Phosphate and Borate Glasses. *Materials Science Forum*. 1997;239-241: 283-286.
- [15] Verwey JWM, Coronado JM, Blasse G. The luminescence of  $\text{Cu(I)}$  in strontium tetraborate. *Journal of Solid State Chemistry*. 1991;92(2): 531-536.
- [16] Debnath R, Das SK. Site-dependent luminescence of  $\text{Cu}^+$  ions in silica glass. *Chemical Physics Letters*. 1989;155(1): 52-58.
- [17] Babkina AN, Kiprushkina TS, Shirshnev PS, Nikonorov NV. Luminescence thermochromism in glass with copper-containing molecular clusters. *Journal of Optical Technology*. 2016;83(7): 434-437.
- [18] Chen H, Matsuoka M, Zhang J, Anpo M. The reduction behavior of the Cu ion species exchanged into Y zeolite during the thermovacuum treatment. *Journal of Catalysis*. 2004;228(1): 75-79.
- [19] Srikumar T, Kityk IV, Srinivasa RC, Gandhi Y, Piasecki M, Bragiel P, Kumar VR, Veeraiaha N. Photostimulated optical effects and some related features of  $\text{CuO}$  mixed  $\text{Li}_2\text{O-Nb}_2\text{O}_5\text{-ZrO}_2\text{-SiO}_2$  glass ceramics. *Ceramics International*. 2011;37(7): 2763-2779.
- [20] YiZhong LU, WenTao WEI, Wei C. Copper nanoclusters: Synthesis, characterization and properties. *Chinese Science Bulletin*. 2011;57(1): 41-47.
- [21] Babkina AN, Sidorov AI, Shirshnev PS. Thermochromic effect in aluminoborate glasses with copper (i) and chlorine ions. *Journal of Optical Technology*. 2014;81(1): 50-52.
- [22] Babkina AN, Gorbachev AD, Zyryanova KS, Nikonorov NV, Nuryev RK, Stepanov SA. A study of the effect of lithium oxide on the spectral properties of potassium-aluminoborate glass activated by chromium ions. *Optics and Spectroscopy*. 2017;123(3): 369-374.
- [23] Crestani MG, Manbeck GF, Brennessel WW, McCormick TM, Eisenberg R. Synthesis and Characterization of Neutral Luminescent Diphosphine Pyrrole- and Indole-Aldimine Copper(I) Complexes. *Inorganic Chemistry*. 2011;50(15): 7172-7188.

# BORON AND NITROGEN DOPANT ATOMS PRECISE TUNING (INCREMENT AND REDUCTION) OF CHARGE-TRANSFER RATES IN HYDROGENATED GRAPHENE

G.K. Sunnardianto<sup>1,2\*</sup>, F. Triawan<sup>2</sup>, A.M. Aamer<sup>2</sup>, S. Hastuty<sup>3</sup>, A.B.D. Nandiyanto<sup>4</sup>,  
A.G. Abdullah<sup>5</sup>

<sup>1</sup>Research Center for Chemistry, Indonesian Institute of Sciences (LIPI), Kawasan Puspitek Serpong, Tangerang Selatan, 15314, Indonesia

<sup>2</sup>Faculty of Engineering and Technology, Sampoerna University, Jl. Raya Pasar Minggu, Kav 16, Jakarta, Indonesia

<sup>3</sup>Department of Mechanical Engineering, Universitas Pertamina, Jl. Teuku Nyak Arief, Kebayoran Lama, Jakarta, Indonesia

<sup>4</sup>Departemen Kimia, Universitas Pendidikan Indonesia, Jl. Dr. Setiabudi no 229, Bandung 40154, Indonesia

<sup>5</sup>Departemen Teknik Elektro, Universitas Pendidikan Indonesia, Jl. Dr. Setiabudi no 229, Bandung 40154, Indonesia

\*e-mail: gagus.ketut.sunnardianto@lipi.go.id

**Abstract.** Graphene is a new remarkable material for diverse applications, especially when grapheme is interacted with hydrogen. The charge-transfer rates (CTR) from hydrogen to graphene is substantial to determine the electronic properties. A new approach to increase and decreases the charge-transfer from hydrogen to graphene is proposed. By using density functional theory calculation method, the effect of B and N doping on the CTR of hydrogenated graphene is investigated. The results found that both of dopants (B and N) had opposite effect on the CTR of hydrogenated graphene. B doping increased CTR, while N doping decreased CTR from hydrogen to graphene. The research finding may provide a promising rule for quantitatively tuning and or controlling of CTR in hydrogenation graphene by atom dopant, which is potential importance for their use in electrochemical and energy-related application.

**Keywords:** charge-transfer rates (CTR), graphene, hydrogenation, coverage, dopant

## 1. Introduction

The Chemical functionalization is an attractive way to modify physical and chemical properties of graphene. The chemical inertness of graphene surface and the absence of band gap motivates researcher in modifying graphene by substituting dopant atom in order to improve the integration of graphene in electronic and chemical device application.

The most common dopant atom for carbon materials is Boron (B) and Nitrogen (N) [1]. It has been reported that B or N substitution in CNT has been widely studied experimentally and theoretically [2,3]. Not only in CNT, B and N doping in graphitic carbon materials also has been widely studied experimentally and theoretically [4,5]. Also, B and N doped graphene have been successful realized [6,7]. Experimental works show that the electrochemical

performance of B and N doped graphene is better than pristine graphene [8]. B and N can form the most stable defect and can be readily incorporated in graphene lattice [1,9]. Additionally, B and N doped graphene materials are highly promising materials for electronic, electrochemical applications, and transport properties [10, 11], such as energy storage [12], sensing [13] and capacitors [14].

Doping of graphene with N was realized experimentally [15,16] and has promising properties towards application in the field of electrochemical sensing [15], lithium-ion batteries [17], p-n junction [18] and fuel cells [19].

Hydrogen is a widely available element, an ideal partner for carbon atoms to make strong covalent [20] and the most broadly used as adsorbate to functionalize graphene [21]. Furthermore, hydrogen on graphene surface has been the subject of intense studies for hydrogen storage [22,23]. Hydrogenations of these doped graphene appear to be feasible route to have hydrogenated of doped graphene. The charge-transfer rate from hydrogen to graphene is substantial to determine the electronic properties of graphene for diverse applications. Therefore, how to tune the CTR from hydrogen to graphene is important to be revealed.

Recently, Sunnardianto et al. [24] succeeded to derive the rule to determine the charge-transfer rates (CTR) from hydrogen to graphene in wide range of coverage. The finding reveals that the CTR roughly shows a linear behavior from 0.22e for the dilute limit to 0.15e for the half-coverage limit [24]. The next step is how to control the CTR (increase and decrease of CTR) by dopant atom.

To the best of our knowledge, the impact of dopant (B and/or N atoms) on CTR of hydrogenated graphene has not been explored yet. In order to fundamentally understand how to tune and or control of CTR value in optimizing graphene for device application, a simple strategy to control and conveniently tune of CTR from hydrogen to graphene was proposed in this study. This study would give a tremendous impact on the design of doped graphene system from the electrochemical device application point of view. On the other hand, it would also open new ways on how to design and control CTR of hydrogenated doped graphene.

## 2. Materials and method

In this study, the arrangement of hydrogen atom randomly on B and N doped graphene were considered. At each coverage (H/C: 0.125, 0.25, 0.375), ten possible configurations of hydrogen arrangement were used. In this case, the effect of single dopant on the CTR of hydrogenated graphene was proposed. As for N doped graphene, three common C-N bonding configurations are normally obtained when doping nitrogen into the graphene lattice; pyridinic N, pyrrolic N, and graphitic N. Graphitic N is the substitution of carbon atom by nitrogen, pyridinic N is the substitution of carbon atom by nitrogen at the edge of vacancy. Experimentally observed pyridinic N type is energetically favorable for high concentration of N, but thermally unstable, while graphitic N type is the most energetically favorable than other N types doping for low concentration of N [25]. Since a single doping was used, so N-graphene in the form of graphitic N was considered.

The structure models used for simulation are graphene sheets consisting 47 carbon atoms in rectangular super cells (see Fig. 1). For low coverage of H adsorption, the most favorable H adsorption site is the nearest-neighbor position of the dopant site for B and N doped graphene and for larger H coverage the formation of dimers close to the dopant site is energetically favorable over hydrogenation [20]. In these simulations, we keep at least two or three of hydrogen atoms lie on the carbon atoms neighboring the substitution boron sites to know the effect of dopant to the CTR.

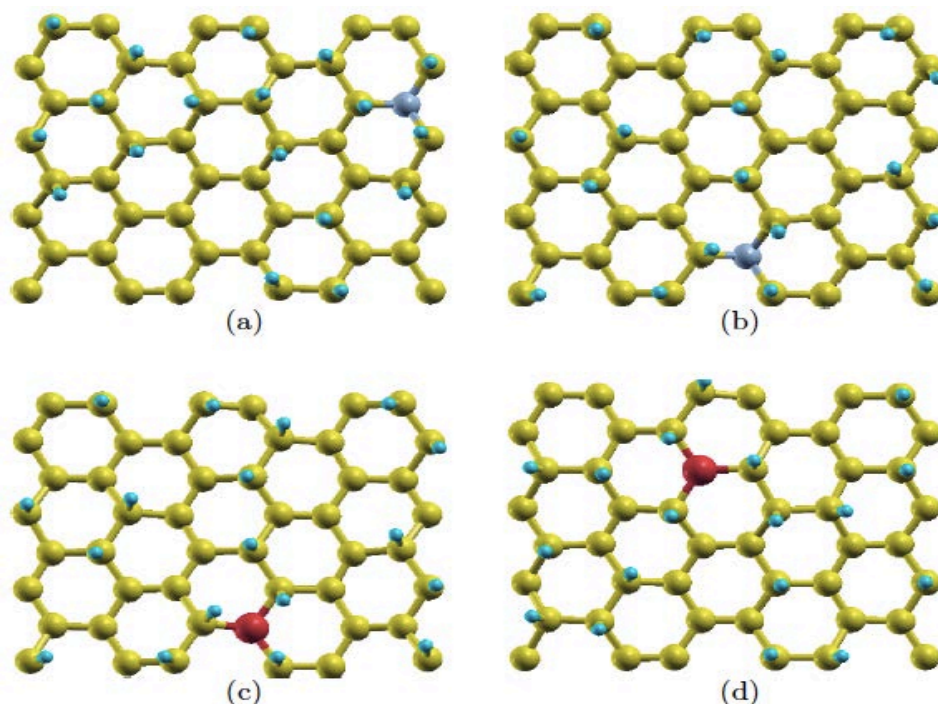


**Fig. 1.** The structures of N and B doped graphene in certain hydrogen coverage (H/C: 0.375). The upper is N doped graphene and the lower panel is B doped graphene. The yellow, blue, purple and red atoms denote carbon, hydrogen, nitrogen and boron, respectively

Calculations were done using density functional theory [25] implemented in the quantum espresso (QE) code [26, 27]. The local density approximation by the Perdew-Zunger parametrization was adopted [28]. The projector-augmented wave method and ultra-soft pseudo potential were used [29, 30]. The parameters for hydrogenated of doped graphene in a super cell were the energy cut off of 40 Ry for the plane wave expansion of the wave function and 400 Ry for the expansion of the augmented charge. The convergence criterion for the structural optimization was that the total absolute value of the inter-atomic force vector became less than  $10^{-4}$  Ry/a.u. The distance between graphene planes was separated by 10 Å in order to avoid interaction between layers. Distribution of k-points on a mesh of 12x12x1 was selected via Monkhorst Pack scheme [31]. The distribution of the transferred charge was estimated by determining charge difference from the neutral value on each atom site of graphene. The local charge assigned at each atomic site was obtained by the Löwdin charge analysis [32].

### 3. Results and discussion

**Reduction of CTR by nitrogen doping.** We found that N doped graphene is energetically favorable than B doped graphene, this is in agreement with the previously calculation [1]. In this case, the N atom form covalent bonds with the C atom with bond length of C-N of 1.41 Å. If we compare it with bond length of C-C in pristine graphene which is around 1.42 Å, we could conclude that the N doped only a little bit distort the graphene lattice and N atom a little bit moves downward but still keeping the planar graphene structure. Once hydrogenation is introduced, the nitrogen atom moves more downward of 0.13 Å and hydrogenated carbon atom move upward of 0.37 Å with C-H bond length 1.15 Å. Since the C-H bond length a bit longer/weaker, the CTR from hydrogen atom to carbon atom in graphene decrease.

As seen in Fig. 2 and Table 1, we found CTR is around 0.1852e for low H coverage (represented by H/C = 0.125), when the more hydrogen are sequentially introduced into

N-graphene up to  $H/C = 0.25$  (middle coverage), CTR decrease to be around  $0.1727e$ , after continuously H adsorbs on the N-graphene up to  $H/C = 0.375$  (high coverage), CTR decrease to be around  $0.1584e$ . There are two conclusions based on the result. Firstly, substitution of N doping modulates CTR from hydrogen to grapheme. In this case, CTR per hydrogen decrease is about by  $0.01e$  for low coverage and middle coverage and by  $0.002 e/H$  for high coverage of adsorbed H. Secondly at the whole, in accordance with hydrogenation on pristine graphene, hydrogenated on N doped graphene also show CTR from hydrogen to N doped graphene decrease linearly with respect to increasing of hydrogen coverage.

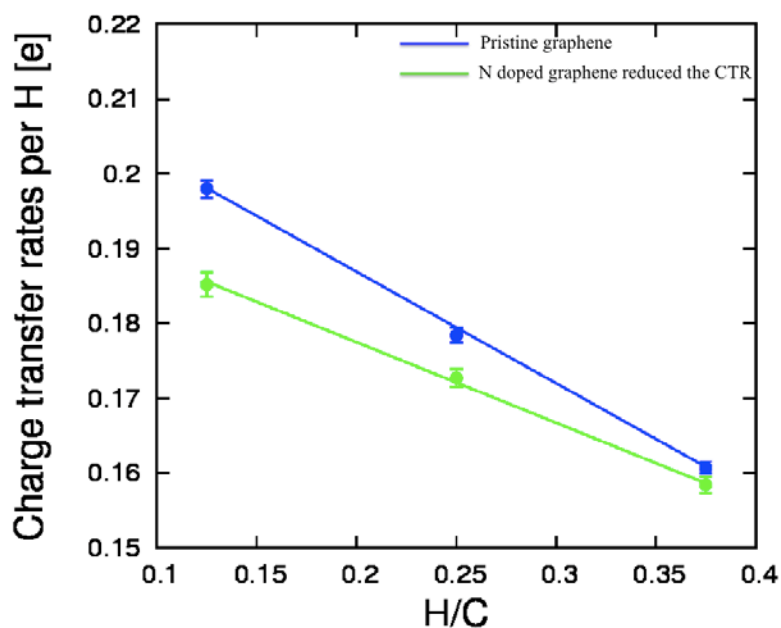


**Fig. 2.** The CTR of hydrogen on N doped graphene. For comparison, the data CTR for hydrogenation on pristine graphene is shown. A solid blue circle and solid green circle denote CTR of hydrogen on pristine graphene and N doped graphene, respectively

Table 1. The averaged CTR value (Av-CTR) of hydrogenation of N doped graphene in different coverage of H. The standard deviation of CTR (SD) coming from random arrangement is also shown

Materials	H/C	Av-CTR [e]	SD [e]
Graphene (47C+6H+N)	0.125	$0.1852 \pm 0.0016$	0.0051
Graphene+(47C+12H+N)	0.25	$0.1727 \pm 0.0012$	0.0038
Graphene+(47C+18H+N)	0.375	$0.1584 \pm 0.0011$	0.0034

**Enhancement of CTR by boron doping.** As for B doped graphene, we found a B-C bond length before hydrogenation is around  $1.49 \text{ \AA}$  in consistent with previously calculation [20], while the nearest-neighbor of C-C bond length are slightly shortened of  $1.40 \text{ \AA}$ . After hydrogenation the B-C bond length weaker to be  $1.52 \text{ \AA}$ , Boron move upward of  $0.42 \text{ \AA}$  and hydrogenated carbon atom move upward of  $0.52 \text{ \AA}$  with the nearest C-H bond length B doping is around  $1.14 \text{ \AA}$ .

If we compare the C-H bond length on N doped graphene, the C-H bond length on B doped graphene is strengthened. It is indicated that CTR increase. Also compared with N doped, B atom induces a bigger lattice distortion in graphene system because the size of boron atom is larger than carbon so the presence of boron modifies the structure of graphene, while the size of N atom is close to the carbon.

As seen in Fig. 3 and Table 2, we found CTR is around  $0.2133e$  for low H coverage

(represented by  $H/C = 0.125$ ), when the more hydrogen are sequentially introduced into B-graphene up to  $H/C = 0.25$  (middle coverage), CTR decrease to be around  $0.1870e$ , after continuously H adsorbs on the B-graphene up to  $H/C = 0.375$  (high coverage), CTR decrease to be around  $0.1703e$ . As a result, we could conclude that first, substitution of B doping modulates CTR from hydrogen to graphene, in this case, CTR per hydrogen increase is about by  $0.02e/H$  for low coverage and by  $0.01e/H$  for middle coverage and high coverage of adsorbed H. Secondly at the whole, in accordance with hydrogenation on pristine graphene, hydrogenated on B doped graphene also show CTR from hydrogen to B doped graphene decrease linearly with respect to increasing of hydrogen coverage.

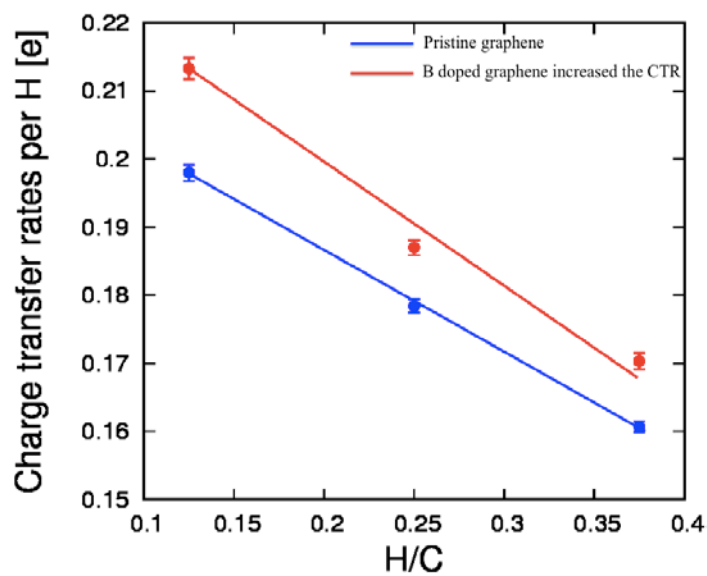


**Fig. 3.** The CTR of hydrogen on B- doped graphene. For comparison, CTR for hydrogenation on pristine graphene is shown. A solid blue circle and solid red circle denote CTR of hydrogen on pristine graphene and B- doped graphene, respectively

Table 2. The averaged CTR value (av-CTR) of hydrogenation of B doped graphene in different coverage of H. The standard deviation of CTR (SD) coming from random arrangement is also shown

Materials	H/C	Av-CTR [e]	SD [e]
Graphene (47C+6H+B)	0.125	$0.2133 \pm 0.0016$	0.0049
Graphene+(47C+12H+B)	0.25	$0.1870 \pm 0.0011$	0.0032
Graphene+(47C+18H+B)	0.375	$0.1703 \pm 0.0012$	0.0038

The reduced and increased CTR by nitrogen and boron doping, which caused the different of electronic properties, would be important to meet the requirement of diverse engineering applications, such as in hydrogen storage application [22-24,33] and hydrogen molecule conversion system to  $NH_3$ [34] effectively.

#### 4. Conclusion

The CTR of H atoms on B and N doped graphene has been investigated and discussed based on the DFT calculations. We provided a feasible way on how to increase and decrease CTR from hydrogen to doped graphene by introducing dopant such as boron and nitrogen. B doping enhances CTR, while N doping reduces CTR. The presence of a single substitution boron atom increases the CTR from hydrogen to graphene by  $0.02e/H$  for low coverage and by  $0.01e/H$  for middle coverage and high coverage of adsorbed H. While the presence of a

single substitution nitrogen atom decreases the CTR from hydrogen to graphene by 0.01e for low and middle coverage and by 0.002 e/H for high coverage of adsorbed H. Those results indicated that the increment and reduction of CTR from hydrogen to graphene could be tuned by B and N substitutional dopant and its concentrations.

**Acknowledgements.** *The calculations were done in the computer centers of Faculty of Engineering and Technology, Sampoerna University and supported by supercomputer facilities of Graduate school of Engineering Science, Osaka University. GKS gratefully acknowledges to Prof. Koichi Kusakabe at Osaka University, Japan for his continuous support.*

## References

- [1] Leenaerts O, Sahin H, Partoens B, Peeters FM. First-principles investigation of B- and N-doped fluorographene. *Phys. Rev. B*. 2013;88: 035434.
- [2] Han W, Bando Y, Kurashima K, Sato T. Boron-doped carbon nanotubes prepared through a substitution reaction. *Chemical Physics Letters*. 1999;299(5): 368-373.
- [3] Zhou YG, Zu XT, Gao F, Nie JL, Xiao HY. Adsorption of hydrogen on boron-doped graphene: A first-principles prediction. *Journal of Applied Physics*. 2009;105(1): 014309.
- [4] Kurita N. Molecular orbital calculations on lithium absorption in boron- or nitrogen-substituted disordered carbon. *Carbon*. 2000;38(1): 65-75.
- [5] Endo M, Hayashi T, Hong SH, Enoki T, Dresselhaus MS. Scanning tunneling microscope study of boron-doped highly oriented pyrolytic graphite. *Journal of Applied Physics*. 2001;90(11): 5670-5674.
- [6] Panchakarla LS, Subrahmanyam KS, Saha SK, Govindaraj A, Krishnamurthy HR, Waghmare UV, Rao CNR. Synthesis, structure, and properties of boron and nitrogen doped graphene. *Advanced Materials*. 2009;21(46): 4726-4730.
- [7] Liu H, Liu Y, Zhu D. Chemical doping of graphene. *J. Mater. Chem*. 2011;21: 3335-3345.
- [8] Wu ZS, Ren W, Xu L, Li F, Cheng HM. Doped graphene sheets as anode materials with superhigh rate and large capacity for lithium ion batteries, *ACS Nano*. 2011;5(7): 5463-5471.
- [9] Panchakarla LS, Subrahmanyam KS, Saha SK, Govindaraj A, Krishnamurthy HR, Waghmare UV, Rao CNR. Synthesis, structure, and properties of boron- and nitrogen-doped graphene. *Advanced Materials* 2009;21(46): 4726-4730.
- [10] Carroll DL, Redlich P, Blase X, Charlier JC, Curran S, Ajayan PM, Roth S, Rühle M. Effects of nanodomain formation on the electronic structure of doped carbon nanotubes. *Phys. Rev. Lett*. 1998;81: 2332-2335.
- [11] Endo M, Hayashi T, Hong SH, Enoki T, Dresselhaus MS. Scanning tunneling microscope study of boron-doped highly oriented pyrolytic graphite. *Journal of Applied Physics*. 2001;90(11): 5670-5674.
- [12] Firlej L, Roszak S, Kuchta B, Pfeifer P, Wexler C. Enhanced hydrogen adsorption in boron substituted carbon nanopores. *The Journal of Chemical Physics*. 2009;131(16): 164702.
- [13] Lazar P, Zboril R, Pumera M, Otyepka M. Chemical nature of boron and nitrogen dopant atoms in graphene strongly influences its electronic properties. *Phys. Chem. Chem. Phys*. 2014;16: 14231-14235.
- [14] Endo M, Kim C, Karaki T, Tamaki T, Nishimura Y, Matthews M, Brown SDM, Dresselhaus MS. Structural analysis of the b-doped mesophase pitch-based graphite fibers by raman spectroscopy. *Phys. Rev. B*. 1998;58: 8991-8996.
- [15] Wang X, Li X, Zhang L, Yoon Y, Weber PK, Wang H, Guo J, Dai H. N-doping of graphene through electrothermal reactions with ammonia. *Science*. 2009;324(5928): 768-771.

- [16] Zhao L, He R, Rim KT, Schiros T, Kim KS, Zhou H, Gutiérrez C, Chockalingam SP, Arguello CJ, Pálová L, Nordlund D, Hybertsen MS, Reichman DR, Heinz TF, Kim P, Pinczuk A, Flynn GW, Pasupathy AN. Visualizing individual nitrogen dopants in monolayer graphene. *Science*. 2011;333(6045): 999-1003.
- [17] Reddy ALM, Srivastava A, Gowda SR, Gullapalli H, Dubey M, Ajayan PM. Synthesis of nitrogen-doped graphene films for lithium battery application. *ACS Nano*. 2010;4(11): 6337-6342.
- [18] Cheianov VV, Fal'ko V, Altshuler BL. The focusing of electron flow and a veselago lens in graphene p-n junctions. *Science*. 2007;315(5816): 1252-1255.
- [19] Qu L, Liu Y, Baek JB, Dai L. Nitrogen-doped graphene as efficient metal-free electrocatalyst for oxygen reduction in fuel cells. *ACS Nano*. 2010;4(3): 1321-1326.
- [20] Pizzochero M, Leenaerts O, Partoens B, Martinazzo R, Peeters FM. Hydrogen adsorption on nitrogen and boron doped graphene. *Journal of Physics: Condensed Matter*. 2015;27(42): 425502.
- [21] Elias C, Nair RR, Mohiuddin TMG, Morozov SV, Blake P, Halsall MP, Ferrari AC, Boukhvalov DW, Katsnelson MI, Geim AK, Novoselov KS. Control of graphene's properties by reversible hydrogenation: Evidence for graphene. *Science*. 2009;323(5914): 610-613.
- [22] Sunnardianto GK, Maruyama I, Kusakabe K. Storing-hydrogen processes on graphene activated by atomic-vacancies. *Int. J. Hydrogen Energy* 2017;42(37): 23691-23697
- [23] Sunnardianto GK, Maruyama I, Kusakabe K. Dissociation chemisorption pathways of H<sub>2</sub> molecule on graphene activated by a hydrogenated mono-vacancy V<sub>11</sub>. *Adv. Sci. Eng. Med*. 2016;8(6): 421-426.
- [24] Sunnardianto GK, Maruyama I, Kusakabe K. Systematic study of the effect of H adsorption on the electron transfer rate in graphene. *J. Comput. Theor. Nanosci*. 2016;13(8): 4883-4887
- [25] Martin RM. *Electronic Structure, Basic Theory, and Practical Methods*. Cambridge; 2004.
- [26] Kresse G, Hafner J. Ab initio molecular dynamics for liquid metals. *Phys. Rev. B*. 1993;47: 558-561.
- [27] Giannozzi P, Baroni S, Bonini N, Calandra M, Car R, Cavazzoni C, Ceresoli D, Chiarotti GL, Cococcioni M, Dabo I, Corso AD, de Gironcoli S, Fabris S, Fratesi G, Gebauer R, Gerstmann U, Gougoussis C, Kokalj A, Lazzeri M, Martin-Samos L, Marzari N, Mauri F, Mazzarello R, Paolini S, Pasquarello A, Paulatto L, Sbraccia C, Scandolo S, Sclauzero G, Seitsonen AP, Smogunov A, Umari P, Wentzcovitch RM. Quantum espresso: a modular and open-source software project for quantum simulations of materials. *Journal of Physics: Condensed Matter*. 2009;21(39): 395502.
- [28] Perdew JP, Zunger A. Self-interaction correction to density-functional approximations for many-electron systems. *Phys. Rev. B*. 1981;23: 5048-5079.
- [29] Blöchl PE. Projector augmented-wave method. *Phys. Rev. B*. 1994;50: 17953-17979.
- [30] Vanderbilt D. Soft self-consistent pseudopotentials in a generalized eigenvalue formalism. *Phys. Rev. B*. 1990;41: 7892-7895.
- [31] Monkhorst HJ, Pack JD. Special points for brillouin-zone integrations. *Phys. Rev. B*. 1977;16: 1748.
- [32] Sanchez-Portal D, Artacho E, Soler JM. Projection of plane-wave calculations into atomic orbitals. *Solid State Communications*. 1995;95(10): 685-690.
- [33] Sunnardianto GK, Larasati IA, Triawan F, Aamer MA. Effect of charge on graphene vacancy for hydrogen storage application. *MATEC Web Conf*. 2018;197: 04001.
- [34] Aziz M, Juangsa FB, Triawan F, Nandiyanto ABD, Abdullah AG. Integrated Nitrogen Production and Conversion of Hydrogen to Ammonia. *Chemical Engineering Transactions* 2018;70: 571-576.

# THE STRUCTURAL TRANSFORMATION AND MECHANICAL STRENGTH OF Ni, Ti NANOWIRES AND NITINOL ALLOYS AT VARIOUS VACANCY RATES: MOLECULAR DYNAMIC STUDY USING CLERI-ROSATO POTENTIAL

M.M. Aish\*

Physics department, Faculty of science, Menoufia university, Egypt

\*e-mail: mohamedeash2@yahoo.com

**Abstract.** A many-body interatomic potential was used for Nickel (Ni) crystal with face-centered cubic (FCC) lattice and Titanium (Ti) with hexagonal close-packed (HCP) lattice and Nitinol alloys within the second-moment approximation. The tight-binding model (the Cleri and Rosato potentials) was employed to carry out three dimensional molecular dynamics simulations upon application of uniaxial tension at nanoscale of studied materials, which contained various vacancy rates. We performed molecular dynamics (MD) simulations to study the yield mechanisms in Ni and Ti nanowires and Nitinol alloys. The coupled effects of various shapes, sizes, and locations of vacancy defects on the mechanical strength and structural deformation of nanowires are presented. The formation energies of vacancy defects are also evaluated. It was found that as the number of vacancies increases, the yield stress decreases. The results showed that breaking time changes with the increase in number of vacancy. To understand the effects of the vacancies on the mechanical properties of Ni and Ti nanowires and Nitinol alloys, tensile and fatigue tests are simulated.

**Keywords:** many-body, Nitinol, alloys, vacancy, defects

## 1. Introduction

MD simulations are used to simulate the movement of interacting atoms under the Newtonian mechanics. Given the instantaneous position and velocity vectors of the atoms, the dynamical history of the composition is generated by integrating the equations of motion numerically. The energy and force of the system are calculated. Computer simulation process was produced for systems under equilibrium, minimal interatomic energy and force through development of suitable interatomic potentials.

Vacancies which had little effect on the mechanical properties while seriously affecting the electrical properties. Vacancies Would be very effective in increasing the electrical resistance. Perhaps the clearest example of a phenomenon in which vacancies are created and absorbed by stationary edge dislocations is the Kirkendall effect. This explanation, however, requires that sources of vacancies should be presented within the grains of the alloy. The sources can only be dislocations (or grain boundaries), unless the vacancies condense in the form of macroscopic holes. The presence of such holes has in fact been reported in certain cases. The vacancies formed when dislocations move will bring slipping in the plane of a given Frank-Read source, even if no deformation bands are formed. It is shown that one has to expect cross-slip and formation of deformation bands.

It is shown moreover that the formation of vacancies by moving dislocations plays an essential role in these processes. It is suggested that the movement of vacancies (self-diffusion) plays an essential role in polygonization, recovery and steady-state creep, enabling dislocations in deformation bands to move out of their slip planes and so relieve stress. Except by slipping right out of the crystal, it can disappear only by vacancy diffusion, which can remove the extra layer of atoms.

The mechanical properties of nanowires have been studied by use of nano indentation [1]. On the other hand, the mechanical properties of silicon carbide-silica biaxial nanowires and their structural transformation between a biaxial and coaxial configuration have been studied by use of transmission electron microscopy [2]. The mechanical properties of Ni nanowires dependence on size, shape, as well as the temperature have been studied [3-9]. Characterization of strain-induced structural transformations in CdSe nanowires using molecular dynamics simulation were also studied in [10].

This work was performed using our new MD program "Structural Transformation of Metallic FCC, BCC and HCP Nanowires and Their Alloys Using Cleri- Rosato potential". Ni and Ti nanowires and Nitinol alloys were taken as an object of investigation. The structures were presented in the form of a FCC for Ni, HCP for Ti and austenite for Nitinol alloys. The molecular dynamics method based on Cleri Rosato potential function [11,12] was used for calculation of the dynamics of the atomic structure in this paper.

## 2. Molecular dynamic potential: Cleri and Rosato

The interatomic interactions were calculated using the tight-binding potentials [11], we used a computer program for simulating a system involving several thousands of atoms in the time interval up to several nanoseconds. It should be noted that, even in the current state in the development of high-performance computers, an ab initio simulation of this system remains impossible. On the other hand, the potentials proposed by Cleri and Rosato [11] have already worked well in cluster studies [13–15]. In the EAM formalism, the binding energy of an  $i^{\text{th}}$  atom in a crystal with  $N$  atoms is a sum of contributions from the pair potential and embedding potential functions.

In our model, the potential energy of the system was calculated according to the relation:

$$U = \sum_i (E_b^i + E_r^i), \quad (1)$$

where

$$E_r^i = \sum_{j \neq i} U_{ij}(r_{ij}) = \sum_j A \cdot \exp[-p(\frac{r_{ij}}{r_0} - 1)] \quad (2)$$

is the two-body term, and

$$E_b^i = - \sqrt{\sum_{j \neq i} \phi(r_{ij})}, \quad (3)$$

$$\phi(r_{ij}) = \xi^2 \cdot \exp[2q(\frac{r_{ij}}{r_0} - 1)] \quad (4)$$

is the many-body term. In Eqs. (2)-(4),  $r_0$  is the equilibrium distance between atoms,  $r_{ij}$  is the separation between the  $i^{\text{th}}$  and  $j^{\text{th}}$  atoms, and  $A$ ,  $\xi$ ,  $p$ ,  $q$  are adjustable parameters governing the interaction between those atoms. These parameters (table 1 and 2) were taken directly from [11]. Eqs. (1) and (2) are similar to the Finnis-Sinclair (FS) scheme [13], but Eq. (1) uses a double summation convention for the repulsive functions, whereas the convention in the FS scheme is to sum this term for  $j > i$  rather than  $j \leq i$ . For s, p-bonded metals there are no strong

theoretical motivation for representing the band energy part of the potential by a square-root term. However, this functional form can be rationalized as an empirical representation of the volume-dependent term required by the electron gas model of simple metals [11]. The length scale parameter  $r_0$  in Eq. (1) is set to the lattice nearest neighbor distance. The remaining parameters ( $A$ ,  $\xi$ ,  $p$ ,  $q$ ) of the TB potentials were fitted for each element using the lattice constant, cohesive energy ( $E_J$ , elastic constants ( $C_{11}$ ,  $C_{12}$ ,  $C_{44}$ ) and vacancy formation energy ( $E''$ ).

Table 1. Parameters of tight-binding potentials for FCC metals. The potentials are cut off beyond the second neighbor distance ( $r > \sqrt{2}r_0$ )

	A (eV)	$\xi$ (eV)	P	q	$r_0$	G/ $\xi$
Ni	0.0565	1.4005	14.0867	1.7937	2.4918	3.655

Table 2. Parameters of TB potentials for HCP Ti metals, parameters obtained with the experimental value, and theoretical fitting [12]

	A (eV)	$\xi$ (eV)	P	q	$r_0$	G/ $\xi$
Ti (Ex)	0.1519	1.8112	8.620	2.390	2.896	3.936
Ti (Th)	0.0741	1.4163	11.418	1.643	2.896	3.936

The model can be used to describe quite well elastic, plastic, fracture and mechanical properties of a wide range of FCC, BCC and HCP-metals. The velocities of atomic motion in the simulation were determined using the Verlet algorithm. The potentials proposed by Cleri and Rosato [11] have already worked well in nanowires studies.

For a many-body attractive potential of the pair functional type (TB, EAM etc.), this normally entails joining one of the nodes of the function to an effective pair potential,  $V_{ij}$ , which was derived from a series expansion of the many-body potential in the bulk environment [16,22]. For TB potentials of the form of Eqs. (1)-(4), the effective pair potential acting between atoms  $i$  and  $j$  is given by:

$$V_{ij}(r_{ij}) = 2U_{ij}(r_{ij}) - \frac{\varphi(r_{ij})}{G} + \frac{[\varphi(r_{ij})]^2}{4G^3}. \quad (5)$$

Equation (5) assumes the usual pair potential evaluation convention. That interaction terms are only counted once for each distinct pair of atoms (in contrast to Eq. (1)). The functions  $U_{ij}(r_{ij})$  and  $\varphi(r_{ij})$  are defined in Eqs. (2) and (4) respectively.  $G$  is a lattice sum which represents the value of the total band energy associated with any atom  $k$  in the reference environment (normally a site in the bulk of the ideal lattice):

$$G = \sqrt{\sum_{k \neq l} \varphi(r_{kl})}. \quad (6)$$

The ratio  $G/\xi$  is dimensionless, for a lattice sum (Eq. (6)) corresponding to a bulk metallic environment. In all cases, this ratio takes values between 3.4 and 4.0. The larger values imply relatively greater long-range contributions to the potential. The attractive part of an effective pair potential derived for a surface environment may differ somewhat from that of a bulk environment, because of fewer contributions to the lattice sum in Eq. (6) [22]. However, this should have minimal impact on a composite potential designed for these

simulations, since the simulation was carried out at a separation where the repulsive part of the potential dominates.

In practical applications of TB potentials, it is also desirable to employ a switching function in order to terminate the potential and forces smoothly at the cut off distance, thereby preventing energy book-keeping errors due to the non-conservative nature of the many-body potential at the cut off distance. For this purpose, a simple polynomial switching function,  $S(x)$ , can be applied to the potential in a region just below the cut off distance ( $r_{cut}$ ) [16]:

$$s(x) = 1 - 6x^5 + 15x^4 - 10x^3, \rightarrow r_{sw} \leq r \leq r_{cut}, \quad (7)$$

where  $x = (r - r_{sw}) / (r_{cut} - r_{sw})$ , and  $r_{sw}$  is the distance at which the switching function was applied.

Finally, the TB potential formalism can be extended to describe bimetallic systems, using the fitting methods described in Refs. [12,16-19].

In general, the fitting parameters for a bimetallic system cannot be deduced from those of the pure elements alone. However, an approximate combination rule which has been used for TB and Finnis-Sinclair potentials may be useful in the absence of specific parameterizations [16,21]. This help for choosing the potential parameters in such way that the hetero-nuclear interaction terms ( $\alpha$ - $\beta$ , for elements  $\alpha$  and  $\beta$ ) correspond to the geometric means of the respective elemental terms ( $\alpha$ - $\alpha$ ,  $\beta$ - $\beta$ ):

$$\varphi^{\alpha\beta}(r_{ij}) = [\varphi^{\alpha\alpha}(r_{ij})\varphi^{\beta\beta}(r_{ij})]^{1/2}, \dots U^{\alpha\beta} = [U^{\alpha\alpha}(r_{ij})U^{\beta\beta}(r_{ij})]^{1/2}. \quad (8)$$

The accuracy of this approximation needs to be evaluated on a case- by-case basis using suitable thermodynamic measures, and corrections may be required. This is an environment in which many-body potentials, despite their defect, are known to perform better than pair potentials [20]. When considering a closed system, the force acting on the  $i^{\text{th}}$  atom, will be:

$$F_i = - \sum_{i=1, i \neq j}^N \sum_{j=1}^N \frac{d\phi_{KL}(|r_i - r_j|)}{d(r_i - r_j)}. \quad (9)$$

Temperature of the atoms in a perfect crystal was calculated according to the relation:

$$T = \frac{2k}{3Nk_b} = \frac{1}{3Nk_b} \sum_I^N m_i v_i^2, \quad (10)$$

where  $k_b$  is the Boltzmann constant and  $k$  is the total Kinetic energy.

Computer simulation using a many-body interatomic potential for Ni and Ti nanowires and Nitinol alloys within the second-moment approximation of the tight-binding model (the Cleri and Rosato potentials) was employed to carry out three dimensional molecular dynamics simulations of the mechanical properties of Ni and Ti nanowires and Nitinol alloys. We studied the extension properties of investigated nanowires for different number of vacancies at 300K and 1000K, which was adjusted every  $10^{-13}$  seconds. The estimated size of the crystal unit was for various experiments of  $10 \times 10 \times 10$ ,  $12 \times 12 \times 12$  and  $18 \times 18 \times 18$  atomic plane (AP). The average result is from 300 samples at 300 K and 1000 K.

It was assumed that the specimens have some random vacancies within materials in the simulation. The random distribution of vacancies were modeled by: (i) first calculating the number of vacancies according to the given vacancy fraction and the total atomic numbers; (ii) numbering the random vacancies in order; (iii) obtaining the occupation positions of the vacancies; (iv) converting the atoms and the vacancies to their actual positions in simulation. To understand the effects of the vacancies on the mechanical properties of Ni, Ti nanowires and Nitinol alloys, the tensile tests are simulated.

### 3. Results and discussion:

In this paper, the mechanical properties of nanoscale wires and their alloys were studied. Since the breaking and the yielding of Ni and Ti nanowires and Nitinol are of main interest in this work (Table 3), it seems to be reasonable to adopt small  $L_x$ ,  $L_y$  and  $L_z$  for the simulations. To save the computing time, the dimensions of the MD models used in the following simulations are set to be  $L_x=L_y=L_z$ . The nature of deformation, slipping, twinning and necking were studied.

**Three stages deformation.** The experiments were obtained plots of the stored energy of deformation with the time, reflecting the processes in the nanowires during deformation. There are three stages of deformation: the quasi-elastic deformation (I), plastic deformation (II) until breaking, and failure (III). At all computer experiments, in the first stage there was almost linear increase in stress. The initial stage quasi-elastic area there is only relative displacement of atoms and there are no defects. Therefore, in this region the energy stored varies periodically.

**FCC Ni nanowires at 300 K.** First stage was completed at 16 ps for 10 x 10 x 10 Ni nanowires without vacancies, 11 ps, 10 Ps and 8 Ps, for vacancy rates equal 1%, 2% and 5%, respectively. The sharp fall takes place only at the point of transition from the first to second stages of deformation (Fig. 1 to 4). Experiments have shown that when the vacancy number increases the first stage of deformation was narrowed, and the second stage was also narrowed (Fig.1 to 4).

Table 3. The typical MD results of uniaxial tensile loading using Cleri-Rosato to 10 x 10 x 10 AP of Ni, Ti nanowires and Nitinol alloys at various vacancies at 300K, including the Yielding stress and breaking time

	vacancies V (%)	Yielding Stress				Breaking time ( $t_b$ , Ps)			
		$\sigma$ (GPa)				Ni	Ti		Nitinol
		Ni	Ti		Ni		Th	Ex	
			Th	Ex					
1	0.0	24	25	18	21	120	110	140	220
2	0.55	23	24.3	16.8	19	95	90	130	210
3	1	20	22	15	17	93	85	126	199
4	1.66	17	19.1	13.6	15	75	71	120	180
5	2	14	16	12	13	72	69	110	150
6	4	9	13	9	8	40	41	70	120
7	5	8	12	7	7	30	30	60	110
8	10	6	7	3	4	28	25	55	90

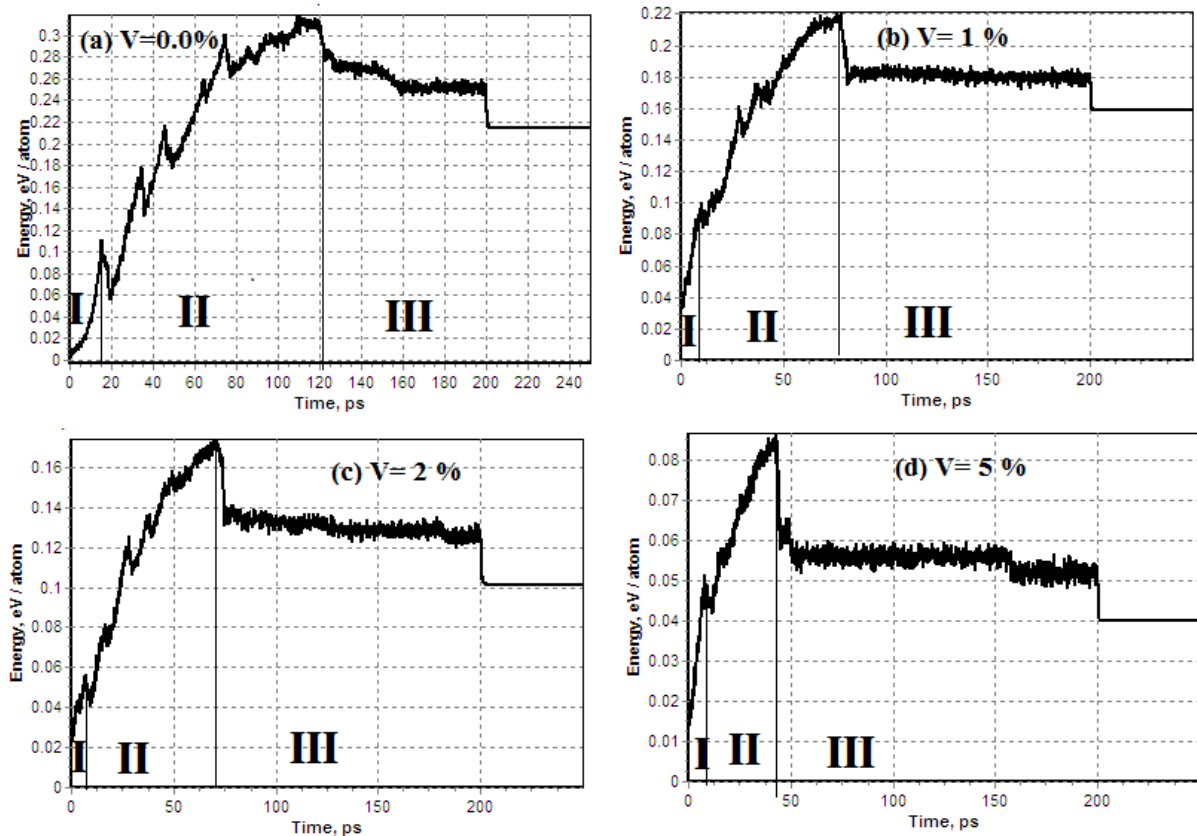
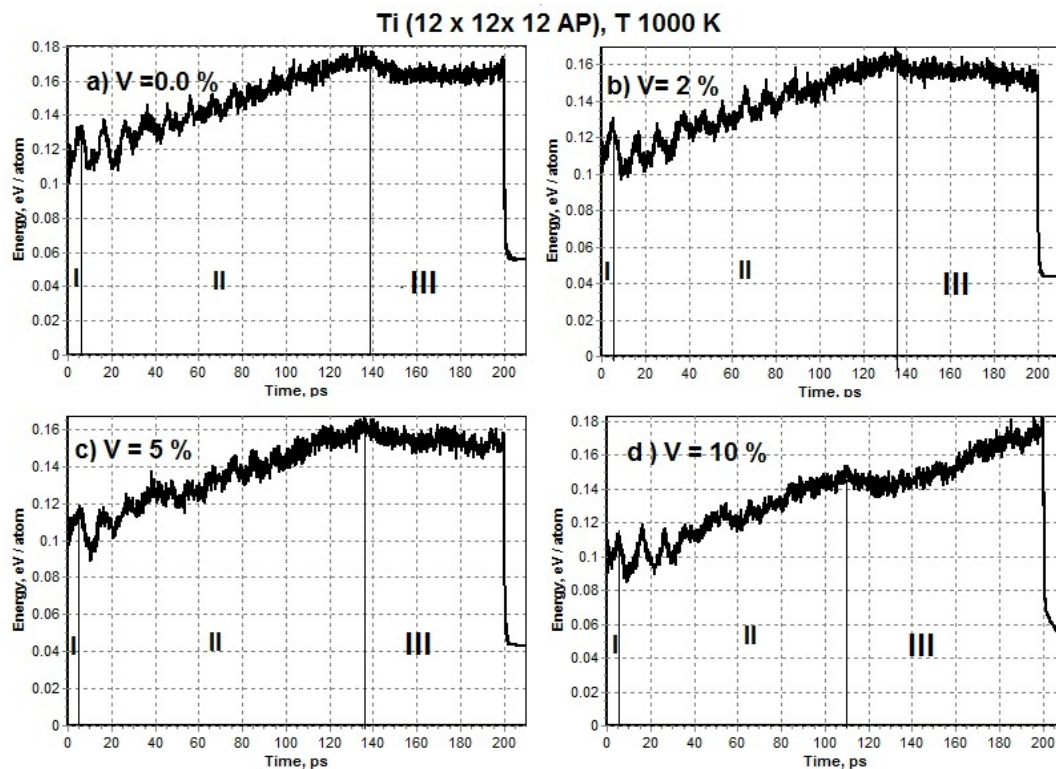
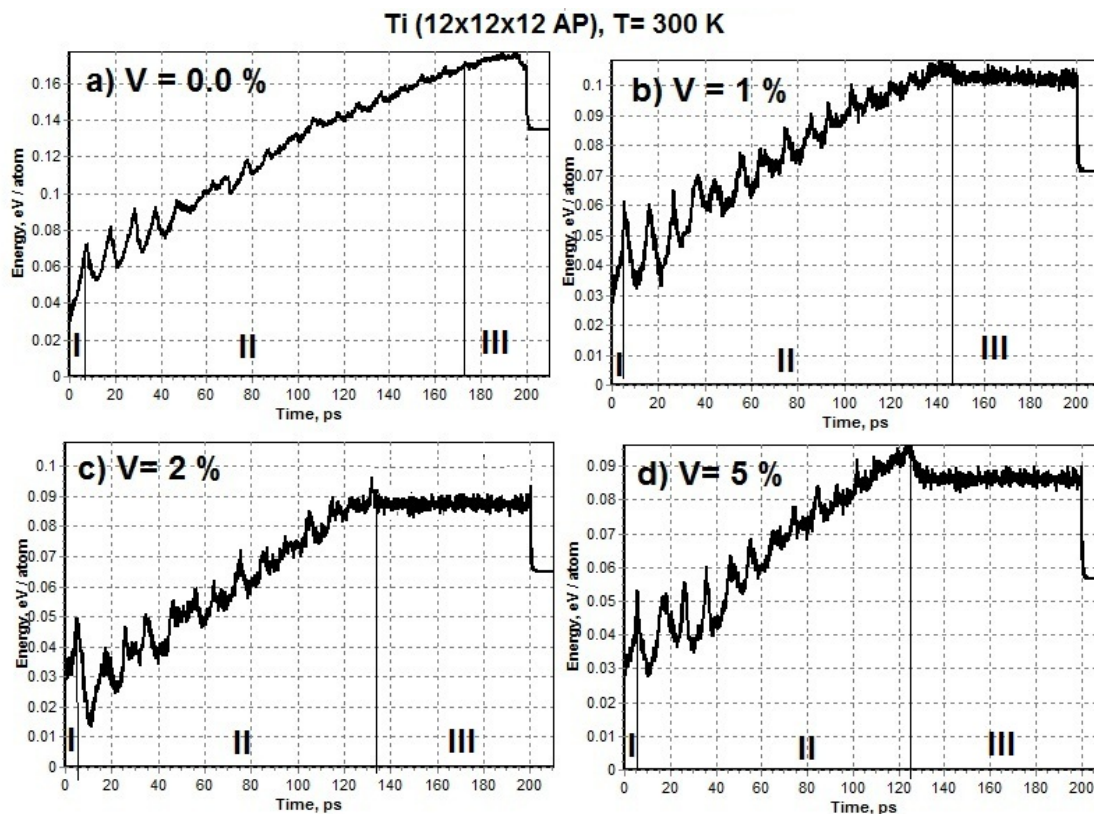


**Fig. 1.** The dependence of the stored energy of deformation at 300 K for FCC Ni 10 x 10 x 10 AP using Cleri-Rosato potential, a) without vacancies, b)  $V = 1\%$ , c)  $V = 2\%$  and d)  $V = 5\%$

**Feature 12 x 12 x 12 AP of HCP Ti nanowires at 300K and 1000K.** Figures 2, 3 indicates the change in the stored energy of the deformed crystal as a function of time at 300 K and 1000 K for 12 x 12 x 12 AP of HCP Ti nanowires at different vacancy concentrations. Experiments have shown that when the number of vacancies increases, the first stage of deformation narrowed, and the second stage also narrowed (Figs. 2 and 3).

Analysis of the graphs in Fig. 2 showed that the stored energy values at the peak of the strain curve at the end of the first stage for 0.0%, 1%, 2% and 5% vacancies rate of Ti nanowires are 0.09, 0.061, 0.05 and 0.046 eV / atom at 300 K, respectively. The level of stored energy at the end of the second stage (plastic deformation) for the investigated nanowire are 0.18, 0.109, 0.095 and 0.094 eV / atom at 300 K, respectively.

Analysis of the graphs in Fig. 3 showed that the stored energy values at the peak of the strain curve at the end of the first stage for 0.0%, 2%, 5% and 10% vacancies rate of HCP Ti 12 x 12 x 12 AP using theoretical value of Cleri-Rosato potential are 0.135, 0.132, 0.12 and 0.115 eV / atom at 1000 K, respectively. The level of stored energy at the end of the second stage (plastic deformation) for the investigated nanowire are 0.177, 0.164, 0.162 and 0.148 eV / atom at 1000 K, respectively.



**Feature of 18 x 18 x 18 AP of Nitinol alloys.** Analysis of the graphs in Fig. 4 showed that the stored energy values at the peak of the strain curve at the end of the first stage at 0.0%, 1%, 5% and 10% vacancies rate of Nitinol alloy with size 18 x 18 x 18 AP are 0.06, 0.055, 0.043 and 0.04 eV / atom at 1000 K, respectively. The level of stored energy at the end of the second stage (plastic deformation) for the investigated nanowire are 0.12, 0.116, 0.11 and 0.111 eV / atom at 1000 K, respectively.

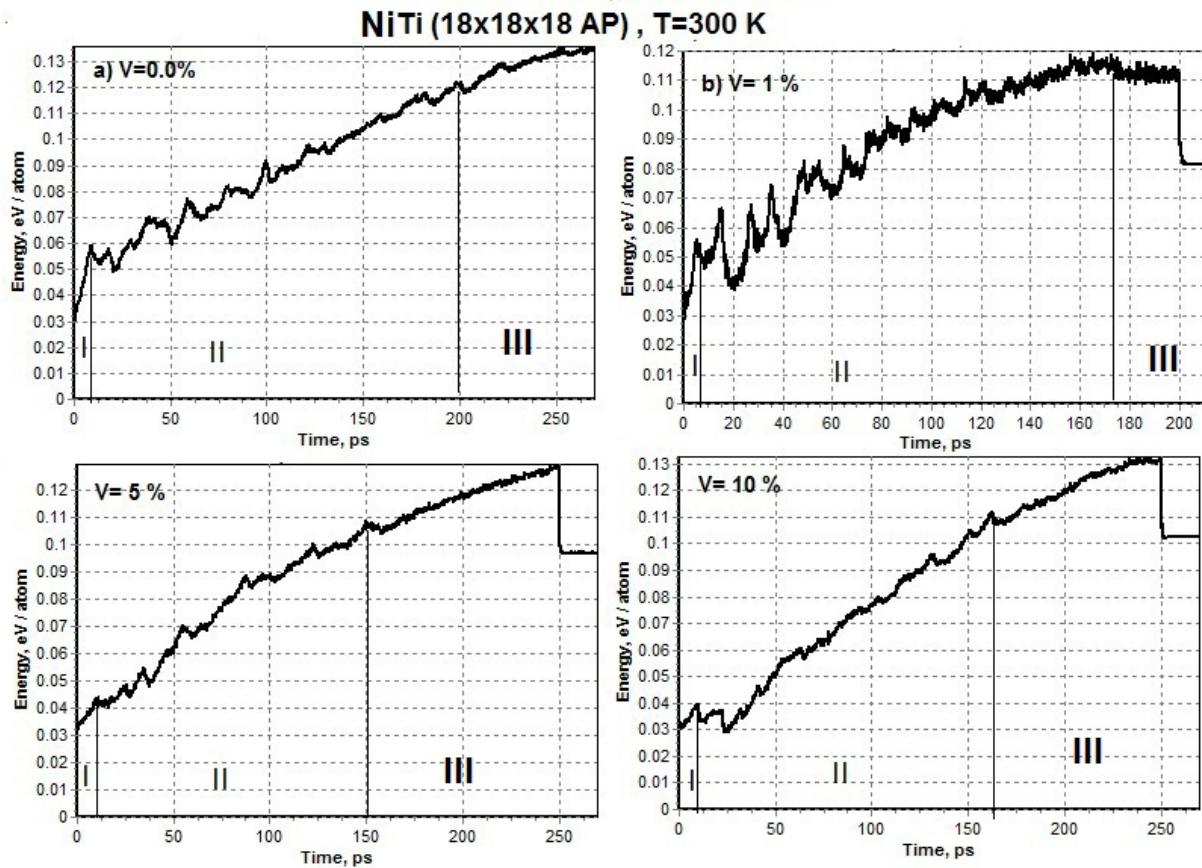


**Fig. 4.** The dependence of the stored energy of deformation at 300 K for NiTi 18 x 18 x 18 AP using Cleri-Rosato potential [11], a) without vacancies, b) V = 1%, c) V = 5% and d) V = 10%

**Tensile deformation.** The mechanical properties at different vacancy rates with MD simulations are studied (Table 3), the uniaxial tension of the Ni and Ti nanowires and Nitinol alloys are studied with different vacancy rates at 300 K and 1000K. Figure 5 gives the stress-strain relationships of the (12 x 12 x 12 AP FCC) Ni nanowires subjected to uniaxial tension at different vacancies rate at temperatures 300 K and 1000K. The effect of vacancy rates on the stress strain curve of the (12 x 12 x 12 AP) HCP Ti nanowires was shown in Fig. 6 at temperatures 300 K and 1000K. Figure 7 gives the stress-strain relation of the (18 x 18 x 18 AP) Nitinol alloys at various vacancy rates at 300 K and 1000K.

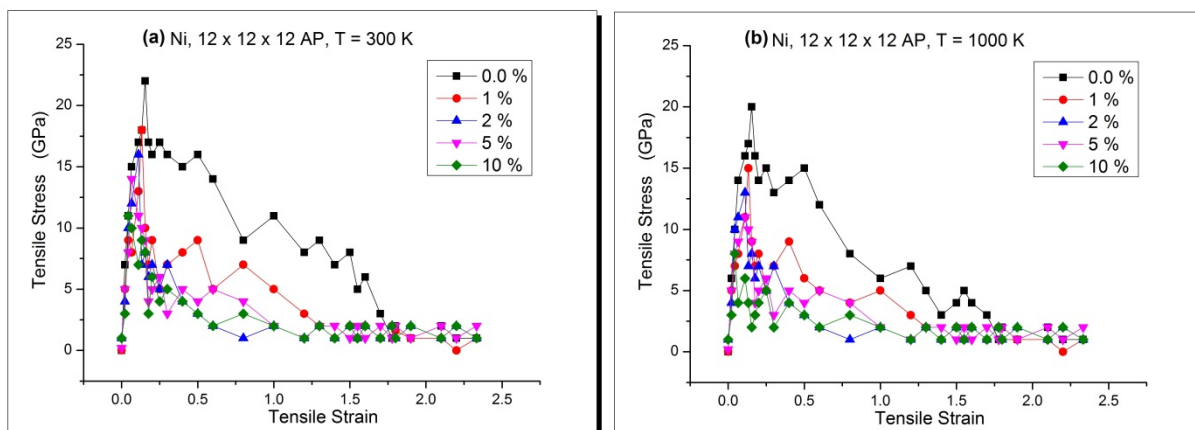


**Fig. 5.** Tensile stress vs. tensile strain for FCC Ni 12 x 12 x 12 AP nanowires at various vacancy rates at (a) 300 K, (b) 1000 K

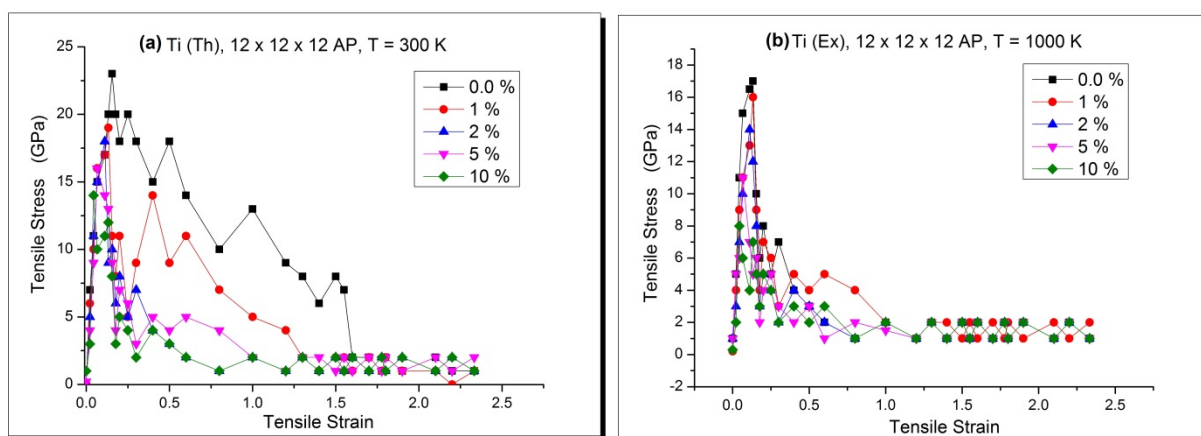


**Fig. 6.** Tensile stress vs. tensile strain for HCP Ti nanowires at various vacancy rates at (a) 300 K, (b) 1000 K

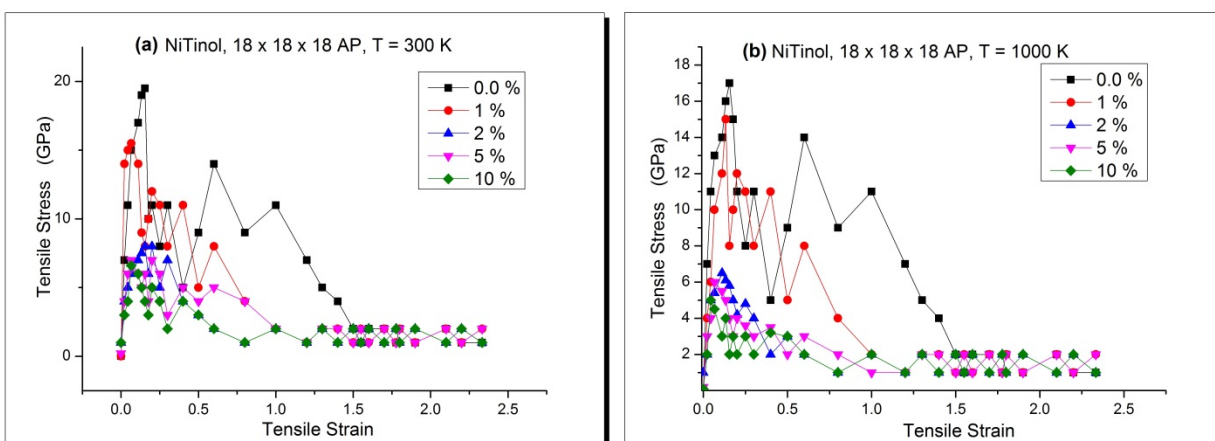


**Fig. 7.** Tensile stress vs. tensile strain for NiTi alloys at various vacancy rates at (a) 300 K, (b) 1000 K

With the increasing initial strain, stress increases linearly at various vacancies. This process corresponds to the elastic deformation of the nanowires. With the increasing strain, stress decrease as shown in the stress–strain response of the nanowires, indicating the beginning of the plastic deformation of the nanowire. The stress–strain curves are smooth at

no vacancies, some "minipeaks" exhibit with increasing vacancy rates. The results demonstrate that the tensile strength decreases with increasing vacancy rates.

Deformation of the nanowires is in a fast stage of the atomic damage process. It was observed that the yield stress decreases as the vacancy number increases (Fig. 8). When the plastic deformation of the nanowire begins, the drop of the first yield stress also decreases. Figure 8 shows the simulated ultimate strength of Ni and Ti (for both experimental and theoretical parameters) nanowire and Nitinol alloy as a function of vacancy rates. As expected, the nanowire strength decreases with increase the vacancy number.

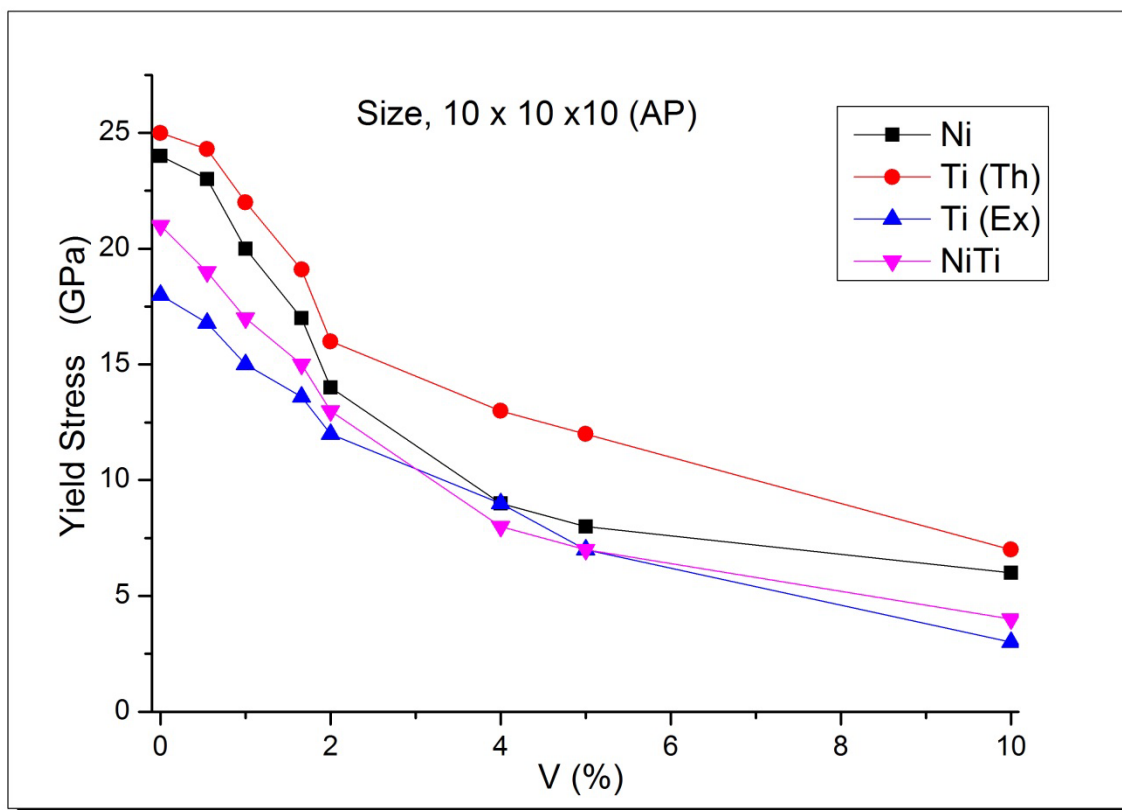


**Fig. 8.** Relationship between yield strength for 10 x 10 x 10 AP Ni and Ti (theoretical and experimental values) nanowires and Nitinol alloys with various vacancy rates at T=300 K

**Breaking time and position.** The results showed that the breaking time depended on the vacancy rates as in Fig. 9. The most probable breaking position was located at the center of the nanowires. Figure 9 presents the calculated breaking time for 10 x 10 x 10 AP Ni and Ti (theoretical and experimental values) nanowire and Nitinol alloys as a function of vacancy rates.

If the breaking position and breaking time are predictable, the nanowire can be strengthened near the breaking position and time to avoid failure. Although the single breaking case is not predictable, many breaking cases show a statistic feature. Figures 10 and 11 presents the representative snapshots of 12 x 12 x 12 AP Ti nanowire and for 18 x 18 x 18 Ap Nitinol alloys with different vacancies at the breaking moment at 300 K, respectively. In most cases, the final breaking position occurs at the central part of this Ti nanowire but for NiTinol the position gradually shifts to the ends.

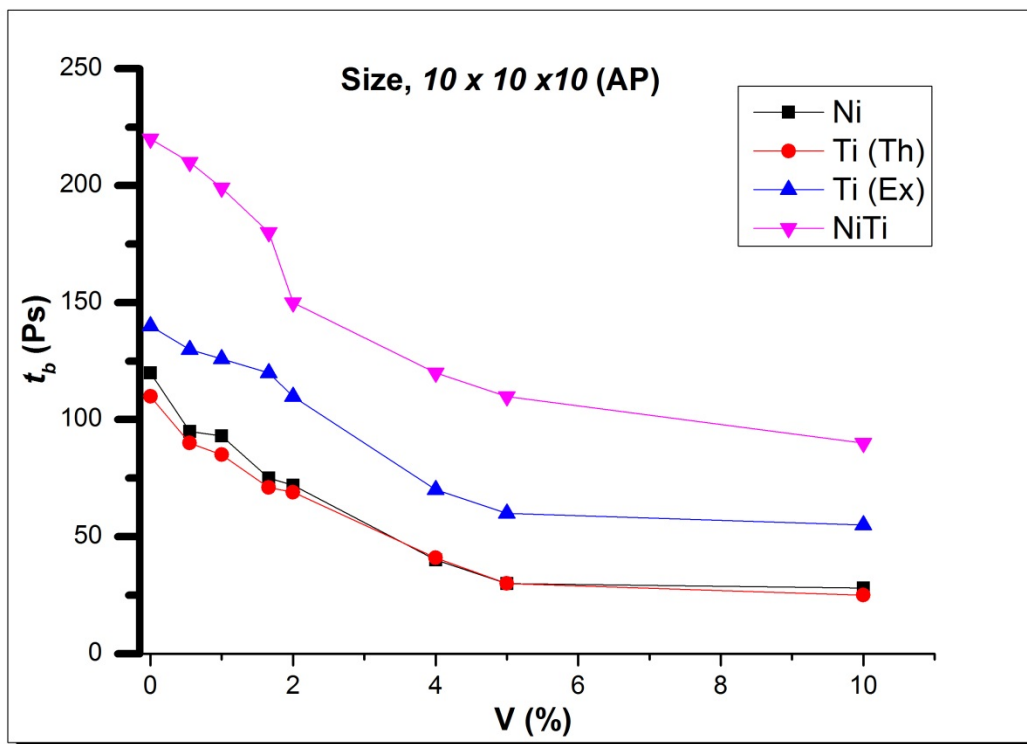


**Fig. 9.** Relationship between breaking time for 10 x 10 x 10 AP Ni and Ti (theoretical and experimental values) nanowire and Nitinol alloys with various vacancies at T=300 K

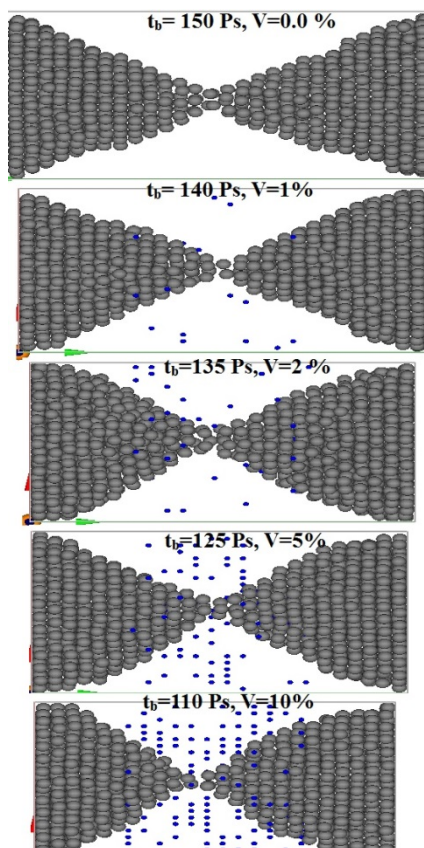


**Fig. 10.** Snapshots of 12 x 12 x 12 (AP) Ti alloy with different vacancies and the breaking moment at 300K

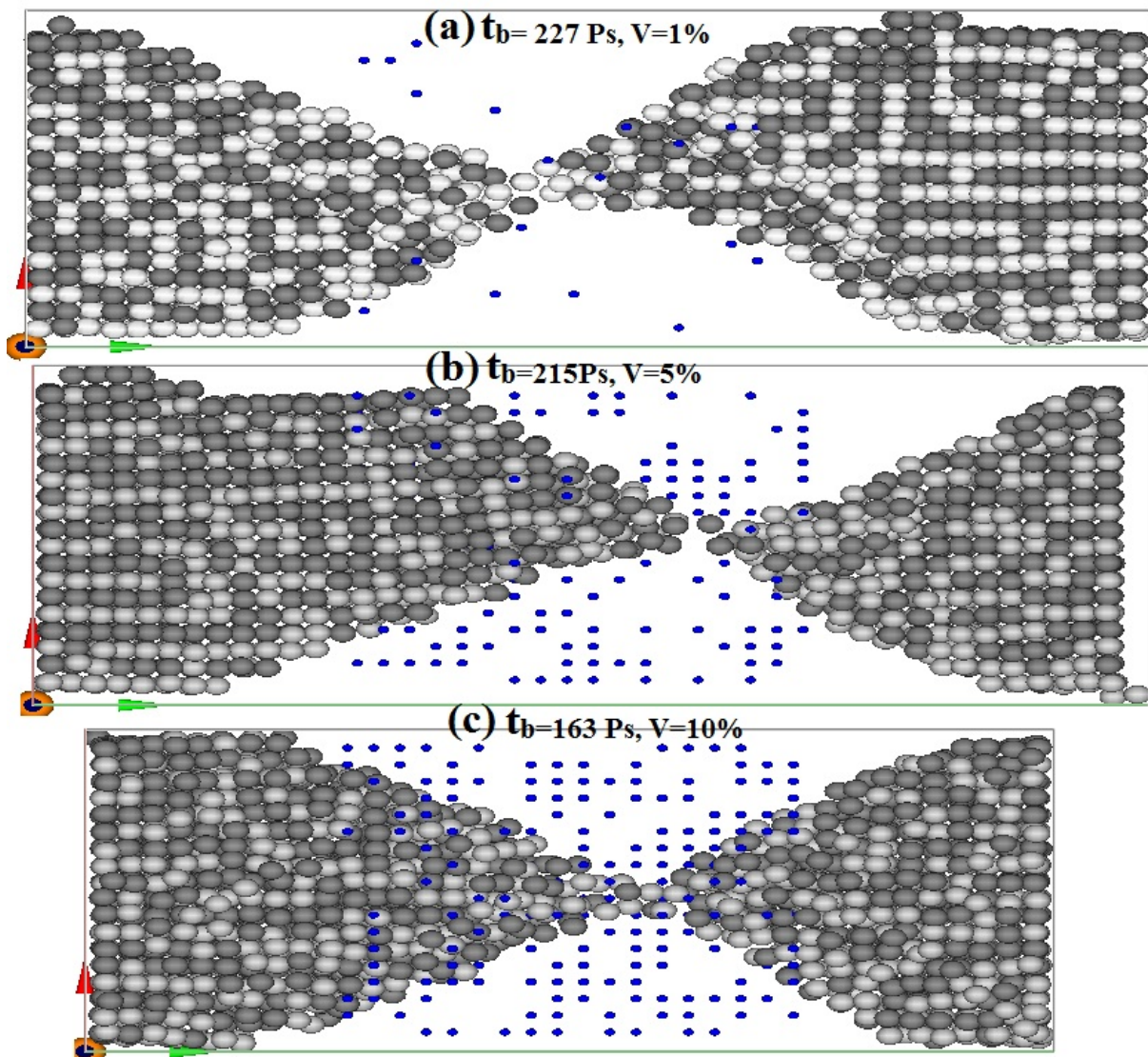


**Fig. 11.** Snapshots of 18 x 18 x 18 (AP) NiTi alloy with different vacancies and the breaking moment at 300K

#### 4. Conclusion

In this work, MD simulations are performed for Ni and Ti nanowire and Nitinol alloy subject to uniaxial tensile strain loading. A many-body interatomic potential within the second-moment approximation of the tight-binding model (the Cleri and Rosato potentials) was employed to carry out three dimensional molecular dynamics simulations. MD simulation results at 300K and 1000K temperature were presented. The stress–strain curves for nanowires were simulated. The breaking and yield stress of nanowires are dependent on the size, temperature and vacancy rates.

The tensile stress decreases with increasing vacancy fraction of the material and the maximum stress founded at zero vacancies. The studied materials shows very high ultimate tensile stress and elongation rate. Increasing vacancy fraction was also affect the yield stress to decrease. It was observed that the Ni and Ti nanowires and Nitinol alloys has a higher fatigue limit when the vacancy fraction is lower, and when the value of applied stress is less-than-critical.

The necking, plastic deformation and breaking of nanowires are demonstrated. The effect of temperature was successfully studied; the elastic modulus and the stress were

linearly decreased. The simulation results would be helpful to avoid the materials failure by predicting the breaking position. This study of mechanical properties of metal nanowires will be helpful to the design, manufacture and manipulation of nano-devices.

**Acknowledgements.** No external funding was received for this study.

## References

- [1] Feng G, Nix WD, Yoon Y, Lee CJ. A study of the mechanical properties of nanowires using nanoindentation. *J. Appl. Phys.* 2006;99(1): 074304.
- [2] Wang ZL, Dai ZR, Gao RP, Bai ZG, Gole JL. Side-by-side silicon carbide–silica biaxial nanowires: Synthesis, structure, and mechanical properties. *Appl. Phys. Lett.* 2000;77(21): 3349.
- [3] Starostenkov MD, Aish MM. Effect of Length and Cross-Sectional Area on Ni<sub>3</sub>Fe Alloy Plasticity. *Advanced Materials Research.* 2014;1013(1): 242-248.
- [4] Aish MM, Starostenkov MD. Mechanical properties of metallic nanowires using tight-binding model. *AIP Conf. Proc.* 2016;1698: 040006.
- [5] Starostenkov MD, Aish MM. Molecular dynamic study for ultrathin Nickel nanowires at the same temperature. *Materials Physics and Mechanics.* 2014;21(1): 1-7.
- [6] Starostenkov MD, Aish MM, Sitnikov AA, Kotrechko SA. Deformation of different nickel nanowires at 300 K. *Letters on Materials.* 2013;3(3): 180.
- [7] Starostenkov MD, Aish MM. Feature deformation and breaking of Ni nanowire. *Letters on Materials.* 2014;4(2): 89.
- [8] Starostenkov MD, Aish MM. Effect of volume on the mechanical properties of nickel nanowire. *Materials Physics and Mechanics.* 2013;18(1): 53-62.
- [9] Starostenkov MD, Aish MM. Deformation and Fracture of Metallic Nanowires Solid State. *Phenomena.* 2017;258(1): 277-280.
- [10] Aish MM, Shatnawi MTM, Starostenkov MD. Characterization of strain-induced structural transformations in CdSe nanowires using molecular dynamics simulation. *Materials Physics and Mechanics.* 2015;24(4): 403-409.
- [11] Cleri F, Rosato V. Tight-binding potentials for transition metals and alloys. *Phys. Rev. B.* 1993;48(1): 22-33.
- [12] Aish MM, Starostenkov MD. Features of structural transformations of HCP metallic Ti nanowires using Cleri-Rosato potential at low temperature. *Letters on Materials.* 2016;6(4): 317.
- [13] Rexer EF, Jellinek J, Krissinel EB, Parks EK. Theoretical and experimental studies of the structures of 12-, 13-, and 14-atom bimetallic nickel/aluminum clusters. *J. Chem. Phys.* 2002;117(1): 82.
- [14] Darby S, Mortimer-Jones TV, Johnston RL, Roberts C. Theoretical study of Cu–Au nanoalloy clusters using a genetic algorithm. *J. Chem. Phys.* 2002;116: 1536.
- [15] Michaelian K, Beltran MR, Garzon IL. Disordered global-minima structures for Zn and Cd nanoclusters. *Phys. Rev. B.* 2002;65: 041403(R).
- [16] Gades H, Urbassek HM. Preferential sputtering of alloys: a molecular-dynamics study. *Nucl. Instr. Meth. B.* 1995;102(1-4): 261.
- [17] Hobbs L. Point defect stabilization in ionic crystals at high defect concentrations. *Journal de Physique Colloques.* 1976;37(C7): C7-3 - C7-26.
- [18] Mazzone G, Rosato V, Pintore M. Molecular-dynamics calculations of thermodynamic properties of metastable alloys. *Phys. Rev. B.* 1997;55: 837.
- [19] Levanov K, Stepanyuk VS, Hergert W, Trushin S, Kokko K. Molecular dynamics simulation of Co thin films growth on Cu(001). *Surface Science.* 1998;400(1): 54-62.
- [20] Garrison BJ, Winograd N, Deaven DM, Reimann CT, Lo DY, Tombrello TA, Harrison DE Jr, Shapiro MH. Many-body embedded-atom potential for describing the energy and angular distributions of Rh atoms desorbed from ion-bombarded Rh{111}. *Phys. Rev. B.* 1988;37(13): 7197-7204.
- [21] Rafi-Tabar H, Sutton AP. Long-range Finnis-Sinclair potentials for f.c.c. metallic alloys. *Phil. Mag. Lett.* 1991;63: 217-224.
- [22] Daw MS, Foiles SM, Baskes M. The embedded-atom method: a review of theory and applications. *Materials Science Reports.* 1993;9(7): 251-310.

# INVESTIGATION OF MECHANICAL PROPERTIES OF GRAPHENE REINFORCED EPOXY NANOCOMPOSITE USING MOLECULAR DYNAMICS

Mithilesh K. Dixit\*, Gokul S. Nair, Vimal Kumar Pathak, Ashish K. Srivastava

Department of Mechanical Engineering

Manipal University Jaipur, Dehmi Kalan, Jaipur-Ajmer Expressway, Near GVK Toll Plaza, Jaipur, Rajasthan  
303007, India

\*e-mail: dixit.mithilesh@gmail.com

**Abstract.** Graphene is a two-dimensional hexagonal type of carbon allotropes in the form of a sheet. It is a one atom thick sheet of carbon atoms, which has extraordinary thermal, mechanical, electronic and electrical properties. In the present research, a molecular dynamic study has been done to investigate the mechanical properties of graphene reinforced epoxy nanocomposite. A single layer of graphene sheet has been randomly reinforced into the epoxy matrix at 5%, 10%, 15% and 20% weight percentages. A dense amorphous cell is created using the Forcite module of Material Studio software and simulation is performed. Young's modulus is predicted at varying strain rate from 0-1. Results have revealed that Young's modulus increases with increase in reinforcement quantity. Moreover, graphene reinforced epoxy nanocomposite exhibits better properties than CNT reinforced nanocomposites.

**Keywords:** atomistic model, epoxy, graphene, molecular dynamics, Young's modulus

## 1. Introduction

The nanocomposite is a multiphase solid material where one of the phases has one, two or three dimensions of less than 100 nanometers (nm). Nanocomposite materials have emerged as suitable alternatives to overcome limitations of microcomposites and monolithic while posing preparation challenges related to the control of elemental composition and stoichiometry in the nanocluster phase. These are reported to be the materials of the 21<sup>st</sup> century in the view of possessing design uniqueness and property combinations that are not found in conventional composites. The effectiveness of the nanoparticles is such that the amount of material added is normally only between 0.5 and 5% by weight.

Over the past decade, advanced material researchers had focused on the development of polymer based nanocomposites reinforced with well-defined nanostructured compounds, which are expected to provide high performance materials, with potential application in a wide range of technological areas such as defense, aerospace, automotive industries etc. The properties of materials may be enhanced by reinforcing with a different type of superior materials like carbon nanotubes (CNTs), Graphene (GR), nano rope, nanoclay and metal/polymer based nanoparticles. However, Graphene has attracted the significant attention of researchers of various areas and has been found to be a suitable reinforcing candidate due to its superior properties over CNT and other nanoparticles. Graphene reinforced polymer nanocomposites have attracted the attention of researchers and material scientists due to its superior properties over other reinforcement materials like CNTs etc. As per the literatures,

nearly 98% of CNTs are produced defective and having structural discontinuities which restrict the application of CNTs in reinforced nanocomposites. The defective CNTs may react with the base material due to which the desired properties may not be achieved. A certain advantage of GR such as high aspect ratio, non-functionality, better electronic and thermal conductivity, thermal stability over the CNTs makes it a potential reinforcement candidate for polymer based nanocomposites. Moreover, mechanical properties and gas barrier behavior appears as a highly promising additive for the improvement of the overall performance of the host polymeric component. In general, the physical properties of such mixed systems were found to depend on several parameters, among others on the characteristics of the dispersion of the GR layers and the nature of the interactions between GR and the polymeric matrix, the amount of wrinkling in the GR, the polymer architecture and the sample preparation procedure [1-3]. Graphene is also envisioned as the key ingredients of many futuristic applications. In particular, epoxy nanocomposites with improved properties (elastic modulus, tensile strength, and toughness) are obtained by reinforcing Graphene into epoxy matrix [4], which make the nanocomposites ideal for various applications viz. lightweight gasoline tanks, strong wind turbines, medical implants, sports equipment, etc. [5]. In addition to the improvement in mechanical properties, graphene reinforced nanocomposites often exhibit enhanced thermal properties and electrical properties as well [6]. Moreover, graphene based nanocomposites have unique applications in a broader range of industries. Thin-film capacitors for a computer chip, Solid polymer electrolytes for batteries, automotive and aircraft engine parts and fuel tanks etc.

Epoxy resins are the well-known class of thermosetting polymers which are widely used as adhesives, electronic encapsulating compounds, coating materials and the organic phase of composite materials due to their high mechanical strength, high chemical corrosion and erosion resistance, excellent electrical insulation. DGEBA (Diglycidyl Ether of Bisphenol-A) categorizes as a thermosetting polymer which has excellent cross linking property and forms polymer chains which may have an irreversible network structure. In this context, various researches have been done highlighting the importance of polymer based nanocomposites and reinforcement of GR and carbon nanotubes (CNTs). Xia et al. [7] investigated the interfacial mechanical behavior of multilayered graphene-PMMA layered nanocomposites by performing pull-out simulations using MD. The results revealed two distinct failure mechanisms; namely, pull-out failure (failure along graphene-PMMA interface) and yielding failure (failure within the multilayered graphene). A one-step cross-linking of epoxy networks was performed by Yarovsky and Evans [8]. The cross linking was based on local proximity keeping the cutoff distance and reactivity orders of the various epoxy. Site pairing was done considering the cutoff distance of 6 Å and crosslinking were based on proximity and reactivity weights. It was observed that the adopted method was not precise enough to obtain a high percentage of curing compared to that obtained synthetically. The cross-linking mechanism was reported by Rottach et al. [9] stated two-stages cross-linking which consists of unstrained and uniaxial strained. Xia et al. [10] conducted coarse-grained molecular dynamics (MD) simulations of nano-indentation of PMMA polymer to study the variation of the elastic properties near the interface between the indenter and the substrate. Characterization of elastic properties was performed by Griebel et al. [11] on polymer-carbon nanotube composites by applying MD simulations, wherein polyethylene was reinforced with CNT. Zhao et al. [12] reported improvement in compressive fracture strength and plastic strain of the composite based on his study regarding the impact of CNTs on the mechanical properties of Magnesium based amorphous alloys. Microstructure characterization method was used by Wan and Chen [13] to examine changes in modulus improvement as a result of interfacial interactions between graphene oxide and the polymer matrix. Awasthi et al. [14] studied the amount of load transfer between a graphene sheet and polyethylene on a nano

scale by utilizing the method of MD simulations. The authors had concluded that the graphene sheets appeared to be adhered to polymer chains in a specific zone and the interphase layer remained unaffected. Shin et al. [15] adopted modelling approaches on epoxy nanocomposites to identify and permeate the interfacial behavior and interphase properties. A reduction in interfacial adhesion with an increase in crosslink conversion was observed between the matrix and the filler. Through MD simulation work of crosslink density on the molecular structure of the interface for the graphite fiber/epoxy matrix, Hadden et al. [16] proved that the effective surface thickness from the graphene sheet is insensitive to the variation of crosslinking. Li et al. [17] dealt with multilayer graphene for the investigation of the interfacial layer of cross-linked epoxy, focusing on the various orientation of the layers by MD simulations.

Dai and Mishnaevsky [18] studied the damage and fracture of graphene reinforced nanocomposites using 3D computational model. The damage mechanisms were studied considering the effect of the aspect ratio, shape, clustering, orientation and volume fraction of graphene platelets. It was observed that the Young modulus of the nanocomposites significantly influences by these parameters and increases with increasing aspect ratio, volume content, elastic properties of graphene/polymer interface layer, and decreasing the degree of intercalation. Roussou and Karatasos [19] employed a full atomistic molecular dynamics simulation and studied the melt dispersions of graphene nanosheets in a poly (ethylene glycol) (PEG) matrix at various temperature ranges. Two different polymer sizes were investigated and resultant mixtures were characterized after reinforcement of graphene in PEG oligomeric clusters. Sharma et al. [20] had used molecular dynamics simulation to study the mechanical and thermal properties of graphene–carbon nanotube-reinforced metal matrix composites. The authors had considered two different computational models viz. single layer graphene sheets–copper and carbon nanotube–copper composites at various temperature and volume fraction of the reinforcing materials. It was found that with an increase in volume fraction Young's modulus as well as the thermal conductivity of single layer graphene sheets–Cu composites increased at a faster rate than that for carbon nanotube–Cu composite. Keeping the volume fraction constant for carbon nanotube and graphene, it has been reported that Young's modulus of single layer graphene sheets–Cu composite was higher than carbon nanotube–Cu composite. Tensile behavior of graphene reinforced polymer nanocomposite was reported by Sun et al. [21]. The authors had used defective single layer graphene which contained single or double vacancies using molecular dynamics simulations. It has been concluded that the mechanical properties such as Young's modulus, ultimate strength and strain in both directions decrease with an increase in defects.

In the present study, molecular dynamics simulation has been employed to determine the mechanical properties of graphene reinforced epoxy nanocomposite. A fully atomistic model of epoxy has been built in Material Studio visualizer and curing has been done using hardener Diethyltoluenediamine (DETDA). Diglycidyl ether of bisphenol A (DGEBA) has been selected for matrix material. An amorphous cell has been created using a single layer of a graphene sheet by random reinforcement. Mechanical properties of epoxy nanocomposite have been determined with and without the reinforcement of graphene sheet.

## 2. Model and Method

In the present research, molecular dynamics simulation has been performed using Material Studio software. MD is the most detailed molecular simulation method [22] which computes the motions of individual molecules. Coupled Newton's equations of motion, which describe the positions and momenta, are solved for a large number of particles in an isolated cluster or in the bulk using periodic boundary conditions. The equations of motion for these particles which interact with each other via intra and inter-molecular potentials can be solved

accurately using the following numerical integration methods (a) common predictor-corrector and (b) Verlet method. MD efficiently evaluates different configurational properties and dynamic quantities which cannot generally be obtained by Monte Carlo simulations [23]. In the present research, a fully atomistic model has been built in the material Studio visualizer environment. A rigid triangular structure has been modeled (shown in Fig. 1) and densely packed in an amorphous cell which is a representative of the actual composite as reported by Dikshit and Engle [24] as shown in Fig. 2.

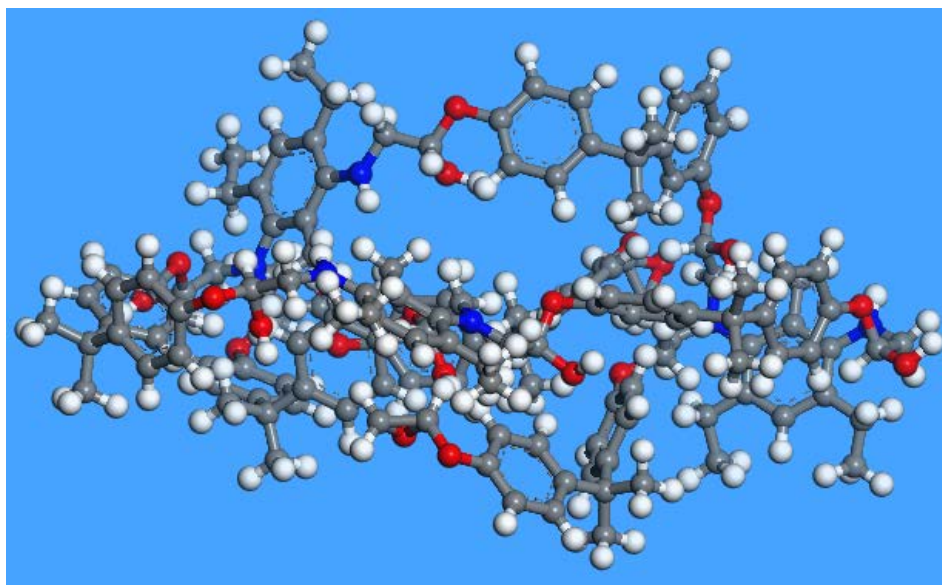


**Fig. 1.** Triangular model of cured DGEBA [24]

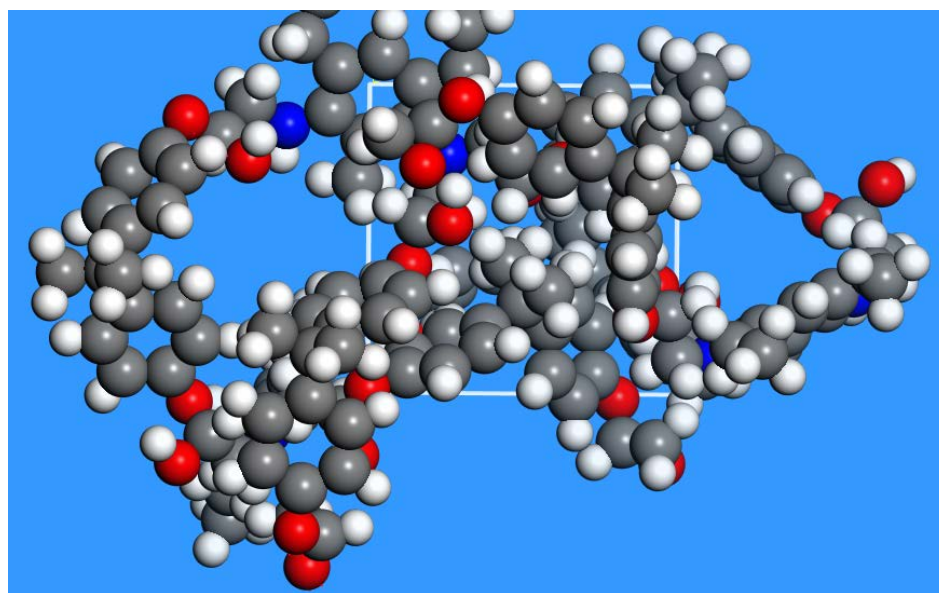


**Fig. 2.** Amorphous cell of the triangular model

In the course of building an amorphous cell the target density of cell was kept equivalent to the real density of the epoxy DGEBA i.e.  $1.2 \text{ gm/cm}^3$ . In densely packed amorphous cell 20 molecules of the triangular model have been used (Fig. 2). Energy minimization and geometric optimization have been employed to stabilize the structure. Dynamic stability has been done using the Forcite module employing NPT ensembles. Furthermore, annealing has been performed using the NVT ensemble to keep volume and density intact. The dynamic run has been done followed by energy minimization and

geometry optimization. The control parameters for Forcite Dynamics and Forcite Anneal Dynamics are depicted in Table 1 and Table 2 respectively.

Table 1. Control Parameter Employed for MD Simulation (Forcite Dynamics)

Force-field	COMPASS II
Temperature control	Berendsen
Pressure Control	Berendsen
Initial velocity	Random
Temperature	298 K
MD ensemble	NPT
Pressure	0.3 GPa
Time step	1 femtosecond (fs)
Duration of simulation	10 pico second (ps)
Periodic boundary condition	On
Number of steps	20000
Frame output every	1000 steps

Table 2. Control Parameter used for Forcite Anneal Dynamics

Anneal cycles	10
Initial Temperature	298 K
Mid-cycle temperature	500 K
Heating ramps per cycle	5
Dynamics step per ramp	100
Total number of step	10000
Geometry optimization after each cycle	yes

The simulation has been done at room temperature i.e. 25°C (298 K) and external pressure was 0.3 GPa. Fig. 3 shows the temperature stability of the developed model with time. From Fig. 3 it can be seen that initially, the temperature of the model increases and rose to the room temperature. As the simulation proceeds, there is no change in the temperature profile which suggests that the model is dynamically stable. Using the control parameters as depicted in Table 1, the predicted density of the developed amorphous cell is 1.202 gm/cm<sup>3</sup> (shown in Fig. 4) which is very close to the actual density of the epoxy DGEBA at room temperature. Furthermore, the stability of the developed model has also confirmed the Forcite Dynamics energies trajectory as shown in Fig. 5.

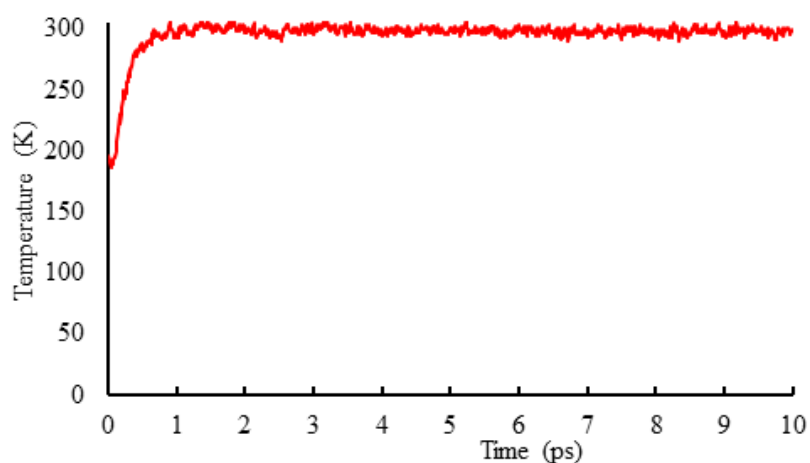
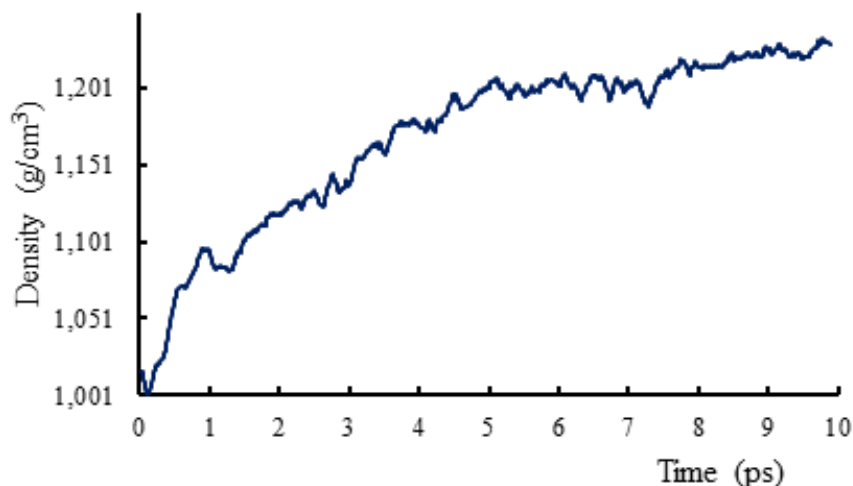
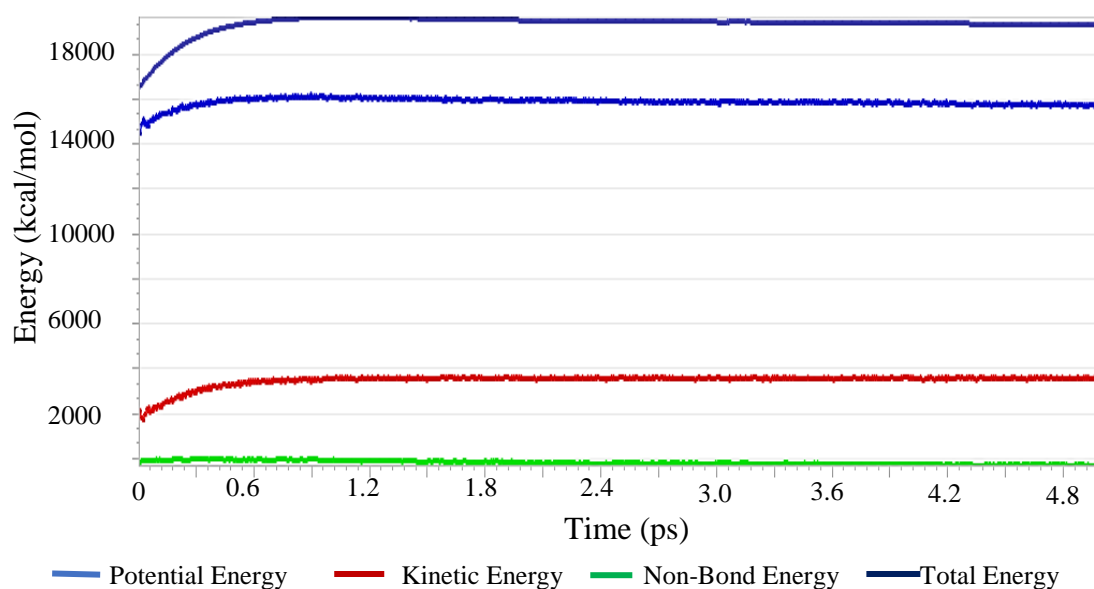


Fig. 3. Simulated data for temperature (K)



**Fig. 4.** Simulation data for density ( $\text{g/cm}^3$ )



**Fig. 5.** Forcite energy diagram for the simulated amorphous cell of DGEBA

From Fig. 5, it is observed all the energies (potential energy, kinetic energy, non-bond energy and total energy) are constant as the simulation progresses. Lower the kinetic energy more stable is the model which also confirm the thermal stability of the model. The optimized structure is further used for creating graphene sheet reinforcement to obtain a graphene based nanocomposite. A single layer graphene sheet (5 repeat units and consisting of 72 atoms) has been randomly reinforced into the epoxy matrix shown in Fig. 6. In the present research, reinforcements have been done at a various weight percentage of graphene viz. 5%, 10%, 15% and 20%.

Similar simulation processes have been adopted using the control parameters depicted in Table 1 and Table 2. After ensuring the stability of the developed model, the model has been further processed for predicting mechanical property.

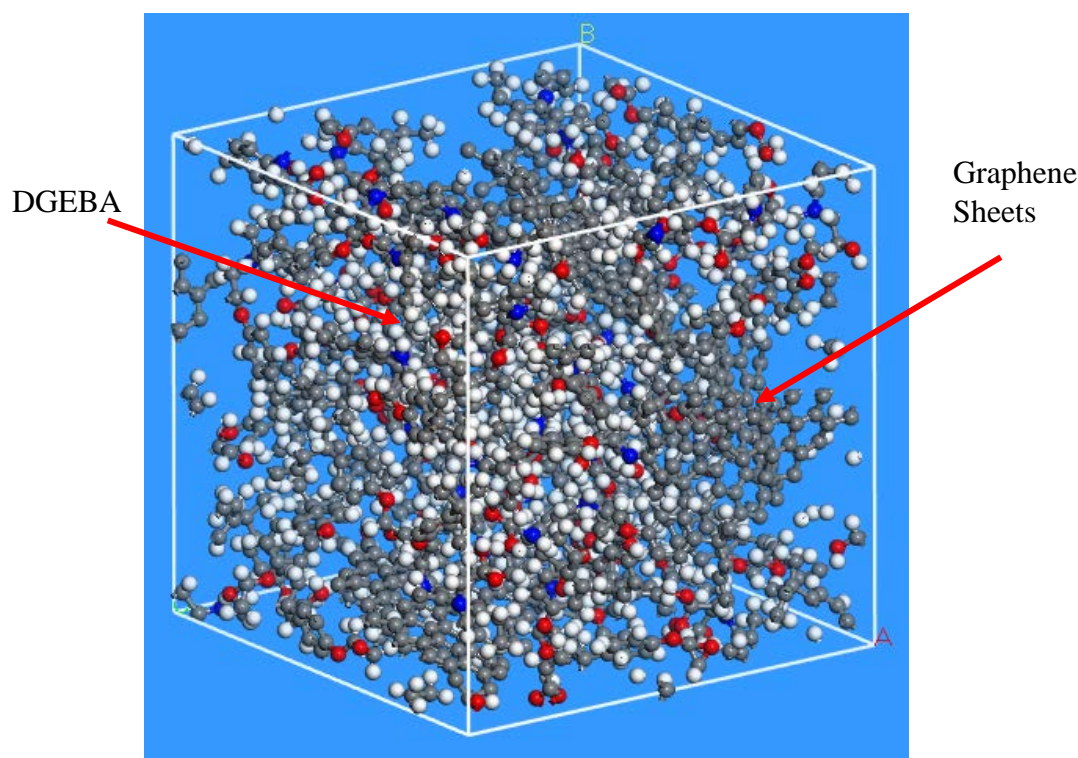


**Fig. 6.** Amorphous cell model for graphene reinforced epoxy

### 3. Results and Analysis

MD simulation has been employed on two amorphous cell models. One model consists of cured DGEBA and another model is obtained after reinforcement of a graphene sheet into the matrix of DGEBA. The simulation has been performed according to the discussions depicted in section 2. The mechanical properties have been obtained after the Forcite dynamic simulation with constant strain minimization. Simulations using COMPASS II force-field have been performed in the Forcite module. Simulations have been performed at room temperature (298 K) using the triangular model as described in section 2. Young's modulus has been predicted at 0%, 2%, 4%, 6%, 8%, and 10% of strains. Predicted Young's modulus of DGEBA without reinforcement at 0% strain is reported to be 2.429 GPa at 298 K and the corresponding Poisson ratio 0.42 [24]. The simulation has been done on the developed graphene reinforced epoxy nanocomposite at a different weight percentage of the graphene sheet. Stress vs. strain curves are plotted for each weight percentage (i.e. 5%, 10%, 15% and 20%) shown in Fig. 7.

The figure (Fig. 7) depicts the stress at various strain rates of DGEBA reinforced with a different weight percentage of graphene and the one without reinforcement. From Fig. 7 it can be seen that there is a significant improvement in the stress value of the epoxy with the increasing value of reinforcement. Superior property is obtained at 20% weight fraction of graphene. However, nonlinearity has been observed in the stress vs. strain curve of graphene reinforced epoxy nanocomposite at 20% weight of graphene, this might be due to improper interphase or improper dispersion of large quantity of graphene.

The plot of Young's modulus against various strain rate at different weight percentages of graphene and without reinforcement is shown in Fig. 8. From Fig. 8, it can be observed that there is a substantial increase in Young's modulus with reinforcement at the same strain rate. Similarly, the maximum value of Young's modulus at 0% strain rate for the simulations involving reinforcement of graphene at a weight of 20% and 15% were found to be around 17.8 GPa and 12.4 GPa respectively and the values of those with 10% and 5% graphene were 8.45 GPa and 4.8 GPa respectively. It is also observed that the value of Young's modulus

decreases with increase in strain rate. Moreover, the obtained results of the graphene reinforced epoxy nanocomposite are compared to CNT reinforced epoxy nanocomposite as reported by Dikshit and Engle [24]. It has been found that graphene reinforced epoxy nanocomposite exhibits better mechanical properties when compared to CNT reinforced epoxy nanocomposite.

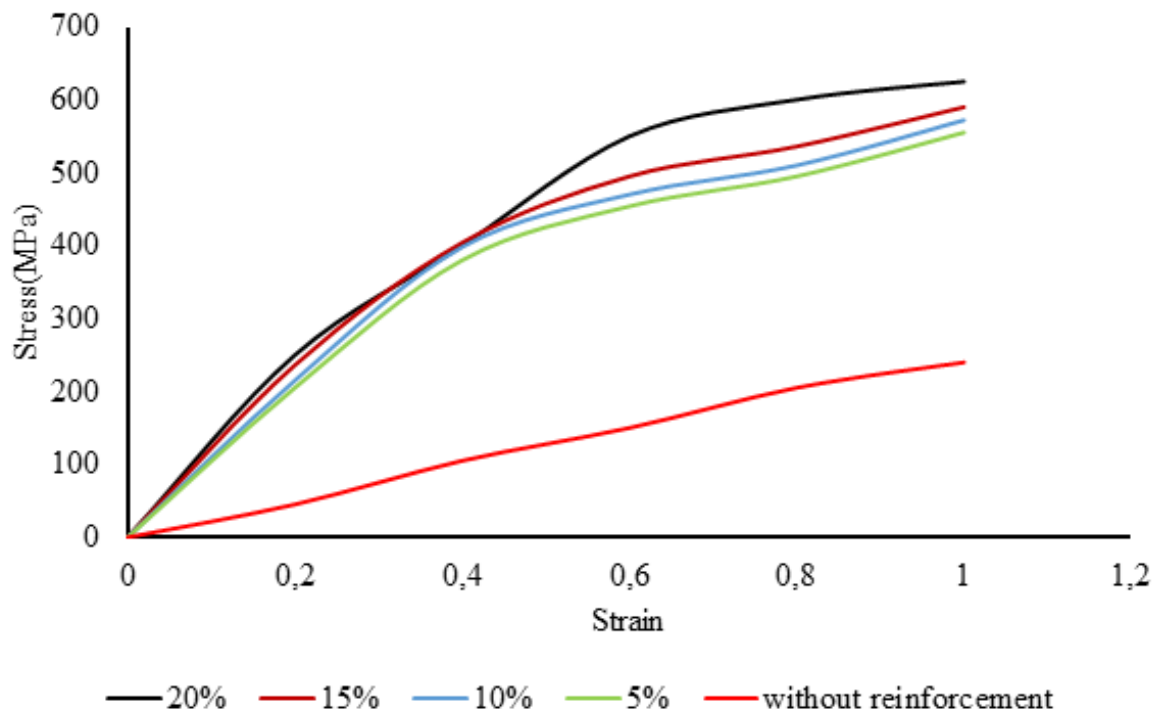


Fig. 7. Stress v/s Strain at different weight percentage

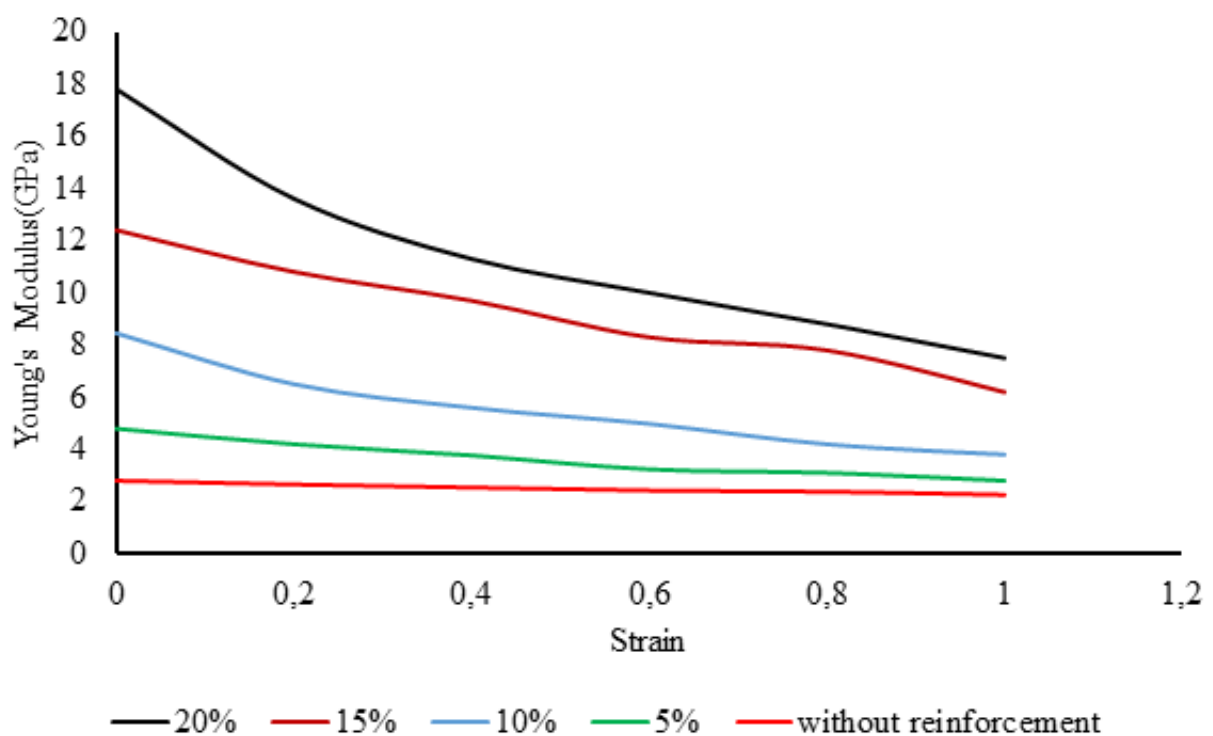


Fig. 8. Young's Modulus v/s Strain at different weight percentage

#### 4. Conclusions

Molecular Dynamics simulations have been employed to study the elastic properties of the epoxy DGEBA cured with DETDA, graphene reinforced epoxy/graphene nanocomposite. Two models of composites have been studied: (a) epoxy matrix with graphene reinforcement and (b) without graphene reinforcement. The following conclusions are drawn from the present research.

1. The predicted MD simulations results for epoxy DGEBA-DETDA indicate that the elastic modulus decreases consistently with the increase in strain. Elastic moduli of the epoxy DGEBA cured with DETDA decreases with the increasing strain levels.

2. The elastic modulus of the epoxy nanocomposite (with or without reinforcement) decrease with increase in strain levels (from 0.0 to 0.1). The MD simulation results clearly indicate that Young's modulus of the Graphene reinforced composites is superior to the DGEBA epoxy matrix.

3. At any given strain level graphene reinforced epoxy composite is 8 times stiffer than the pure epoxy matrix. Whereas in the case of DGEBA reinforced with CNT [24] it is found that the composite is 4 times stiffer than its pure form.

*Acknowledgements.* No external funding was received for this study.

#### References

- [1] Kim H, Abdala AA, Macosko CW. Graphene/Polymer Nanocomposites. *Macromolecules*. 2010;43(16): 6515-6530.
- [2] Mahmoud WE. Morphology and physical properties of poly (ethylene oxide) loaded graphene nanocomposites prepared by two different techniques. *Eur. Polym. J.* 2011;47(8): 1534-1540.
- [3] Du H, Cheng HM. The fabrication, properties and use of graphene/polymer based composites, *Macromol. Chem. Phys.* 2012;213(10-11): 1060-1077.
- [4] Liu X, Metcalf TH, Robinson JT, Houston BH, Scarpa F. Shear modulus of monolayer graphene prepared by chemical vapor deposition. *Nano Lett.* 2012;12(2): 1013–1017.
- [5] Ghosh S, Calizo I, Teweldebrhan D, Pokatilov EP, Nika DL, Balandin AA, Bao W, Miao F, Lau CN. Extremely high thermal conductivity of graphene: Prospects for thermal management applications in nanoelectronic circuits. *Appl Phys Lett.* 2008;92(15): 151911-151913.
- [6] Ghosh S, Bao W, Nika DL, Subrina S, Pokatilov EP, Lau CN, Balandin AA. Dimensional crossover of thermal transport in few-layer graphene. *Nat Mater.* 2010;9: 555-558.
- [7] Xia W, Song J, Meng Z, Shao C, Keten S. Designing multi-layer graphene-based assemblies for enhanced toughness in nacre-inspired nanocomposites. *Mol. Syst. Eng.* 2016;1(1): 40-47.
- [8] Yarovsky I, Evans E. Computer simulation of structure and properties of crosslinked polymers: application to epoxy resins. *Polymer.* 2002;43(3): 963-969.
- [9] Rottach DR, Curro JG, Budzien J, Grest GS, Svaneborg C, Everaers R. Molecular Dynamics Simulations of Polymer Networks Undergoing Sequential Cross-Linking and Scission Reactions. *Macromolecules.* 2007;40(1): 131-139.
- [10] Xia W, Song J, Hsu DD, Keten S. Understanding the interfacial mechanical response of nanoscale polymer thin films via nanoindentation. *Macromolecules.* 2016;49(10): 3810-3817.
- [11] Griebel M, Hamaekers J. Molecular dynamics simulations of the elastic moduli of polymer-carbon nanotube composites. *Computer Methods in Applied Mechanics and Engineering.* 2004;193(17-20): 1773-1788.
- [12] Zhao P, Li S, Gao G, Bai B, Misra RDI. Mechanical behavior of carbon nanotube-reinforced Mg-Cu-Gd-Ag bulk metallic glasses. *Mater. Sci. Eng. A.* 2015;641: 116-122.

- [13] Wan C, Chen B. Metal oxides for interface engineering in polymer solar cells. *J. Mater. Chem.* 2012;22(46): 24202-24212.
- [14] Awasthi AP, Lagoudas DC, Hammerand DC. Modeling of graphene–polymer interfacial mechanical behavior using molecular dynamics. *Modell. Simul. Mater. Sci. Eng.* 2009;17(1): 015002.
- [15] Shin H, Kim B, Han J, Lee MY, Park JK, Cho M. Fracture toughness enhancement of thermoplastic/epoxy blends by the plastic yield of toughening agents: A multiscale analysis. *Composites Science and Technology.* 2017;145: 173-180.
- [16] Hadden CM, Jensen BD, Bandyopadhyay A, Olegard GM, Koo A, Liang R. Molecular modeling of EPON-862/graphite composites: interfacial characteristics for multiple crosslink densities. *Compos Sci Technol.* 2013;76: 92-99.
- [17] Li C, Browning AR, Christensen S, Strachan A. Atomistic simulations on multilayer graphene reinforced epoxy composites. *Compos Part A Appl SciManuf.* 2012;43(8): 1293-1300.
- [18] Dai G, Mishnaevsky JL. Graphene reinforced nanocomposites: 3D simulation of damage and fracture. *Computational Materials Science.* 2014;95: 684-692.
- [19] Roussou RE, Karatasos K. Graphene/poly(ethylene glycol) nanocomposites as studied by molecular dynamics simulations. *Materials and Design.* 2016;97: 163-174.
- [20] Sharma S, Kumar P, Chandra R. Mechanical and thermal properties of graphene–carbon nanotube-reinforced metal matrix composites: A molecular dynamics study. *Journal of Composite Materials.* 2017;51(23): 3299-3313.
- [21] Sun R, Li L, Feng C, Kitipornchai S, Yang J. Tensile behavior of polymer nanocomposite reinforced with graphene containing defects. *European Polymer Journal.* 2018;98: 475-482.
- [22] Allen MP, Tildesley DJ. *Computer simulation of liquids.* 2nd ed. Oxford University Press; 1989.
- [23] Haile JM. *Molecular Dynamics Simulation: Elementary Methods.* Wiley-Interscience; 1997.
- [24] Dikshit MK, Engle P. Investigation of mechanical properties of CNT reinforced epoxy nanocomposite: A molecular dynamic simulation. *Materials Physics and Mechanics.* 2018;37(1): 7-15.

# A MOLECULAR DYNAMICS STUDY OF THE BUCKLING BEHAVIOUR OF GRAPHENE-REINFORCED ALUMINUM NANOCOMPOSITE PLATE

Ashish K. Srivastava<sup>1\*</sup>, Mithilesh K. Dikshit<sup>1</sup>, Vimal K. Pathak<sup>1</sup>, Lakshya Khurana<sup>2</sup>

<sup>1</sup>Asst. Prof., Mechanical Engineering Department, Manipal University Jaipur, India

<sup>2</sup>M.Tech. Scholar, Mechanical Engineering Department, Manipal University Jaipur, India

\*e-mail: ashishkumar.srivastava@jaipur.manipal.edu

**Abstract.** In this study, effects of aspect ratio and perforation on the buckling response of graphene nanosheet (GNS)-embedded aluminum (Al) nanocomposite plate are studied using molecular dynamics (MD) simulations. The periodic system of GS-Al nanocomposite plate is built and simulated using molecular dynamics (MD) based software LAMMPS (Large-scale Atomic/Molecular Massively Parallel Simulator). Embedded atom method (EAM) and Adaptive Intermolecular Reactive Empirical Bond Order (AIREBO) potentials are employed to model the interactions between the atoms of Al and carbon atoms, respectively. It is observed that the buckling strength of square GNS-Al nanocomposite plate deteriorates drastically due to perforation and the same is also true for plates of higher aspect ratio.

**Keywords:** molecular dynamics, nanocomposites, graphene, buckling, plate

## 1. Introduction

Two-dimensional (2-D) honeycomb lattice structure of  $sp^2$ -hybridized carbon (C) atoms, Graphene nanosheet (GNS) with extraordinary mechanical properties [1] has been theoretically analysed for more than seven decades [2,3]. Though, these nanosheets were observed as the integral part of 3-D materials, but it was assumed that GNSs were unstable with respect to the formation of curved carbon nanostructures such as fullerenes and nanotubes [4]. In 2004, Novoselov et al. [5] reported naturally-occurring GNSs by experimentation and opened a new window of nanoscience for researchers around the world. Stiffness and failure properties of GNSs are found to be approximately the same as that of carbon nanotubes (CNTs) [6]. However, the high aspect ratio, surface area and thermal conductivity and low production cost, GNSs are favoured over CNTs as a nanofiller reinforcing agent. With the reinforcement of only a small percentage (by weight/volume) of GNSs in polymers, the mechanical properties of the resulting nanocomposite enhances substantially [7].

GNSs have higher surface area than CNTs and can interact with the matrix at its both upper and lower surfaces. The 2-D shape of GNS has improved interlocking with the matrix material and demonstrates a larger interfacial region at GNS–matrix interface than CNT–matrix interface, which leads to better mechanical properties of GNS-reinforced nanocomposite material [8,9]. For example, for 3% reinforcement of GS by weight, the tensile strength and elastic modulus of polyethylene (PE) are enhanced by approximately 77% and 87%, respectively. On the other hand, addition of the same weight fraction of CNTs in PE increases the tensile strength and elastic modulus of PE by only 58% and 57%, respectively [10].

[http://dx.doi.org/10.18720/MPM.4222019\\_10](http://dx.doi.org/10.18720/MPM.4222019_10)

© 2019, Peter the Great St. Petersburg Polytechnic University

© 2019, Institute of Problems of Mechanical Engineering RAS

Compressive mechanical response of carbon (C) nanofillers are analyzed by various researchers experimentally [11], analytically [12] and through numerical experiments including molecular simulations [13–15]. With continuous improvement and development of less empirical force fields, molecular dynamics (MD) simulations are playing a crucial role in studying the mechanical response of nanofillers. Zhang et al. [16] employed the reactive empirical bond order (REBO) force-field along with Lennard-Jones (LJ) potential to define the interaction between C atoms, similarly, Wang [17] utilized the condensed-phased optimized molecular potential for atomistic simulation studies (COMPASS). Buckling failure behavior of defective CNTs have been examined by Hao et al. [18] with Morse potential integrated with LJ potential.

The extraordinary stiffness and failure properties of GNSs and therefore, enhanced mechanical responses of GNS-reinforced nanocomposites further requires the study of widely used plate-like structures along with the GNS-reinforcement [19]. The load carrying capacity of these GNS-nanostructures subjected to in-plane compression/shear or thermal load is a current area of intense study. For example, the post-buckling response of functionally graded (FG) GNS-reinforced nanocomposite plate under to thermal loading was examined by Shen et al. [20]. In 2018, Srivastava & Kumar [21] have studied the post-buckling behavior of GNS-reinforced nanocomposite plate including the effect of interfacial region. Very recently, Yang et al.[22] have looked into the nonlinear in-plane equilibrium, buckling and post-buckling responses of FG-GNS reinforced fixed and pinned arches subjected to central point load. All these studies are majorly focused on continuum mechanics based study of nanocomposite plate. In order to better understand the buckling or post-buckling response of nanocomposite plate, it is necessary to take care of material response at various loading stages. To capture the response of nanomaterial at nano-level, it is important to employ the molecular simulations while studying the buckling and post-buckling response of GNS-reinforced nanocomposite plate.

In the present study, MD simulations are performed to study the non-linear in-plane instability of nanocomposite plate. Widely used, economical and lightweight metal, aluminum (Al), is chosen as matrix material. Adaptive Intermolecular Reactive Empirical Bond Order Potential function (AIREBO) and Embedded atom method (EAM) are employed, respectively, between the C-C and Al-Al atoms to study the effect of bonded and non-bonded interactions. The effects of aspect ratio and perforation on the buckling and post-buckling responses of nanocomposite plate are also highlighted.

## 2. Atomistic Modeling

In the current study, a square GNS of sides 250 Å is selected as reinforcing nanofiller and Al is taken as matrix material to model a simplified nanocomposite plate. Open source code, Visual Molecular Dynamics (VMD) is utilized to generate the structure of GNS. The data file generated by VMD was utilized along with the face centered structure of Al atoms, generated in LAMMPS (Large-scale Atomic/Molecular Massively Parallel Simulator) input code. The thickness of nanocomposite plate is taken as 15 Å, thus the width to thickness ratio (i.e.,  $w/h$ ) of nanocomposite plate is 16.67 ( $> 20$ ) and will behave as thick plate.

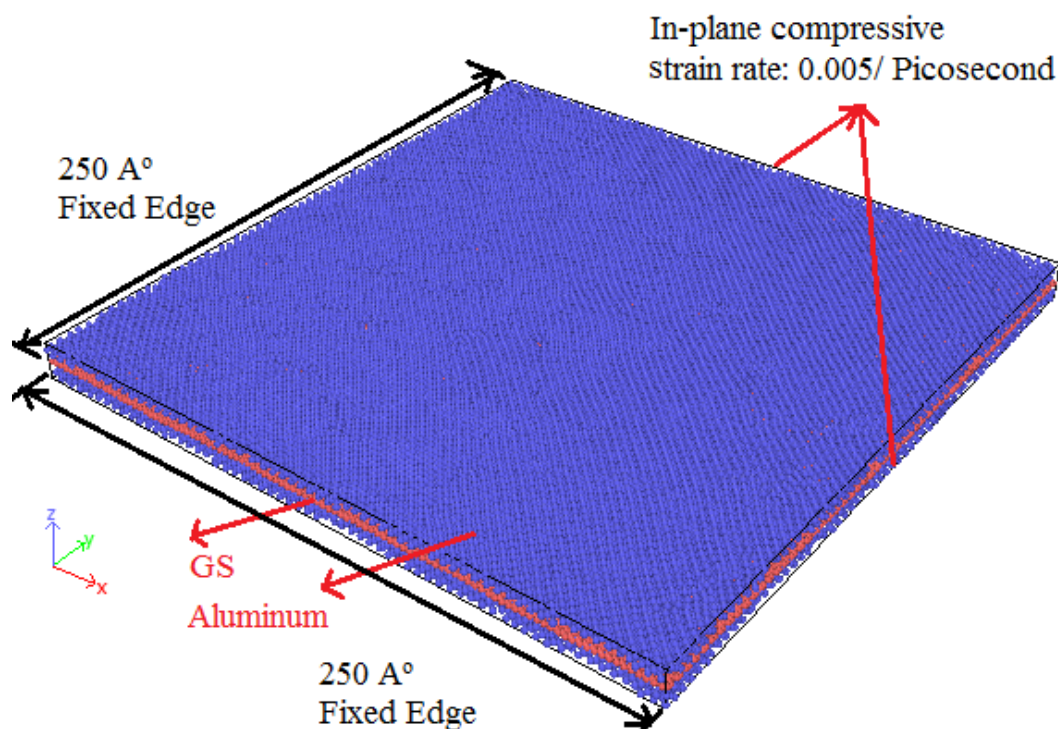


**Fig. 1.** Simplified GNS-reinforced Al nanocomposite plate subjected to biaxial compressive loading

The interaction potentials that act between the covalently bonded C atoms of GNS are evaluated by AIREBO (Adaptive Intermolecular Reactive Empirical Bond Order) potential function. On the other hand, widely employed Embedded Atom Method (EAM) is utilized to model the pair-wise interactions between Al atoms by EAM/ALLOY potential, which describes the interactions between metals and metal-alloy. The Lennard-Jones (L-J) 12-6 interaction potential (Eq. 1), is also utilized to take care of the non-bonded interactions between GNS and Al matrix material.

$$E = 4\varepsilon \left[ \left( \frac{\sigma}{r} \right)^{12} - \left( \frac{\sigma}{r} \right)^6 \right], \quad r < r_c, \quad (1)$$

where,  $r_c$  is the L-J cutoff radius, beyond which van-der-Waals (vdW) interaction becomes very weak and therefore neglected.  $r_c$  is taken as  $2.5 \sigma$  (i.e.  $7.83125 \text{ \AA}$ ). The potential parameter  $\varepsilon$  represents the coefficient of well depth energy and  $\sigma$  represents the equilibrium distance between C and Al atoms. The potential parameters for the interactions between C and Al atoms are calculated by widely employed Lorentz-Bertholet (L-B) rule [23]. The potential parameters for individual Al and C atoms are given in Table 1 and thus for interaction zone these are  $\sigma = 3.1325 \text{ \AA}$  and  $\varepsilon = 0.003457 \text{ eV}$ .

Table 1. L-J pair potential parameters for C and Al atoms

L-J Potential parameters	Carbon, C	Aluminum, Al
$\sigma$ [ $\text{\AA}$ ]	3.41500	2.8500
$\varepsilon$ [eV]	0.00239	0.0050

### 3. Simulation Procedure

After modeling the initial structure of the nanocomposite plate, initially the periodic boundary condition is employed in all the three directions of nanocomposite plate. The potential energy of nanostructure is minimized by conjugate gradient (CG) approach as shown in Fig. 2.

Thereafter, nanostructure was equilibrated by using isothermal–isobaric (i.e., NPT) ensemble at the temperature of 300 K, so that the potential energy and volume of the nanostructure remain relaxed and stable. After the equilibrium process, to observe and analyze the buckling and post-buckling response of nanocomposite plate, the periodic boundary condition in  $z$ -direction (i.e., out-of-plane) is replaced with non-periodic shrink-wrapped boundary condition. Therefore, the out-of-plane deformation of nanocomposite plate is accommodated within the system boundary. All edges of the structure are clamped by fixing the forces on them to zero. Thereafter, a constant strain rate of 0.005/picosecond is applied on the  $x$ - and  $y$ -boundaries of the equilibrated nanostructure.

#### 4. Present Study

**Validation.** In this section, the MD based approach, utilized to characterize the nanocomposite material and study the buckling and post-buckling response of nanocomposite, is verified with the Rule of mixtures (ROM). An equilibrated dimension of nanocomposite plate is shown in Fig. 2 and corresponding stress-strain diagram in armchair and zigzag direction of GNS is plotted in Fig. 3. The modulus and thickness of interphase zone are taken from literature Srivastava & Kumar [24]. It can be observed from Table 2 that, results are in good comparison with that of analytical solution obtained by ROM.

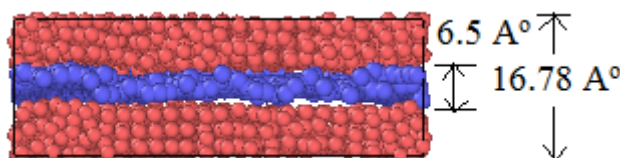


Fig. 2. Equilibrated structure of nanocomposite plate

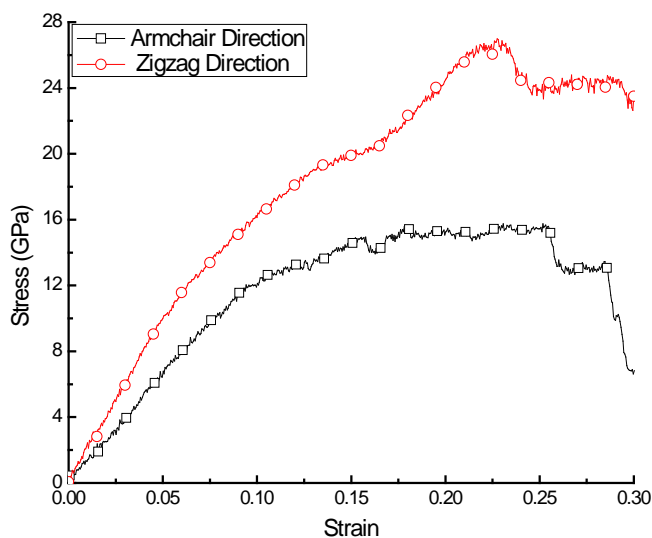


Fig. 3. Stress-strain diagram of nanocomposite material

Table 2. Comparison of Young's modulus for Al -GS aligned nanocomposite

Molecular Dynamics			ROM	% Difference
Armchair	Zigzag	Average		
201.7705	275.6492	238.7099	248.9351	4.1101

**Results and Discussion.** In this section, initially the post-buckling response of pure Al plate is compared with the results obtained from FEM based software ANSYS. All plates

considered for study are subjected to bi-axial compressive loading and all edges of the plates are clamped. The bi-axial compressive load ( $N$ ) and the maximum transverse deflection ( $w_{max}$ ) of the Al plate are normalized as follows

$$\lambda = \frac{Nb^2}{E_m h^3} \quad (\text{with } N = N_x = N_y \text{ for bi-axial loading});$$

$$W^* = \frac{w_{max}}{h}, \quad (2)$$

where  $E_m$  represents the elastic modulus of Al matrix material,  $b$  and  $h$  are the side and thickness of the Al plate.

Thereafter, a separate study is performed to highlight the effect of GNS-reinforcement, aspect ratio and perforation of nanocomposite plate. Since, to analyze the post-buckling response of nanocomposite plate, a constant strain rate is applied in both  $x$ - and  $y$ -directions, thus the results are also reported in terms of applied strain and  $W^*$  (i.e., maximal value of out-of-plane deformation/thickness) of plate.

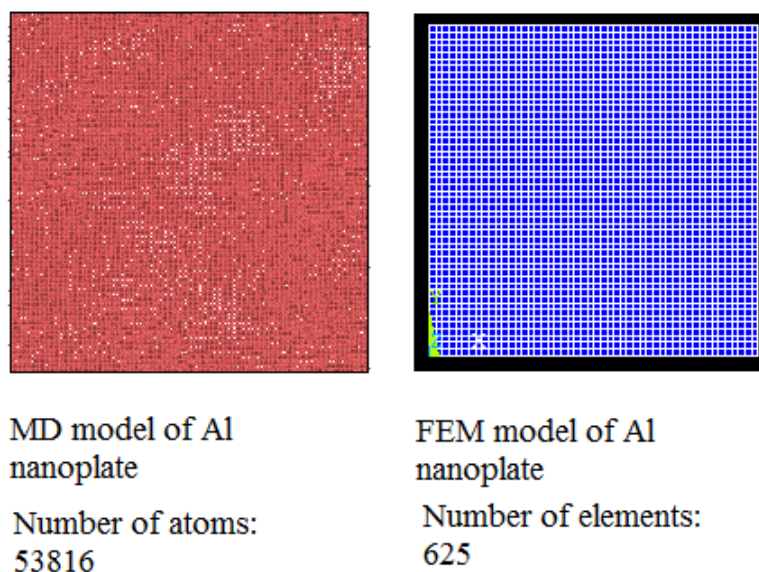


**Fig. 4.** Comparative diagram between MD and FEM model of plate of same dimension

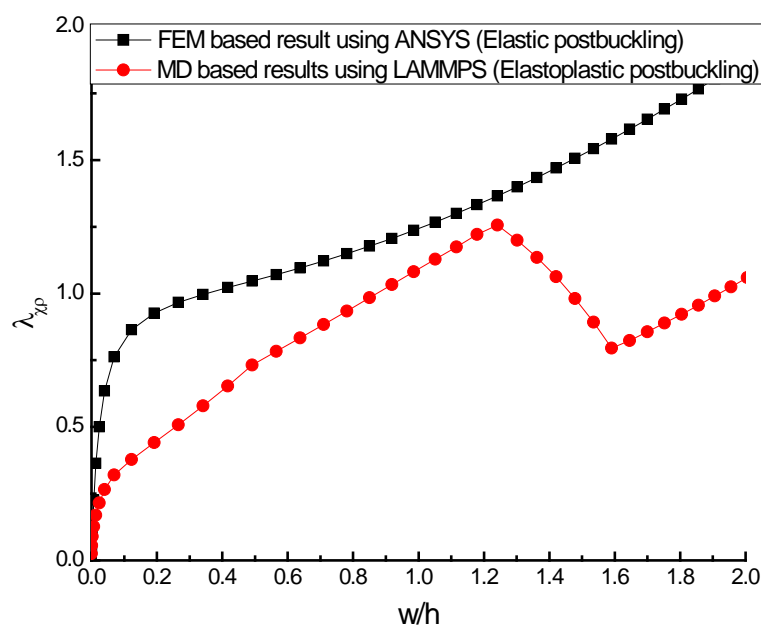


**Fig. 5.** Comparative post-buckling response of pure Al plate with MD and FEM study

The schematic diagrams of MD and FEM models of nanocomposite plate with number of atoms and elements, respectively, are given in Fig. 4. All edges are taken as clamped in both of the models. The buckling and post-buckling responses of Al plate obtained in both of the methodologies are also given in Fig. 5. It can be observed from Fig. 5 that, using MD, the plate buckles far before than the results reported by the FEM based results. The reason for earlier buckling response is that, in MD simulations, the elastic-plastic behavior of material is taken care whereas, the FEM based study reported in Fig. 5 only considers the elastic response of plate. After, equilibrating the MD model, the plate never remains flat (in contrast to FEM model), and surface irregularity of the plate reduces the buckling strength of the plate, substantially.

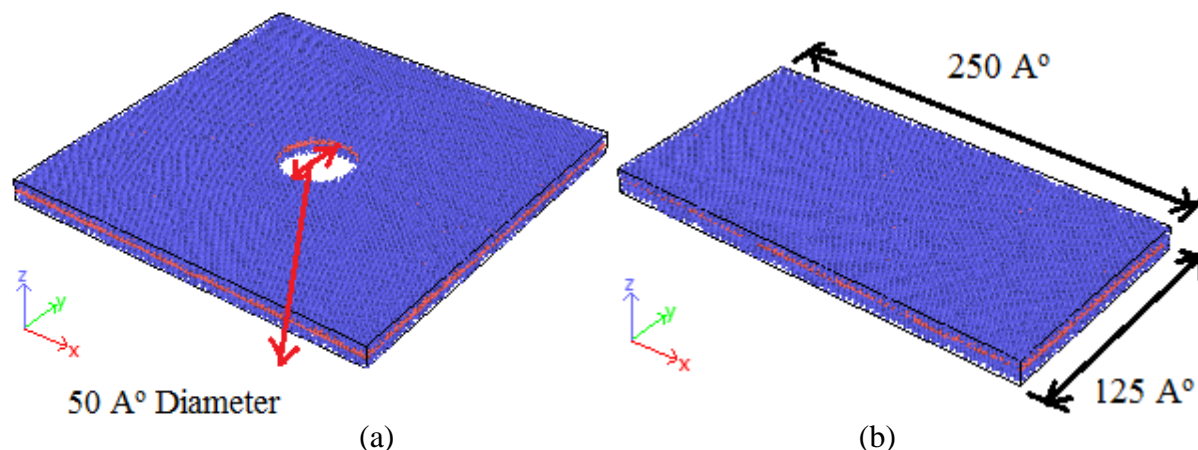


**Fig. 6.** (a) Perforated GNS-Al nanocomposite plate, (b) GNS-Al nanocomposite plate with aspect ratio ( $a/b = 2$ )

To visualize the effect of perforation and aspect ratio on the post-buckling response of nanocomposite plate, two different MD models of nanocomposite plate are modeled as shown in Fig. 6. Nanocomposite plate is perforated by a circular hole of 50 Å diameter, and to study the effect of aspect ratio, the width of model is divided by 2.

Figure 7 shows a comparative study between, pure Al plate, GNS-Al nanocomposite plate, effect of perforation and aspect ratio. Results are shown in terms of Strain and normalized out-of-plane deformation of different plates. Buckling strains found from the results are shown in Table 3. It can be observed from Fig. 7 and Table 3, that, GNS-reinforcement enhances the buckling and post-buckling response of nanocomposite plate substantially. Whereas, the higher aspect ratio and perforation have the negative effect on both the buckling load and load carrying capacity of the plate beyond buckling point. By perforating the current plate by a circle of diameter 50 Å, its buckling strength reduces by 36%.

**Table 3.** Buckling strain for plates considered in the study

S.N.	Type of Plate	Buckling Strain
1	Pure Al	0.001
2	GNS-Al plate	0.03
3	GNS-Al plate with hole	0.019
4	GNS-Al plate having aspect ratio, $a/b = 2$	0.016

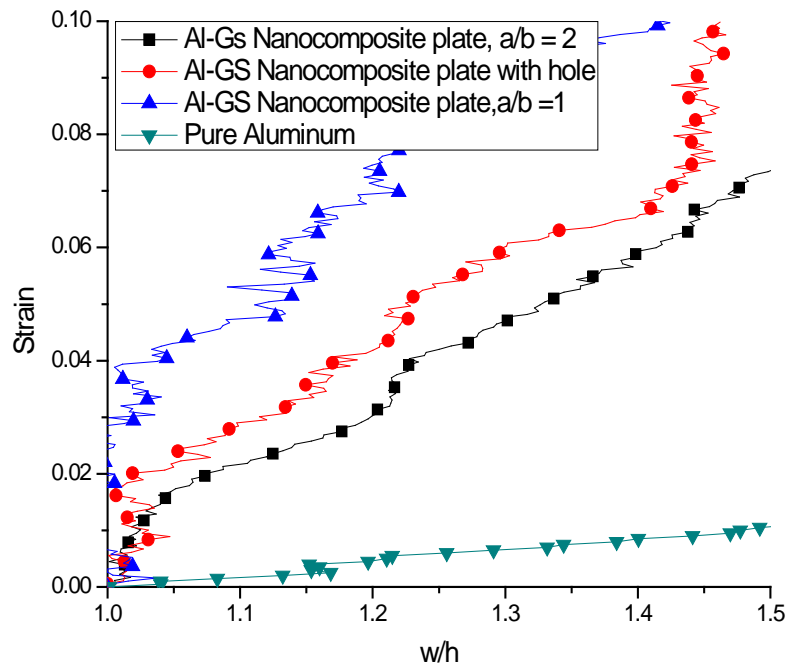


**Fig. 7.** Post-buckling response of GNS-nanocomposite plate showing the effect of perforation and aspect ratio

## 5. Concluding Remarks

In the current study, a MD based simulation is performed to study the buckling and post-buckling response of GNS-Al nanocomposite plate. The AIREBO and Embedded Atom Method (EAM) potential are utilized to represent the pair-wise interactions between C and Al atoms, respectively. Bi-axial loading is applied on the nanocomposite plate with the aid of constant strain rate and clamped boundary conditions are enforced on the all edges of plates. Based on the study performed to investigate the effects of GNS-reinforcement, aspect ratio and perforation on the buckling and post-buckling behavior of nanocomposite plate, and the following conclusions are reported:

- GNS-reinforcement in Al matrix leads to substantial increase in the elastic properties of Al matrix material. This enhancement is further substantial in zigzag direction of GNS.
- Enhanced stiffness properties of nanocomposite materials, further enhances the buckling and post-buckling strength of nanocomposite plate.
- The plates having higher aspect ratios demonstrate lesser buckling and post-buckling strength than square plates.
- Perforation reduces the buckling and post-buckling strength of nanocomposite plate.
- It can be established that present approach offers more realistic results than continuum mechanics based studies, due to ability of MD-approach to capture the effect of inherent surface waviness of the plate and to trace the material response at different loading condition at higher geometric scale.

**Acknowledgements.** The present research work is carried out by utilizing the computation research facilities at the Multiscale Simulation Research Center (MSRC), Manipal University Jaipur (MUJ), India. The authors would like to kindly acknowledge the MSRC, MUJ Jaipur.

## References

- [1] Geim AK, Novoselov KS. The rise of graphene. *Nature*. 2007;6: 183–191.
- [2] Wallace PR. The band theory of graphite. *Phys. Rev.* 1947;71(9): 622–634.
- [3] Sharma MP, Johnson LG, McClure JW. Diamagnetism of graphite. *Phys. Lett. A*.

1973;44(7): 445–446.

[4] Fradkin E. Critical behavior of disordered degenerate semiconductors. I. Models, symmetries, and formalism. *Phys. Rev. B*. 1986;33(5): 3257–3262.

[5] Novoselov KS, Geim AK, Morozov SV, Jiang D, Zhang Y, Dubonos SV, Grigorieva IV, Firsov AA. Electric field effect in atomically thin carbon films. *Science*. 2004;306(5696): 666–669.

[6] Ovid'ko I. Mechanical Properties of Graphene. *Rev. Adv. Mater. Sci.* 2013;34(1): 1–11.

[7] Kuilla T, Bhadra S, Yao D, Kim NH, Bose S, Lee JH. Recent advances in graphene based polymer composites. *Prog. Polym. Sci.* 2010;35(11): 1350–1375.

[8] Stankovich S, Dikin DA, Dommett GHB, Kohlhaas KM, Zimney EJ, Stach EA, Piner RD, Nguyen ST, Ruoff RS. Graphene-based composite materials. *Nature*. 2006;442: 282–286.

[9] Kim H, Macosko CW. Processing-property relationships of polycarbonate/graphene composites. *Polymer*. 2009;50(15): 3797–3809.

[10] El Achaby M, Qaiss A. Processing and properties of polyethylene reinforced by graphene nanosheets and carbon nanotubes. *Mater. Des.* 2013;44: 81–89.

[11] Ayatollahi MR, Shadlou S, Shokrieh MM. Multiscale modeling for mechanical properties of carbon nanotube reinforced nanocomposites subjected to different types of loading. *Compos. Struct.* 2011;93(9): 2250–2259.

[12] Li C, Guo W. Continuum mechanics simulation of post-buckling of single-walled nanotubes. *Int. J. Nonlinear Sci. Numer. Simul.* 2003;4(4): 387–393.

[13] Cao G, Chen X. Buckling behavior of single-walled carbon nanotubes and a targeted molecular mechanics approach. *Phys. Rev. B*. 2006;74(16): 165422.

[14] Chang IL, Chiang BC. Mechanical buckling of single-walled carbon nanotubes: Atomistic simulations. *J. Appl. Phys.* 2009;106(11): 114313.

[15] Singh A, Kumar D. Effect of temperature on elastic properties of CNT-polyethylene nanocomposite and its interface using MD simulations. *J. Mol. Model.* 2018;24: 177–178.

[16] Zhang YY, Tan VBC, Wang CM. Effect of strain rate on the buckling behavior of single- and double-walled carbon nanotubes. *Carbon*. 2007;45(3): 514–523.

[17] Wang Q. Buckling of carbon nanotubes wrapped by polyethylene molecules. *Phys. Lett. A*. 2011;375(3): 624–627.

[18] Hao X, Qiang H, Xiaohu Y. Buckling of defective single-walled and double-walled carbon nanotubes under axial compression by molecular dynamics simulation. *Compos. Sci. Technol.* 2008;68(7-8): 1809–1814.

[19] Song M, Kitipornchai S, Yang J. Free and forced vibrations of functionally graded polymer composite plates reinforced with graphene nanoplatelets. *Compos. Struct.* 2017;159: 579–588.

[20] Shen H-S, Xiang Y, Lin F. Buckling and postbuckling of functionally graded graphene-reinforced composite laminated plates in thermal environments. *Compos. Part B*. 2017;119: 67–78.

[21] Srivastava AK, Kumar D. Postbuckling behaviour of graphene-reinforced plate with interfacial effect. *Arch. Mech.* 2018;70(1): 1–34.

[22] Yang Z, Yang J, Liu A, Fu J. Nonlinear in-plane instability of functionally graded multilayer graphene reinforced composite shallow arches. *Compos. Struct.* 2018;204: 301–312.

[23] Boda D, Henderson D. The effects of deviations from Lorentz–Berthelot rules on the properties of a simple mixture. *Mol. Phys. An Int. J. Interface Between Chem Phys.* 2008;106(20): 2367–2370.

[24] Srivastava A, Kumar D. A continuum model to study interphase effects on elastic properties of CNT/GS-nanocomposite. *Mater. Res. Express*. 2017;4(2): 025036.

# APPLIED THEORY FOR ELECTRO-ELASTIC PLATES WITH NON-HOMOGENEOUS POLARIZATION

A.N. Soloviev<sup>1,2\*</sup>, V.A. Chebanenko<sup>3</sup>, P.A. Oganessian<sup>2</sup>, Shih-Fong Chao<sup>4</sup>, Y.-M. Liu<sup>5</sup>

<sup>1</sup>Don State Technical University, Rostov-on-Don, Russia

<sup>2</sup>I.I. Vorovich Mathematics, Mechanics and Computer Science Institute,  
Southern Federal University, Rostov-on-Don, Russia

<sup>3</sup>Federal Research Center "Southern Scientific Center of the Russian Academy of Sciences", Rostov-on-Don,  
Russia

<sup>4</sup>Department of Microelectronics Engineering, National Kaohsiung University of Science and Technology,  
Kaohsiung, Taiwan

<sup>5</sup>Department of Electric Communication Engineering, National Kaohsiung University of Science and  
Technology, Kaohsiung, Taiwan

\*e-mail: solovievarc@gmail.com

**Abstract.** Non-uniformly polarized piezoceramic materials can be used in effective energy harvesting devices. Axisymmetric and plane models of electric elastic bodies were studied using applied theory and finite element method (FEM). Applied theory for devices made of parts with longitudinal and transverse polarization was developed. It was based on bending of electric elastic plates models. Numerical experiments for FEM models were performed in ACELAN package. Applied theory of second order vibrations was introduced.

**Keywords:** functionally graded material (FGM), prescribed temperature, design optimization, residual stresses minimization

## 1. Introduction

Inhomogeneously polarized piezoelectric devices can be designed to outperform homogeneous puzzlements in electro-mechanical properties as electrotechnical coupling coefficient, output voltage and working bandwidth. FEM is one of the most widely used methods in modelling of such devices and solving problems with non-uniformly polarized devices, which requires specific additions. Such analysis can be performed in ACELAN package. In some cases, proper simplifications can be applied to the model, namely some parts with inhomogeneous polarization can be replaced with set of blocks with uniform polarization. Furthermore, applied theory for model is built with uniformly polarized blocks. Such theory was developed for electric elastic plates in plane and axisymmetric problems.

Application of polarization to the device is an important part of manufacturing process. In some cases, parts can be polarized with imperfections as incomplete polarization or deviation of polarization direction. Modeling the polarization process for predefined model geometry and electrode scheme can be performed in ACELAN package. Vector field of the polarization is transferred to finite element meshes and used for solving problems with non-uniform polarization. Difference between simplified block model presented in applied theory and full model solved with FEM is estimated. Some problems can be reduced from full to simplified model without significant accuracy loss. Described programs, models and

[http://dx.doi.org/10.18720/MPM.4222019\\_11](http://dx.doi.org/10.18720/MPM.4222019_11)

© 2019, Peter the Great St. Petersburg Polytechnic University

© 2019, Institute of Problems of Mechanical Engineering RAS

techniques are developed for advanced analysis of non-uniformly polarized energy harvesting devices.

It is known that piezoelectric materials are widely used as actuators, sensors and generators in the engineering and aerospace field for monitoring the state of structures, shape control, active suppression of parasitic vibrations, noise suppression, etc. Such wide application is achieved due to their good electromechanical properties, flexibility in the design process, ease of production, as well as high conversion efficiency, both electrical energy in the mechanical and in the opposite direction. When using piezoelectric materials as actuators, deformations can be controlled by changing the magnitude of the applied electric potential. In the sensors, deformation measurement is also performed by measuring the induced potential. In the field of energy storage by means of piezoelectric materials, the free mechanical energy, that is present in the designs, is converted into electrical energy and then transferred to a suitable low-power device. A detailed survey is given in [1-3].

Typical actuators, sensors and generators, working on bending, are a multi-layered structure consisting of several layers with different mechanical and electrical properties. The conventional design, consisting of two piezoelectric layers, glued to the substrate or to each other, is called a bimorph. More complex multilayered structures are referred already to functional gradient materials.

To model the layered structures, performing as sensors, actuators and generators, various mathematical models were proposed. Thus, in the previous papers [4,5] analytical solutions of the  $z$ -dimensional equations of the theory of electric elasticity were presented for static cylindrical bending and free vibrations. Nevertheless, the derivation and obtaining of analytic solutions of such equations in the case of arbitrary geometry is a complex problem. Another approach is to use models with induced deformation to simulate the response of the actuator, which were used in [6,7]. However, there the electric potential was not considered as a variable describing the state. This did not allow one to get the related electromechanical responses, but only allowed simulating the response of the actuator. Finite-element models have been proposed in several works, for example, in [8-12]. Some of those models have limitations, the need for large computational resources by using three-dimensional elements in problems, when the thickness of one layer is much less than other design sizes.

In the simulation of piezoelectric designs, the hypothesis of a linear distribution of the electric potential over a thickness is widely used. This means that the induced potential is considered. This is convenient for simulating actuators [13] and piezoelectric generators [14]. Nevertheless, in some materials with a thickness polarization, when an electric field is applied, shear deformations and stresses can arise [12]. In addition, shear stresses and strains arise in multilayer piezoelectric composites [15]. In this connection, accounting for the nonlinear part of the electric potential is of some interest.

In [16], a sandwich model of the third order was considered. The authors have shown that this model gives an additional contribution to rigidity due to the quadratic deformation of the shift and the cubic term of the electric potential. This fact was confirmed by higher natural frequencies. A few papers [17,18] are devoted to the development of a related refined layer-by-layer theory for finite element analysis of multilayer functionally gradient piezoelectric materials. The authors used both the quadratic and cubic electric potential and considered the longitudinal distribution of the potential. This made it possible to consider shear stresses and deformations. We considered forced and free oscillations, which showed good convergence with analytical solutions and commercial FE-software. Nevertheless, the longitudinal distribution of the potential was not presented. In [19] a refined coupled global-local theory was presented for the finite element analysis of thick piezoelectric composites operating on a shear mode. The authors used the quadratic distribution of the thickness potential.

The brief review showed that the use of the nonlinear electric potential distribution, along with considering the longitudinal distribution, is of interest in the problems of calculating multilayer actuators, since it allows more accurate modeling of shear stresses and deformations arising in such structures. Nevertheless, the behavior of the nonlinear electric potential near the resonances has not been sufficiently studied. In connection with this, we developed an applied theory of cylindrical bending of bimorph piezoelectric structures, taking into consideration the quadratic distribution of the thickness potential along with its longitudinal variation.

## 2. Mathematical model

Both basic coupled electromechanical problem formulation and specific applied theory for second order vibrations are presented in this section.

Let us examine a piezoelectric transducer  $\Omega$ , presented by a set of areas  $\Omega_j = \Omega_{pk}$ ;  $k = 1, 2, \dots, N_p$ ;  $j = k$  with the properties of piezoelectric materials, and a set of areas  $\Omega_j = \Omega_{em}$ ;  $m = 1, 2, \dots, N_e$ ;  $j = N_p + m$  with the properties of elastic materials. It is appropriate to describe the physical-mechanical processes taking place in the media  $\Omega_{pk}$  and  $\Omega_{em}$  into framework of piezoelectricity (electric elasticity) and elasticity theory [20,21].

We assume that the following constitutive equations are satisfied (piezoelectric medium is  $\Omega_j = \Omega_{pk}$ ):

$$\rho_{pk} \ddot{\mathbf{u}} + \alpha_{dj} \rho_j \dot{\mathbf{u}} - \nabla \cdot \boldsymbol{\sigma} = \mathbf{f}_j; \nabla \cdot \mathbf{D} = 0, \quad (1)$$

$$\boldsymbol{\sigma} = \mathbf{c}_j^E \cdot (\boldsymbol{\varepsilon} + \beta_{dj} \dot{\boldsymbol{\varepsilon}}) - \mathbf{e}_j^T \cdot \mathbf{E}; \mathbf{D} + \zeta_d \dot{\mathbf{D}} = \mathbf{e}_j \cdot (\boldsymbol{\varepsilon} + \zeta_d \dot{\boldsymbol{\varepsilon}}) + \boldsymbol{\varepsilon}_j^S \cdot \mathbf{E}, \quad (2)$$

$$\boldsymbol{\varepsilon} = (\nabla \mathbf{u} + \nabla \mathbf{u}^T) / 2; \mathbf{E} = -\nabla \varphi, \quad (3)$$

where  $\rho(\mathbf{x}, t)$  is the continuous function of coordinates (density),  $\mathbf{u}(\mathbf{x})$  is the displacement vector-function,  $\boldsymbol{\sigma}$  is the stress tensor,  $\mathbf{f}$  are the mass forces,  $\mathbf{D}$  is the electric induction vector;  $\mathbf{c}_j^E$  are the components of the elastic constant tensor;  $\mathbf{e}_j^T$  are the piezoelectric stress components,  $\boldsymbol{\varepsilon}$  is the strain tensor,  $\mathbf{E}$  is the electric field vector;  $\varphi(\mathbf{x})$  is the electric potential function;  $\boldsymbol{\varepsilon}_j^S$  are the components of the dielectric permittivity tensor;  $\alpha_{dj}, \beta_{dj}, \zeta_d$  are non-negative damping coefficients, and the other symbols are the standard designations for theory of electric elasticity with the exception of index  $j$ , corresponding to area  $\Omega_j$  (for elastic media  $\Omega_j = \Omega_{ek}$  the piezomoduli  $\mathbf{e}_j^T$  are equal to zero).

For the media  $\Omega_j = \Omega_{em}$  with pure elastic properties, only stress fields would be considered. Similar Equations (1) – (3) are constitutive relationships, used with neglect electric fields and piezoelectric connectivity effects. Equations (1) – (3) are added to the mechanical and electrical boundary conditions, as well as the initial conditions in the case of non-stationary problem. Numerical modeling of devices that can be described with Equations (1) – (3) is performed by using finite element method.

In addition to previous equations, all material properties are handled as functions of coordinates:

$$\rho_k = \rho_{pk}(\mathbf{x}), \quad \mathbf{c}_j^E = \mathbf{c}_j^E(\mathbf{x}), \quad \boldsymbol{\varepsilon}_{aj}^S = \boldsymbol{\varepsilon}_{aj}^S(\mathbf{x}), \quad \mathbf{e}_j^T = \mathbf{e}_j^T(\mathbf{x}); \quad (4)$$

$$g = g^i + |P|(g^a - g^i) \text{ for tensors } \mathbf{c}_j^E \text{ and } \boldsymbol{\varepsilon}_j^S \text{ and } g = |P|g^a \text{ for tensor } \boldsymbol{\varepsilon}_{aj}^S; \quad (5)$$

here  $g$  is corresponding tensor component,  $i$  marks isotropic state,  $a$  marks anisotropic state. Tensor of piezoelectric constants will be zero for isotropic bodies.

We consider piezoelectric device consisting of two piezoelectric layers and a middle passive layer. The piezoelectric layers are inhomogeneously polarized according to the process presented in [22] (Fig. 1).

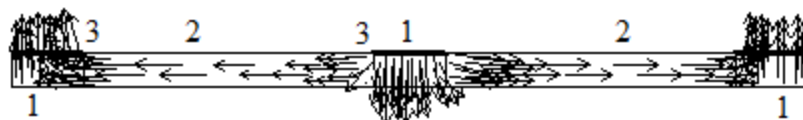


**Fig 1.** Inhomogeneously polarized ceramic layer

This piezoelectric layer has several specific regions with transverse and longitudinal polarization (regions 1, 2 in Fig. 1) and some transition zones from one polarization to another (region 3 in Fig. 1). In [22], an assessment was made of the effect of these transition regions on the characteristics of the piezoelectric device consisting of two piezoelectric layers and a comparison was made with the piezoelectric cell shown in Fig. 2a with piecewise inhomogeneous polarization. In the limits of geometrical parameters specified in [22], this simplified model can be used to calculate the output characteristics of a piezoelectric device with non-uniform polarization. In the case of a small thickness in comparison with the characteristic length dimension (which is typical for the full-scale implementation), the static behavior and steady-state oscillations of these piezoelectric devices on the first flexural modes can be described by applied theories. In such theories, a certain distribution of mechanical and electric fields over the thickness of the piezoelectric element is assumed (for example, the invariance of the normal, etc.).

One of the applied theory variants for plane case was described for geometry presented in Fig. 1a. Theory based on studies presented in [3,4] and some implementation details were provided in paper [1]. Model consists from transversally polarized part and longitudinally polarized part with two layers.

Such devices can be made with specific elastic layer to improve mechanical properties. This layer is usually placed between active layers as shown In Fig. 1b. Geometrical parameters of the model are: inner layer thickness  $h$ , piezoelectric layers thickness  $H$  and lengths  $L_1$  and  $L_2$  for each segment. Median line of the transducer is placed on  $x$ -axis for the first segment and on  $z$ -axis for the second segment.

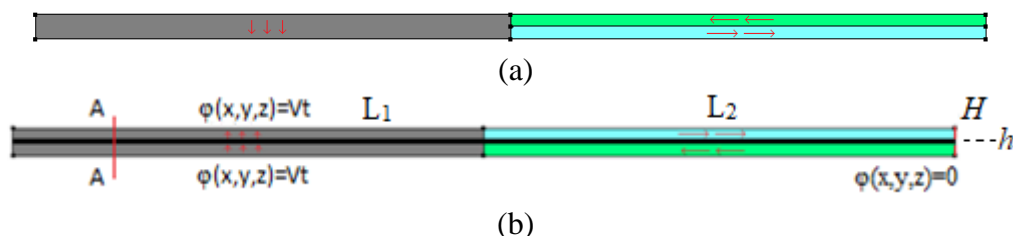


**Fig. 2.** Device with uniformly polarized parts, initial construction (a) and with medium layer (b)

### 3. Applied theory

The static deflection was calculated in the finite element package ACELAN for a uniformly distributed normal load and the modal analysis of the piezoelectric element hinged around the edges (determination of frequencies and modes of resonance and antiresonance), presented in Fig. 2b, for  $h = 1$  mm,  $H = 2$  mm  $L_1 = L_2 = 100$  mm, piezoelectric PZT-4, steel substrate.

Figure 3 shows the distribution of the transverse displacement under a static load on the deformed state, and Fig. 4 presents distribution of electrical potential.

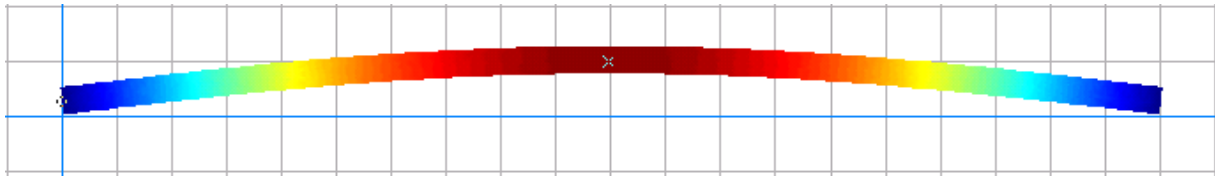


**Fig. 3.** Vertical component of displacement distribution

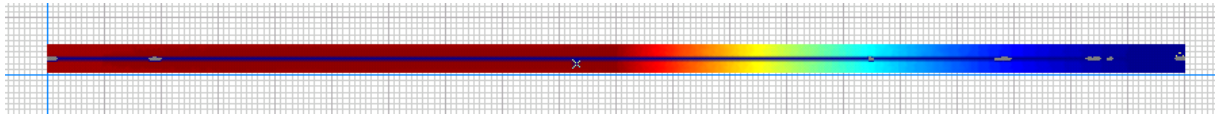


**Fig. 4.** Electric potential distribution

Figure 5 demonstrates distribution of the electrical potential along the thickness of the upper piezoceramic layer in section A-A (see Fig. 2b).

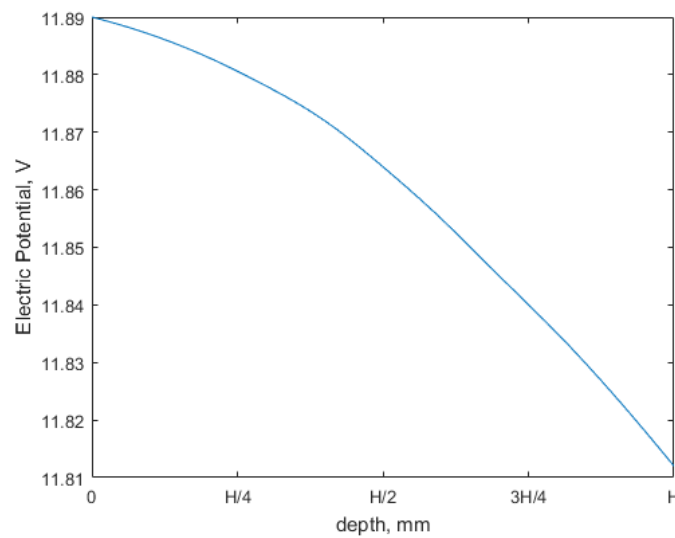


**Fig. 5.** Distribution of the electrical potential along the thickness of the upper piezoceramic layer in section A-A

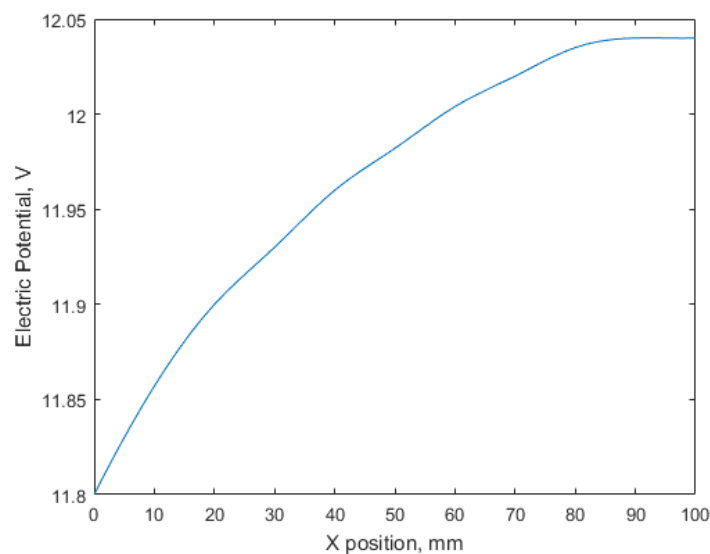


**Fig. 6.** Distribution along the length of the first section ( $L_1$ ) of the electric potential at the lower boundary of ceramic layer

Figures 6 and 7 show the distribution along the length of the first section ( $L_1$ ) of the electric potential at the lower boundary of this layer and in its middle, respectively.

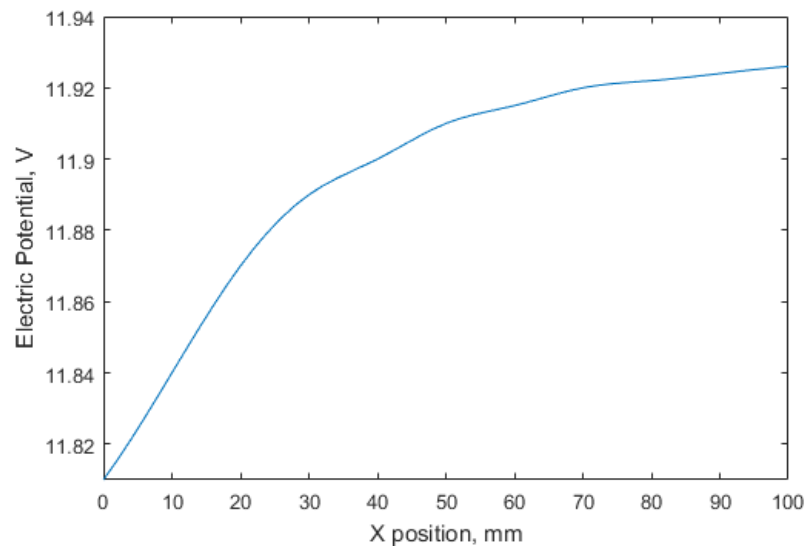


**Fig. 7.** Distribution along the length of the first section ( $L_1$ ) of the electric potential at the middle line of ceramic layer

Figures 8 – 11 show results similar to Figs. 4 – 7 for the first resonance  $F_r = 0.2049 \times 10^3$  Hz, and Figs. 12 – 15 for the first antiresonance  $F_a = 0.2287 \times 10^3$  Hz.

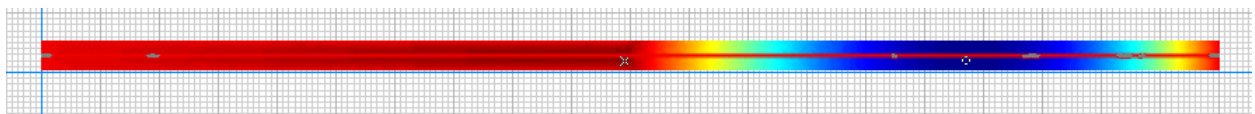


**Fig. 8.** Potential distribution at resonance frequency

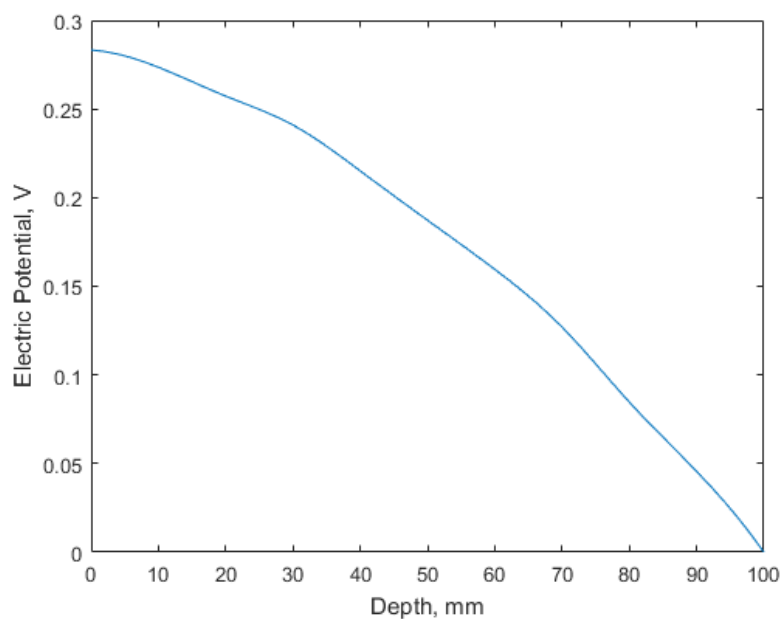


**Fig. 9.** Distribution of the electrical potential along the thickness of the upper piezoceramic layer in section A-A at resonance frequency

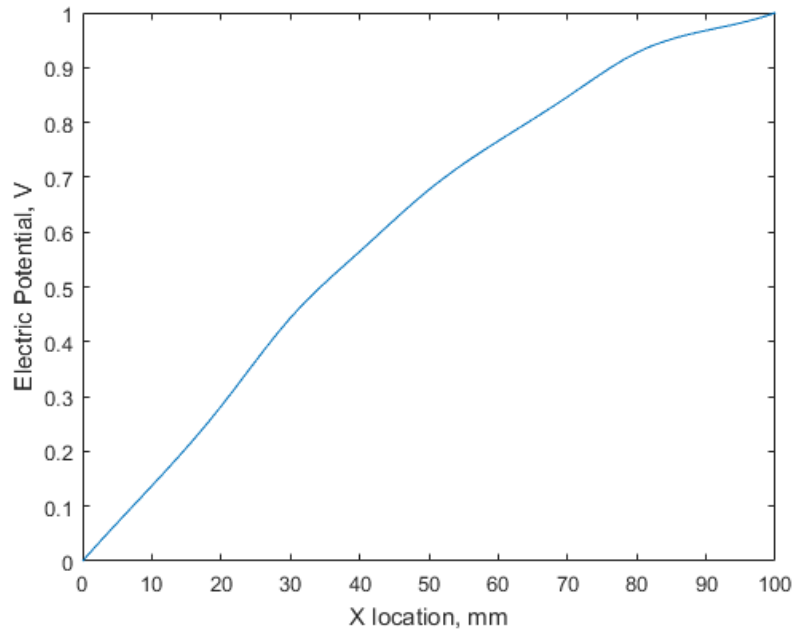


**Fig. 10.** Distribution along the length of the first section ( $L_1$ ) of the electric potential at the lower boundary of ceramic layer at resonance

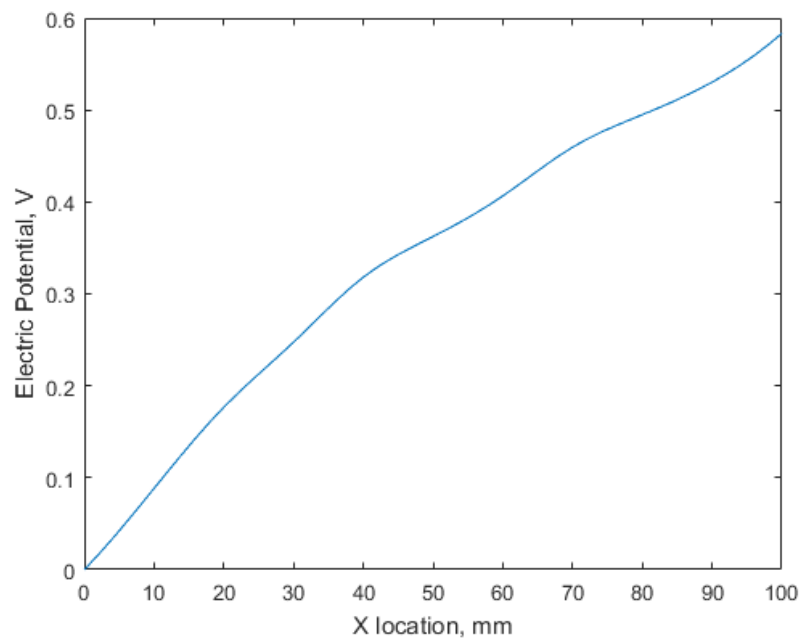


**Fig.11.** Distribution along the length of the first section ( $L_1$ ) of the electric potential at the middle line of ceramic layer

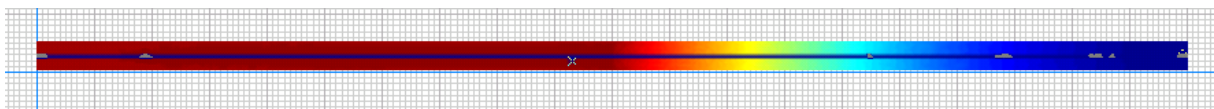


**Fig.12.** Electric potential distribution at antiresonance frequency

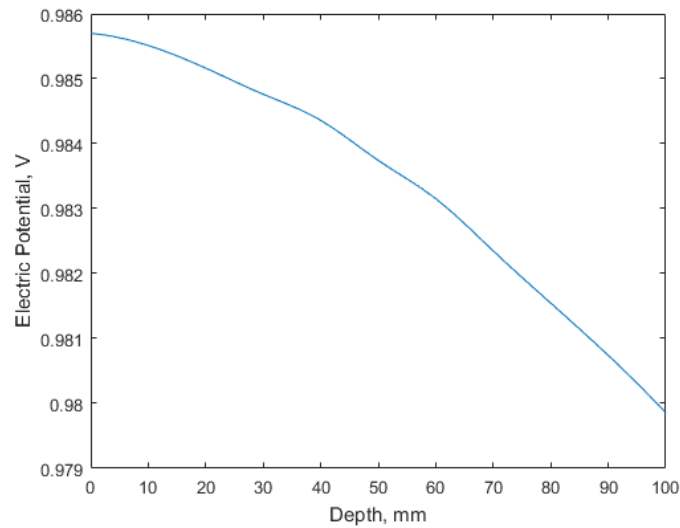


**Fig. 13.** Distribution of the electrical potential along the thickness of the upper piezoceramic layer in section A-A at antiresonance frequency

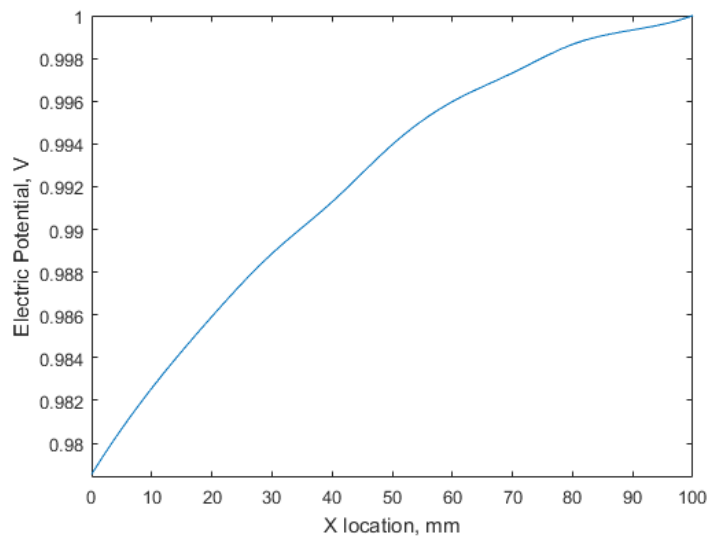


**Fig. 14.** Distribution along the length of the first section ( $L_1$ ) of the electric potential at the lower boundary of ceramic layer at antiresonance frequency

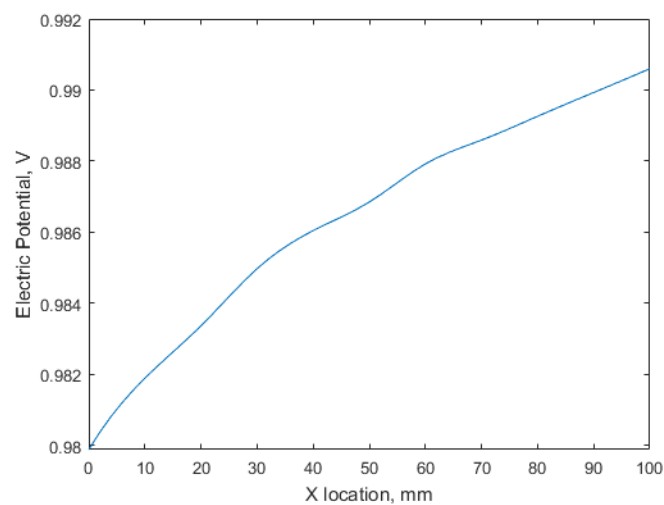


**Fig. 15.** Distribution along the length of the first section ( $L_1$ ) of the electric potential at the middle line of ceramic layer at antiresonance frequency

Analysis of numerical results of calculations, including those presented in Figs. 3 – 15 allows us to conclude that the hypothesis of the general normal for the mechanical characteristics of the entire piezoelement is valid. The quadratic law of the electric potential distribution over the thickness in the first fragment of the piezoelement (Fig. 1b) and the constant distribution in the second one is also correct. System of constitutive Equations (2), (3) bending electric elastic plate can be written as follows:

$$\begin{aligned}
\sigma_{11} &= c_{11}\varepsilon_{11} + c_{12}\varepsilon_{22} + c_{13}\varepsilon_{33} + e_{31} \frac{\partial\varphi}{\partial z}, & \sigma_{23} &= c_{44}\left(\frac{\partial u_y}{\partial z} + \frac{\partial u_z}{\partial y}\right) + e_{15} \frac{\partial\varphi}{\partial y}, \\
\sigma_{22} &= c_{12}\varepsilon_{11} + c_{11}\varepsilon_{22} + c_{13}\varepsilon_{33} + e_{31} \frac{\partial\varphi}{\partial z}, & \sigma_{13} &= c_{44}\left(\frac{\partial u_x}{\partial z} + \frac{\partial u_z}{\partial x}\right) + e_{15} \frac{\partial\varphi}{\partial x}, \\
\sigma_{33} &= c_{13}\varepsilon_{11} + c_{13}\varepsilon_{22} + c_{33}\varepsilon_{33} + e_{33} \frac{\partial\varphi}{\partial z}, & \sigma_{12} &= \left(\frac{c_{11}}{2} - \frac{c_{12}}{2}\right)\left(\frac{\partial u_x}{\partial y} + \frac{\partial u_y}{\partial x}\right), \\
D_1 &= e_{15}\left(\frac{\partial u_x}{\partial z} + \frac{\partial u_z}{\partial x}\right) - g_{11}\left(\frac{\partial\varphi}{\partial x}\right), \\
D_2 &= e_{15}\left(\frac{\partial u_y}{\partial z} + \frac{\partial u_z}{\partial y}\right) - g_{11}\left(\frac{\partial\varphi}{\partial y}\right), \\
D_3 &= e_{31}\varepsilon_{11} + e_{31}\varepsilon_{22} + e_{33}\varepsilon_{33} - g_{33} \frac{\partial\varphi}{\partial z},
\end{aligned} \tag{6}$$

where notations are the same as in (1) – (3).

Elastic layer (black color in Fig. 1b) is an isotropic material with following model, based on model of plates bending [23,24]:

$$c_{ii} = \lambda + 2\mu, \quad i = 1, 2, 3; \quad c_{ij} = \mu, \quad i = 4, 5, 6; \quad c_{ij} = \lambda, \quad i \neq j, \quad i, j = 1, 2, 3.$$

Assuming  $\sigma_{33} = 0$  in a whole volume,  $\varepsilon_{33}$  can be presented as

$$\varepsilon_{33} = -\frac{c_{13}e_{11} + c_{13}\varepsilon_{22} + e_{33} \frac{\partial\varphi}{\partial z}}{c_{33}}. \tag{7}$$

Assuming a cylindrical bending of the plate and  $\varepsilon_{22} = 0$ , we have

$$\begin{aligned}
\sigma_{11} &= c_{11}\varepsilon_{11} - c_{13} \frac{c_{13}e_{11} + e_{33} \frac{\partial\varphi}{\partial z}}{c_{33}} + e_{31} \frac{\partial\varphi}{\partial z}, \\
\sigma_{22} &= c_{12}\varepsilon_{11} - c_{13} \frac{c_{13}e_{11} + e_{33} \frac{\partial\varphi}{\partial z}}{c_{33}} + e_{31} \frac{\partial\varphi}{\partial z}.
\end{aligned} \tag{8}$$

Electric potential distribution for joints on edges of plate is

$$\begin{aligned}
\varphi(x, y, z) &= S_1(z)\Phi(x) + S_2(z)\Phi_1(x) + S_3(z)V_t, \\
S_1(z) &= \frac{1}{4} \frac{(H+h-2z)(h+2H-2z)}{H^2}, \\
S_2(z) &= \frac{(h-2z)(h+2H-2z)}{H^2}, \\
S_3(z) &= \frac{1}{4} \frac{(h-2z)(H+h-2z)}{H^2},
\end{aligned} \tag{9}$$

where  $V_t$  is constant electric potential value on the electrodes of the plate.  $\Phi(x)$  is an electric potential distribution on the bottom surfaces of piezoelectric layers,  $\Phi_1(x)$  is an electric potential distribution on the inner middle surfaces of piezoelectric layer.

Displacement distribution variable, in the frame of common normal, can be described as

$$U_x(x, y, z) = -\frac{\partial U_z(x)}{\partial x} \cdot z. \quad (10)$$

Now we can write relations for bending moment  $M_1$  and cutting force  $Q_1$  and  $D_1$ :

$$M_1 = \int_{-h/2-H}^{h/2+H} \sigma_{11} z dz = K_1 V_t + K_2 \Phi(x) + K_3 \Phi_1(x) + K_4 \frac{d^2}{dx^2} U_z(x)$$

$$Q_1 = -\frac{\partial M_{11}}{\partial x} = K_5 \frac{\partial}{\partial x} \Phi(x) + K_6 \frac{\partial}{\partial x} \Phi_1(x) + K_4 \frac{d^3}{dx^3} U_z(x)$$

$$C_0 = \frac{c_{13} e_{33}}{c_{33}} - e_{31}$$

$$C_1 = \frac{1}{12} \frac{\mu(\lambda + \mu) h^3}{\lambda + 2\mu}$$

$$C_2 = \frac{2H}{3} (c_{11} - \frac{c_{13}^2}{c_{33}}) (\frac{3}{4} h^2 + \frac{3}{2} hH + H^2)$$

$$K_1 = -\frac{5}{3} C_0 (H + \frac{3}{5} h)$$

$$K_2 = \frac{1}{3} C_0 (H + 3h)$$

$$K_3 = \frac{4}{3} C_0 H$$

$$K_4 = C_1 + C_2$$

$$K_5 = -\frac{1}{3} C_0 (H + 3h)$$

$$K_6 = -\frac{4}{3} C_0 H$$

$$D_1 = -\frac{1}{3} g_{11} \Phi_1(x) - \frac{4}{3} g_{11} \Phi(x)$$

(11)

Equations of oscillations and averaged equation for electric potential:

$$\frac{\partial Q_1}{\partial x} - p(x) - W^2 \rho h U_z(x) = 0,$$

$$\int_{-h/2-H}^{h/2+H} (\frac{\partial D_3}{\partial x} + \frac{\partial D_1}{\partial x}) dz = 0, \quad (12)$$

where  $\rho$  is the material density,  $p(x)$  is the external force,  $W = 2\pi\omega$ ,  $\omega$  is the oscillation frequency. After substitution of all known values, (12) becomes:

$$\begin{cases} K_5 \frac{\partial}{\partial x} \Phi(x) + K_6 \frac{\partial}{\partial x} \Phi_1(x) + K_4 \frac{d^4}{dx^4} U_z(x) - W^2 \rho h U_z(x) - p(x) = 0; \\ K_7 V_t + K_7 \Phi(x) - 2K_7 \Phi_1(x) - \frac{1}{3} g_{11} \frac{d^2}{dx^2} \Phi(x) - \frac{4}{3} g_{11} \frac{d^2}{dx^2} \Phi_1(x) + C_0 \frac{d^2}{dx^2} U_z(x) = 0 \end{cases} \quad (13)$$

$$K_7 = -\frac{8}{H^2} (g_{33} + \frac{e_{33}^2}{c_{33}}).$$

From the conditions on the surface of the ceramic layer, we have.

$$V_t = \frac{1}{3L_1} \int_0^{L_1} (4\Phi_1(x) - \Phi(x)) dx - \frac{C_0 H (H + 2h)}{6L_1 (g_{33} + \frac{e_{33}^2}{c_{33}})} \left[ \frac{d}{dx} U_z(L_1) - \frac{d}{dx} U_z(0) \right]$$

and

$$K_8 V_t + 3K_8 \Phi(x) - 4K_8 \Phi_1(x) + \frac{1}{2} h C_0 \frac{d^2}{dx^2} U_z(x) = 0.$$

For the other part of the transducer, we add local coordinate system with starting point at  $(L_1, 0)$ . Axes  $x$  and  $z$  are switched in this local coordinate system. Constitutive equations are the same, at mutually replacing the axes. Potential distribution will be in the next form:

$$\phi(x, y, z) = \Phi(z).$$

Expressions for  $D_3$ ,  $M_3$  and  $Q_3$  can be written as follows, using the same technique as in previous part:

$$\begin{aligned} D_3 &= \left( -\frac{2e_{31}^2}{c_{11}} - 2g_{33} \right) \frac{\partial}{\partial z} \Phi(z) + \left( -\frac{2e_{31}^2 x}{c_{11}} - 2g_{33} x \right) \frac{\partial^2}{\partial z^2} U_x(z) \\ M_3 &= \frac{1}{2} \left( -\frac{2c_{13}e_{31}}{c_{11}} + 2e_{33} \right) \left( \left( \frac{1}{2}h + H \right)^2 - \frac{1}{4}h^2 \right) \frac{\partial}{\partial z} \Phi(z) + \\ &+ \frac{1}{3} \left( \frac{2c_{13}^2}{c_{11}} - 2c_{33} \right) \left( \left( \frac{1}{2}h + H \right)^3 - \frac{1}{8}h^3 \right) \frac{\partial^2}{\partial z^2} \Phi(z) \\ Q_3 &= -\frac{1}{2} \left( -\frac{2c_{13}e_{31}}{c_{11}} + 2e_{33} \right) \left( \left( \frac{1}{2}h + H \right)^2 - \frac{1}{4}h^2 \right) \frac{\partial^2}{\partial z^2} \Phi(z) + \\ &+ \left( -\frac{1}{3} \left( \frac{2c_{13}^2}{c_{11}} - 2c_{33} \right) \left( \left( \frac{1}{2}h + H \right)^3 - \frac{1}{8}h^3 \right) - \frac{1}{24} \left( -2\lambda - 4\mu + \frac{2\lambda^2}{\lambda + 2\mu} \right) h^3 \right) \frac{\partial^3}{\partial z^3} U_x(z). \end{aligned} \quad (14)$$

By using (14) Equations (12) reduce to the following form:

$$\left\{ \begin{aligned} &-\frac{1}{2} \left( -\frac{2c_{13}e_{31}}{c_{11}} + 2e_{33} \right) \left( \left( \frac{1}{2}h + H \right)^2 - \frac{1}{4}h^2 \right) \frac{\partial^3}{\partial z^3} \Phi(z) + \left( -\frac{1}{3} \left( \frac{2c_{13}^2}{c_{11}} - 2c_{33} \right) \left( \left( \frac{1}{2}h + H \right)^3 - \frac{1}{8}h^3 \right) - \right. \\ &\left. - \frac{1}{24} \left( -2\lambda - 4\mu + \frac{2\lambda^2}{\lambda + 2\mu} \right) h^3 \right) \frac{\partial^4}{\partial z^4} U_x(z) - W^2 \rho h U_x(z) - p(y, z) = 0; \\ &\left( -\frac{2e_{31}^2}{c_{11}} - 2g_{33} \right) \frac{\partial^2}{\partial z^2} \Phi(z) + \frac{\left( \frac{c_{13}e_{31}}{c_{11}} - e_{33} \right) \left( \left( \frac{1}{2}h + H \right)^2 - \frac{1}{4}h^2 \right) \frac{\partial^3}{\partial z^3} U_x(z)}{H} = 0. \end{aligned} \right. \quad (15)$$

General solutions of these linear differential equations can be found with common methods. Upper indices 1 and 2 will be used to mark the first and the second parts of the transducer. So,  $U^1(x)$  and  $\Phi^1(x)$  will be solutions for (13);  $U^2(x)$  and  $\Phi^2(x)$  will be solutions for (15).

Let us consider the conditions under which hard fixation and zero potential are given at the left and right ends of the transducer, and the equality of the fields is established at the junction of the ceramics with different polarization. Writing the boundary conditions in local coordinates for joints on edges of plate, we obtain the following set of twelve equations:

$$\begin{aligned}
U^1(0) = 0 & & U^1(L_1) = U^2(0) \\
M^1(0) = 0 & & M^1(L_1) = M^2(0) \\
\frac{1}{3}g_{11}\Phi_1(0) - \frac{4}{3}g_{11}\Phi(0) = 0 & & \Theta^1(L_1) = \Theta^2(0) \\
& & Q^1(L_1) = Q^2(0) \\
U^2(L_2) = 0 & & \frac{1}{3}V_t + \frac{1}{3}\Phi(L_1) + \frac{4}{3}\Phi_1(L_1) = \Phi^2(0) \\
M^2(L_2) = 0 & & \\
\Phi^2(L_2) = 0 & & \frac{1}{H}\left(\frac{1}{3}g_{11}\Phi_1(L_1) - \frac{4}{3}g_{11}\Phi(L_1)\right) = D_3(0)
\end{aligned} \tag{16}$$

The boundary conditions (16) allow us, using solution of equations (13), (15), to write down a system of linear algebraic equations and calculate the integration constant. Applied theory for the asymmetrical part (Fig. 3) can be obtained in same manner. Geometry and material properties were parametrized in Maple software to enable automation of numerical experiments.

#### 4. Numerical experiments

Numerical experiments were carried out with the help of the developed model of cylindrical bending of a three-layer piezoelement (Fig. 1b) with piecewise homogeneous piezoceramic layers. We estimated the influence of the ratio of the sizes of the first and second fragments and methods of fixing them at the ends on resonance frequencies, antiresonance, electromechanical coupling coefficient (EMCC) and output potential  $V_t$  at static load. So, these results are presented in Table 1 for a pinned piezoelement.

Table 1. Results for joint connection

$L_1$ , mm	$F_r$ , kHz	$F_a$ , kHz	EMCC	Electric potential, V
180	0.2274	0.2276	0.042	0.08334
160	0.2253	0.2277	0.145	0.6331
140	0.2206	0.2279	0.251	1.966
120	0.2133	0.2282	0.355	8.291
100	0.2049	0.2287	0.444	11.81
80	0.1971	0.2292	0.510	15.34
60	0.1910	0.2297	0.555	18.59
40	0.1873	0.2300	0.580	21.27
20	0.1862	0.2302	0.588	23.10

Tables 2 and 3 present results for a piezoelectric element rigidly fixed at the right and left ends, respectively, with the second line corresponding to the hinge fixation, the third fixing of the substrate only, and last fixing both the substrate and the piezoceramic layers.

Table 2. Right fixation

$L_1 = 100$ mm	$F_r$ , kHz	$F_a$ , kHz	EMCC	Electric potential, V
Joint	0.2049	0.2287	0.444	11.81
Substrate only	0.2961	0.2980	0.113	2.591
Ceramics and substrate	0.3554	0.3571	0.097	1.588

Table 3. Left fixation

$L_1 = 100$ mm	$F_r$ , kHz	$F_a$ , kHz	EMCC	Electric potential, V
Joint	0.2049	0.2287	0.444	0.2287
Substrate only	0.2736	0.3045	0.439	0.3045
Ceramics and substrate	0.3185	0.3571	0.452	0.3571

## 5. Conclusions

Presented tools and models can be used for analysis of electric elastic materials in different types of transducers, including energy harvesting devices. Due to greater output voltage and wider bandwidth such devices are more effective than uniformly polarized transducers. In some cases, models can be reduced to simplified uniformly polarized blocks and further to theoretical solutions.

Numerical experiments have shown that pivoting of the piezoelectric element is most preferable. The output potential and EMCC increases with the decrease in the relative size of the first fragment, but it is obvious that the capacity decreases.

**Acknowledgements.** This research was supported by grant RFBR number 16-01-00354 A.

## References

- [1] Gaudenzi P. *Smart Structures: Physical Behavior, Mathematical Modeling and Applications*. New York: John Wiley & Sons; 2009.
- [2] Chopra I. Review of state of art of smart structures and integrated systems. *AIAA J*. 2002;40(11): 2145-2187.
- [3] Chebanenko VA, Akopyan VA, Parinov IA. Piezoelectric Generators and Energy Harvesters: Modern State of the Art. In: Parinov IA. (ed.) *Piezoelectrics and Nanomaterials: Fundamentals, Developments and Applications*. New York: Nova Science Publishers; 2015. p.243-277.
- [4] Ray MCH, Rao KM, Samanta B. Exact solution for static analysis of an intelligent structure under cylindrical bending. *Comput. Struct*. 1993;47(6): 1031-1042.
- [5] Heyliger PR, Brooks SB. Free vibration of piezoelectric laminates in cylindrical bending. *Int J Solids Struct*. 1995;32(20): 2945-2960.
- [6] Sung CK, Chen TF, Chen SG. Piezoelectric modal sensor/actuator design for monitoring/generating flexural and torsional vibrations of cylindrical shells. *J Sound Vib*. 1996;118(1): 48-55.
- [7] Saravanos DA, Heyliger PR. Mechanics and computational models for laminated piezoelectric beams, plates, and shells. *Appl Mech Rev*. 1999;52(10): 305-320.
- [8] Allik H, Hughes TJR. Finite element method for piezoelectric vibration. *Int J Numer Methods Eng*. 1970;2(2): 151-157.
- [9] Benjeddou A. Advances in piezoelectric finite element modeling of adaptive structural elements: a survey. *Computers & Structures*. 2000;76(1-3): 347-363.
- [10] Sheikh AH, Topdar P, Halder S. An appropriate FE model for through thickness variation of displacement and potential in thin/moderately thick smart laminates. *Compos Struct*. 2001;51(4):401-409.
- [11] Kogl M, Bucalem ML. Analysis of smart laminates using piezoelectric MITC plate and shell elements. *Comput Struct*. 2005;83(15-16): 1153-1163.
- [12] Benjeddou A, Trindade MA, Ohayon RA. A unified beam finite element model for extension and shear piezoelectric actuation mechanisms. *J Intell Mater Syst Struct*. 1997;8(12): 1012-1025.

- [13] Maurini C, Pouget J, Dell'Isola F. Extension of the Euler–Bernoulli model of piezoelectric laminates to include 3D effects via a mixed approach. *Computers & structures*. 2006;84(22-23): 1438-1458.
- [14] Soloviev AN, Chebanenko VA, Parinov IA. Mathematical Modelling of Piezoelectric Generators on the Base of the Kantorovich Method. In: Altenbach H, Carrera E, Kulikov G. (eds.) *Analysis and Modelling of Advanced Structures and Smart Systems*. Singapore: Springer; 2018. p.227-258.
- [15] Kapuria S, Kumari P, Nath JK. Efficient modeling of smart piezoelectric composite laminates: a review. *Acta Mechanica*. 2010;214(1-2): 31-48.
- [16] Trindade MA, Benjeddou A. Refined sandwich model for the vibration of beams with embedded shear piezoelectric actuators and sensors. *Computers & Structures*. 2008;86(9): 859-869.
- [17] Beheshti-Aval SB, Lezgy-Nazargah M. Coupled refined layerwise theory for dynamic free and forced response of piezoelectric laminated composite and sandwich beams. *Meccanica*. 2013;48(6): 1479-1500.
- [18] Lezgy-Nazargah M, Vidal P, Polit O. An efficient finite element model for static and dynamic analyses of functionally graded piezoelectric beams. *Composite Structures*. 2013;104: 71-84.
- [19] Beheshti-Aval SB, Shahvaghari-Asl S, Lezgy-Nazargah M, Noori M. A finite element model based on coupled refined high-order global-local theory for static analysis of electromechanical embedded shear-mode piezoelectric sandwich composite beams with various widths. *Thin-Walled Structures*. 2013;72: 139-163.
- [20] Soloviev AN, Oganessian PA, Skaliukh AS, Duong LV, Gupta VK, Panfilov IA. Comparison Between Applied Theory and Finite Element Method for Energy Harvesting Non-homogeneous Piezoelements Modeling. In: Parinov IA, Chang SH, Jani MA. (eds.) *Advanced Materials Techniques, Physics, Mechanics and Applications*. Springer Proceedings in Physics book series (SPPHY, volume 173). Cham: Springer; 2017. p.473-484.
- [21] Belokon AV, Eremeyev VA, Nasedkin AV, Solov'yev AN. Partitioned schemes of the finite element method for dynamic problems of acoustoelectroelasticity. *Journal of Applied Mathematics and Mechanics*. 2000;64(3): 367-377.
- [22] Soloviev AN, Oganessian PA, Lupeiko TG, Kirillova EV, Chang S-H, Yang C-D. Modeling of Non-uniform Polarization for Multi-layered Piezoelectric Transducer for Energy Harvesting Devices. *Advanced Materials: Manufacturing, Physics, Mechanics and Applications*. Springer Proceedings in Physics book series (SPPHY, volume 175). Cham: Springer; 2016. p.651-659.
- [23] Vatulian AO, Getman IP, Lapnitskaya NB. About the bending of piezoelectric bimorph plate. *Applied Mechanics*. 1991;27(10): 101-105.
- [24] Vatul'yan AO, Rynkova AA. Flexural Vibrations of a piezoelectric bimorph with a Cut Internal Electrode. *Journal of Applied Mechanics and Technical Physics*. 2001;42(1): 164-168.

# BOUNDARY ELEMENT TIME-HARMONIC ANALYSIS OF 3D LINEAR PIEZOELECTRIC SOLIDS

L.A. Igumnov, I.P. Markov\*, A.V. Boev

Research Institute for Mechanics, National Research Lobachevsky State University of Nizhny Novgorod, 23,  
bldg. 6, Gagarin Ave, Nizhny Novgorod, 603950, Russia

\*e-mail: markov@mech.unn.ru

**Abstract.** In this work, a boundary element method (BEM) is applied for time-harmonic analysis of three-dimensional linear piezoelectric solids. Coupled frequency domain boundary value problems of the linear theory of piezoelectricity are considered assuming zero initial conditions, in the absence of the body forces and free electric charges. The elastic and electric variables are combined into the extended vectors and tensors. Proposed boundary element approach employs regularized weakly singular frequency domain boundary integral equations (BIEs) for the extended displacements. A standard collocation procedure for the mixed boundary elements is used. Integral expressions of the three-dimensional frequency domain dynamic piezoelectric fundamental solutions are employed. Results of the boundary-element analysis of a test problem are provided to validate the proposed BEM formulation.

**Keywords:** piezoelectricity, boundary element method, time-harmonic analysis, fundamental solutions

## 1. Introduction

Piezoelectric materials show two kinds of coupling effects and are extensively used to convert energy between two different forms: electric and mechanic. The direct effect consists in the ability to accumulate electric charge as a response to applied mechanical loads; the converse effect is characterized by the ability to produce mechanical deformation when electric loads are applied. Piezoelectric materials proved to be indispensable and very effective in many engineering applications such as vibration-based energy harvesters [1–3], microelectromechanical systems devices [4,5], active damping in structural vibrations, acoustic noise suppression, etc. To utilize the potential of piezoelectric structures subjected to transient dynamic or time-harmonic loadings to full extent it is essential to properly model their coupled behavior with reliable numerical method.

Various numerical techniques, such as Finite Difference Method (FDM) or Finite Element Method (FEM), can be employed to study dynamic behavior of complex piezoelectric structures. Among them is Boundary Element Method, a well-known boundary integral equations based method. Compared to the domain-based numerical methods like FDM and FEM, BEM has the distinct advantage of unknown field variables being located only on the boundary of the domain under consideration. This feature leads to the lack of necessity to mesh the interior of the domain, which results in the smaller number of unknowns in the discrete model.

The development of conventional direct boundary element procedure for transient dynamic and time-harmonic problems in linear piezoelectric solids as usual relies on reduction of the boundary value problems to a corresponding system of boundary integral

equations with utilization of the reciprocal theorem and fundamental solutions. It is known, that the dynamic fundamental solutions and the corresponding stress fields for generally anisotropic piezoelectric materials are not available in the closed-form expressions. Various approaches for numerical and semi-analytical treatment of the static anisotropic elastic and piezoelectric fundamental solutions were proposed (e.g. [6–13]). Review of the available scientific literature reveals only a few BEM implementations concerning time-harmonic analysis for piezoelectric solids [14–18] including those based on Dual Reciprocity approach, which utilizes only the static fundamental solution.

In this paper, a formulation of the frequency domain direct boundary element approach is present and applied for the time-harmonic analysis of three-dimensional (3D) homogeneous anisotropic and linear piezoelectric solids. The boundary integral equations are regularized employing the static part of the fundamental solution. The frequency domain displacement fundamental solutions for linear piezoelectric material are expressed in an integral form. Mixed boundary elements and standard collocation procedure are used for the spatial discretization. The versatility and reliability of the proposed formulation is demonstrated by numerical examples for piezoelectric solid under complex electro-mechanical loading. The obtained boundary element results are compared with those obtained by a finite element method.

## 2. Problem statement

Consider a three-dimensional homogeneous finite anisotropic and piezoelectric solid  $\Omega \in R^3$  with smooth boundary  $\Gamma = \partial\Omega$ . Piezoelectric linear constitutive equations are given as follows [19,20]:

$$\sigma_{ij} = C_{ijkl}^E s_{kl} - e_{ijk} E_k, \quad i, j, k, l = \overline{1, 3}, \quad (1)$$

$$D_i = e_{ikl} s_{kl} + \varepsilon_{ik} E_k, \quad (2)$$

where  $\sigma_{ij}$  is the stress tensor,  $D_i$  are the electric displacements,  $s_{kl}$  is the strain tensor and  $E_k$  is the electric field. The tensors  $C_{ijkl}^E$ ,  $e_{ijk}$  and  $\varepsilon_{ik}$  denote, respectively, the elastic stiffness constants, the piezoelectric coupling coefficients and the dielectric properties.

For the generally anisotropic piezoelectric material, the following symmetry conditions are satisfied:

$$C_{ijkl}^E = C_{klij}^E = C_{jikl}^E = C_{ijlk}^E, \quad (3)$$

$$e_{ijk} = e_{ikj}, \quad (4)$$

$$\varepsilon_{ij} = \varepsilon_{ji}. \quad (5)$$

Applying the quasi-electrostatic assumption, the strain – displacement and the electric field – electric potential relationships are written as

$$s_{ij} = \frac{1}{2}(u_{i,j} + u_{j,i}), \quad (6)$$

$$E_i = -\phi_{,i}, \quad (7)$$

where  $u_i$  are the elastic displacements and  $\phi$  is the electric potential.

In the absence of applied volume forces and free electrical charges the equilibrium equations and the electrical balance equations (the electrostatic equations) in the time domain are given as follows

$$\sigma_{ij,j} = \rho \ddot{u}_i, \quad (8)$$

$$D_{i,i} = 0, \quad (9)$$

where  $\rho$  is the mass density.

It is practical to combine the elastic and electric variables into the extended vectors and matrices using the extended notation [6] as follows

$$U_k = \begin{cases} u_k, & k = \overline{1,3}, \\ \phi, & k = 4, \end{cases} \quad (10)$$

$$S_{kl} = \begin{cases} s_{kl}, & k, l = \overline{1,3}, \\ -E_l, & k = 4, l = \overline{1,3}, \end{cases} \quad (11)$$

$$\Sigma_{ij} = \begin{cases} \sigma_{ij}, & i, j = \overline{1,3}, \\ D_i, & i = \overline{1,3}, j = 4, \end{cases} \quad (12)$$

$$C_{ijkl} = \begin{cases} C_{ijkl}^E, & i, j, k, l = \overline{1,3}, \\ e_{ij}, & i, l, j = \overline{1,3}, k = 4, \\ e_{ikl}, & i, l, k = \overline{1,3}, j = 4, \\ -\varepsilon_{il}, & i, l = \overline{1,3}, k, j = 4. \end{cases} \quad (13)$$

Considering the symmetry conditions (3) – (5) we can write the following relationship for the extended piezoelectricity matrix  $C_{ijkl}$ :

$$C_{ijkl} = C_{lkji}. \quad (14)$$

Taking into account the extended notation (10) – (13) we rewrite the time-domain equations of motion of a linear piezoelectric solid in a simplified form in terms of the extended displacements:

$$C_{ijkl} U_{k,il} = \rho \delta_{jk}^* \ddot{U}_k, \quad i, l = \overline{1,3}, \quad j, k = \overline{1,4}, \quad (15)$$

$$\delta_{jk}^* = \begin{cases} \delta_{jk}, & j, k = \overline{1,3}, \\ 0, & \text{otherwise.} \end{cases} \quad (16)$$

We consider vanishing initial conditions and the following boundary conditions:

$$U_i(\mathbf{x}, t) = \dot{U}_i(\mathbf{x}, t) = 0, \quad t \leq 0, \quad (17)$$

$$U_i(\mathbf{x}, t) = U_i^*(\mathbf{x}, t), \quad \mathbf{x} \in \Gamma_U, \quad (18)$$

$$T_i(\mathbf{x}, t) = T_i^*(\mathbf{x}, t), \quad \mathbf{x} \in \Gamma_T, \quad (19)$$

where  $\Gamma_U$  is the part of  $\Gamma$  on which the extended displacements  $U_i(\mathbf{x}, t)$  have the prescribed values  $U_i^*$  and  $\Gamma_T$  is the part of  $\Gamma$  on which the extended tractions  $T_k$ :

$$T_k = \begin{cases} t_k = \sigma_{ik} n_k, & k = \overline{1,3}, \\ D_n = D_i n_i, & k = 4, \end{cases} \quad (20)$$

have the prescribed values  $T_i^*$  with  $n_i$  being the outward unit normal vector.

For the prescribed frequency  $\omega$  and zero initial conditions (17), we rewrite the governing equations (15) and boundary conditions (18) – (19) in the frequency domain:

$$C_{ijkl} \bar{U}_{k,il} + \rho \omega^2 \delta_{jk}^* \bar{U}_k = 0, \quad i, l = \overline{1,3}, \quad j, k = \overline{1,4}, \quad (21)$$

$$\bar{U}_i(\mathbf{x}, \omega) = \bar{U}_i^*(\mathbf{x}, \omega), \quad \mathbf{x} \in \Gamma_U, \quad (22)$$

$$\bar{T}_i(\mathbf{x}, \omega) = \bar{T}_i^*(\mathbf{x}, \omega), \quad \mathbf{x} \in \Gamma_T, \quad (23)$$

where overbar denotes a variable in the frequency domain.

### 3. BEM formulation

In the present work, we use the frequency domain direct BEM approach to solve the linear boundary-value problem defined in equations (21) – (23). To solve the prescribed boundary-value problem first it is needed to be reformulated as boundary integral equations. For the extended displacement in the frequency domain, the following system of non-strongly

singular BIEs can be obtained using the static singular part of the piezoelectric traction fundamental solution:

$$\int_{\Gamma} \left[ \bar{U}_k(\mathbf{y}, \omega) \bar{h}_{jk}(\mathbf{y}, \mathbf{x}, \omega) - \bar{U}_k(\mathbf{x}, \omega) h_{jk}^S(\mathbf{y}, \mathbf{x}, \omega) \right] d\Gamma(\mathbf{y}) - \int_{\Gamma} \bar{T}_k(\mathbf{y}, \omega) \bar{g}_{jk}(\mathbf{y}, \mathbf{x}, \omega) d\Gamma(\mathbf{y}) = 0, \quad (24)$$

where  $\bar{g}_{jk}$ ,  $\bar{h}_{jk}$  and  $h_{jk}^S$  are the frequency domain dynamic piezoelectric extended displacement and traction fundamental solutions and the static part of traction fundamental solution, respectively;  $\mathbf{x} \in \Gamma$  is the source point and  $\mathbf{y}$  is the field point. All integrals in the regularized boundary integral equations (24) have the  $O(1/r)$  singularity.

For numerical solving the BIEs (24), we follow the standard boundary element procedure and start with the discretization of the boundary  $\Gamma$ . Geometry of the boundary is approximated with the quadrangular boundary elements with quadratic shape functions. To describe the behavior of the extended displacements and tractions on the boundary elements we implement the mixed representation approach: for the displacements, linear interpolation functions are adopted and tractions are approximated by constant functions. After collocation procedure a system of complex-valued linear algebraic equations is obtained for the prescribed frequency  $\omega$ :

$$[\bar{\mathbf{A}}(\omega)] \{ \bar{\mathbf{p}}(\omega) \} = \{ \bar{\mathbf{f}}(\omega) \}, \quad (25)$$

where  $[\bar{\mathbf{A}}(\omega)]$  is the rearranged system matrix according to the boundary conditions,  $\{ \bar{\mathbf{f}}(\omega) \}$  and  $\{ \bar{\mathbf{p}}(\omega) \}$  are the vectors, containing the known and unknown boundary data.

#### 4. Frequency domain piezoelectric fundamental solutions

For homogeneous generally anisotropic linear piezoelectric solids, dynamic fundamental solutions are not available in an explicit form. Representations of the fundamental solutions in the frequency domain can be separated into singular (static, denoted with superscript "S") and regular (dynamic, denoted with superscript "D") parts as

$$\bar{g}_{ij}(\mathbf{y}, \mathbf{x}, \omega) = \bar{g}_{ij}(\mathbf{r}, \omega) = g_{ij}^S(\mathbf{r}) + \bar{g}_{ij}^D(\mathbf{r}, \omega), \quad (26)$$

$$\bar{h}_{ij}(\mathbf{y}, \mathbf{x}, \omega) = \bar{h}_{ij}(\mathbf{r}, \omega) = h_{ij}^S(\mathbf{r}) + \bar{h}_{ij}^D(\mathbf{r}, \omega), \quad (27)$$

with  $\mathbf{r} = \mathbf{y} - \mathbf{x}$ ,  $r = |\mathbf{r}|$ .

Using the approach based on the application of the Radon transform [21,22] the expressions for the dynamic and static parts of the piezoelectric displacement fundamental solutions are given as follows [11]:

$$\bar{g}_{jp}^D(\mathbf{r}, \omega) = \frac{i}{8\pi^2} \int_{\substack{|\mathbf{n}|=1 \\ \mathbf{n} \cdot \mathbf{r} > 0}} \sum_{m=1}^Q \frac{k_m \bar{P}_{jp}^m(\mathbf{n})}{\rho c_m^2} e^{ik_m |\mathbf{n} \cdot \mathbf{r}|} dS(\mathbf{n}), \quad j, p = \overline{1, 4}, \quad (28)$$

$$g_{jp}^S(\mathbf{r}) = \frac{1}{8\pi^2 r} \int_{|\mathbf{d}|=1} \Gamma_{jp}^{-1}(\mathbf{d}) dL(\mathbf{d}), \quad (29)$$

here

$$\bar{P}_{jp}^m = \begin{cases} P_{jp}^m, & j, p = \overline{1, 3}, \\ -\frac{\Gamma_{k4} P_{jk}^m}{\Gamma_{44}}, & j = \overline{1, 3}, p = 4, \\ \frac{\Gamma_{4k} P_{kl}^m \Gamma_{l4}}{\Gamma_{44}^2}, & j = p = 4, \end{cases} \quad (30)$$

$$P_{jp}^m = \frac{A_{jp}^m}{A_{ii}^m}, \quad A_{jp}^m = \text{adj}(L_{jp} - \rho c_m^2 \delta_{jp}), \quad L_{jp}(\mathbf{n}) = \Gamma_{jp}(\mathbf{n}) - \frac{\Gamma_{j4}(\mathbf{n})\Gamma_{4p}(\mathbf{n})}{\Gamma_{44}(\mathbf{n})}, \quad (31)$$

$$c_m = \sqrt{\frac{\lambda_m}{\rho}}, \quad k_m = \frac{\omega}{c_m}, \quad \Gamma_{ij}(\mathbf{d}) = C_{kijl} d_k d_l, \quad \Gamma_{ij}(\mathbf{n}) = C_{kijl} n_k n_l, \quad (32)$$

where  $\lambda_m$  are the  $Q$  distinct eigenvalues of  $L_{jp}$ .

The variables involved in the definition of domains of integration (see Fig. 1), i.e. a half of a unit sphere for the dynamic part and a unit circumference for the static part are defined as follows:

$$dL(\mathbf{d}(\varphi)) \in D^S = \{0 \leq \varphi \leq 2\pi\}, \quad dS(\mathbf{n}(b, \varphi)) \in D^D = \{0 \leq b \leq 1; 0 \leq \varphi \leq 2\pi\}, \quad (33)$$

$$\mathbf{n}(b, \varphi) = \sqrt{1-b^2} \mathbf{d} + b \mathbf{e}, \quad \mathbf{e} = \mathbf{r}/r, \quad \mathbf{e} = [e_1, e_2, e_3], \quad (34)$$

$$\mathbf{d}(\varphi) = \frac{[e_2 \cos \varphi + e_1 e_3 \sin \varphi, -e_1 \cos \varphi + e_2 e_3 \sin \varphi, -(1-e_3^2) \sin \varphi]}{\sqrt{1-e_3^2}}. \quad (35)$$

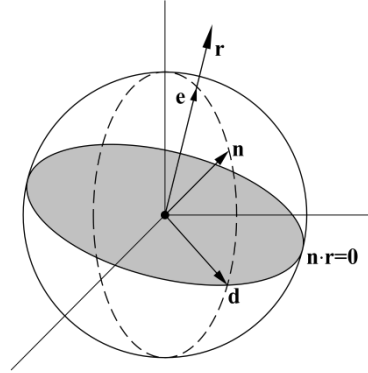


**Fig. 1.** Geometry of  $\mathbf{r}$ ,  $\mathbf{e}$ ,  $\mathbf{n}$  and  $\mathbf{d}$

For the unit normal vector to the boundary  $n_i(\mathbf{y})$  at the field point  $\mathbf{y}$ , the piezoelectric traction fundamental solutions are defined by

$$\bar{h}_{jp}(\mathbf{y}, \mathbf{x}, \omega) = C_{ijkl} \bar{g}_{kp,l}(\mathbf{y}, \mathbf{x}, \omega) n_i(\mathbf{y}), \quad j, p = \overline{1, 4}. \quad (36)$$

## 5. Numerical example

Our test model involves rectangular piezoelectric solid as shown in Fig. 2. The solid is clamped at  $x_3 = 0$  m. On the surface  $x_2 = 0.2$  m the electric potential is assumed to be zero. Two cases of harmonic excitation on the surface  $x_3 = 1$  m is considered: traction  $t_3 = -1 \cdot 10^9$  Pa and electric potential  $\phi = 0$  V (case A), traction  $t_3 = -1 \cdot 10^9$  Pa and electric displacements  $D_n = 1$  C/m<sup>2</sup> (case B). Other surfaces are free of the extended tractions. For both loading cases, two frequencies are considered:  $\omega_1 = 10000$  rad/s and  $\omega_2 = 20000$  rad/s.

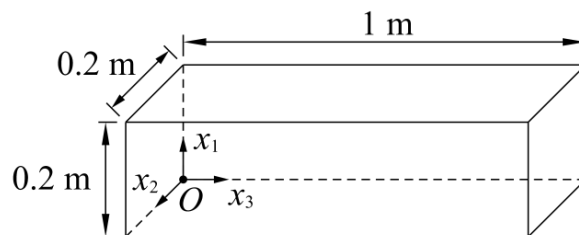


**Fig. 2.** A rectangular piezoelectric solid

PVDF is chosen as a piezoelectric material, which has the mass density  $\rho = 1780 \text{ kg/m}^3$  and the following material parameters:

$$\mathbf{C}^E = \begin{bmatrix} 238 & 3.98 & 2.19 & 0 & 0 & 0 \\ 3.98 & 23.6 & 1.92 & 0 & 0 & 0 \\ 2.19 & 1.92 & 10.6 & 0 & 0 & 0 \\ 0 & 0 & 0 & 2.15 & 0 & 0 \\ 0 & 0 & 0 & 0 & 4.4 & 0 \\ 0 & 0 & 0 & 0 & 0 & 6.43 \end{bmatrix} \text{ GPa}, \quad (37)$$

$$\boldsymbol{\varepsilon} = \begin{bmatrix} 1.1068 & 0 & 0 \\ 0 & 1.0607 & 0 \\ 0 & 0 & 1.0607 \end{bmatrix} \cdot 10^{-10} \text{ C/Vm}, \quad (38)$$

$$\mathbf{e} = \begin{bmatrix} 0 & 0 & 0 & 0 & -0.010 \\ 0 & 0 & 0 & -0.01 & 0 & 0 \\ -0.13 & -0.14 & -0.28 & 0 & 0 & 0 \end{bmatrix} \text{ C/m}^2. \quad (39)$$

The solid is uniformly meshed with 1408 boundary elements in total. For loading case A, Figs. 3 – 6 and for loading case B, Figs. 7 – 10 show a comparison of the obtained BEM solutions and results of FEM analyses for the displacements  $u_2$  and  $u_3$ , electric potential  $\phi$  and electric displacements  $D_n$ . Results for the  $u_2$ ,  $u_3$ ,  $\phi$  are calculated along the line  $(0.1, 0, x_3)$  and for the  $D_n$  along the line  $(0.1, 0.2, x_3)$ .

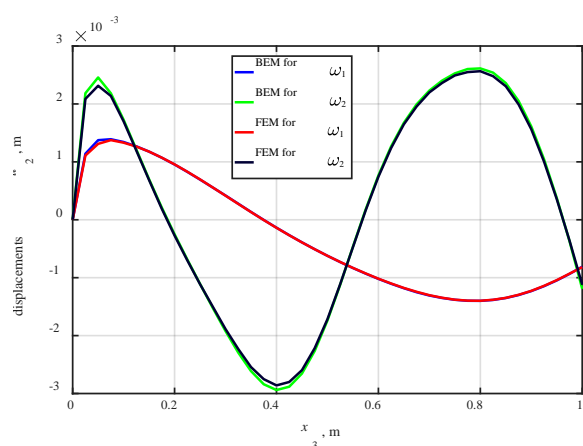


**Fig. 3.** Displacements  $u_2(0.1, 0, x_3)$

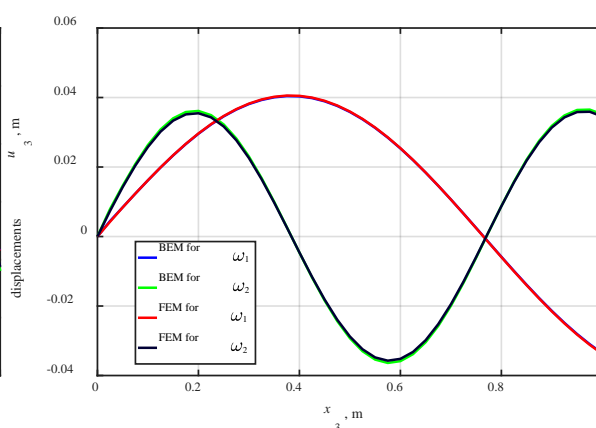


**Fig. 4.** Displacements  $u_3(0.1, 0, x_3)$

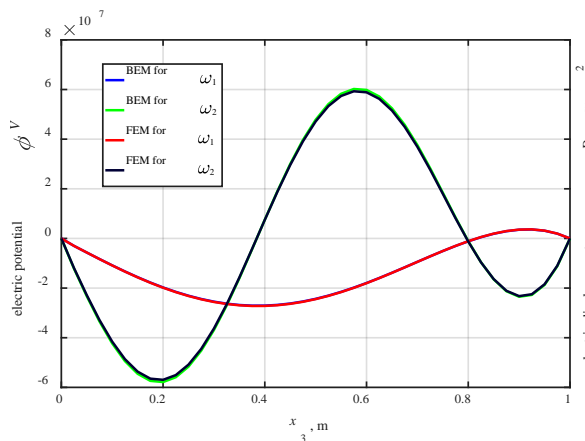


**Fig. 5.** Electric potential  $\phi(0.1, 0, x_3)$

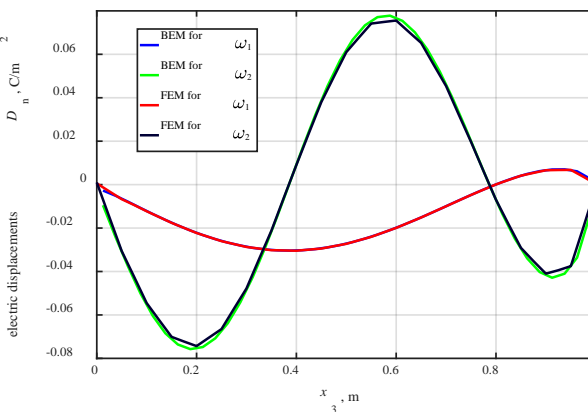


**Fig. 6.** Electric displacements  $D_n(0.1, 0.2, x_3)$

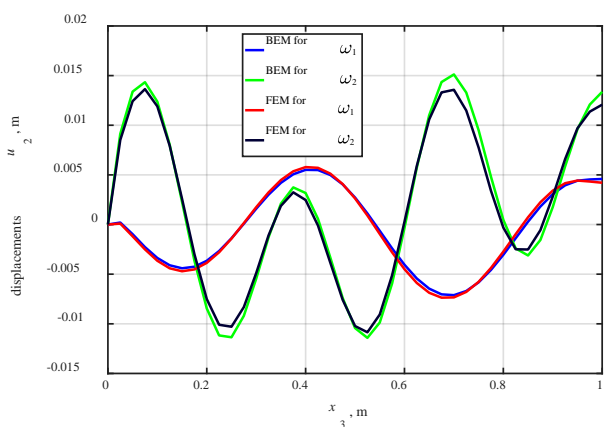


**Fig. 7.** Displacements  $u_2(0.1, 0, x_3)$

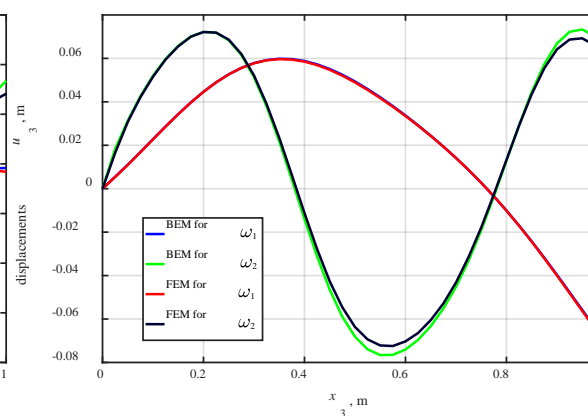


**Fig. 8.** Displacements  $u_3(0.1, 0, x_3)$

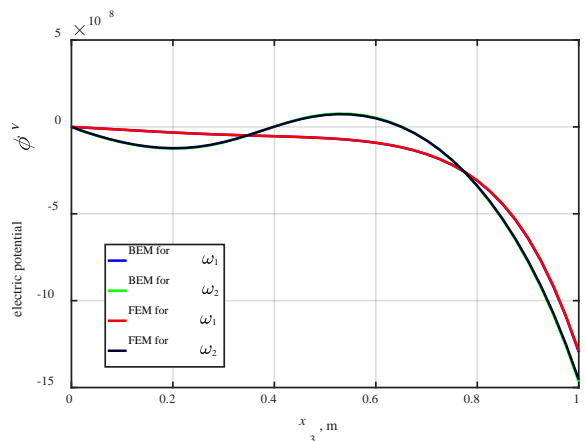


**Fig. 9.** Electric potential  $\phi(0.1, 0, x_3)$

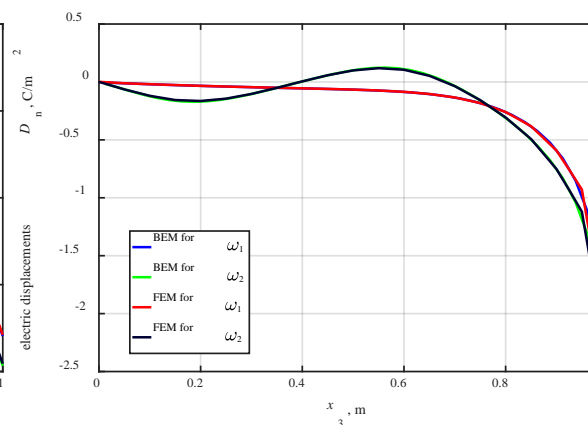


**Fig. 10.** Elect. displacements  $D_n(0.1, 0.2, x_3)$

**6. Conclusions**

The frequency domain boundary element formulation based on non-strongly singular displacement BIEs for homogeneous three-dimensional linear piezoelectric solids is presented. Mixed boundary elements are used for the spatial discretization. Integral expressions of the piezoelectric fundamental solutions are adopted. The versatility and reliability of the present boundary element formulation for time-harmonic piezoelectric

analysis is demonstrated by numerical examples. Obtained solutions show good agreement with the finite element results.

**Acknowledgements.** *The reported study was funded by Russian Foundation for Basic Research (RFBR), according to the research project No. 16-38-60097 mol\_a\_dk.*

## References

- [1] Arroyo E, Badel A, Formosa F, Wu Y, Qiu J. Comparison of electromagnetic and piezoelectric vibration energy harvesters: Model and experiments. *Sensors and Actuators A: Physical*. 2012;183: 148-156. Available from: doi.org/10.1016/j.sna.2012.04.033.
- [2] Erturk A, Inman D. Piezoelectric energy harvesting. Chichester: Wiley; 2011. Available from: doi.org/10.1002/9781119991151.
- [3] Siddique A, Mahmud S, Heyst B. A comprehensive review on vibration based micro power generators using electromagnetic and piezoelectric transducer mechanisms. *Energy Conversion and Management*. 2015;106: 728-747. Available from: doi.org/10.1016/j.enconman.2015.09.071.
- [4] Trolier-McKinstry S, Muralt P. Thin Film Piezoelectrics for MEMS. *Journal of Electroceramics*. 2004;12(1/2): 7-17. Available from: doi.org/10.1023/b:jecr.0000033998.72845.51.
- [5] Smith G, Pulskamp J, Sanchez L, Potrepka D, Proie R, Ivanov T et al. PZT-Based Piezoelectric MEMS Technology. *Journal of the American Ceramic Society*. 2012;95(6): 1777-1792. Available from: doi.org/10.1111/j.1551-2916.2012.05155.x.
- [6] Barnett D, Lothe J. Dislocations and line charges in anisotropic piezoelectric insulators. *physica status solidi (b)*. 1975;67(1): 105-111. Available from: doi.org/10.1002/pssb.2220670108.
- [7] Ting T. The three-dimensional elastostatic Green's function for general anisotropic linear elastic solids. *The Quarterly Journal of Mechanics and Applied Mathematics*. 1997;50(3): 407-426. Available from: doi.org/10.1093/qjmam/50.3.407.
- [8] Wu K. Generalization of the Stroh Formalism to 3-Dimensional Anisotropic Elasticity. *Journal of Elasticity*. 1998;51(3): 213-225. Available from: doi.org/10.1023/a:1007523219357.
- [9] Nakamura G, Tanuma K. A formula for the fundamental solution of anisotropic elasticity. *The Quarterly Journal of Mechanics and Applied Mathematics*. 1997;50(2): 179-194. Available from: doi.org/10.1093/qjmam/50.2.179.
- [10] Pan E, Tonon F. Three-dimensional Green's functions in anisotropic piezoelectric solids. *International Journal of Solids and Structures*. 2000;37(6): 943-958. Available from: doi.org/10.1016/s0020-7683(99)00073-6.
- [11] Wang C, Zhang C. 3-D and 2-D Dynamic Green's functions and time-domain BIEs for piezoelectric solids. *Engineering Analysis with Boundary Elements*. 2005;29(5): 454-465. Available from: doi.org/10.1016/j.enganabound.2005.01.006.
- [12] Shiah Y, Tan C, Wang C. Efficient computation of the Green's function and its derivatives for three-dimensional anisotropic elasticity in BEM analysis. *Engineering Analysis with Boundary Elements*. 2012;36(12): 1746-1755. Available from: doi.org/10.1016/j.enganabound.2012.05.008.
- [13] Xie L, Zhang C, Hwu C, Sladek J, Sladek V. On two accurate methods for computing 3D Green's function and its first and second derivatives in piezoelectricity. *Engineering Analysis with Boundary Elements*. 2015;61: 183-193. Available from: doi.org/10.1016/j.enganabound.2015.07.014.
- [14] Hill L, Farris T. Three-Dimensional Piezoelectric Boundary Element Method. *AIAA Journal*. 1998;36(1): 102-108. Available from: doi.org/10.2514/2.358.

- [15] Kogl M, Gaul L. Dual reciprocity Boundary Element Method for three-dimensional problems of dynamic piezoelectricity. In: Brebbia CA, Power H (eds.) *WIT Transactions on Modelling and Simulation*. Southampton: WIT Press; 1999;25. p.537-548. Available from: <https://www.witpress.com/elibrary/wit-transactions-on-modelling-and-simulation/25/6054> [Accessed 26th March 2019].
- [16] Kogl M, Gaul L. A boundary element method for transient piezoelectric analysis. *Engineering Analysis with Boundary Elements*. 2000;24(7-8): 591-598. Available from: [doi.org/10.1016/s0955-7997\(00\)00039-4](https://doi.org/10.1016/s0955-7997(00)00039-4).
- [17] Denda M, Araki Y. 2-D general anisotropic and piezoelectric time-harmonic BEM for eigenvalue analysis. In: Smyth AW (ed.) *Proceedings of the 15th ASCE Engineering Mechanics Conference*. New York: Columbia University; 2002; p.77-84.
- [18] Gaul L, Kogl M, Wagner M. *Boundary element methods for engineers and scientists*. Berlin: Springer; 2003.
- [19] Parton VZ, Kudryavtsev BA. *Electrocmagnetoelasticity*. New York: Gordon and Breach Science Publishers; 1988.
- [20] Tiersten HF. *Linear Piezoelectric Plate Vibrations*. Boston, MA: Springer US; 1969.
- [21] Wang C, Achenbach J. Elastodynamic fundamental solutions for anisotropic solids. *Geophysical Journal International*. 1994;118(2): 384-392. Available from: [doi.org/10.1111/j.1365-246x.1994.tb03970.x](https://doi.org/10.1111/j.1365-246x.1994.tb03970.x).
- [22] Wang C, Achenbach J. Three-Dimensional Time-Harmonic Elastodynamic Green's Functions for Anisotropic Solids. *Proceedings of the Royal Society A: Mathematical, Physical and Engineering Sciences*. 1995;449(1937): 441-458. Available from: [doi.org/10.1098/rspa.1995.0052](https://doi.org/10.1098/rspa.1995.0052).

### **Submission of papers:**

Manuscript should be submitted (**both MS Word and PDF**) by e-mail to: **mpmjournal@spbstu.ru**

After a confirmation of the paper acceptance, the authors should send the signed hard copy of the "Transfer of Copyright Agreement" form (available at <http://www.mpm.spbstu.ru> section "Authors") by regular post to "Materials Physics and Mechanics" editorial office:

*Periodicals Editorial Office, Institute of Advanced Manufacturing Technologies, Peter the Great St.Petersburg Polytechnic University, Polytechnicheskaya, 29, St.Petersburg 195251, Russia.*

The scanned copy of the signed "Transfer of Copyright Agreement" should be send by e-mail to: **mpmjournal@spbstu.ru**.

### **Filetype:**

Authors are invited to send their manuscripts **as MS Word file with PDF format copy**.

MS Word file should be prepared according to the general instructions bellow; we are kindly asking the authors to look through the detail instruction at: <http://www.mpm.spbstu.ru>.

### **Length:**

Papers should be limited to 30 typewritten pages (including Tables and Figures placed in the proper positions in the text).

### **Structure of the manuscript:**

**PAPER TITLE: CENTERED,**

**TIMES NEW ROMAN 14 BOLD, CAPITAL LETTERS**

**A.B. Firstauthor<sup>1</sup>, C.D. Secondauthor<sup>2\*</sup>** -Times New Roman 12, bold, centered

<sup>1</sup>Affiliation, address, country - Times New Roman 10, centered

\*e-mail: e-mail of the corresponding author - Times New Roman 10, centered

**Abstract.** Times New Roman 12 font, single line spacing. Abstract should not exceed 12 lines.

**Keywords:** please, specify paper keywords right after the abstract.

**Paper organization.** Use Times New Roman 12 font with single line spacing. Use *Italic* font in order to stress something; if possible, please, use **bold** for headlines only.

**Page numbering.** Please, do not use page numbering.

**Tables, Figures, Equations.** Please, see the sample file at <http://www.mpm.spbstu.ru> for more details.

### **References**

References should be subsequently numbered by Arabic numerals in square brackets, e.g. [1,3,5-9], following the sample style below:

[1] Koch CC, Ovid'ko IA, Seal S, Veprek S. *Structural Nanocrystalline Materials: Fundamentals and Applications*. Cambridge: Cambridge University Press; 2007.

[2] Hull D, Bacon DJ. *Introduction to Dislocations*. 5nd ed. Amsterdam: Butterworth-Heinemann; 2011 Available from: <https://www.sciencedirect.com/science/book/9780080966724?via%3Dihub> [Accessed 19th June 2018].

[3] Romanov AE, Vladimirov VI. Disclinations in crystalline solids. In: Nabarro FRN (ed.) *Dislocations in Solids*. Amsterdam: North Holland; 1992;9. p.191-402.

[4] Mukherjee AK. An examination of the constitutive equation for elevated temperature plasticity. *Materials Science and Engineering: A*. 2002;322(1-2): 1-22.

- [5] Soer WA, De Hosson JTM, Minor AM, Morris JW, Stach EA. Effects of solute Mg on grain boundary and dislocation dynamics during nanoindentation of Al–Mg thin films. *Acta Materialia*. 2004;52(20): 5783-5790.
- [6] Matzen ME, Bischoff M. A weighted point-based formulation for isogeometric contact. *Computer Methods in Applied Mechanics and Engineering*. 2016;308: 73-95. Available from: [doi.org/10.1016/j.cma.2016.04.010](https://doi.org/10.1016/j.cma.2016.04.010).
- [7] Joseph S, Lindley TC, Dye D. Dislocation interactions and crack nucleation in a fatigued near-alpha titanium alloy. To be published in *International Journal of Plasticity*. *Arxiv*. [Preprint] 2018. Available from: <https://arxiv.org/abs/1806.06367> [Accessed 19th June 2018].
- [8] Pollak W, Blecha M, Specht G. *Process for the production of molded bodies from silicon-infiltrated, reaction-bonded silicon carbide*. US4572848A (Patent) 1983.
- [9] Brogan C. *Experts build pulsed air rig to test 3D printed parts for low carbon engines*. Available from: <http://www.imperial.ac.uk/news/186572/experts-build-pulsed-test-3d-printed/> [Accessed 19th June 2018].

### **Правила подготовки статей:**

Рукопись (**английский язык, MS Word и копия PDF**) должна быть направлена в редакцию журнала по электронной почте: [mpmjournal@spbstu.ru](mailto:mpmjournal@spbstu.ru).

После подтверждения принятия статьи в печать, авторы должны отправить подписанные:

1. Соглашение о передаче авторских прав (<http://www.mpm.spbstu.ru>, раздел «Авторам»);
2. Экспертные заключения о том, что материалы статьи не содержат сведений, составляющих государственную тайну, и информацию, подлежащую экспортному контролю; по адресу:

*Россия, 195251, Санкт-Петербург, Политехническая, д. 29, Санкт-Петербургский политехнический университет Петра Великого, Институт передовых производственных технологий, Редакция периодических изданий.*

Скан-копии подписанных документов просим направить по электронной почте: [mpmjournal@spbstu.ru](mailto:mpmjournal@spbstu.ru)

### **Тип файла:**

Редакция принимает **файлы MS Word с копией в формате PDF**. Статья должна быть подготовлена в соответствии с настоящей инструкцией, мы просим авторов также следовать более подробным инструкциям на сайте журнала <http://www.mpm.spbstu.ru> в разделе «Авторам».

### **Длина статьи:**

Статья не должна превышать 30 страниц формата А4, включая Таблицы и Рисунки, размещенные непосредственно в соответствующих местах.

### **Общие правила оформления статьи:**

**НАЗВАНИЕ СТАТЬИ: ВЫРОВНЯТЬ ПО ЦЕНТРУ,**

**ШРИФТ, TIMES NEW ROMAN 14 BOLD, ЗАГЛАВНЫЕ БУКВЫ**

Автор(ы): **А.Б. Первыйавтор<sup>1</sup>, В.Г. Автор<sup>2\*</sup>** - шрифт Times New Roman 12, bold, по центру

<sup>1</sup>Наименование организации, адрес, страна - шрифт Times New Roman 10, по центру

\* e-mail автора, представившего статью - шрифт Times New Roman 10, по центру

**Аннотация.** Аннотация статьи составляет не более 12 строк. Используйте шрифт Times New Roman 12, одинарный межстрочный интервал.

**Ключевые слова:** укажите ключевые слова после аннотации.

**Как организовать текст статьи.** Используйте шрифт Times New Roman 12, одинарный межстрочный интервал. При необходимости выделить какую-либо информацию используйте *курсив*. Используйте **полужирный** шрифт только для заголовков и подзаголовков.

**Номера страниц.** Пожалуйста, не используйте нумерацию страниц

**Таблицы, Рисунки, Уравнения.** Подробные правила оформления данных элементов статьи приведены в инструкции на сайте журнала <http://www.mpm.spbstu.ru>

### **Литература**

Ссылки приводятся в тексте в квадратных скобках [1,3,5-9]. Стиль оформления ссылок:

[1] Koch CC, Ovid'ko IA, Seal S, Veprck S. *Structural Nanocrystalline Materials: Fundamentals and Applications*. Cambridge: Cambridge University Press; 2007.

[2] Hull D, Bacon DJ. *Introduction to Dislocations*. 5nd ed. Amsterdam: Butterworth-Heinemann; 2011 Available from: <https://www.sciencedirect.com/science/book/9780080966724?via%3Dihub> [Accessed 19th June 2018].

[3] Romanov AE, Vladimirov VI. Disclinations in crystalline solids. In: Nabarro FRN (ed.) *Dislocations in Solids*. Amsterdam: North Holland; 1992;9. p.191-402.

[4] Mukherjee AK. An examination of the constitutive equation for elevated temperature plasticity. *Materials Science and Engineering: A*. 2002;322(1-2): 1-22.

- [5] Soer WA, De Hosson JTM, Minor AM, Morris JW, Stach EA. Effects of solute Mg on grain boundary and dislocation dynamics during nanoindentation of Al–Mg thin films. *Acta Materialia*. 2004;52(20): 5783-5790.
- [6] Matzen ME, Bischoff M. A weighted point-based formulation for isogeometric contact. *Computer Methods in Applied Mechanics and Engineering*. 2016;308: 73-95. Available from: [doi.org/10.1016/j.cma.2016.04.010](https://doi.org/10.1016/j.cma.2016.04.010).
- [7] Joseph S, Lindley TC, Dye D. Dislocation interactions and crack nucleation in a fatigued near-alpha titanium alloy. To be published in *International Journal of Plasticity*. *Arxiv*. [Preprint] 2018. Available from: <https://arxiv.org/abs/1806.06367> [Accessed 19th June 2018].
- [8] Pollak W, Blecha M, Specht G. *Process for the production of molded bodies from silicon-infiltrated, reaction-bonded silicon carbide*. US4572848A (Patent) 1983.
- [9] Brogan C. *Experts build pulsed air rig to test 3D printed parts for low carbon engines*. Available from: <http://www.imperial.ac.uk/news/186572/experts-build-pulsed-test-3d-printed/> [Accessed 19th June 2018].

МЕХАНИКА И ФИЗИКА МАТЕРИАЛОВ

42 (2) 2019

Учредители: Санкт-Петербургский политехнический университет Петра Великого,

Институт проблем Машиноведения Российской академии наук

Издание зарегистрировано федеральной службой по надзору в сфере связи,  
информационных технологий и массовых коммуникаций (РОСКОМНАДЗОР),

свидетельство ПИ №ФС77-69287 от 06.04.2017 г.

Редакция журнала

Профессор, д.т.н., академик РАН, А.И. Рудской – главный редактор

Профессор, д.ф.-м.н., член-корр. РАН, Д.А. Индейцев – главный редактор

Профессор, д.ф.-м.н. И.А. Овидько (1961 - 2017) – основатель и почетный редактор

Профессор, д.ф.-м.н. А.Л. Колесникова – ответственный редактор

Доцент, к.т.н. А.С. Немов – ответственный редактор

А.Ю. Зобачева, к.т.н. – выпускающий редактор

Л.И. Гузилова – редактор, корректор

Телефон редакции

+7 (812) 591-65-28

E-mail: [mpmjournal@spbstu.ru](mailto:mpmjournal@spbstu.ru)

Компьютерная верстка А.Ю. Зобачева

---

Подписано в печать 11.06.2019 г. Формат 60x84/8. Печать цифровая  
Усл. печ. л. 10,0. Тираж 100. Заказ \_\_\_\_.

---

Отпечатано с готового оригинал-макета, предоставленного автором  
в Издательско-полиграфическом центре Политехнического университета Петра  
Великого. 195251, Санкт-Петербург, Политехническая ул., 29.  
Тел.: (812) 552-77-17; 550-40-14.

<b>Nucleation of islands with vertical or truncated corner facets in vapor-liquid-solid nanowires .....</b>	<b>159-164</b>
V.G. Dubrovskii, Zh.V. Sokolova, M.V. Rylkova, A.A. Zhiglinsky	
<b>Densification rate influence on nanopowder compactibility.....</b>	<b>165-177</b>
G.Sh. Boltachev, E.A. Chingina, A.V. Spirin, N.B. Volkov	
<b>Mechanism of molecule migration of carbon and silicon monoxides in silicon carbide crystal .....</b>	<b>178-182</b>
S.A. Kukushkin, A.V. Osipov, E.V. Osipova	
<b>Artifacts of stress relaxation technique to fit recovery activation parameters for low carbon steels .....</b>	<b>183-190</b>
Alexander A. Vasilyev, Semen F. Sokolov, Nikita A. Golubkov, Alexander A. Zisman, Dmitry F. Sokolov, Andrey I. Rudskoy	
<b>Bulk Green's functions in one-dimensional unsteady problems of elastic diffusion.....</b>	<b>191-197</b>
L.A. Igumnov, D.V. Tarlakovskii, A.V. Zemskov	
<b>The influence of gamma rays radiation on optically induced luminescence of copper-containing potassium-lithium-borate glass.....</b>	<b>198-203</b>
P.S. Shirshnev, V.A. Spiridonov, D.I. Panov, E.V. Shirshneva-Vaschenko, A.R.Gafarova, R.M. Eremina, A.E. Romanov, V.E. Bougrov	
<b>Boron and nitrogen dopant atoms precise tuning (increment and reduction) of charge-transfer rates in hydrogenated graphene.....</b>	<b>204-210</b>
G.K. Sunnardianto, F. Triawan, A.M. Amer, S. Hastuty, A.B.D. Nandiyanto, A.G. Abdullah	
<b>The structural transformation and mechanical strength OF Ni, Ti nanowires and Nitinol alloys at various vacancy rates: molecular dynamic study using Cleri-Rosato potential.....</b>	<b>211-223</b>
M.M. Aish	
<b>A molecular dynamics study of the buckling behaviour of graphene-reinforced aluminum nanocomposite plate.....</b>	<b>224-233</b>
Mithilesh K. Dikshit, Gokul S. Nair, Vimal Kumar Pathak, Ashish K. Srivastava	
<b>First principle electronic, magnetic and thermodynamic characterization of heavy fermion ternary rare earth metal alloys .....</b>	<b>234-241</b>
Ashish K. Srivastava, Mithilesh K. Dikshit, Vimal K. Pathak, Lakshya Khurana	
<b>Applied theory for electro-elastic plates with non-homogeneous polarization .....</b>	<b>242-255</b>
A.N. Soloviev, V.A. Chebanenko, P.A. Oganessian, Shih-Fong Chao, Y.-M. Liu	
<b>Boundary element time-harmonic analysis of 3D linear piezoelectric solids .....</b>	<b>256-264</b>
L.A. Igumnov, I.P. Markov, A.V. Boev	